UNIVERSITY OF BIRMINGHAM

MIXING IN HIGH THROUGHPUT EXPERIMENTATION REACTORS

by

Kenneth Hoi Kan Chung

A thesis submitted to
The University of Birmingham
for the degree of
DOCTOR OF PHILOSOPHY

Department of Chemical Engineering
School of Engineering
The University of Birmingham
December 2008

ABSTRACT

The application of High Throughput Experimentation (HTE) stirred vessels in the catalyst and pharmaceutical industries enable the parallel screening of potential formulations. Such tasks only require a fraction of the raw material and experimental time that are needed in conventional lab scale reactors. However their small sizes (~ 15-250 ml) contribute to a low Reynolds Number, *Re*, which results in poor mixing efficiencies. Together with unconventional geometries, i.e. lack of baffles and simple impeller designs, their fundamentals are not fully understood. The present study applies Particle Image Velocimetry (2-D PIV) and Planar Laser Induced Fluorescence (PLIF) techniques to a HTE scale stirred vessel (T = 45 mm, V = 72 ml) to determine the mixing behaviour.

Three mixing strategies: centreline unbaffled (U), conventional baffled (B) and off-centre eccentric agitator (E) configurations, were investigated using a pitched blade turbine (PBT). Experiments were performed in the high transitional regime ($Re \approx 6000$) using distilled water as the working fluid. A uniform power input of P/V = 168Wm^{-3} was applied. A method based on multiple horizontal and vertical 2-D PIV measurements was used to reconstruct the 3-D flow field in each of these configurations, since the conventional 3-D PIV is unusable at this scale. It was found that the determination of turbulent kinetic energy (TKE) using the isotropic assumption was perfectly valid for (B), but will lead to a considerable underestimation in both (U) and (E).

In addition to the three configurations, a square section vessel (S) (T = 41.5 mm, V = 72 ml) and regular vessel with a tilted impeller axis (T) were also studied. With a modified experimental procedure a log variance method for mixing time was applied using PLIF where all the usable pixels in an image were accounted for. Not only was (U) found to be highly inefficient, (B) also registered a slower mixing time due to a small amount of tracer being trapped behind the baffles, which makes the (E), (S) and (T) an even better choice in turbulent mixing. The use of (S) enabled the formation of a more compact HTE unit, also its trailing vortices were able to reach a height of y/H = 0.6, bringing more energy to the upper reaches of vessel, as visualised by angle resolved PIV measurements. The flow number of impeller and the amount of pseudo-turbulence were also determined and they agreed well with literature values.

However in the laminar mixing regime using Polypropylene Glycol (PPG) as the Newtonian working fluid (μ = 0.4–0.8 Pa s, P/V = 0.6–5.5 kWm^{-3}, Re = 5–35), at low Re values, (S) only managed a mixing performance comparable to the (U) configuration as the baffling effect of its four corners are less pronounced. However, mixing performance improves in (S) at higher Re values. (B) and (E) gave a comparable mixing performance, suggesting (E) should always be adopted for its viability in both turbulent and laminar mixing regimes.

For gas-liquid mixing using air and water (P_G/V = 168 Wm^{-3}, Q_G = 0.5–1.0 vvm), an image analysis algorithm was developed which enabled measurement of gas and liquid phase velocities separately. In addition to the PBT, a Rushton Disk Turbine (RDT) was also used ($C = D = 0.33T$). The power input required for the small mixing vessel to achieve complete gas dispersion was not achievable at the required gas flow rate; hence the experiments are carried out in the flooding regime. This had the advantage of clearly discernible differences between gas and liquid flow pattern for validation purposes. A new image algorithm was written to separate out bubbles in the imaging plane which transforms the in-plane bubbles into tracer particles. The local velocities of the gas phase are then obtained using the conventional cross-correlation technique. The results showed qualitative agreement with experimental observations of global gas phase flow patterns in literature.

Dedicated to my beloved parents

who lost their lives in a tragic accident,

but will always live in my heart.

"Enjoy failure and learn from it. You can never learn from success."

James Dyson, Engineer, Artist & Inventor

“In this world there exist no such impossible tasks

for those with perseverance.”

世上無難事，只怕有心人。

Chinese Proverb

ACKNOWLEDGEMENTS

First and foremost, I would like to express my gratitude towards supervisors Prof. Mostafa Barigou and Dr. Mark Simmons for not only their constant guidance, valuable input and supervision throughout the course of this research, but also for their friendship and encouragement. Without whom I would never have achieved so much.

I would also like to thank Dr. Waldemar Bujalski and Dr. Andreas Tsoligkas for the initial training of PIV equipments I have received and always being my first point of call during a hardware malfunction. I would like to thank Prof. Hugh Stitt and Dr. Jonathan Hall from Johnson Matthey Catalyst, along with colleagues Dr. Robert Fishwick, Dr. Fabio Chiti, Antonio Guida, Sophie Zhu and all the others who work in the field of fluid mechanics for the constructive discussions we have had. In addition, I really do appreciate the masterpieces produced by glassblower Steven Williams and Peter Hinton, David Boylin, Robert Sharpe and Philip Harris from the Mechanical Engineering workshop team. I would also like to thank the ever changing faces in the Multiphase Flow, Food, Micromanipulation and *all* the other research groups; Liz Hares, Lynn Draper, Jason Mahoney and all other great people form the General Office for their friendship and continuous support.

I would also like to thank my grandfather who raised me for his love, encouragement and understanding. I wish him good health and will always be happy.

Last but not least, I would like to thank my *then* classmate in Birmingham, friend, research project partner, *now* my beautiful wife and fellow PhD student Katie M. Liu for being there. I could not have done it without you.

TABLE OF CONTENTS

LIST OF FIGURES

LIST OF TABLES

NOMENCLATURE

A	Apparatus constant in fluorescent intensity calculation
AF	Assumption factor
a	Gas bubble interfacial area, m^2
b	Impeller blade thickness, m
b_L	Laser plane thickness, m
C	Impeller clearance from the bottom of vessel, m
$C(s)$	Cross correlation function
C_i, C_∞	Instantaneous and equilibrium tracer concentration, kg m^{-3}
C_{INJ}	Injection concentration of tracer, kg m^{-3}
Cs	Smagorinski Constant, 0.17 – 0.21
C_F	Frequency of seeding particle motion, Hz
C_t'	Desired mixedness
C_W	Impeller clearance to vessel wall, m
d_{10}	Arithmetic bubble mean diameter, m
d_{32}	Sauter mean diameter, m
d_p	Seeding particle diameter, m
dT	Time interval between two captures in PIV measurement, s
D	Impeller diameter, m
D_{HUB}	Impeller hub diameter, m
Fl	Impeller flow (pumping) number
Fl_G	Gas flow number
Fr	Froude number

g	Gravitational constant, 9.81 m s^{-2}
G_B, G_i, $G_{C\infty}$	Background, instantaneous and equilibrium greyscale level
G_T, G_∞	Threshold and final greyscale
h_g, h_u	Liquid height under gassed and ungassed condition, m
H	Liquid height in vessel, m
i, j, k	Cartesian coordinates
I_0	Intensity of exciting light at measuring point
I_1, I_2	Light intensity from the two images captured in PIV
I_F	Fluorescence Intensity
k	Turbulent kinetic energy, m^2 s^{-2}
k^*	Normalised turbulent kinetic energy
k_La	Gas liquid mass transfer coefficient, s^{-1}
L_{IA}	Length of Interrogation Area, m
M	Camera Magnification
n	Number of sampling points
N	Impeller rotation speed, s^{-1}
N_F, $N_{CD,}$ N_R	Impeller rotation speed for flooding, complete dispersion and gross recirculation, s^{-1}
P, P_G	Impeller power draw and gassed power draw, W
P_{MECH}	Mechanical losses, W
Po	Ungassed power number
$Px_{IMP,}$ Px_{IMP}	Pixels occupied by segregation and impeller
Q, Q_z, Q_r	Total, axial and radial impeller discharge flow, m^3 s^{-1}
$Q_{G,}$ Q_{GR}	Gas flow rate and gas recirculation, m^3 s^{-1}
Re	Impeller Reynolds number
s_x, s_y	Displacement in x and y directions, m

$\overline{S_{ij}}$	Filtered rate of strain, s^{-1}
$\langle S_{xy} \rangle$	Resolved strain rate, s^{-1}
t	Time elapsed since tracer injection in PLIF, s
T	Vessel diameter, m
u, v, w	Instantaneous velocity, m s^{-1}
u_p	Periodic velocity component, m s^{-1}
u', v', w'	Fluctuating velocity, m s^{-1}
$\overline{u}$, $\overline{v}$, $\overline{w}$	Ensemble averaged velocity, m s^{-1}
$\tilde{u}$, $\tilde{v}$, $\tilde{w}$	r.m.s. fluctuating velocity component, m s^{-1}
U_G	Superficial gas velocity, m s^{-1}
U_T	Terminal velocity of gas bubble, m s^{-1}
U_{TIP}	Impeller tip speed, m s^{-1}
$\overline{\langle v \rangle}$	Ensemble averaged *r-y* velocity, m s^{-1}
V_{INJ}	Volume of tracer injected, m^3
W	Impeller vertical width, m
z_W, z_0	Upper and lower boundary of impeller blades, m

Greek Symbols

ϕ	Circularity
Φ	Quantum yield
ϕ	Gas hold up
ε	Local specific energy dissipation rate, $m^2 s^{-3}$
ε_M	Molar absorption coefficient
$\bar{\varepsilon}_T$	Tank averaged specific energy dissipation rate, W m^3
λ	Wavelength, m

λ_{ex}, λ_{em}	Excitation and emitted wavelength, m
ρ, ρ_p	Fluid and seeding particle density, kg m^{-3}
η	Kolmogorov length scale, m
μ	Fluid dynamic viscosity, Pa s
σ^2	Variance
τ	Shear stress, Pa
τ_{90}, τ_{95}	Mixing time for 90% and 95% mixedness, s
$\tau_{i,j}$	SGS stress tenor, Pa
τ_R	Relaxation time of seeding particles, s
θ	Angular position, °
ω	Vorticity, s^{-1}
ν	Fluid kinematic viscosity, m^2 s^{-1}
γ	Gamma adjustment
$\dot{\gamma}$	Shear rate, s^{-1}

Abbreviations

2-D, 3-D	Two and three dimension
AOI	Area Of Interest
CARPT	Computer Automated Radioactive Particle Tracking
CCD	Charge-Coupled Device
CFD	Computational Fluid Dynamics
DNS	Direct Numerical Simulation
FFT	Fast Fourier Transform
HTE / HTS	High Throughput Experimentation / Screening
HWA	Hot Wire Anemometry
IA	Interrogation Area

LDA / LDV	Laser Doppler Anemometry / Velocimetry
LED	Light Emitting Diode
LES	Large Eddy Simulation
MRI	Magnetic Resonance Imaging
Nd:YAG	Neodymium Yttrium Aluminium Garnet
PBT (PBTu, PBTd)	Pitched Blade Turbine (in the up- and down- pumping mode)
PEPT	Positron Emission Particle Tracking
PIV	Particle Image Velocimetry
PPG	Polypropylene Glycol
PTV	Particle Tracking Velocimetry
r.m.s.	Root Mean Square
RDT	Rushton Disk Turbine
ROS	Rate Of Strain
SGS	Sub-Grid Scale
SLS	Selective Laser Sintering
SNR	Signal to Noise Ratio
TIFF	Tag Image File Format
TKE	Turbulent Kinetic Energy
TON	Catalyst Turnover Number
vvm	Vessel Volumes per Minute

1. INTRODUCTION

The stirred vessel is one of the most reviewed and commonly encountered industrial apparatus. During the development of a new process, the design of the industrial scale reactor and its operational conditions are always based on a smaller vessel in the laboratory scales in the order of at least 10 dm^3. A huge body of literature have provided researchers with methods for the translation of information regarding the various aspects of mixing from the pilot vessels to industrial size units. However, one should not assume that the scale-up methodologies remain appropriate if the volume of the laboratory scale vessels is further reduced, where even smaller vessels may be used to conserve both chemical volumes and reduce reaction time. Such vessels were introduced as mechanically agitated High Throughput Experimentation (HTE) reactors and are increasingly gaining in popularity within the pharmaceutical, catalyst and fine chemical industries as an efficient tool for molecule discovery and catalyst development. For example, automated HTE reactors such as the Advantage Series™ (Biotage, Sweden) are often used to test new catalyst formulations for use in hydrogenation and polymerisation reactions, where the operating conditions or even the viability of a process are based on the information produced by the HTE technique.

The size of these stirred vessels used is very small (~ 15-250 ml) and the associated low Reynolds numbers can cause poor mixing efficiency, particularly in viscous liquids, which can limit mass transfer rates and, thus, reaction rates. In addition to their miniature size, these vessels are often of unconventional geometry including the lack of baffles, off-centre or eccentric positioning of the agitator and low impeller off-bottom clearances, which

tends to preclude their characterisation via conventional scaling rules described in the literature.

As the applications of HTE technology are becoming more widespread, more detailed understanding of the hydrodynamics and mixing within such vessels is required to optimise their operation and, thus, maximise the screening efficiency of formulations. The current study on these small stirred vessels is very limited. Some previous work has been carried out within the School of Chemical Engineering to determine the hydrodynamics in single phase turbulent (Hall *et al.* 2004; 2005a), single phase laminar (Hall *et al.* 2005b) and gas liquid two phase flow (Hall *et al.* 2005c). The flow field studies and turbulence analysis were carried out using ensemble averaged data in the axial-radial direction obtained from 2-D Particle Image Velocimetry (PIV) and mixing times from an analysis based on Planar Laser Induced Fluorescence (PLIF). It was concluded that the mixing efficiencies were greatly improved if the impeller is allowed to relocate to an off-centre position (E), and the flow behaviours in HTE vessels were comparable to the mixing tanks in the lab scale.

For analysis of turbulent single phase systems, the assumption of isotropy would be expected to be valid for a fully baffled (B) configuration; however as a highly anisotropic flow arises from the use of other unconventional configurations, the omission of flow measurements in the tangential direction using 2D-PIV may affect the accuracy. Furthermore, the application of ensemble averaged PIV measurements for the analysis of turbulence quantities may also include pseudo-turbulence caused by periodicity due to blade passage, which can lead to serious overestimation of turbulent kinetic energy in parts of vessel as previously reported by Yianneskis and Whitelaw (1993), amongst others.

The calculations of mixing time by Hall *et al.* (2005b) using the PLIF technique was limited by the small number of sampling points that were permitted using their methodology. Moreover, mixing time analysis was not carried out in the laminar flow

regime. Since many HTE reactions such as polymerisations, may involve orders of magnitude changes in apparent viscosity as the reaction proceeds, determination of mixing times in the laminar regime is of considerable importance.

In terms of the gas / liquid two phase mixing, the mass transfer is affected by the hydrodynamics of both gas and liquid phases, and how they are coupled together. In the literature, flow visualisation of the gas phase in gas-liquid systems has been limited to very low gas hold-ups with small bubbles. Montante *et al.* (2007) and Horn *et al*. (2007) applied 2-D PI*V* to measure gas phase velocities in lab scale vessels. Measurements at the HTE scale by Hall *et al* (2005b; 2005c) only provided measurement of the liquid flow fields, along with parameters such as global gas hold-up. Measurement of gas phase velocity was not attempted. Since many HTE reactions involve gas-liquid reactions such as oxidations and hydrogenations, further exploration of methods to measure the gas phase and liquid phase hydrodynamics together would be highly beneficial.

The objectives of this study were therefore to examine aspects of the turbulent and laminar mixing performance of single phase systems using more detailed measurements, whilst investigating the possibilities of obtaining the full flow field in multiphase gas-liquid systems.

1.1 OBJECTIVES

The objectives of this study are

- *Measurement of three dimensional flow components for different configurations of the HTE vessel*. 2-D PIV measurements are taken in many vertical and horizontal planes and used to reconstruct the 3-D flow field inside the small vessel. Not only can the

degree of anisotropy then be quantified, the error induced by omitting the tangential component can also be determined.

- *The viability of each alternative configuration for different mixing duties.* The absence of baffles in an unbaffled vessel (U) creates solid body rotations in fluid. This results in a great degree of central vortex which hinders the efficiency of mixing. Hydrodynamic studies are carried out to compare alternative mixing strategies such as square section vessel (S) and tilting impeller configuration (T) with the ones previously studied.

- *Application of angle resolved PIV measurements and determination of pseudo-turbulence.* Angle resolved PIV measurements are made over a 60º sector located between two successive impeller blades. Trailing vortices, which carry the bulk of turbulence generated by impeller blades, are visualised. Periodicities are also observed from the animation of flow field in the azimuthal direction, along with the quantification of pseudo-turbulence.

- *Improved accuracy in mixing time analysis.* The experimental procedures are modified in PLIF in order to enable the application of log variance analytical method. Instead of monitoring the mixing performance from only a handful of sampling points, such technique utilises samples from all over the measurable volume which results in an analysis using information from the entirety of the field of view.

- *Further studies in the laminar mixing regime.* PLIF analyses are carried out in the laminar mixing regime with the use of viscous Newtonian fluids. Such method provides a direct comparison of the mixing efficiencies across the configurations, as well as the flow field studies and rate of strain (ROS) analysis which computes the localised value of total shear.

- *Measurement of gas phase velocities*. A new algorithm based on image analysis has been successfully employed to separate bubbles that are supposed to be tracked, and bubbles out of the laser plane which should be rejected. This enables measurement of the gas phase velocities and estimation of the local bubble size distribution. The effect of gassing on TKE distribution in the liquid phase is also studied.

1.2 THESIS LAYOUT

The subsequent layout of this thesis is as follows. A thorough review of existing literature on different aspects of fluid mixing in stirred tanks, an introduction to HTE technique and a review on the available flow visualisation techniques, are given in Chapter 2. The experimental procedures, experimental apparatus and equipment used and the underlying theory are described in Chapter 3.

Chapter 4 is the first of five results Chapters. Here the details of modifications made to the PLIF experimental procedure are given, in order to render the log variance method usable on the PLIF images. The application of 3-D reconstruction of PIV data and the benefit it brings over conventional 2-D ensemble averaged PIV measurements are shown in Chapter 5. Chapter 6 provides an insight into the flow field, turbulence and trailing vortices in the HTE scale vessels with the use of 2-D angle resolved PIV.

An investigation of the performance of the various configurations in the laminar mixing regime with the use of 2-D ensemble averaged PIV is described in Chapter 7, where the new algorithm which preconditions the raw images of gas bubbles captured by PIV cameras is described in Chapter 8. The algorithm selects only those that should be visualised and subsequently turning them into seeding particles and be measured by the

PIV. Finally, Chapter 9 summarises the key results of the thesis and gives recommendation for future work.

1.3 PUBLICATIONS ARISING FROM THESIS

1.3.1. JOURNAL

1. **Chung, K.H.K.**, **Barigou, M.**, **Simmons, M.J.H. (2007)** Reconstruction of 3-D flow field inside miniature stirred vessels using a 2-D PIV technique, *Transactions of the Institution of Chemical Engineers Part A*, **85**, 560. ISSN: 0263-8762.

2. **Chung, K.H.K.**, **Simmons, M.J.H.**, **Barigou, M. (2008)** Local gas and liquid phase velocity measurement in a miniature stirred vessel using PIV combined with a new image processing algorithm, submitted to *Experimental Thermal & Fluid Science*. ISSN: 0894-1777.

3. **Chung, K.H.K.**, **Simmons, M.J.H.**, **Barigou, M. (2008)** Angle resolved PIV measurements of flow and turbulence fields in small scale stirred vessels of different mixer configurations, submitted to & accepted for publication in *Industrial & Engineering Chemistry Research*. ISSN: 0888-5885 / 1520-5045.

1.3.2. CONFERENCE PROCEEDINGS

1. **Chung, K.H.K., Barigou, M., Simmons, M.J.H. (2006)** Reconstruction of 3-D flow field inside miniature stirred vessels using a 2-D PIV technique, *Proceeding of 12th European Conference on Mixing*, Bologna, Italy, 27th-30th June, 407-414. ISBN: 88-910915-9-7. (Oral Presentation)

2. **Chung, K.H.K., Barigou, M., Simmons, M.J.H. (2006)** Reconstruction of 3-D flow field inside miniature stirred vessels using a 2-D PIV technique, *Proceeding of 12th Formulation Engineering*, Birmingham, UK. (Poster Presentation)

3. **Chung, K.H.K., Barigou, M., Simmons, M.J.H. (2007)** PIV measurement of phase velocities in a miniature high throughput Gas/Liquid stirred vessel reactor, *Proceeding of the International Conference of Multiphase Flow*, Leipzig, Germany, 9th-13th July, CD. ISBN: 978-3-86010-913-7. (Oral Presentation)

4. **Chung, K.H.K., Simmons, M.J.H., Barigou, M. (2008)** Use of PLIF and PIV to characterise the laminar mixing of viscous fluids in a model High Throughput Experimentation stirred reactor, *Proceeding of the Sixth International Symposium on Mixing in Industrial Process Industries*, Niagara Falls, Canada, 17th-21st August. (Poster Presentation)

2. LITERATURE REVIEW

2.1 INTRODUCTION

2.1.1. MECHANICALLY AGITATED VESSELS

Over 50% of the world's chemical production involves the use of mechanically agitated stirred vessels for manufacturing high-added-value products (Hemrajani & Tatterson, 2004). The fundamental mechanism for these vessels is the transfer of momentum to the material within the vessel via the physical movement of rotating impeller blades. Some common examples of the uses of stirred vessels are given below:

- Homogenisation/blending of miscible liquids (dilution or gasoline additives) or emulsification of immiscible liquids (polymerisation or production of mayonnaise)
- Suspension of solids in a liquid phase (catalysis, crystallisation or solvent extraction)
- Gas dispersion in liquid (hydrogenation or oxidation reactions)
- Heat transfer

The huge variety of processes carried out in stirred vessels span a wide range of vessel sizes and geometries for optimal process efficiency. The standard nomenclature for the dimensions of a vertical cylindrical tank equipped with an impeller is shown in Figure 2.1. In the case where fluid is filled to a height, H, larger than tank diameter, T, multiple coaxial impellers may be installed. Four longitudinal wall baffles (of width usually equal to $T/10$) are usually installed for mixing in the transitional and turbulent regime to prevent

solid body rotation of the fluid, otherwise termed as fluid swirl, and to promote axial mixing between top and bottom parts of the vessel.

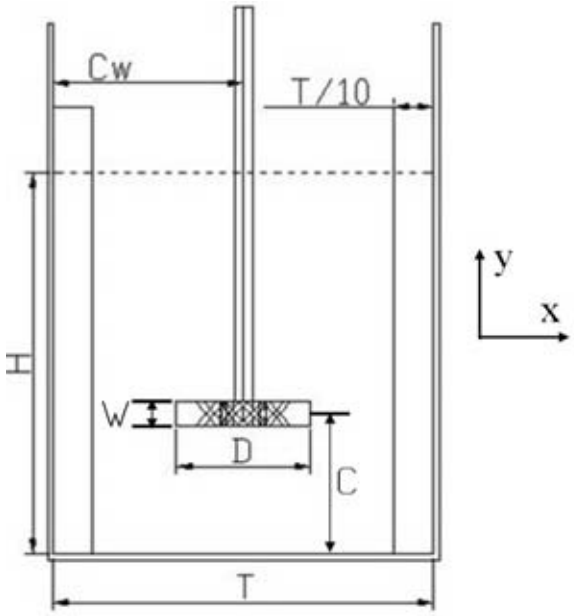

Figure 2.1 Standard nomenclature of a stirred vessel with an impeller. The vessel, of diameter, *T*, is filled to a liquid height, *H*. The impeller is of diameter, *D* and has a vertical width, *W*. The clearance from the bottom of the vessel to the centre of the impeller is *C*.

Impeller Choice and Resulting Flow Pattern

In a baffled vessel with standard configuration (i.e. $H = T$, $D = 1/3\ T$ & $C = 1/3\ T$), Edwards *et al.* (1992) illustrated axial and radial flow patterns as shown in Figure 2.2(a) & (b), where Figure 2.2(c) shows the experimental data of a mixed flow pattern published by Hall *et al.* (2005a). In a vessel with radial flow pattern, the strongly swirling flow is discharged radially from the impeller and separated into two streams at the vessel walls, forming upper and lower circulation loops. Whereas in an axial flow field, in this case a down pumping impeller is used, the strong downward impeller discharge impinges on the vessel bottom and rises along the vessel wall, which aids the suspension of solid particles before finally returning back into the impeller, forming one circulation loop.

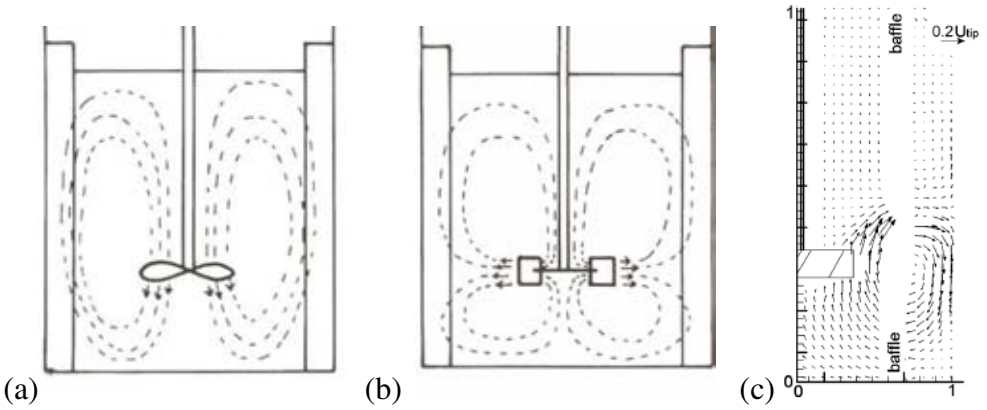

Figure 2.2 Typical flow pattern expected for a fully baffled vessel with (a) axial flow and (b) radial flow impeller (Edwards *et al.*, 1992) & (c) mixed flow impeller (Hall *et al.*, 2005a).

The type of impeller has a significant impact on the flow pattern and mixing efficiency, hence it should be carefully chosen based on the type of process being carried out. Down-pumping axial flow impellers, i.e., marine propellers and hydrofoils, are best used for suspension of solid particles. The simplest radial flow impellers on the other hand, are flat paddles and the Rushton Disc Turbine (RDT), as shown in Figure 2.3(a). When used for gas dispersion purposes, RDT suffers from a significant drop in power draw upon gassing, which is attributed to the formation of cavities behind the impeller blades. As a result, radial flow impellers with more complicated designs have been introduced such as the Scaba SRGT where the impeller blades are curved to prevent cavity formation; this in turn provides a better gas dispersion, higher gassed power and improved gas holdup compared to the standard RDT.

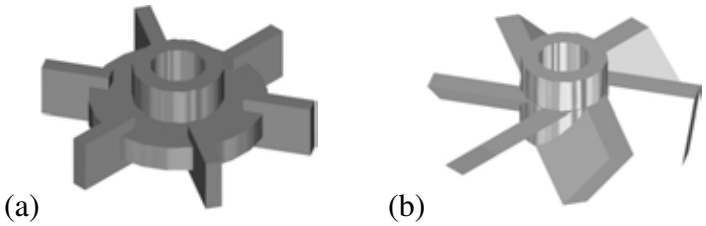

Figure 2.3 (a)RDT and (b)6-PBTu as used in this work.

If the blades of a flat paddle impeller are constructed at an angle to vertical, the direction of flow in the impeller discharge can be altered. An example of impellers of this type is the

Pitched Blade Turbine (PBT), as shown in Figure 2.3(b). The blades may be pitched at any angle between 10° and 90° but the most commonly adopted inclination is 45°. If the angle of the blade pushes the fluid downwards as the PBT is rotated, the flow is said to be in the down pumping mode i.e. PBTd. If the blade pushes the fluid upwards, either by reversing the direction of rotation or by rotating the blades by 90^{o}, the flow is in the up-pumping mode i.e. PBTu. In the down-pumping mode, the PBTd displays the characteristic of an axial impeller as shown in Figure 2.2(a) above. The up-pumping mode, using a PBTu has been proven to be very effective in general liquid blending and for gas dispersion (Bujalski & Nienow, 1990). The flow is discharged in both axial and radial directions in low to medium viscosity fluids as shown in the vector plot in Figure 2.2(c) published by Hall *et al.* (2005a); hence it is sometimes termed mixed flow. In the high transition to turbulent regime, the authors found that the mixed flow generated from PBTu produced a very strong lower circulation loop; such flow in the clockwise direction induced an upper circulation loop, but at a much weaker strength. However, if the impeller *D*/*T* ratio is raised above 0.55, the PBTu will become a radial flow impeller as centrifugal forces become dominant (Hemrajani & Tatterson, 2004).

A detailed summary which describes the impellers commonly used in liquids of different ranges of viscosity and the resulting flow patterns can be found in Zlokarnik (2001).

2.1.2. DIMENSIONLESS NUMBERS

Since the fluid mechanics and mixing within stirred vessels is highly complex, researchers have used dimensional analysis and reasoning as a means of characterisation. Some of the key dimensionless numbers are displayed in Table 2.1.

Table 2.1 Dimensionless numbers governing the mixing characteristics in stirred vessels (Edwards *et al.,* 1992)

Dimensionless number group	Components	Govern
Impeller Reynolds number, *Re*	$\frac{\rho ND^2}{\mu}$	The flow regime
Ungassed Power number, *Po*	$\frac{P}{\rho N^3 D^5}$	The power consumption
Froude number, *Fr*	$\frac{N^2 D}{g}$	The effect of gross vortex (neglected if *Re* < 300 for vessels with baffles installed or off centre agitation)
Impeller flow (pumping) number, *Fl*	$\frac{Q}{ND^3}$	The pumping efficiency of impeller

These parameters are interrelated (Edwards *et al.* 1992),

$$\frac{P}{\rho N^3 D^5} = fn\left\{\frac{\rho ND^2}{\mu}, \frac{N^2 D}{g}, \frac{T}{D}, \frac{W}{D}, \frac{H}{D}, etc\right\} \qquad (2.1)$$

where ρ and μ is the density and dynamic viscosity of the working fluid. g is the gravitational constant, taken to be 9.81 ms^{-2}. P is the impeller power draw, N is the impeller rotational speed and Q is the volumetric flow rate of impeller discharge.

The power consumption of stirred tanks contributes to a large proportion of the operating cost, therefore it is the interest of the process engineers to minimise such usage, while maintaining a satisfactory level of mixing efficiency. Power consumption measured at the impeller shaft is made up of two components, mechanical losses, P_{MECH}, and power draw, P. The impeller power number, *Po*, which is a dimensionless means of comparing the power drawn between impellers of various type and sizes, can in turn be calculated from P. Presently *Po* cannot be directly predicted by correlation; it can only be calculated from experimental power draw data or via Computational Fluid Dynamics (CFD) simulations (Brucato *et al.* 1998).

According to Hemrajani & Tatterson (2004), *Po* remains constant throughout the turbulent regime ($Re > 10^4$) and hence independent of liquid viscosity. However in the laminar regime ($Re < 10$), *Po* is inversely proportional to the impeller Reynolds number, *Re*. *Po* varies with *Re* for flow throughout the transition regime ($10^2 < Re < 10^4$). In a fully baffled vessel under single phase turbulent mixing conditions, *Po* is 5 and 1.7 for RDT and 45° PBT ($D = 0.33T$) impellers respectively (Jaworski & Nienow, 1994).

Pumping capacity, *Q*, which is described as the nominal volumetric flow rate of fluid passing through the planes surrounding the impeller as it rotates as illustrated in Figure 2.4, is often reported in terms of the pumping or flow number, *Fl*,

$$Fl = \frac{Q}{ND^3} \tag{2.2}$$

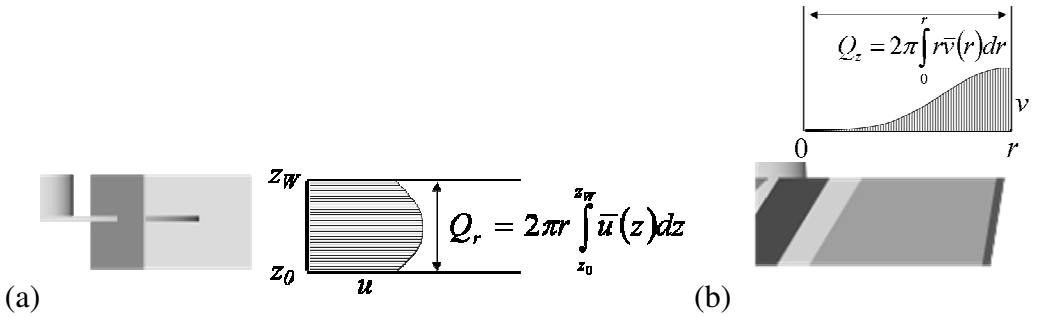

Figure 2.4 Measurement planes for an (a) radial flow and (b) axial flow impeller (PBTu shown here).

The plane of measurement depends on the direction of major flow discharge. For a radial flow impeller, *Q* can be calculated using,

$$Q_r = 2\pi r \int_{z_0}^{z_W} \bar{u}(z)dz \tag{2.3}$$

where z_0, z_W denotes the height at the bottom and top of impeller and $\bar{u}(z)$ is the ensemble averaged radial velocity at axial co-ordinate *z*.

For the axial flow impellers Q can be calculated from,

$$Q_z = 2\pi \int_0^r r\bar{v} dr \qquad (2.4)$$

where $\bar{v}(r)$ is the ensemble averaged radial velocity at axial co-ordinate r.

In cases when a mixed flow impeller is used, where a proportion of the discharge can be anticipated in both the axial and radial directions, the total flow may be determined by summing Q_z and Q_r.

Some of the *Fl* reported in literature concerning mixing vessels with fully turbulent flow are shown in Table 2.2.

Table 2.2 Examples of *Fl* reported in literature.

Authors	Impeller Type	Geometry*	*Fl*	Comment
Gunkel & Weber (1975)	RDT	T = 0.457m $D = 0.5T$, $C = 0.5T$	1.0	(-)
Fort *et al.* (1972[a],1974[b])	RDT	$D = 0.25T$[a], $D = 0.33T$[b]	0.7[a], 0.76[b]	(-)
Rutherford *et al.* (1996)	RDT	T = 0.294 m b = 0.008-0.033 T	0.75 – 0.84	*Fl* was found to decrease by as much as 15% if *b/T*, was increased from 0.008 to 0.033
Khan *et al.* (2004)	4-PBTd	T = 0.29m	0.86	*Fl* sensitive to the distance from measuring plane to impeller.
Hemrajani & Tatterson (2004)	RDT[a], PBT[b]	-	0.72[a], 0.79[b]	Averaged value from available literature (standard configurations)
Hemrajani & Tatterson (2004)	PBT	$D = 0.25T$[a], $D = 0.4T$[b] $D = 0.5T$[c]	0.88[a], 0.68[b], 0.62[c]	*Fl* is sensitive to *D/T*.
Aubin et al. (2004)	6-PBTu[a], 6-PBTd[b]	T = 0.19m, $D = 0.5T$	0.72[a], 0.68[b]	Similar *Fl* determined for a 6-PBT in up- and down-pumping mode.

*Unless stated otherwise, geometries described here are fully baffled stirred vessel with $H = T$, $D = 0.33T$, $C = 0.33T$.

The reported literature in Table 2.2 clearly showed that the *Fl* reduces significantly with increasing *D/T* ratio in fully turbulent flow. Therefore for HTE vessels where typically impellers with large *D/T* are employed, *Fl* is expected to be low.

2.1.3. HIGH THROUGHTPUT EXPERIMENTATION (HTE)

The discovery of new material and the rapid advancement in scientific research create a rising need for screening of potential compounds in the catalysis, pharmaceutical and fine chemical industries. To expedite this process, High Throughput Experimentation (HTE), sometimes referred to as High Throughput Screening (HTS) was introduced. The actual hardware used varies with the specific application but principally utilises automated parallel sampling units at much smaller scale compared to traditional screening processes. Since a large number of reactions and their subsequent analysis can be carried out simultaneously, HTE reduces both time and material required. Although HTE technologies have only been the subject of research in recent years, there is already literature published across a wide range of applications such as fixed packed bed (Moulijn *et al.* 2003), channel monolith module (Hendershot *et al.* 2003) and other types of reactors. The focus for this work, of course, concentrates on HTE technologies employing stirred vessels.

In many types of the commercially available HTE units, *D/T* ratio is enlarged and other additional features (such as gas inducing impellers and absence of baffles) are adopted for maximum efficiency, ease of cleaning and fouling prevention. Previous work at the University of Birmingham (Hall, 2005d) has focused on general aspects of mixing in HTE reactors. The turbulent kinetic energy (TKE) distribution in HTE scale vessels was examined using water as agitated medium and PIV/PLIF as the primary analytical tool (Hall *et al.*, 2004; Hall *et al.*, 2005a). It was found that HTE vessels with an off-centre impeller position (eccentric agitation) give a comparable mixing performance to that of fully baffled vessels, in terms of flow pattern and mixing time. As expected, a high level of solid body rotation existed in the concentric unbaffled vessels.

Mixing in HTE vessels under laminar flow condition was also investigated with the use of viscous Newtonian fluids (Hall *et al.*, 2005b). Polypropylene glycol (PPG) was used as the agitated medium in 45 and 60 mm vessels, utilising both baffled and eccentric configurations. It was found that the flow pattern of such systems is similar in orientation with the agitation of water in turbulent flow. However, the impeller showed radial flow behaviour in both vessels instead of the combined axial and radial flow anticipated. Shear field and elongation / deformational flow fields are found to be equivalent for baffled and eccentric configurations.

The same PIV technique was applied to the study of hydrodynamics in gas-liquid HTE vessels with the eccentric impeller configuration (Hall *et al.*, 2005b; 2005c). Bubble size distribution and gas hold-up were measured at gassing rates of 0.25 and 0.5 vvm in a 45 mm un-baffled vessel, agitated by 6-bladed up-pumping pitched-blade turbine. In this study, two gas sparger positions were used: directly below impeller and on the opposite side of vessel with the same degree of eccentricity. It was found that TKE distribution is similar for both sparger positions but showed significant difference with un-gassed results from previous studies.

Due to the direct relevance of this work to the current study, a detailed review for each of the three subject areas, single phase turbulence, laminar flow and gas-liquid two phase flow, can be found in later Sections 2.3.3, 2.4.1 and 2.5 respectively.

The work on HTE technologies produced by other groups however, concentrated much less on the aspects of mixing and hydrodynamics. For example, the determination of the gas liquid mass transfer coefficient, k_La, for hydrogenation reactions using an empirical correlation obtained for a conventional scaled vessel was proved to be inadequate in HTE

applications by Meille *et al*. (2004). The k_La versus global energy dissipation (P/V) in a 6 ml baffled bioreactor (T = 16mm, H = 48mm) with three coaxial Rushton Turbines (D = 0.435T) however, was found to be within ±40% deviation (accounting for all uncertainties and difference in measurement technique) from Van't Riet's equation; such accuracy cannot be contested by CFD simulations (Lamping *et al.*, 2003). Moreover, k_La versus P/V ratio in the 6 ml micro-bioreactor was found to be identical to a similar bioreactor of 20 litres in volume.

In terms of HTE stirred vessels, the impeller design and geometry (T = 25mm) were modified in a commercially available HTE system (Figure 2.5) by Grasso *et al*. (2003), for catalyst manufacturing by wet and dry impregnation. Tests were carried out on the sample prepared with the robotic system and the results illustrated good reproducibility of data and a close similarity with data obtained with equivalent manually prepared materials. It marks a major step of modification of standard configuration in HTE vessels for better efficiencies.

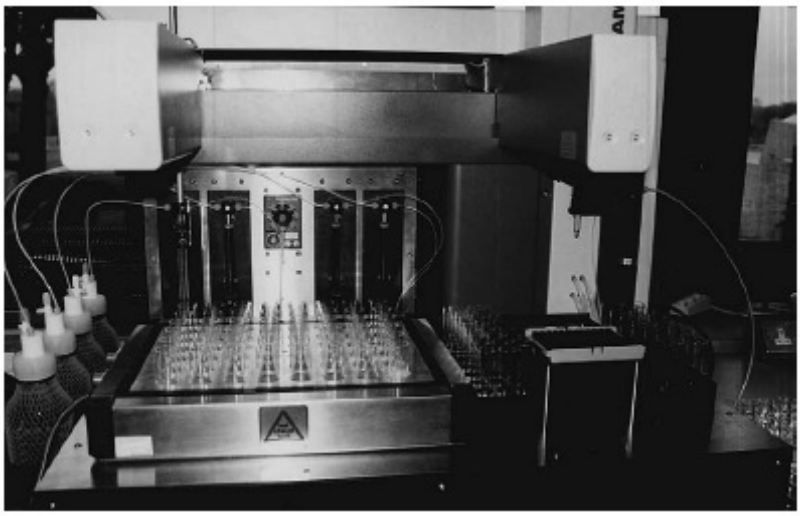

Figure 2.5 Hamilton Microlab Duo HTE system with two arms arrangement (Grasso *et al.* 2003).

The performance of a 2ml non-agitated HTE reactor for catalyst manufacturing was compared with a 450ml geometrically similar stirred autoclave (Spivack *et al.*, 2003). An important discovery in this research is that the screening result predicted the outcome of both lab and pilot scales. Good correlation ($R^2 > 0.98$) was achieved between the two scales in terms of catalyst turnover number (TON).

2.2 FLOW DIAGNOSTICS

Modern flow diagnosis techniques are broadly divided into two categories: single point and whole field measurements. The former detects the instantaneous flow velocity at a fixed point at a defined frequency in time, while the latter generates flow velocities over an entire area or volume at an instant in time.

Examples are:

- Single point: Hot wire anemometry (HWA), Positron Emission Particle Tracking (PEPT), Laser Doppler Velocimetry (LDV), Computer Automated Radioactive Particle Tracking (CARPT)

- Whole field: Particle Image Velocimetry (PIV), Magnetic Resonance Imaging (MRI).

The techniques of most relevance to this work are the optical techniques of LDV and PIV, hence this review is mainly based on these two methods and their derivatives.

2.2.1. LASER DOPPLER VELOCIMETRY (LDV)

Laser Doppler Velocimetry is a point based non-intrusive optical visualisation technique for liquid flow, whereas Laser Doppler Anemometry (LDA) is used to visualise flow in the gas phase with the use of the same experimental equipment. It uses the Doppler effect to measure the instantaneous velocities of seeding particles suspended in fluid. As shown in Figure 2.6, a single laser beam is divided into two beams with equal intensity, and then focused into a single point. The frequency of light scattered from particle located within the measurement volume is different from that of incident beam; this difference in frequency is known as Doppler shift and it is linearly related to the particle velocity (Brown *et al.* 2004).

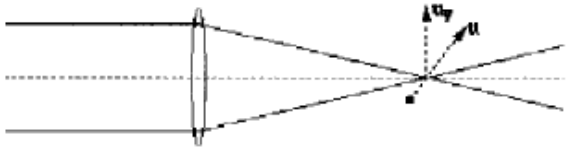

Figure 2.6 Intersection of two coherent laser beams (Mavros, 2001).

LDV can either be performed on forward- or back-scattered light. Data obtained from forward scattering LDV has a better signal-to-noise ratio, which benefits the measurement of high speed flows and flows with very low turbulence intensities as the turbulent fluctuations can be drowned out by noise. The simplicity of back scattering LDV, where all units are contained within a common housing, makes it the favourable choice for the average user since it saves the time required to align separate units.

Yianneskis & Whitelaw (1993) carried out angle resolved measurements around the blades of a RDT, with the use of LDV. It was found that a vortical pattern existed at all times up to 20° behind each blade. The turbulence quantities were shown to be overestimated by 400% if measurement is based on the mean velocities measured over a 360° cycle, which

includes the periodic contribution to the mean and fluctuating velocity from the blade passage. Similarly angle resolved measurements on a small scale vessel with a diameter of 100 mm were obtained by Baldi & Yianneskis (2003), with the use of 2-D PIV and LDA. In fully turbulent system where a hydrofoil impeller was used, it was found that the path of trailing vortices agreed well with previous literature. Furthermore, the variation of turbulence level with phase angle was found to be significant in the impeller region. With refractive index matching liquid and solid beads, Haam *et al.* (2000) was able to apply LDV to a multiphase system; it was shown that the presence of beads extracted energy from mean flow and subsequently provided that energy to fluctuating turbulence level.

2.2.2. PARTICLE IMAGE VELOCIMETRY (PIV)

Particle Image Velocimetry is a non-intrusive optical Eulerian whole-field technique. An insightful publication was produced by Raffel *et al.* (1998) including information regarding all aspects of PIV. It is based on measuring the displacement of tracer particles suspended within a thin plane of laser light. A PIV system typically consists of several sub-systems. As shown in Figure 2.7, the main component of a PIV setup includes a laser emitting unit, imaging optics and data processor.

Tracer particles are added to the volume of interest prior to experiments, in which they are to be illuminated by a pulse of laser light twice within a short controlled time interval. The laser is converted into a thin sheet via a series of lenses. The light scattered by the particles is recorded via charge-coupled device (CCD) camera on two separate frames as employed in this work, or via double exposure on a single frame of silver halide photographic film as used in earlier PIV systems. Tracer particle displacement is analysed by either cross-

correlation for the former method and autocorrelation for the latter. Within the known time interval, localised velocity vectors can be determined.

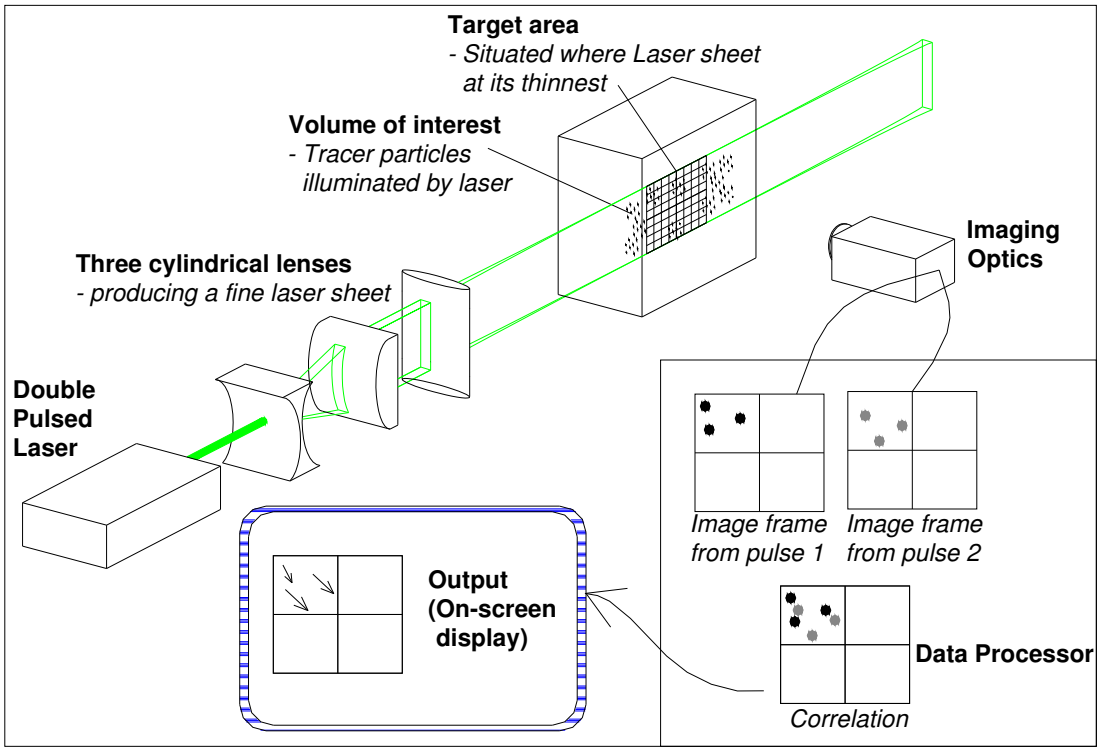

Figure 2.7 Simplified setup of a commercial PIV system.

Although the basic principles of PIV originated in the 1930s, it was not until the 1980's that the roots of modern PIV were developed (Chang *et al.*, 1985a; 1985b). A thorough description and review were given by Buchhave (1994). It was emphasized by Keane (1994) that the most important parameters that affect the cross correlation are as follows:

- Temporal resolution and time interval between image pairs
- Spatial resolution and the size of interrogation area
- The accuracy and reliability of velocity measurement

The tracer particles used are designed to follow the flow; hence they should be naturally buoyant. Melling (1997) produced a comprehensive study on relationship of the properties

of the tracer particles and measurement quality. Areas that affect measurement quality included the size of tracer particles with relevance to the area of interest, the scattered light intensity and the quantity of particles (optimal number = 15) in the interrogation volume. In addition, the particle must have a short relaxation time so it will truthfully represent the flow by following the fluid streamlines. Relaxation time, τ_R, is defined as the inverse of the frequency of particle motion, C_F,

$$C_F = \frac{1}{\tau_R} = \frac{18\mu}{\rho_p d_p^2} \tag{2.5}$$

where μ and ρ are the dynamic viscosity and density of the fluid respectively. It is shown that τ_R is proportional to the square of seeding particle size, i.e. $\tau_R \propto d_p^{\,2}$, hence the smallest permissible particle should be used. Fluorescence particles of d_p = 3 μm applied in low viscosity fluid and silver coated spheres of d_p = 10 μm used in high viscosity fluid in this work have τ_R of 5.25×10^{-7}s for and 1.46×10^{-8}s respectively; this is sufficiently small for the purpose of tracing the flow, which normally requires a temporal resolution in the region of 1×10^{-3}s.

The quantity of particles is usually vast in liquid flow and hence the identifying and tracking of individual tracer particles from both of the frames are impossible. Instead, the velocity fields are determined by statistical methods where the field of view is split into a grid. The movement of a group of particles within each grid element area is determined; this area is usually referred as Interrogation Area (IA). The increment of IA size is the power of 2 (16×16, 32×32 or 64×64) and the physical length of the side of each element is the length of the IA, L_{IA}. Cross correlation is carried out within each IA from digitally captured images. This process correlates the image intensity field of the two spatially identical IA in the first and second image; hence the signal strength is vastly improved

compared to the autocorrelation carried out on the single frame double exposure films. This increase in signal strength allowed the use of higher seeding density and flow visualisation can also be carried out at a higher spatial resolution. Most importantly of all, zero velocities and direction can be identified, which is impossible for autocorrelation.

The cross correlation function of the two intensities from the interrogation spots is defined to be (Keane, 1994),

$$C(s) = \int\int I_1(X,Y) I_2(X + s_x, Y + s_y) dXdY \qquad (2.6)$$

where I_1 and I_2 are the light intensity from the first and second image respectively and s is a two dimensional displacement vector $(s_x, s_y)^T$. Fast Fourier Transforms (FFT) is used to perform the calculation and the probability distribution of particle displacement is generated across the IA as shown in Figure 2.8. The distinctive peak represents the highest particle displacement probability from the centre of IA, therefore the displacements, s_x and s_y, in x and y directions respectively for the particular IA are determined and subsequently transformed into instantaneous velocity u and v, since the time interval between the two images is known.

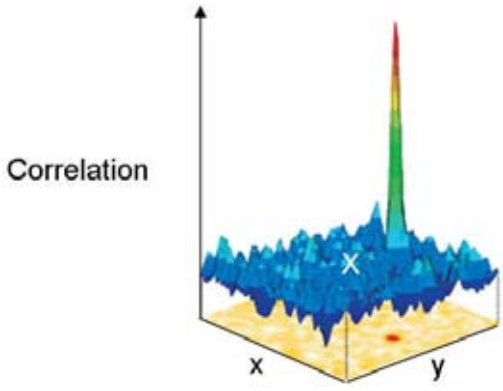

Figure 2.8 Illustration of cross-correlation process (La Vision).

The first notable work of 2-D PIV measurement on stirred vessels was carried out by La Fontaine & Shepherd (1996), who measured the time-averaged velocities at planes in

numerous locations across the vessel. Stagnant flow regions, circulation patterns and the turbulent nature of the flow were observed. In the laminar mixing regime, PIV flow maps were used to validate those obtained by CFD made on a multiple coaxial RDT driven stirred vessel at Re = 20-160 by Zalc *et al.* (1999) with good agreement.

Three dimensional PIV (3-D PIV) was developed to determine velocity information in all three directions and is usually of the holographic or stereoscopic type (Fomin, 1998). The principle of holographic PIV (HPIV) is explained by Hinsch (1995), who also reviewed recent developments (Hinsch, 2002). Holography is a method used to store the amplitude and phase of a light wave by recording the interference pattern that occurs when a reference wave is superimposed. The processed interference pattern, the hologram, is used to reconstruct the original wave field by illuminating it with a replica of the reference wave. However, it is practically very costly in terms of both equipment and computing power; a 100×100 mm^2 holographic plate contains at least 50 Gb of digital information. Stereoscopic PIV, on the other hand, is a simple and low cost alternative. Commercial 3-D PIV units are often constructed in the Scheimpflug configuration (Figure 2.9) where two cameras visualise flow in the same area of interest (AOI) at different angles. 2-D flow data obtained from images captured by both cameras through the use of a calibration graticule are re-sampled and this yields the third velocity component (Hinsch, 1995).

Stereoscopic PIV has been used by the mixing community and there is already a large number of papers utilising such flow visualisation in stirred vessels (Hill *et al.,* 2000; Khan *et al.,* 2006).

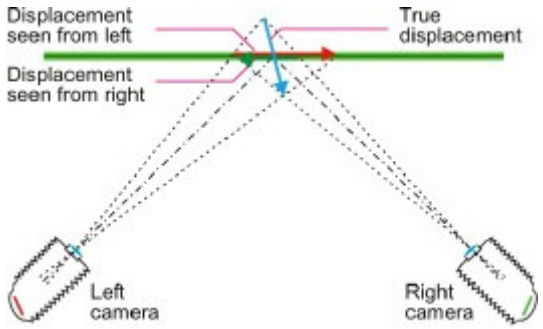

Figure 2.9 Stereoscopic PIV utilising the Scheimpflug configuration (Dantec Dynamics).

Summary

A brief summary of the flow visualisation techniques discussed is given in Table 2.3,

Table 2.3 Summary of available flow visualisation techniques.

Flow diagnostic technique	Spatial Resolution (m)	Maximum Temporal resolution (Hz)	Category
LDV	5×10^{-5}	4×10^{-7}	Point-by-point measurement.
PIV	2×10^{-4} [whole field] 7×10^{-5} [μPIV]	5×10^{-5}	Instantaneous global measurement [whole-field method].

Furthermore, a summary of the most relevant studies to this work using LDV/PIV is given in Table 2.4

Table 2.4 Summarisation of relevant work.

Authors	Impeller Type	Geometry*	Measurement Technique	*Re*	Main Findings / Comment
Yianneskis & Whitelaw (1993)	RDT	T = 0.294m	LDV	4.8×10^{4}	400% overestimation of turbulence quantities in time averaged measurement
Kresta & Wood (1993)	4-PBTd	T = 0.15m, D = 0.5T, C =0.25T	LDV	3.75×10^{4}	Maximum k^{*} = 0.1 U_{TIP}^{2} in the impeller region
Hockey & Nouri (1996)	60º 4-PBTd & RDT	T = 0.3m	LDV	4.8×10^{4}	Performance of PBT is superior compare to RDT

Saareninne *et al.* (1997)	2-paddle	T = 0.09m, D = 0.54T, H = 2.0T	PIV	600	95% of TKE can be determined for a spatial resolution of 20η, where 2η is required for 90% accuracy in energy dissipation calculation.
Armenante *et al.* (1997)	6-PBTd	T = 0.29m	LDV	7.1-11.1×10^4	LDV data on unbaffled tanks compared to simulation. k-ε turbulent model does not correlate well
Schäfer *et al.* (1998)	4-PBTd	T = 0.15m	LDV	7.3×10^3	Maximum k^* = 0.04-0.085 U_{TIP}^2 in the impeller region
Zalc *et al.* (1999)	3-coaxial RDT	T = 0.24m H = 1.5T	PIV	20-160	Validation of PIV result with CFD simluations
Sheng *et al.* (2000)	6-PBTd	T = 0.292m, D = 0.35T, C = 0.46T	PIV - LES	9.2×10^3	Application of LES-PIV measured SGS energy flux to estimate turbulence dissipation rate.
Alvarez-Hernández *et al.* (2000)	3 coaxial RDT	T = 0.2m, H = 2T	PLIF	40	Segregation in laminar system was identified by PLIF.
Aubin *et al.* (2004)	4-PBTu/d	T = 0.19m	PIV	4.5×10^4	Measurement of liquid phase velocity in gas / liquid two phase flow.
Baldi & Yianneskis (2003[1], 2004[2])	Hydrofoil[1] RDT[2]	T = 0.1m	2/3-D PIV, LDV	1.5-4×10^4	Significant difference in the direct measurement of ε between PIV and LDA occurs only in high Re range.
Khan *et al.* (2004, 2006)	4-PBTd	T = 0.29m	Angle resolved 3-D PIV	4.75×10^4	'Multi-block' approach to enhance spatial resolution. Trailing vortices exists 120º after blade passage. Maximum k^* > 0.06 U_{TIP}^2 and slightly higher k^* measured in vortex with 3-D PIV.
Hall *et al.* (2004a, 2005a)	6-PBTu	T = 0.035-0.06m, D = 0.54T, C_W = 0.33-0.5T	PIV	4-11×10^3	Turbulent flow behaviour in HTE vessels even at Re = 4×10^3. TKE dependent on scale. SGS model found to be inaccurate in ε calculation.
Hall *et al.* (2005b,c)	6-PBTu	T = 0.045m, D = 0.54T, C_W = 0.33-0.5T	PIV	11-30 [a] 5.5-6.3×10^3 [b]	Pseudo-cavern was defined and their size depend upon the power input. Rate of stain contour was also calculated. [a] Liquid flow field is significantly altered when gas is introduced. Two sparger position was studied in eccentric HTE vessel and this affects the flow field and TKE distribution.[b]
Horn *et al.* (2007)	RDT	T = 0.236m, C = 0.5T	PIV	4.6×10^4	Applied shadow processing software to determine bubble size distribution but found to be unreliable.
Montante *et al.*(2007)	RDT	T = 0.236m, C = 0.5T	PIV	4.6×10^4	Simultaneous gas / liquid phase velocity measurement at low gassing rate of 0.02vvm.

*Unless stated otherwise, geometries described here are fully baffled stirred vessel with H = T, D = 0.33T, C = 0.33T & C_W = 0.5T.

[a] Mixing in the laminar regime and [b] Gas/Liquid two phase flow in Hall *et al.* (2005b)

2.3 MIXING IN THE TURBULENT REGIME

2.3.1. CHARACTERISATION OF TURBULENT FLOW IN STIRRED TANKS

Fluid mixing in the process industries, with a few exceptions such as fermentations, normally takes place in the turbulent regime. Turbulent mixing is caused by mass, momentum and energy transfer from the agitator to the fluid within the stirred vessel, through the formation and dissipation of turbulent eddy structures. The two very basic parameters used in describing turbulence are the turbulent kinetic energy (TKE), *k,* and local specific energy dissipation rate, ε. These parameters appear in the k-ε turbulence closure model which is applied by many Computational Fluid Dynamics (CFD) packages.

Turbulent Kinetic Energy (TKE)

In defining the properties of a turbulent flow, the usual approach is to perform a Reynolds decomposition where the instantaneous velocity, *u,* has a mean velocity, $\overline{u}$, and fluctuating velocity, u' , components as such,

$$u = \overline{u} + u' \tag{2.7}$$

The turbulent kinetic energy, *k*, is obtained from the root mean square (r.m.s.) of the fluctuating velocity components and can hence be obtained from,

$$\tilde{u}^2 = \overline{(u-\overline{u})^2}\,,\ \tilde{v}^2 = \overline{(v-\overline{v})^2}\,,\ \ \tilde{w}^2 = \overline{(w-\overline{w})^2} \tag{2.8}$$

in the radial, axial and tangential directions respectively. Here the overbar indicates resolved time-averaged quantities. The TKE takes the form of the half trace of the Reynolds stress tensor, i.e.

$$k = \frac{1}{2}\left(\tilde{u}^2 + \tilde{v}^2 + \tilde{w}^2\right) \tag{2.9}$$

Within stirred vessels, it is usual to normalise by the impeller tip speed, $U_{tip,}$ for ease of comparison between different configurations, thus

$$\sqrt{\tilde{u}^2}^* = \frac{\sqrt{\tilde{u}^2}}{U_{tip}}, \quad k^* = \frac{k}{U_{tip}^2} \tag{2.10}$$

2-D PIV yields $\tilde{u}^2$ and $\tilde{v}^2$. Assuming isotropy, the missing fluctuating velocity component in the z direction, $\tilde{w}^2$, can be estimated by a 2-D approximation (Sheng *et al*., 2000), thus

$$k = \frac{1}{2}\left(\tilde{u}^2 + \tilde{v}^2 + \frac{1}{2}\left(\tilde{u}^2 + \tilde{v}^2\right)\right) = \frac{3}{4}\left(\tilde{u}^2 + \tilde{v}^2\right) \tag{2.11}$$

The 2-D approximation only gives identical results to the ordinary 3 component TKE calculation under perfect isotropic flow conditions.

Angle Resolved Measurements

For PIV measurements the r.m.s. fluctuating velocity component, $\tilde{u}$, as employed in the turbulent kinetic energy calculation, refers to the a large number of velocity fields captured at a known frequency; hence flow information is averaged over random blade positions. The number of acquisition from PIV required for an accurate representation of mean and r.m.s. flow field in a turbulent system is usually 500 (Saareninne *et al.*, 2001; Khan *et al.*, 2004), although a smaller number may be found in literature, i.e., 300 in Khan *et al.* (2006), 200 in Hall *et al.* (2005) and 100 in Sharp & Adrian (2001); the effect on the number of acquisitions on the accuracy of r.m.s. calculation can be found in Chapter 5. Angle resolved measurements are taken at a fixed angle between two impeller blades, while it is also averaged over a large number of acquisitions as for the $\bar{u}$ calculation.

Angle resolved measurements enable determination of the periodic velocity component, u_p, due to blade passage. Performing a decomposition on angle resolved data yields,

$$u = \bar{u} + u_p - u' \tag{2.12}$$

where u_p is defined as (Khan, 2005),

$$u_p = \bar{u}\big|_\theta - \bar{u}\big|_{all\,\theta} \tag{2.13}$$

Therefore removal of the blade passage frequency reduced the r.m.s. velocity components to a level representing the true turbulent fluctuations rather than fluctuations including the blade passage, which are not random.

Vorticity

Trailing vortices can be quantified by vorticity, ω, which measures the rotation of the fluid. It can be defined as the curl of the velocity vector, u (Marsall & Bakker, 2004),

$$\omega = \nabla \times u \tag{2.14}$$

Vorticity can be defined in both 2D and 3D flows, in the direction normal to the plane of measurement. For a 2D PIV measurement of flow in stirred vessel, the vorticity is always in the circumferential direction as,

$$\omega = \frac{\partial v}{\partial x} - \frac{\partial u}{\partial y} \tag{2.15}$$

where positive ω indicates counter-clockwise rotation and a negative value denotes clockwise rotation. Vorticity analysis not only provides vital information of the size and strength of trailing vortices, but also gives the location of the centre of vortex.

2.3.2. LOCAL SPECIFIC ENERGY DISSIPATION RATE

In turbulent flow k is generated at the largest eddy scales by the passage of the impeller. These large anisotropic eddies contain the bulk of the total kinetic energy and have large velocity fluctuations. They break down to form smaller eddies and the energy is transferred to smaller and smaller length scales until it finally dissipates as heat. Below a certain cut–off length scale, the behaviour of the eddies becomes isotropic and at the smallest scales in the flow, within what is known as the universal equilibrium range, the eddies can be classified as within either the inertial sub-range, where viscous forces do not dominate, or within the viscous sub-range where they decay to produce heat. Via dimensional arguments, Kolmogorov (1941) proposed a relationship for the size of the smallest eddies in the flow, named the Kolmogorov length scale, η, as,

$$\eta = \left(\frac{\nu^3}{\varepsilon_T} \right)^{\frac{1}{4}} \tag{2.16}$$

A very detailed review on the Kolmogorov's 1941 theory and its applications is given in Frisch (1995).

In terms of accuracy, a spatial resolution of 20 η would provide approximately 95% of TKE information (Saarenrinne *et al.*, 2001). However, ε estimation with 90% confidence would require a spatial resolution of at least 2 η. Current technology limitations generally prohibit measurements to this accuracy.

As described earlier, the work of Saarenrinne *et al.* (2001) indicated that ε in stirred vessels can be estimated with 90% confidence if a spatial resolution of at least 2 η is attained. There are a few methods available for the calculation of ε and a detailed summary is given by Sheng *et al.* (2000), such as the direct measurement of strain rate tensors, TKE balance

and Taylor's frozen turbulence hypothesis. Utilising these methods usually involves experiments using LDV and multiple HWA or mathematical models employing Direct Numerical Simulation (DNS), which either lacks the resolution required or is not suitable for the complex 3-D flow field in stirred tank applications. With any standard PIV system it is currently not possible to achieve the spatial resolution required without sacrificing the size of measurable area. However, if a 3D-PIV is employed and the required spatial resolution is achieved, the following expression taken from energy balance on the turbulent flow is valid (Hinze, 1975; Baldi & Yianneskis; 2003 & 2004),

$$\varepsilon = \nu\left\{\begin{array}{l} 2\left(\overline{\left(\frac{\partial u_i}{\partial x_i}\right)^2}+\overline{\left(\frac{\partial u_j}{\partial x_j}\right)^2}+\overline{\left(\frac{\partial u_k}{\partial x_k}\right)^2}\right) \\ +\overline{\left(\frac{\partial u_i}{\partial x_j}\right)^2}+\overline{\left(\frac{\partial u_j}{\partial x_i}\right)^2}+\overline{\left(\frac{\partial u_i}{\partial x_k}\right)^2} \\ +\overline{\left(\frac{\partial u_k}{\partial x_i}\right)^2}+\overline{\left(\frac{\partial u_j}{\partial x_k}\right)^2}+\overline{\left(\frac{\partial u_k}{\partial x_j}\right)^2} \\ +2\left(\overline{\frac{\partial u_i}{\partial x_j}\frac{\partial u_j}{\partial x_i}}+\overline{\frac{\partial u_i}{\partial x_k}\frac{\partial u_k}{\partial x_i}}+\overline{\frac{\partial u_j}{\partial x_k}\frac{\partial u_k}{\partial x_j}}\right) \end{array}\right\} \tag{2.17}$$

where ν is the kinematic viscosity and subscripts i,j,k denote the three directions in Cartesian coordinates. For 2D-PIV however, since only 5 of the 12 terms can be measured, the remaining 7 terms are obtained by employing the local isotropy hypothesis,

$$\varepsilon = \nu\left\{\begin{array}{l} 2\overline{\left(\frac{\partial u_r}{\partial r}\right)^2}+2\overline{\left(\frac{\partial u_z}{\partial z}\right)^2}+3\overline{\left(\frac{\partial u_r}{\partial z}\right)^2} \\ +3\overline{\left(\frac{\partial u_z}{\partial r}\right)^2}+2\overline{\frac{\partial u_r}{\partial z}\frac{\partial u_z}{\partial r}} \end{array}\right\} \tag{2.18}$$

Sheng *et al.* (2000) proposed a dissipation rate estimation method (PIV-LES) which presented as a viable method for PIV users who sacrifice spatial resolution for a larger whole field measurement area. PIV measurements are limited to finite grid size equal to the L_{IA}, this acts as a low pass filter and eddies smaller than the grid size are not resolved.

In LES, eddies larger than the cut-off scale are assumed to be dependent upon the bulk flow and highly anisotropic: their turbulent motion is calculated from the transport equations. Below the cut–off scale, or the sub-grid scale (SGS), the eddies are assumed to be isotropic and due to their universal nature, they can be readily obtained via simple models. The analogy here with PIV-LES measurements, provided an appropriate value of SGS is chosen, is obvious.

The value of local specific energy dissipation rate can be determined from this model as

$$\varepsilon = \left\langle \varepsilon_{SGS} \right\rangle = -2\left\langle \tau_{ij} \overline{S}_{ij} \right\rangle \tag{2.19}$$

where τ_{ij} is the SGS stress tenor and $\overline{S}_{ij}$ is the strain rate tensors in the resolved scale.

$\overline{S}_{ij}$ can be obtained from,

$$\overline{S}_{ij} = \frac{1}{2}\left(\overline{\frac{\partial U_j}{\partial x_i}} + \overline{\frac{\partial U_i}{\partial x_j}} \right) \tag{2.20}$$

whilst $\tau_{ij} = \overline{u_i u_i} + \overline{U}_i \overline{U}_j$, it needs to be closed by a suitable SGS model. Sheng *et al.* (2000) showed that the choice of closure model had no significant effect upon dissipation rate estimation, therefore the Smagorinski eddy viscosity model was employed for its simplicity and ability to analyse experimentally determined velocity information, although it is generally regarded as unsuitable for laminar applications. ε_{SGS} can be determined by Smagorinski model (Smagorinski, 1963) as,

$$\varepsilon_{SGS} = -(C_S L_{IA})^2 \left|\overline{S}\right| \overline{S}_{ij} \tag{2.21}$$

where $\left|\overline{S}\right| = -\left(2\overline{S}_{ij}\overline{S}_{ij}\right)^{\frac{1}{2}}$ and C_S is the Smagorinski constant which varies from 0.17 (Sheng *et al.*, 2000) to 0.21 (Sharp & Adrian, 2001). Equation 2.22 can be expanded in terms of measured gradients in Cartesian coordinates with Equation 2.21 as such (Khan *et al.*, 2005),

$$\varepsilon_{SGS} = (C_S L_{IA})^2 \left(4\overline{\left(\frac{\partial u}{\partial x}\right)^2} + 4\overline{\left(\frac{\partial v}{\partial y}\right)^2} + 2\overline{\left(\frac{\partial u}{\partial y}\right)^2} + 2\overline{\left(\frac{\partial v}{\partial x}\right)^2} \right)^{\frac{3}{2}} \tag{2.22}$$

2.3.3. THE APPLICATION OF LDV/PIV ON STIRRED VESSELS IN THE TURBULENT REGIME

Conventional Lab Scaled Stirred Vessels

Yianneskis & Whitelaw (1993) employed LDV to study the structure of trailing vortices behind RDT blades. It was found that turbulence quantities can be overestimated by 400% if the ordinary time average approach is adopted. TKE is at a maximum of 0.19 U_{TIP}^2 near impeller blades and flow is highly anisotropic around the impeller. This is supported by Hockey & Nouri (1996) who obtained a maximum time averaged TKE of 0.15 U_{TIP}^2, an overestimation of 2 times which was also reported by Schäfer *et al.* (1998). Therefore, angle resolved measurement should always be used if possible.

The work produced by Schäfer *et al.* (1998) has significant relevance to this study. The group employed LDV to measure the angle resolved velocity over seven angular planes of a top-covered vessel agitated by a 4-PBTd (T = 0.15m, D = 0.33T, C = 0.33T, Re = 7300), with silicon oil as working fluid (ρ = 1039kgm^{-3}, μ = 0.0159pa s). A detailed plot was produced which highlights the variation of axial mean and r.m.s. velocity, over the range of

90° angle measured, along with contour plots of TKE at various angular planes. Vorticity was calculated which in turn enable the identification of the vortex centre; diameter of such vortex is found to be 0.3*D*. The findings are concluded in Figure 2.10.

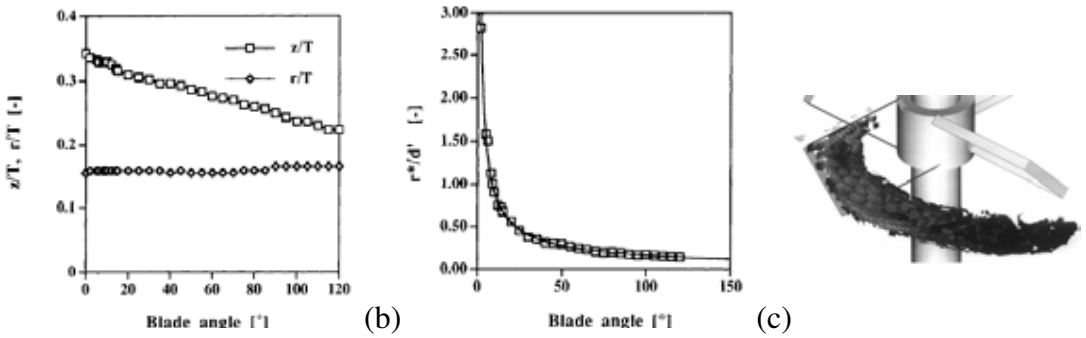

Figure 2.10 (a)Variation of vortex axis with blade angle, (b) Vortex size & (c) iso-surface plot of trailing vortices in a 4-PBTd agitated vessel (*Re*=7300) (Schäfer *et al.* 1998).

Vorticity analysis was also performed on a stirred vessel agitated by RDT (T = 0.15 m, D = 0.33T, C = 0.5T, Re = 4580), from whole field data generated from PIV. It was shown that trailing vortices exist even at an angle of 50° after the passing of impeller blade; it also supported previous literature regarding the severe loss of information if data are captured on time-averaged basis. Also quoted by Schäfer *et al.* (1998), the use of a lid, of which the primary function is to suppress the rise of free surface, only affects the flow in the immediate vicinity of the free surface; it has no effect on the velocity anywhere else in the vessel (Nouri & Whitelaw, 1990).

In a fully baffled stirred vessel agitated by a 60° 4-PBTd (T = 0.3m, D/T = 0.33, C/T = 0.33, Re = 48000) in the turbulent regime, Hockey & Nouri (1996) reported an anisotropic flow; the radial r.m.s. values were greater than that of tangential direction, and both were larger than that in the axial direction. The value of k^* measured in the impeller discharge was 0.15 U_{TIP}^2. An energy balance gave 6% energy dissipation in the impeller region and 70% in the mean flow; the rest went into turbulence production. The performance of the

PBT is superior compared with a RDT, where the latter generates only a quarter of the mean flow per unit power input with the same amount of energy into turbulence, but a larger portion is dissipated in the impeller region.

Schäfer *et al.* (1998) obtained a much lower maximum k^* of 0.04-0.085 U_{TIP}^2 in the impeller region, and > 0.015 U_{TIP}^2 in the bulk with silicone oil as working fluid (T = 0.15 m, $D = 0.33T$, $C = 0.33T$, Re = 7300), agitated by a 45° 4-PBTd. Using a slightly larger 4-PBTd in the same vessel (T = 0.15m, $D = 0.5T$, $C = 0.25T$) filled with water, Kresta & Wood (1993) obtained a maximum k^* of 0.1 U_{TIP}^2 in the impeller region. It should be noted that the velocities in the above work were all measured by LDV where components in all three directions were obtained.

Khan *et al.* (2004) employed angle resolved 2-D PIV for the measurement of TKE distribution in a 90° section of a fully baffled stirred vessel with 4-PBTd ((T = 0.29 m, $D = 0.33T$, $C = 0.33T$, Re = 47500). The authors adopted a 'multi-block' approach for increased spatial resolution while maintaining a whole field measurement; this is achieved by joining sections of multiple small but highly resolved measurement 'blocks' together. It was found that the mean axial velocity was lower than that of Schäfer *et al.* (1998), which is plausibly due to the use of thicker blades; the r.m.s. axial velocity components however, were found to be greater, which is due to a substantially larger Re. It was found that the highest k^* was periodically measured in the trailing vortices at > 0.06 U_{TIP}^2; the trailing vortices existed 120° after blade passage. A very low k^* was measured in the bulk region of vessel in the range of 0-0.003 U_{TIP}^2. The validity of the 2-D TKE approximation method was examined by Khan *et al.* (2006) where the result from the previous work was compared with the 3-D data obtained from stereoscopic PIV without the 'multi-block' approach. At blade angle of 0°, TKE distribution and magnitude were found to be very

similar in the impeller discharge region between two methods of measurement, although a slightly higher k^* was measured in the centre of vortex by stereoscopic PIV.

Vessels with Unconventional Sizes and Geometries

As described in previous sections, HTE vessels are typically unbaffled, with a large *D/T* radius and sometimes adopting an off-centre impeller position. There are studies investigating flows in these unconventional configurations in the larger scales for different purposes, however the amount of such literature is scarce.

The removal of baffles reduces the axial circulation and promotes tangential circulation, therefore the use of unbaffled vessels in turbulent systems is limited to a few applications; for example, in suspension polymerisation, the shear created by baffles results in smaller drops that is highly undesirable. The use of baffles contributes to particle attrition phenomena that are highly undesirable in crystallisation and precipitation processes (Mazzarotta, 1993). In addition, particle liquid mass transfer rate increases for a given power input if baffles are removed (Grisafi *et al.* 1994), hence in some applications the lack of baffles is desired. Without the use of baffles, the amount of solid body rotation increases drastically, forming a gross vortex which causes free surface elevation. Ciofalo *et al.* (1996) simulated three dimensional flows in unbaffled stirred vessels agitated by radial flow impellers, without recourse to empirical data. The height of free surface was also studied based on the potential flow theory from Nagata (1975), which is found to be satisfactory. Flow information in an unbaffled vessel with 45° PBT (T = 0.29 m, D = 0.33T, Re = 50000) was obtained from LDV by Armenante *et al.* (1997). The top of the vessel was sealed with a lid, eliminating formation of free surface. Experimental data was compared with numerical simulation and found that the k-ε turbulent model does not correlate well, due to the substantially elevated tangential velocity component. Large-eddy

simulations (LES) were carried out on the turbulent flow generated by a RDT in an unbaffled stirred vessel (T = 0.19 m) by Alcamo *et al.* (2005). The Smagorinski model was used to model the sub-grid scales and the numerical prediction was found to be closely comparable to that from literature and experimental data from PIV.

One of the mechanisms for the suppression of central vortex due to the absence of baffle is to adopt an off-centre mixer position, or more commonly referred to as eccentric configuration. However this strategy is rarely employed at the industrial scale due to the enormous level of stress imparted on the impeller shaft. In the HTE scales however, the eccentric configuration is proven to be perfectly viable as the effect of mechanical stress is greatly reduced. According to Tatterson (1991), the work of Rushton *et al.* (1950) stressed that the power consumption of stirred vessels adopting an unbaffled eccentric configuration is equivalent to that of baffled configuration; power consumption is maximised in the absence of central vortex.

At the HTE scale, a substantial amount of work was carried out by Hall *et al.* (2004 & 2005a). They studied the hydrodynamics in small vessels (T = 0.035 m – 0.06 m) with the use of 2-D PIV. Three configurations, baffled (B), unbaffled centreline (U) and eccentric (E) were adopted. A constant power to volume ratio at P/V = 168 Wm^{-3} was used for all configurations and sizes; this resulted in a range of Reynolds numbers (Re = 8.2–11.3×10^3 for T = 0.06 m and Re = 4–4.5×10^3 for T = 0.035 m). However, although the value of Re was within the high transitional regime and the commonly regarded turbulent cut-off point (Re = 1×10^4) could not be reached, the r.m.s. velocity fluctuating profile showed the flow in T = 0.035 & 0.045 m was virtually turbulent, with a small scale effect which also affected TKE.

In terms of TKE analysis, it was concluded that the TKE was not scale independent, i.e., for the same power input, a much higher TKE is observed in the axial-radial measurement plane for the $T = 0.06$ m vessel compared to the $T = 0.035$ & 0.045 m vessels; this is partly due to the effect related to the interaction between sub-impeller circulation loop and the bulk flow in the vessel. In terms of eddy dissipation rate estimation, it was found that the Smagorinski SGS model, the more conventional Taylor microscale and the dimensional argument models are all incapable of predicting dissipative behavior in the bulk regions accurately using time averaged measurement. Although not implicated in this work, better results should be obtainable using angle-resolved PIV.

PLIF was also applied and it showed a comparable mixing time in eccentric configurations to fully baffled vessels and the smaller the vessel the shorter the mixing time. As expected, the high level of solid body rotation existed in the concentric unbaffled vessels which greatly increased the mixing time.

2.4 MIXING IN THE LAMINAR REGIME

Certain industrial processes involve the mixing and mass transfer of highly viscous liquids, which results in a significant reduction in *Re* and the flow becomes laminar. The hydrodynamics of laminar mixing within stirred vessels are much simpler to analyse than that in the higher transitional and turbulent flows. The significance of the inertial terms in the equations of motion is replaced by the viscous terms and the mixing is no longer enhanced by turbulent eddies. The difficulty in energy transfer results in stagnant regions and the formation of caverns and unmixed island regions are frequently reported in literature. As a result, laminar stirred tank mixing usually requires modification of the vessel geometry. The agitator of choice is usually of the full-tank type, such as, the helical

ribbon and anchor impeller. If conventional impellers are employed, the diameter usually approaches the size of vessel. The formation of caverns also on occasions renders the exclusion of baffles. The research interest in this topic is mainly on the understanding of the velocity flow field and identification of stagnant zones.

2.4.1. CAVERNS AND PSEUDO-CAVERNS

A cavern is defined as a volume of fluid stirred by turbulent impellers which are cocooned by fluid that is completely stagnant. This phenomenon takes place in the mixing of viscoplastic fluids where the flow outside the cavern away from impeller, is completely stagnant as the shear stress applied to the fluid falls below its yield stress. Elson *et al.* (1986) described a method of measuring the size of a cavern by injecting a heavy metal liquid into the impeller region where such liquid prevents the penetration of X-rays. The tracer reaches the outer edge of the cavern and hence its size and shape can be observed. It was found that with a disk-type impeller, the height of cavern is approximately 40% of its diameter. Adams & Barigou (2007) utilised a Planar Laser Induced Fluorescence (PLIF) technique to validate results obtained from numerical CFD, an example is shown in Figure 2.11. The experimental observation and CFD agreed well in terms of size and shape of cavern only in low *Re* ranges; deviation widens in flow with higher *Re*.

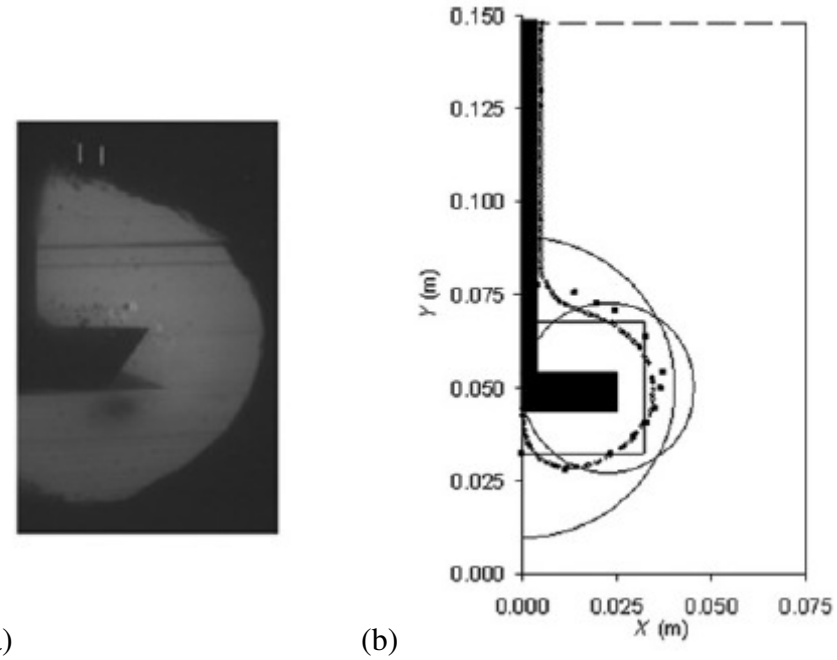

(a) (b)

Figure 2.11 (a) PLIF image captured showing the outline of a cavern, which is subsequently extracted and compared with (b) the resulting CFD simulations. PLIF data is represented by scattered • and the other curves denotes the different types of simulation used. Sample shown here is Herschel-Bulkley fluid agitated at *Re* = 20.4 (Adams *et al.* 2007).

For fluids with shear-thinning properties, the impeller induces high shear and hence fluid close to impeller possessed lower viscosity. As the fluid is pumped away from the impeller, its viscosity increases because of the reduced shear, hence resulting in a significant decrease of motion, which is termed 'pseudo-caverns'. The main difference between the two types of caverns is that the bulk fluid outside the pseudo-cavern is often in motion, although only very slowly. Pseudo-caverns also occur in highly viscous Newtonian fluids which is the working fluid used in this work. Hall *et al.* (2005b) defined the boundary of the pseudo-cavern as the region with a velocity equal to 0.01 U_{TIP}, i.e. the cavern occupies,

$$\sqrt{\left(\overline{u}^2 + \overline{v}^2\right)} \geq 0.01 U_{TIP} \qquad (2.23)$$

A range of power input was applied (*P/V* = 0.6-5.5kWm^{-3}, *Re* = 11–30) in baffled and eccentric configurations. It was found that the volume occupied by pseudo-caverns

increases with rising power input, although the increase may be marginal at higher power input as shown in Figure 2.12(a). The relative velocity map is displayed in Figure 2.12 (b).

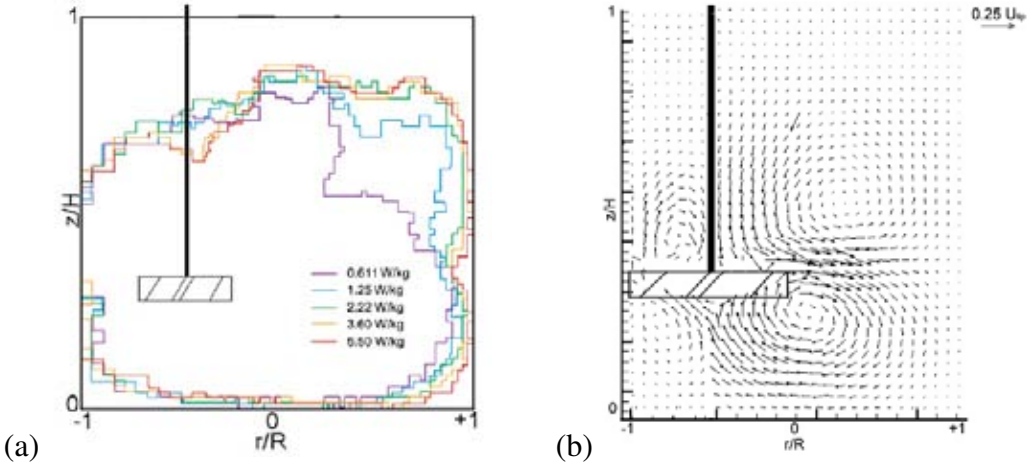

Figure 2.12 (a) Pseudo-cavern & (b) velocity map in an eccentrically configuration vessel at various power input (Hall *et al.* 2007).

The 'rate of strain' was also calculated to determine the axial-radial shear; such parameter, when ploted as contour plots, was found to give a very similar profile to the TKE map obtained in turbulent systems. Since the mixing in laminar system is largely based on the shear stress, rate of strain contours should give a good indication on the quality of mixing.

2.5 GAS-LIQUID TWO PHASE MIXING

Gas-liquid multiphase mixing accounts for at least 25% of chemical reactions in the process industries (Tatterson, 1991). The addition of gas phase into the mixing vessel brings an extra degree of complexity as the gas bubbles not only alter the hydrodynamics, but the behaviour of the gas phase itself and the mass transfer between the two phases also required attention for an effective multiphase reaction. Due to its importance and complication, there is already a huge body of research dedicated to this subject. The majority of such investigations are concentrated on fully baffled stirred vessels fitted with a centrally located Rushton Disk Turbine (RDT), with a gas sparger located directly

underneath impeller; this is widely recognised as the standard configuration as illustrated in Middleton (1992).

Research areas in this topic can be divided into two major headings:

- Bubble flow regime
- Global gas hold up and bubble size distribution which is interrelated with the gas liquid interfacial area.

Flows investigated in this work belong to the homogeneous regime where superficial gas velocity, U_G, is much lower than the value of 0.02-0.03 ms^{-1}, above which a transition to heterogeneous regime occurs (Gezork *et al.*, 2000).

2.5.1. BUBBLE FLOW REGIME

The gas liquid mass transfer coefficient, k_La has been extensively measured over the years for air water systems and an empirical correlation was drawn (Middleton, 1992), which stated that k_La is dependent on the gassed power, P_G. Gassed power is made up of two components, i.e., the actual mechanical power and hydraulic power from the sparged gas stream. The latter of the two is often neglected and hence P_G can be measured directly from the impeller shaft. At a given rotational speed, power is reduced from the unaerated power, P, when gas is introduced to the agitator, thus introducing the new term gassed power, P_G.

The drop in power is primarily caused by the formation of cavities behind the impeller blades of both RDT and PBT used in this work; this is where gas dispersion takes place. Van't Riet & Smith (1973) determined the circumferential velocities in a vortex in a single

phase system as a function of vortex radius, and it was at the same order of magnitude as the impeller tip speed. Therefore it was concluded that substantial centrifugal forces existed in the flow which have a significant effect on the gas dispersion. Vortex with horizontal axis is formed on both top and bottom horizontal edges of the vertical RDT blades; this creates a low pressure region where sparged gas accumulates. Gas naturally migrates towards the core of vortex and forms cavities. Rennie & Valentin (1968) demonstrated the presence of pairs of gas-containing vortices trailing from the backside of blades of a Rushton turbine and stressed the important role played by these vortices in mass-transfer in gas-liquid dispersion. It was pointed out by Warmoskerken & Smith (1985) that for any stable cavity structure to hold behind a RDT, the Froude number, *Fr*, must be larger than 0.045. *Fr* is the ratio of inertial forces to gravitational forces.

Different types of cavity systems have been identified for RDT, including vortex cavities, clinging cavities and large cavities behind a single blade as shown in Figure 2.13 (Tatterson, 1991). For a 6-bladed impeller, there is a common 3-3 cavity structure which consists of three large cavities and three clinging cavities in the form of a symmetrical pattern.

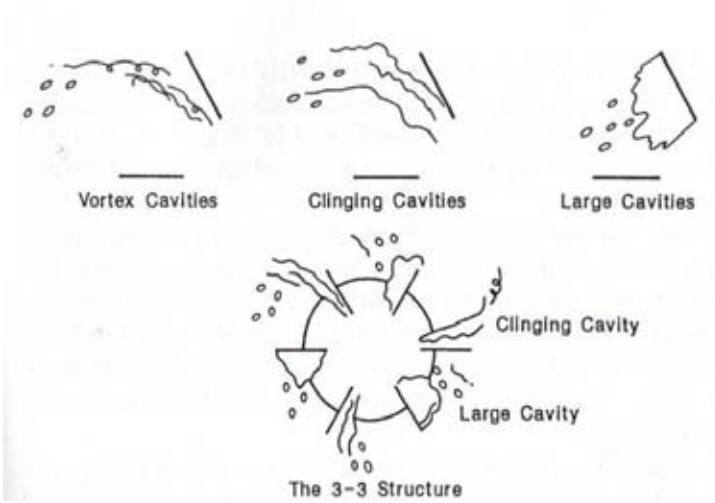

Figure 2.13 Various cavity systems and the 3-3 structure (Tatterson, 1991).

According to van't Riet & Smith (1973), the type of cavity formed behind impeller blades depends on three factors:

- Centrifugal force within the vortex system
- Gas recirculation from the bulk of tank, Q_{GR}
- Gassing rate, Q_G

With a fixed impeller speed, any increase in the gas flow rate, Q_G, will increase the size of cavity, hence influence the resistance to flow and power consumption (Bruijn *et al*, 1974). A dimensionless number Fl_G, the gas flow number, is defined for the description of gas flow rate with respect to the impeller diameter, D, and rotational speed, N.

$$Fl_G = \frac{Q_G}{ND^3} \tag{2.24}$$

It should be noted that Fl_G also appears in literature as N_A or N_Q. Nienow *et al.* (1977) visually observed and identified various bubble bulk flow regimes at different N under a constant flow rate. The sketch from Middleton (1992) also included the effect of the varying Q_G as illustrated in Figure 2.14.

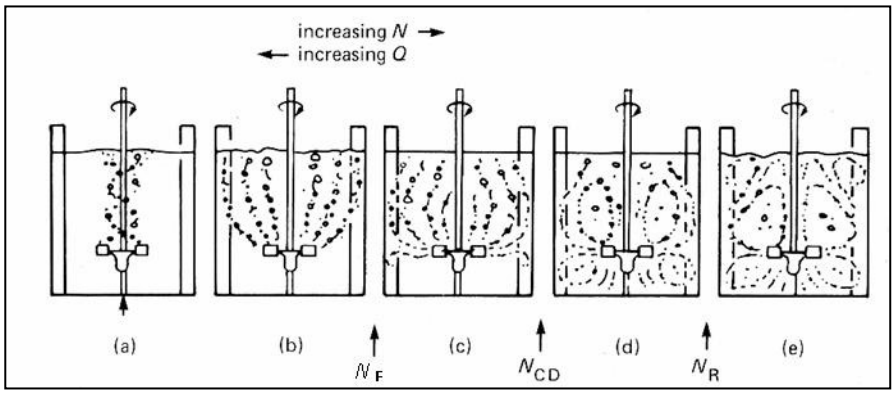

Figure 2.14 Regimes of bubble flow (Nienow *et al*, 1977 & Middleton, 1992).

The bubble flow regime was found to be closely related to the graph of P_G/P against Fl_G, where Q_G is held constant while varying N as shown in Figure 2.15; it should be noted that the lowest N is at the right hand side of the graph. Cavities begin to form in the trailing

vortices when N reaches N_F, hence the sudden drop in P_G/P. The impeller at this point is loaded and gas dispersion begins. Warmoeskerken & Smith (1985) related Fl_G in flow which just entered the flooding regime with Fr, from experimental data in stirred vessels with RDT over three scales as,

$$Fl_G = 1.2Fr \tag{2.25}$$

Nienow *et al.* (1985) also presented an empirical correlation which accounted for the effect of impeller to tank ratio, D/T,

$$Fl_G = 30\left(\frac{D}{T}\right)^{3.5} Fr \tag{2.26}$$

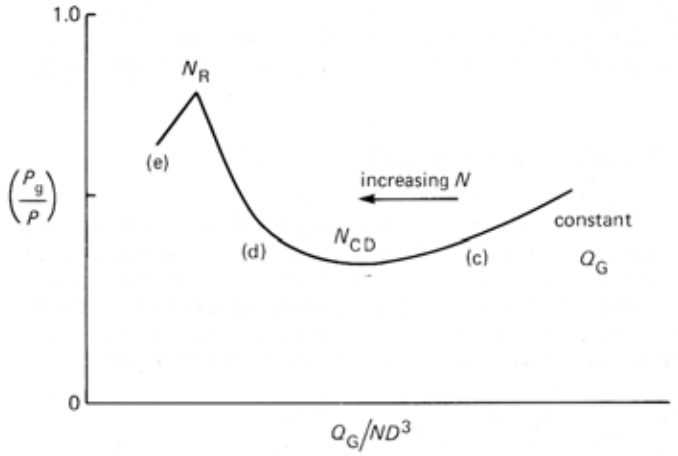

Figure 2.15 Regimes of bubble flow (Middleton, 1992).

The lowest P_G/P corresponds to N_{CD} which represents the greatest loss in power where cavities diminish and their form changes into vortex cavity; this is the minimum point for a complete dispersion of gas in the whole vessel and small recirculation pattern can be observed. The relationship of Fl_G with Fr at this point, is also given by Nienow *et al.* (1977) as,

$$Fl_G = 0.2\left(\frac{D}{T}\right)^{0.5} Fr^{0.5} \tag{2.27}$$

P_G/P rises again if N is allowed to be increased further up to N_R, at which the gross recirculation of gas in the bulk of the vessel into the impeller region starts.

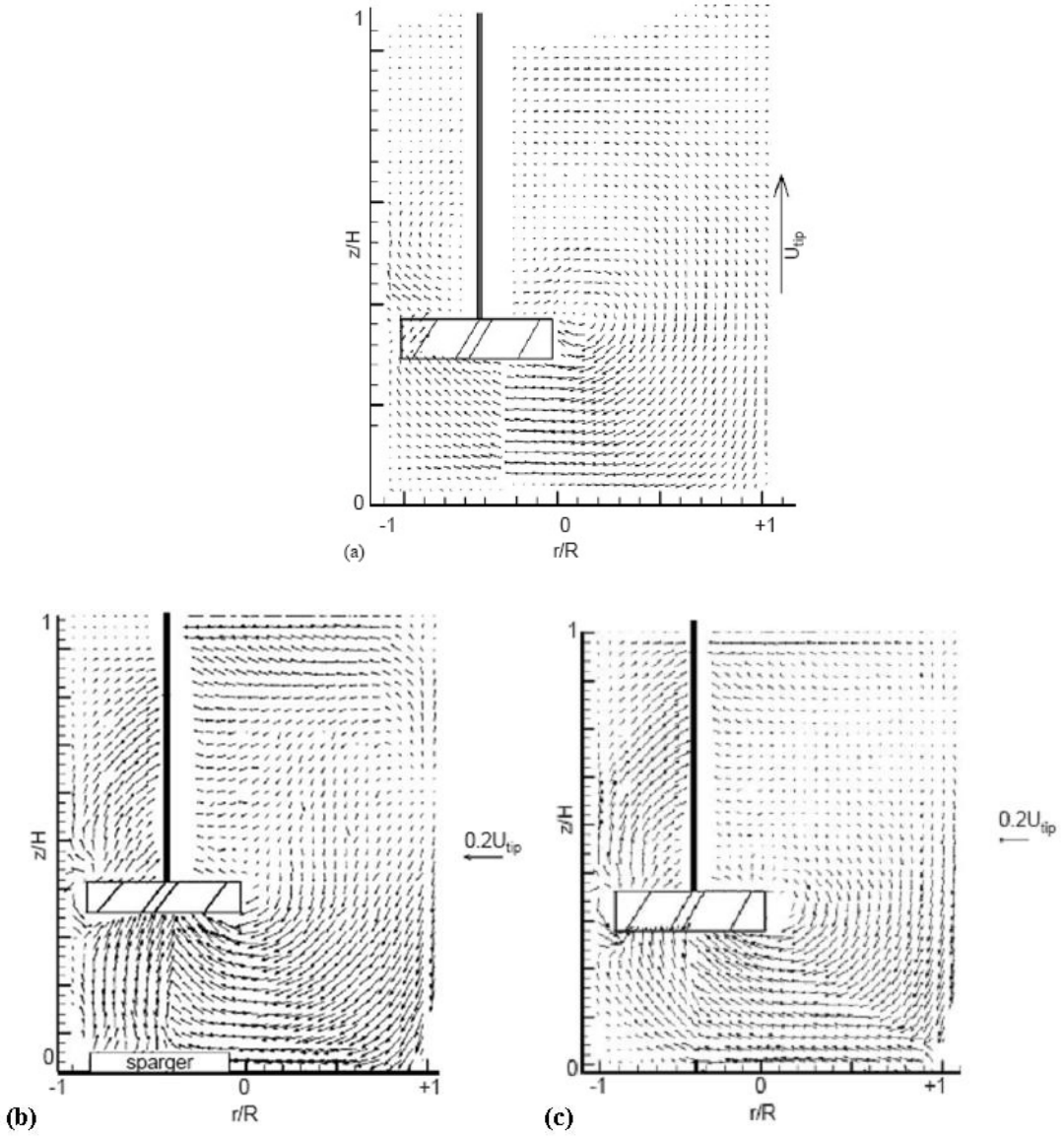

Figure 2.16 Normalised liquid phase mean velocity for a stirred vessel with T = 45mm, D = 0.53T, C = 0.33T & C_W = 0.33T at (a) Q_G = 0vvm (ungassed), (b) Q_G = 0.5vvm and sparger at α position & (c) Q_G=0.5vvm and sparger at β position (Hall, 2005c).

Hall *et al.* (2005b; 2005c) characterised the hydrodynamics within an eccentrically agitated HTE vessel. 2D-PIV was used to determine the liquid phase velocities in the axial plane with a 6-PBTu, and the gas was sparged in two different positions, either directly underneath the impeller (α position) or and further away in the opposite half of vessel (β position). P_G / P was found to be very high which is consistent with the literature. It was

found that the flow pattern of the liquid phase was significantly altered compared with the ungassed condition (Figure 2.16(a)). The flow field was also affected by the position of sparger; strong liquid velocity is observed in the upper half of vessel with α sparger position (Figure 2.16(b)) while liquid velocity was much lower in the same area when β sparger position (Figure 2.16(c)) was adopted. This leads to a different TKE distribution for the two sparger positions. However the distribution of TKE is somewhat similar between two different Q_G of 0.25 and 0.5 vvm.

2.5.2. INTERFACIAL AREA, GAS HOLDUP AND BUBBLE SIZE DISTRIBUTION

The mass transfer coefficient, k_La is a product of k_L, the liquid side mass transfer coefficient and a, the interfacial area. These two factors hold the quality of a reaction in a stirred vessel.

The interfacial area per unit volume, a, along with gas holdup, ϕ, and Sauter mean bubble diameter, d_{32}, also described the quality of gas dispersion (Tatterson, 1991). Bubble concentrations were not discussed in literature but were implied in data on these three factors, which are also interrelated, i.e.,

$$d_{32} = \frac{6\phi}{a} \tag{2.28}$$

where the factor of 6 is based on the volume of sphere divided by the surface area. Holdup usually ranged from 0-25% and air bubbles are normally in the range of 0.5-20mm in water systems, giving an interfacial area between 0.1-5.0 cm^{-1}.

Gas holdup, ϕ, is the dimensionless volume fraction of the gas phase in all the gas / liquid mixture in the whole vessel, which can be measured by detecting the rise in liquid level upon aeration, thus

$$\phi = \frac{h_g - h_u}{h_g} \tag{2.29}$$

where h_g is the gassed dispersion height and h_u is the ungassed liquid height.

Smith *et al.* (1978) proposed that ϕ is related to P_G/V. This relationship can be expressed as (Middleton & Smith (2004)),

$$\phi = \alpha' \left(\frac{P_G}{V} \right)^{\beta'} (U_G)^{\gamma'} \tag{2.30}$$

where U_G is the superficial gas velocity (applicable in the range of 0.005 to 0.05 ms^{-1}). Index α' depends on the physical properties of the fluid. The indices β' & γ' range from 0.2 to 0.7.

Hall *et al.* (2005b; 2005c) stated that U_G in HTE scale vessels is at least an order of magnitude lower than the applicable range in the relation proposed by Smith *et al.* (1978). In this case the U_G was found to be $1.88\times10^{-4} - 3.75\times10^{-4}$ ms^{-1}, hence the final term in the equation is ignored. Holdup was measured over a range of P_G/V, for which a correlation was obtained and the index β' of 0.45 was found to be similar to that of Smith *et al*. (1978) at 0.48,

$$\phi = 0.0078 \left(\frac{P_G}{V} \right)^{0.45} \tag{2.31}$$

Chapman *et al.* (1983) suggested that gas hold up only depends on the gas flow rate, Q_G, and power input, which is related to impeller speed, N. Greaves & Barigou (1988) studied the gas holdup of a disk turbine in a fully baffled 1.0m diameter tank with $C = 0.25T$ and $D = 0.25\text{-}0.5T$, and derived an empirical correlation for the gas holdup in air/water system,

$$\phi = 3.85 N^{0.73} Q_G{}^{0.62} \left(\frac{D}{T} \right)^{1.64} \tag{2.32}$$

for flow in the vortex-clinging cavity regime and,

$$\phi = 1.33N^{0.60}Q_G{}^{0.44}\left(\frac{D}{T}\right)^{1.31} \tag{2.33}$$

for flow in the large cavity regime. The holdup depended upon the cavity regime; i.e., higher holdup is for vortex clinging regime due to reduced pumping capacities of the large cavities.

To put the gas holdup into qualitative prospective, in a standard aerated vessel with radial pumping impeller, the distribution of gas fraction is higher in certain parts of the vessel than the bulk; in the agitated regions near impeller plane, the liquid downflow is centrally above the impeller and near the wall below impeller plane (Middleton & Smith, 2004).

Gas holdup, ϕ, can also be estimated according to Kudrewizki (1982) which was published in English by Kudrewizki & Rabe (1986). The general equation for ϕ is,

$$\frac{\phi}{1-\phi} = \frac{1}{2}\frac{U_g{}^{\frac{2}{3}}}{(gd_{10})^{\frac{1}{3}}}\left(\frac{\rho_L}{\rho_L - \rho_g}\right) \tag{2.34}$$

where d_{10} refers to the general diameter of bubbles formed in the turbulent stream and it can be approximated by,

$$d_{10} = 2\left(\frac{\sigma}{\xi\rho_L}\right)^{\frac{3}{5}}\left(\frac{L^{\frac{2}{5}}}{U_{tip}^{\frac{6}{5}}}\right)\left(\frac{\rho_L}{\rho_g}\right)^{\frac{1}{5}} \tag{2.35}$$

for low-viscous media within the range $1 \times 10^3 < Re < 2 \times 10^5$, $\xi = 0.4$ and L is the turbulent scale of fluid flow; for a standard configuration L is generally 1/6 of the impeller width. Based on the standard configuration, Garcia-Ochoa & Gomez (2004) further elaborated the equation into the following form,

$$\frac{\phi}{1-\phi} = 0.819 \frac{U_g^{0.67} N^{0.4} T^{0.27}}{g^{0.33}} \left(\frac{\rho_L}{\sigma}\right)^{0.2} \left(\frac{\rho_L}{\rho_L - \rho_g}\right) \left(\frac{\rho_L}{\rho_g}\right)^{-0.067} \quad (2.36)$$

Garcia-Ochoa & Gomez (2004) also derived equations for holdup in viscous systems. However this is outside the scope of this work and hence excluded.

The statistical measurement of bubble size is usually based on Sauter Mean Diameter (d_{32}); it is the volume/surface area ratio of the bubble of interest and can be used to calculate interfacial area.

There have been several attempts to measure the size of gas bubbles in stirred vessels. Earliest literature described the interfacial area method for which the d_{32} can be calculated using by $a = 6\phi / d_{32}$ (Calderbank, 1958); a in this case was measured by a light-scattering method. Alternatively a can be determined from the $k_L a$ measured in a reaction (e.g., absorption CO_2 from sparged gas by aqueous alkaline) with known k_L ; this way, a is only accounted for those area where reaction actually takes place (Hassan & Robinson, (1980)). However, these methods do not give the bubble size distribution. Greaves & Kobbacy (1984) used a photoelectric capillary probe, as shown in Figure 2.17, to capture the small bubbles that were in the vicinity of the probe in a $T = 0.2$ m vessel, by vacuum created by a vacuum pump. The length of slug flowed in the capillary was measured by a LED sensor and converted into volume, hence a bubble size distribution and a geometrical a can be determined based on the localised measurement on each individual bubble. Good reproducibility was achieved on the bubble size distributions over the size range of 0.4×10^{-3} - 5×10^{-3} m. A modified version of this probe was used in the work of Greaves & Barigou (1988) and Barigou & Greaves (1992) on a $T = 1.0$ m vessel where a tapering funnel was installed on the tip of the probe to ensure a gradual acceleration of bubble prior to the

capillary flow condition; this minimised bubble breakage. The signal from the dual LED phototransistors was also conditioned (see Figure 2.17 (b)). Bubble size was measured at 22 points throughout the vessel. d_{32} in the vicinity of impeller was found to increase with increasing Q_G and decreasing N. The fact that Q_G and N were reduced in the upper and lower regions of the vessel indicated that a state of dynamic equilibrium existed between the competing process of bubble breakage and coalescence. The cumulative frequency size distribution showed the air-water system was best fitted by the Weibull distribution for a coalescing system; it was an exponential distribution for air-0.15M NaCl solution which has a strong bubble coalescence retardation effect.

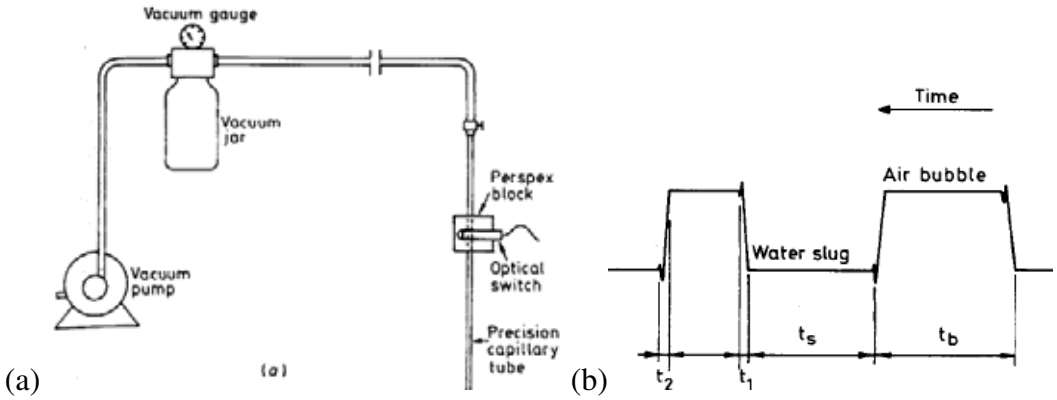

Figure 2.17 (a)Capillary probe measurement system. & (b) Difference in the signal given by the two phases. (Greaves & Kobbacy, 1984).

A few attempts have been reported in the last decade where optical techniques have been used to measure the size of gas bubbles and their motion on a larger scale in bubble columns, provided that the holdup is low enough to maintain a clear view of vision on the measurement plane. These methods can be broadly divided into two categories, using either a diffused halogen or LED light source, or a laser plane to illuminate the bubbles. For example, Honkanen *et al.* (2005) and Horn *et al.* (2007) used an LED background light source in a shadow imaging technique to determine bubble size only in a bubble column and in a stirred vessel, respectively. Bröder & Sommerfeld (2007) also applied such a technique

to study the hydrodynamics in the bubbly flow within a wide rectangular column. They determined bubble size, shape and orientation within the focal plane, as well as the gas phase velocities using an in-house developed code. An array of 551 high performance LEDs provided background diffused illumination to project bubbles situated between the light source and camera as dark circles on the captured image. Planar measurements were achieved by adjusting the depth of the focal plane; for example, in-plane bubbles were recognized by their relatively thin edges whereas the contours of out-of-plane bubbles appeared smudged. However, even with a macro camera lens setup to provide a small depth of view, the thickness of the focal plane was only resolved down to 4 mm, which is about one tenth of the small HTE vessel used in this study. Thus, this precludes the use of the shadow imaging technique in small HTE vessels as the focal plane would be relatively too thick (i.e. 3D instead of 2D).

Hall *et al.* (2005b; 2005c) measured d_{32} in an HTE scale vessel as used in this work, by manually measuring the printed images captured by a PIV camera. It was found that the d_{32} is approximately 0.72 and 0.85 mm for the configuration investigated at P/V = 168Wm^{-3}. This is lower than the average bubble size anticipated (Barigou & Greaves, (2001); Bouaifi *et al.* (2001)), which is larger than 1 mm for coalescing systems. It was suggested that the smaller bubble size is caused by the a combination of the very small initial bubble size at the sparger, a very short recirculation or residence time, and a low bubble-collision frequency due to the swirling flow observed in these eccentric vessel configurations. This method is expensive in terms of labour. Laakkonen *et al.* (2005) utilised a similar experimental technique to measure bubble size as Hall *et al.* (2005b; 2005c) but without the use of seeding particles. The bubble size was measured via a bubble recognition algorithm; an underestimation on the bubble sizes was found hence correction needs to be applied. Horn *et al.* (2007) utilised shadow processing software from Dantec Dynamics to

determine bubble size distributions from captured images illuminated by diffused/coherent light from a neon source, again in a lab scale vessel at relatively low gassing rates (0.02 and 0.07 vvm). The edges of the bubbles at a certain focal depth were detected by Canny method once the contrast of the original image was maximised, and hence the bubble sizes were determined. This method was found to be unreliable as the measurable focal depth was large with respect to the size of HTE vessel, hence the measurement of d_{32} may refer to bubbles at different depths from the camera. Localised bubble size distribution was also measured by the use of CFD modelling Laakkonen *et al.* (2007), although at the present stage this method is not fully developed.

2.5.3. TWO PHASE VELOCITY MEASUREMENT

The knowledge of two phase velocities was traditionally gained from CFD simulations (Lane *et al.* 2005; Khopkar *et al.* 2003). Laser based methods, on the other hand, were introduced more than a decade ago. For example, Tassin & Nikitopoulos (1995) applied phase-Doppler anemometry (PDA) to bubbly flow but the method is only applicable to bubbles less than 1 mm in diameter, which is a rather serious disadvantage. Other early experimental work was based on Laser Doppler Velocimetry experiments also included that by Morud & Hjertager (1996). Whole field experimental measurement techniques such as PIV was mainly used to measure the velocity in the liquid phase (Aubin *et al.* 2004; Hall *et al.* 2005b; 2005c).

A few attempts have been reported in the last decade where PIV or variants of it have been used to measure gas motion on a larger scale in bubble columns. For example, Choi *et al.* (2002) used a combination of 2D PIV to study the flow field around bubbles rising in stagnant water, and Particle Tracking Velocimetry (PTV) to measure their velocities. This

technique, however, relies on the liquid phase being stagnant. Cheng *et al.* (2005) measured gas phase motion in a bubble column using a halogen lamp as light source, but his method is only applicable to two-dimensional motion. Delnoij *et al*. (1999) captured laser light reflected from rising bubbles in a gas plume simultaneously with that from seeding particles, and differentiated between them by their distinct peaks using a cross-correlation procedure.

Very recently, Montante *et al.* (2007) measured gas and liquid phase velocities simultaneously in a laboratory scale vessel (T = 0.236 m) at a low gassing rate of 0.02 vvm (volume per volume per minute) by using two side by side PIV cameras, each imaging one of the two phases. A low-pass optical filter was placed on the first camera to block out the scattering of fluorescence light emitted by seeding particles tracking the liquid phase, hence capturing only the reflected incident laser light from the gas bubbles. Similarly, a high-pass filter was used on the second camera which allowed the fluorescent light from seeding to be captured. However, the technique does not seem to differentiate between bubbles in the laser plane which are the ones that are supposed to be tracked, and bubbles out of the laser plane which should be rejected. The out-of-plane bubbles, certainly those close to the laser plane, are likely to be illuminated by light reflected from the in-plane bubbles making the two groups of bubbles indistinguishable. In a different study (Horn *et al.*, 2007) the authors used this technique to measure phase velocities, and a shadow processing software from Dantec Dynamics to determine bubble size distributions from captured images illuminated by diffused/coherent light from a neon source, in the same vessel and at similar gassing rates of 0.02 and 0.07 vvm. The edges of bubbles at a certain focal depth were detected by the Canny method once the contrast of the original image was maximised, and hence the bubble sizes were determined (Jähne, 2002). Whilst this phase velocity measurement method was used at a gas flowrate of 0.02 vvm and a gas holdup of

0.0165 (Montante *et al*., 2007), there were difficulties with velocity measurements at higher gas inputs (> 0.5 vvm). Evidently, as the gas sparging rate increases, the bubble density will be much greater and, thus, the difficulty in distinguishing between in-plane and out-of-plane bubbles increases. Furthermore, the higher bubble density also restricts visualisation of the two-phase flow to the region near the wall as it becomes increasingly more difficult to focus on inner planes. In real industrial stirred vessels typical gassing rates would be even higher, of the order of 0.5 - 1.0 vvm, and would probably fall outside the workability range of the technique. However, none of the existing optical techniques is likely to work at such high gas holdups. Furthermore, the above method uses the bubbles as tracers for the gas phase; whilst this can work in laboratory scale vessels at relatively low gas inputs, the method is unlikely to be successful when trying to examine flows at a smaller scale.

When using a HTE vessel, for example, the miniature size of the vessel makes it impossible to use two cameras simultaneously. It would be possible in principle to use one camera only and measure the liquid and gas phase velocities separately in successive experiments; but on this scale the bubbles are relatively large compared to the vessel so that the obstruction created by bubbles out of the measurement plane would cause too much degradation in the quality of the PIV images.

2.6 MIXING TIME ANALYSIS

2.6.1. DEFINITIONS

Mixing time can be defined as the time a mixing vessel required to achieve certain uniformity, or mixedness, when a trace of material is added to the batch. The definition of mixedness varies with experimental techniques, although it is always determined from the similarity between localised instantaneous and final concentration of injected tracer.

According to Brown *et al.* (2004), all mixing time analysis techniques are based on the principle of adding a trace of material into the mixing vessel, which has distinctively different properties from the bulk; even though the tracer usually has the same viscosity and density as the bulk liquid with which it is miscible (Edwards *et al.* 1992). The presence of material should be accurately measured and the time history of the decay of material property fluctuations is recorded. Mixing time is determined when the fluctuation of the instantaneous tracer concentration, C_i, reduces to the known equilibrium concentration, C_∞.

As pointed out by Collias & Prud'homme (1985), mixing time is not an absolute measurement by nature and depends upon four factors,

- The sensitivity of the detection probe
- The location of the probe
- The location of the tracer input
- The degree of homogenisation specified.

It is imperative that a sufficient number of measurement probes are in positions distributed evenly in the vessel to provide as much relevant mixing information as possible; however there is a trade off between the number of probes and the amount of flow intrusion they cause. Usually the probes will in theory be at points that are least intensively agitated in a stirred vessel; these points will be the last to be mixed and limit the mixing rate for the entire vessel.

There are a few correlations published that relate mixing time with impeller dimensionless number and other variables. For example, assuming the mixing system is homogenised

after 5 circulations, Nienow (1997) related the Fl to mixing time, τ_{95}, for a standard configured vessel with $H/T = 1$ via the use of a bulk flow model as,

$$\tau_{95} N = 3.9\left(\frac{D}{T}\right)^{-3} Fl^{-1} \tag{2.37}$$

It should be noted that the ratio of impeller to vessel diameter is of utmost importance because it was also suggested that the flow away from impeller determines the mixing time. Therefore an increased swept diameter caused by a larger impeller can shorten the mixing time significantly.

The value of P_O was also found to relate to mixing time, τ_{90}, as such (Cooke *et al.* 1994),

$$\tau_{90} = 3.3\left(\frac{1}{N}\right) Po^{-3.3}\left(\frac{T}{D}\right)^{2.43} \tag{2.38}$$

Or alternatively for τ_{95} (Ruszkowski, 1994),

$$\tau_{95} = 5.91 T^{2/3}\left(\frac{\rho V}{P}\right)^{1/3}\left(\frac{T}{D}\right)^{1/3} \tag{2.39}$$

which highlights the fact that for a reduced power consumption for a given mixing time D should be increased.

Although these empirical correlations may give a satisfactory result without the recourse of experimental work, it should be noted that they are largely based on the experimental work carried out on the laboratory scaled baffled stirred vessels. Therefore, mixing time should be determined experimentally for the unconventional vessels studied in this work.

2.6.2. AVAILABLE TECHNIQUES

The most widely used mechanism from early literature may be based on the change in temperature or conductivity in the working fluid. For example, Hoogendoorn & Hartog (1967) used a thermal method to measure the mixing time across a range of mixer/vessel combinations. A small quantity (1-2% vol.) of heated liquid (20-40°C) was injected into the fluid; during homogenisation the temperature was measured with thermocouples located at several positions in the vessel. Mixing time acquired agreed well with data obtained from decolouration; hence it was concluded that thermal method is very convenient for obtaining reproducible quantitative data in both large and small scale experiments. For experiments based on the conductivity of the working fluid, KCl was used as electrolyte tracer and the probe was made up of two platinum wire coils set a small distance apart; this formed a resistance gauge where the current passing through the gap was measured and proportionally converted to localised KCl concentration (Kramers *et al.* 1952). It proved that very rapid response time can be achieved by the conductivity method and it is cheap and easy to use. Both temperature and conductivity probes, along with their supports are however, regardless of size, intrusive to the natural flow in stirred vessel; these disturbances becomes most severe in small scaled stirred tanks such as the HTE vessels investigated in this work, hence they cannot be applied.

Alternatively mixing time can be measured by optical techniques, which are broadly divided into two categories, colorimetric and decolouration methods. The colorimetric method involves the simplest test of the rate of mixing in the bulk of the tank by monitoring the dissipation of coloured dye visually, and the intensity of colour in the dyed liquid should correspond to the dye concentration. However as pointed out by Brown *et al.* (2004), the last point to be mixed in the whole vessel may not be found because any dye in front or behind the poorly mixed region will mask the last mixed pocket as shown in

Figure 2.18(a). This is especially inconvenient in certain cases (such as the segregation regions within the flow in laminar regime) and can be overcome with decolourisation method which works on a completely opposite principle.

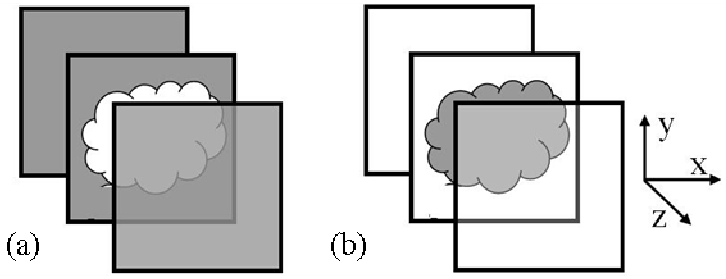

Figure 2.18 Illustration of mixing time analysis by (a) colourisation & (b) decolourisation.

By adding a chemical to the vessel, the content within is coloured; this colour can be entirely removed by the addition of another chemical via a fast reaction. As a result, the poorly mixed region is left standing out when the liquid surrounding such is decolourised as shown in Figure 2.18(b). The neutralisation of sodium hydroxide with sulphuric acid (indicator: phenolphthalein) is based on the pH-values of fluid and sometimes used for its simplicity (Zlokarnik, 2001) but the reaction time is known to be slow. Another pH based reaction involved bromophenol blue as indicator (blue to yellow) but the colour change is not clear in some known cases. Hence, redox reactions of triosulfate with iodine (indicator: starch) have a clear advantage as the reaction is fast and the strong colour change (disappearance of opaque dark colour) makes it a popular choice. Although in some cases such as CMC solutions, there is a tendency for the iodine solution to be slowly decolourised without the addition of triosulfate. There is also the 'Schlieren' method which is based on different refractive indices of both tracer and bulk fluid (Van de Vusse, 1955). The addition of tracer will cloud the fluid because background light is scattered through different layers of liquid until the vessel is fully mixed, then the tank becomes clear once again when the two fluids are blended. The biggest disadvantage in both the decolourisation and 'Schlieren' method is that the choice of working fluid is limited.

2.6.3. PLANAR LASER INDUCED FLUORESCENCE (PLIF)

In recent years, an alternative technique, Planar Laser Induced Fluorescence (PLIF), has been developed which overcomes the weaknesses in the optical techniques described above. PLIF allows measurement of the instantaneous concentration fields of a non-reacting fluorescent dye (Rhodamine B), as shown in Figure 2.19. The method is very similar to that of the colorimetric technique; only the colour of the tracer is substituted with the fluorescence of dye excited by a thin planar laser sheet. Instantaneous concentration field of tracer is determined by the greyscale level from captured image via a calibration procedure. This allows the characterisation of mixing in a Poincaré section, hence eliminates the inability of visualising the 'last point to be mixed' region associated with colorimetric method. This method has been applied to continuous stirred tank reactor (CSTR) by Houcine *et al.* (1996) and Fall *et al.* (2001)

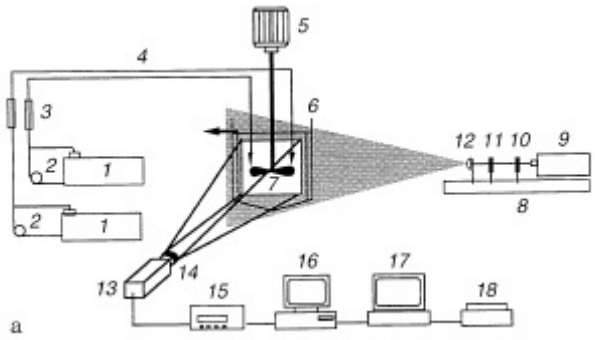

Figure 2.19 PLIF setup (Houcine *et al.* 1996).

A drawback in PLIF is that at a particular laser intensity and lens setting, a non-linear relationship may be exhibited between tracer concentration and the greyscale level; for example beyond the maximum allowable output by the camera (greyscale of 256 in a 8 bit camera), a flat relationship is achieved. This means any increase in actual concentration results in no further increase in greyscale values. With lower tracer concentrations

however, a linear relationship is attained (R^2 = 1) because within this range, the emitted fluorescent intensity, I_F is linearly related to tracer concentration C_i (Baumann & Mühlfriedel, 2002),

$$I_F = A \cdot I_0 \cdot \Phi \cdot \varepsilon \cdot b_L \cdot C_i \tag{2.40}$$

where A is the apparatus constant; I_0 is the incident light intensity; Φ is the quantum yield; ε is the molar absorption coefficient and b_L is layer thickness. The linearity is only valid if $\varepsilon \cdot b \cdot C_i < 0.05$ (Guibault, 1990). The constant terms A, I_0, Φ, ε and b_L are all based on the experimental setup; it is therefore vital that a set of calibration is to be carried out prior to experiments (Kling & Mewes, 2003). Houcine *et al.* (1996) related the linear relationship between greyscale level and tracer concentration at (*i,j*) pixel as,

$$C(x_i, y_j, t) = C_{ij}(t) = \frac{G(x_i, y_j, t) - \overline{G}_B(x_i, y_j)}{\overline{G}_{C_{\text{hom}}}(x_i, y_j, t) - \overline{G}_B(x_i, y_j)} C_\infty \tag{2.41}$$

where $C_{ij}(t)$ is the instantaneous tracer concentration, C_i. $G(x_i,y_i,t)$ is the instantaneous greyscale.

Temporal variance of local concentration, σ_{ij}^2, quantifies the mixing dynamics and can be calculated by,

$$\sigma_{ij}^2 = \frac{1}{n} \sum_n \left(C_{ij} - \overline{C}_{ij} \right)^2 \tag{2.42}$$

where n is the number of tracer concentration fields.

Utilising the difference in emitted wavelength between seeding particles (λ = 532 nm) and Rhodamine B (λ = 590 nm), Law & Wang (2000) applied PIV and PLIF simultaneously on a turbulent discharge jet by fitting the appropriate filters on two cameras. The camera for

PIV measurement was placed perpendicular to the area of interest with the PLIF camera placed alongside tilting at 5° off-axis for PLIF measurement. It was found that the PLIF image distortion caused by the small tilt angle was minimal and hence it is possible to apply PIV and PLIF simultaneously.

Other than Rhodamine B, there are alternative fluorescent dyes that are also applicable in PLIF. For example, a mixture of two dyes was injected into the mixing vessel by Kling & Mewes (2003) with 1% w/w CMC as the working fluid. The inert dye carboxy-SNARF was used to monitor the macro-mixing and a reactive dye Fluo-3 was employed to quantify micro-mixing; Fluo-3 is initially non-fluorescent unless it is bound to the Ca^{2+} ions from $CaCl_2$ presented in fluid, hence the quality of micro-mixing can be determined.

In HTE stirred vessels of interest to this work, Hall *et al.* (2005a) applied PLIF to vessels with various scales (T = 35-60 mm, $D = 0.5T$ & P/V = 168 Wm^{-3}) and configurations (baffled (B), unbaffled centreline (U) & unbaffled eccentric (E)) with flow in the high transition to turbulent regime. The injected dye was at a concentration within the linear C_i / G_i range. $G(x_i,y_i,t)$ were taken at 130 equally spaced points on the horizontal line in the region $0 \leq r/R \leq 1$ for (B) & (U) and 200 points were taken in the region $-0.33 \leq r/R \leq 1$ for (E). This process is repeated at y/H = 0.165 (0.5 C), 0.5 and 0.75. The mean of $G(x_i,y_i,t)$ from all measurement points was defined as G_i, the temporal greyscale representing area across the whole stirred vessel. Time history of normalised concentration was determined for (U), (E) and (B) at T = 35 & 45 mm as shown in Figure 2.20. τ_{95}, which was defined as the time when the normalised concentration fluctuation settled within ±5% of 1, was subsequently found; τ_{95} in vessel with T = 35 mm was found to be 1.39 s and 1.46 s with configurations E & B. For vessel with T = 45 mm, τ_{95} was 1.45 s and 1.59 s with E & B respectively. Very importantly the result confirmed for a homogeneous turbulent system

with water as working fluid, eccentric configuration produces a comparable mixing time to the baffled configuration, which is clearly shown in Figure 2.21.

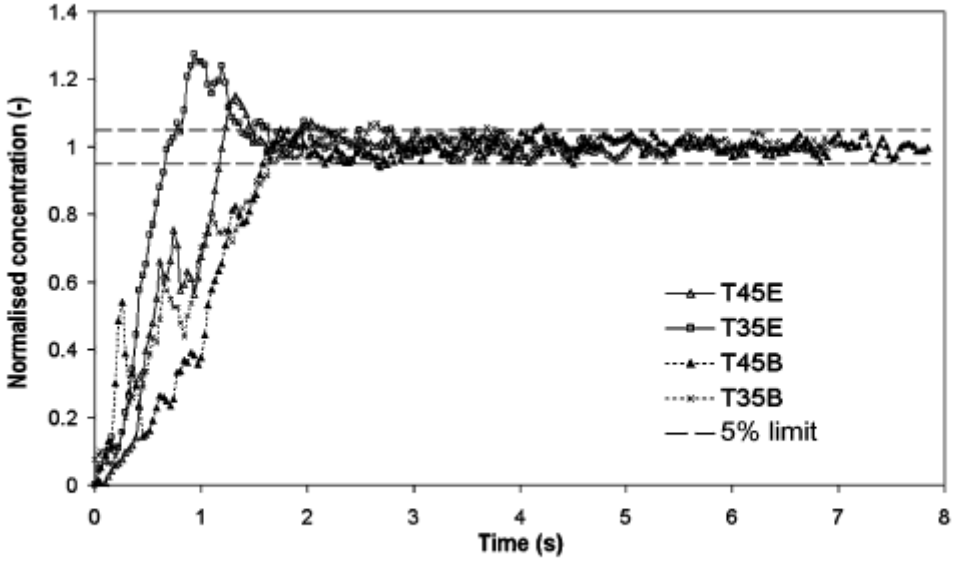

Figure 2.20 PLIF determined mixing times (Hall *et al.* 2005a).

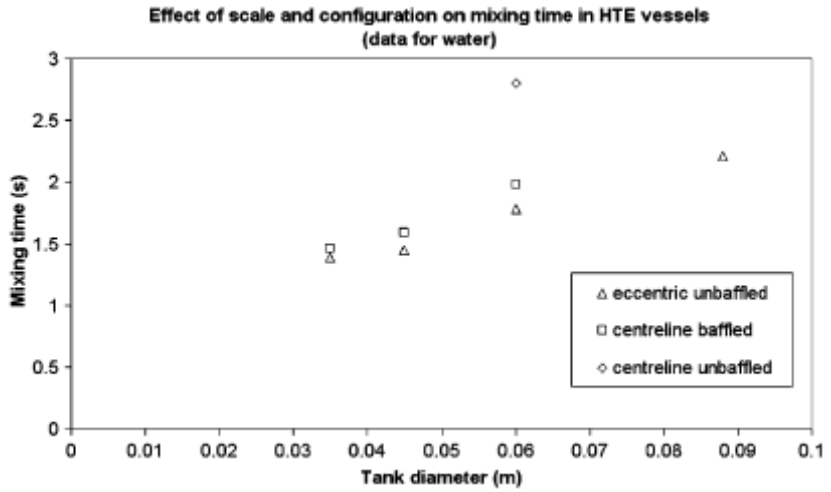

Figure 2.21 The effect of scale (vessel diameter) on mixing time, τ_{95} (Hall *et al.* 2005a).

In the laminar regime, Zalc *et al*. (2001) applied PIV and PLIF separately to validate CFD simulations in a vessel with three co-axial Rushton Turbines ($20 < Re < 200$ with glycerine as the working fluid). Whilst PIV obtained a matching flow field in the bulk of fluid to that of CFD simulation, PLIF images identified stagnant regions with the vessel; the location and size agreed very well with CFD simulation. A vessel with similar dimension

was also investigated by Alvarez-Hernández *et al.* (2002); it was reported that the segregated areas accounted for 20% of the cross sectional area. At increased magnification, ripples were observed to be compressed radially and then elongated vertically outwards from the impeller, as shown in Figure 2.22. The vertical stretch progressively formed a parabolic profile.

Therefore it is demostrated that PLIF is not only capable of measuring mixing time within the bulk of fluid but as with decolourisation method discussed above, it can also identify the last point to be mixed in the vessel; if resolution of the image is sufficiently high, it may even be possible to visualise the finest detail of impeller discharge with flow in the laminar regime. PLIF is highly versatile as it utilises the same hardware setup as PIV, a combination of the two yields both qualitative and quantitative data on the quality of mixing.

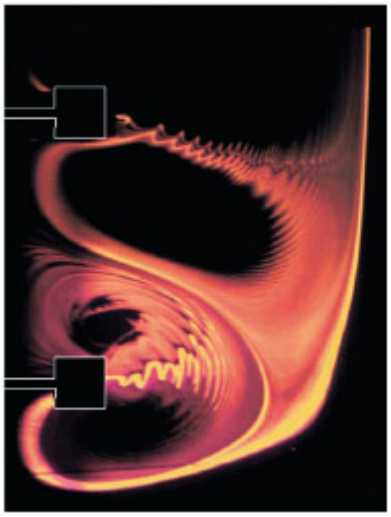

Figure 2.22 Ripples shown in PLIF images in a multi-impeller agitated vessel (Alvarez-Hernández *et al.* 2002).

2.7 CONCLUSION

This Chapter introduced and described the working principle of PIV, in addition to other flow visualisation techniques. The basic theories and recent literature on the mixing of stirred vessels of different sizes and configurations in various hydrodynamic regimes were reviewed; this included both macro- and micro-scale turbulent mixing, laminar chaotic flow, as well as gas-liquid multiphase system. It was understood that there are currently a few areas that required in-depth research, at least at the HTE scale. The following Chapters in this thesis are structured to improve the understanding in these areas, which can be broadly categorised as,

- Three dimensional hydrodynamic studies; a substantial tangential flow existed in unbaffled (U) and eccentric (E) configuration HTE vessels (Hall *et al.*, 2004; Hall *et al.*, 2005a) which may not be approximated by 2-D PIV results. Therefore, it is essential to acquire flow information in all three directions with an alternative technique, since traditional 3-D PIV with the use of two cameras is inapplicable at this scale.

- Angle resolved measurements; this provides information on the vorticity and the omission of 'pseudo- turbulence', which are lacking in the previous research.

- Improvement of mixing time analysis; conventional PLIF experimental and analytical methods may be modified to further improve the accuracy on HTE vessel applications, while mixing time is often very short ($\tau_{95} < 5$ s).

- Gas and liquid phase velocity measurements; the majority of research across all scales only yields the velocity measurements in the liquid phase due to the

limitations in measurement techniques. Of the gas phase velocity measurements with PIV cited in literature, they are either not applicable in stirred vessels, or can only operate with a very low gas flow rate. A new PIV method is required to measure the velocity of gas bubbles in the laser plane at more realistic gas flow rates.

- Laminar chaotic flow; Hall *et al.* (2005b) provided an insight to the flow pattern and information on the 'pseudo-cavern'. However, further research, in terms of the use of alternative configurations and application of PLIF, is required for the proposal of optimal mixing strategy.

3. MATERIALS AND METHODS

3.1 MIXING VESSELS AND STRATEGIES

The stirred vessels used in this work were based on the design of commercial High Throughput Experimentation (HTE) units. Not only the size of vessels in a HTE unit are greatly reduced from the lab scale reactors, unconventional configurations are often adopted and larger impellers are usually used. The mixing vessels employed in the single phase experiements were modified for use in gas-liquid multiphase experiments, in order to aid the delivery of gas into the vessel.

3.1.1 SINGLE PHASE EXPERIMENTS

Five different mixer configurations were adopted in the single phase experiments and their schematic layout are illustrated in Figure 3.1. A number of the configurations did not employ baffles, which is a common feature in a number of HTE systems. The configurations chosen were: baffled with agitation on the vessel vertical axis (centreline) (B), unbaffled centreline (U), unbaffled with the agitator located eccentrically (E) and unbaffled with a tilted impeller, (T). In addition a configuration where the cylindrical vessel was replaced with a cuboid vessel was used (S), with centreline agitation. (B) was considered as a control and it was essentially a scale down from the standard configuration; it was created by inserting a baffle module which consisted of four equally spaced baffles into the (U) vessel, as shown in Figure 3.1(a).

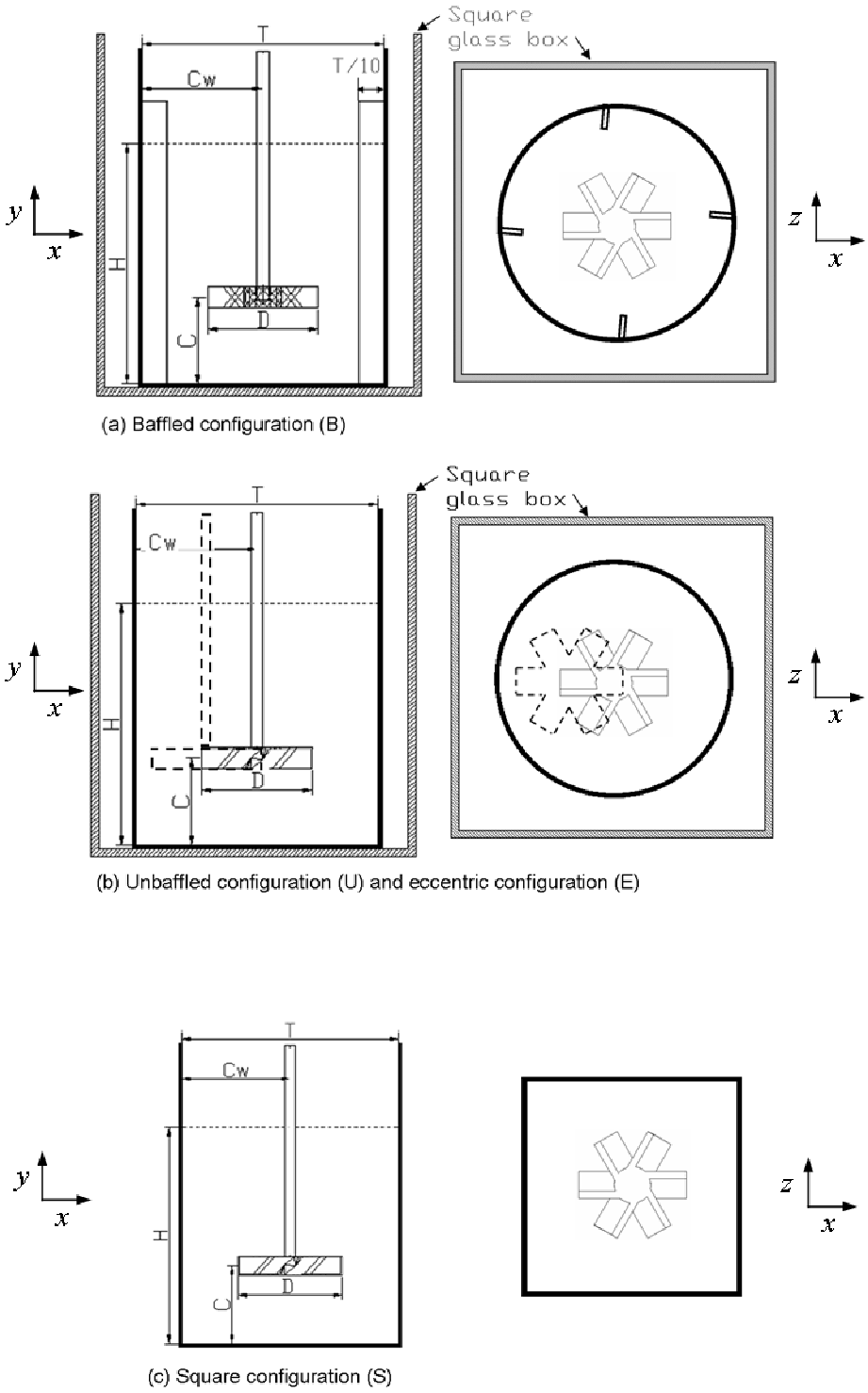

Figure 3.1 Schematic layout of stirred vessels adopted (a) baffled, (b) unbaffled / eccentric & (c) square configuration as used in this work. Diagram on the left shows the side view of vessels and the diagram on the right shows the view from top.

Due to the difficulty in making Perspex/glass baffles which are thin enough and robust enough at this small scale, the baffle module was made of steel. Each baffle has a width of 1/10*T* and a thickness of 1/100*T* and no baffle-wall gap was present. (E) was created by

repositioning the impeller to C_W = 1/3T, as shown in Figure 3.1(b). Likewise for (T), the impeller equipped in (U) was tilted at an angle of 15º from vertical. The mixing vessel in (S) was constructed by bonding four equal sized rectangular glass panes onto a glass base plate, forming the shape of cuboid as illustrated in Figure 3.1(c). In this case, the volume is taken to be the same as the cylindrical cylinder (V = 72 ml) so same power input can be applied to give the same power input per unit volume, P/V. As a result, the width, liquid height and depth of the cuboid were shortened to 41.5 mm. Due to the absence of curvature, no glass box enclosure is required for this configuration. For (B), (U) and (S) configurations, measurements were made on one side of the impeller shaft only. However, for the eccentric configuration (E), due to the lack of symmetry, measurements were made on both sides of the impeller shaft and subsequently recombined during data analysis. For the turbulent flow experiments, details of the dimensions and experimental conditions for each configuration used are given in Table 3.2 in Section 3.3.

Optical quality borosilicate glass (Pyrex) was chosen as raw material for the construction of the vessels to minimise refraction of laser light passing through it. The measurement of PIV data in the horizontal planes, as used in the 3 dimensional flow field reconstruction, required clear visualisation of the flow from underneath the vessel: a construction method was used where an open-ended cylinder of the specified size was glued onto a thin glass sheet to create a perfectly flat vessel bottom. Due to the curvature of the cylindrical vessel, it was enclosed within a square glass box as illustrated in Figure 3.2, with the working fluid filled within to minimise distortions.

Although vessels of different sizes (T = 35, 45 & 60 mm) were constructed and used in the early stage of this work for preliminary trials, all the results in this thesis are based on the T = 45 mm stirred vessel.

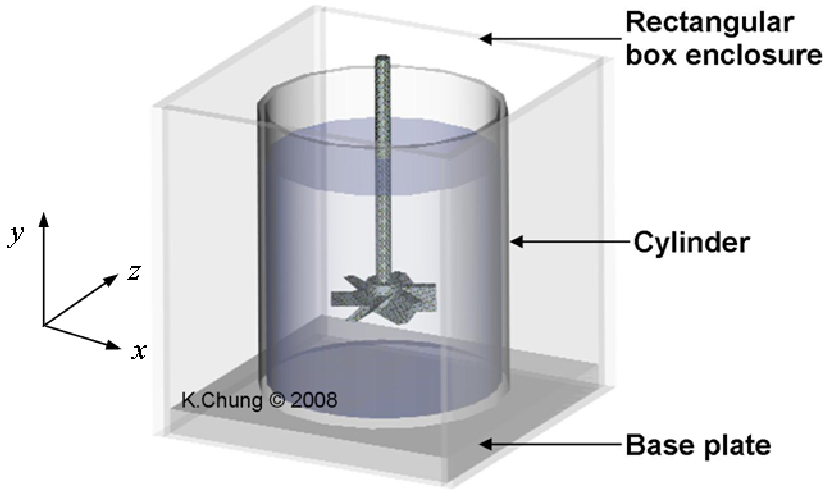

Figure 3.2 Illustration of vessel construction.

A 6 blades up-pumping pitched blade turbine (6-PBTu) was employed for all configurations, to avoid air entrainment from the surface especially in the case of the unbaffled configuration and to some extent the eccentric configuration. This was selected to replicate the agitator fitted to the commercial HTE units produced by Argonaut Technologies (Foster City, California, USA). The commercially available 6-PBTu was manufactured from stainless steel by HEL Group (Barnet, UK), and has a slightly larger *D/T* ratio of 0.54 (24.5 mm in diameter) than the one used conventionally (typical values of *D/T* are generally 0.3-0.5). The blades on the 6-PBTu are angled at 45°. The geometry of the 6-PBTu impeller is shown in Figure 3.3(a). The power number, *Po*, for the 6-PBTu used in the high transitional regime are 1.22 for (U) and 1.57 for (E) & (B) configurations respectively.

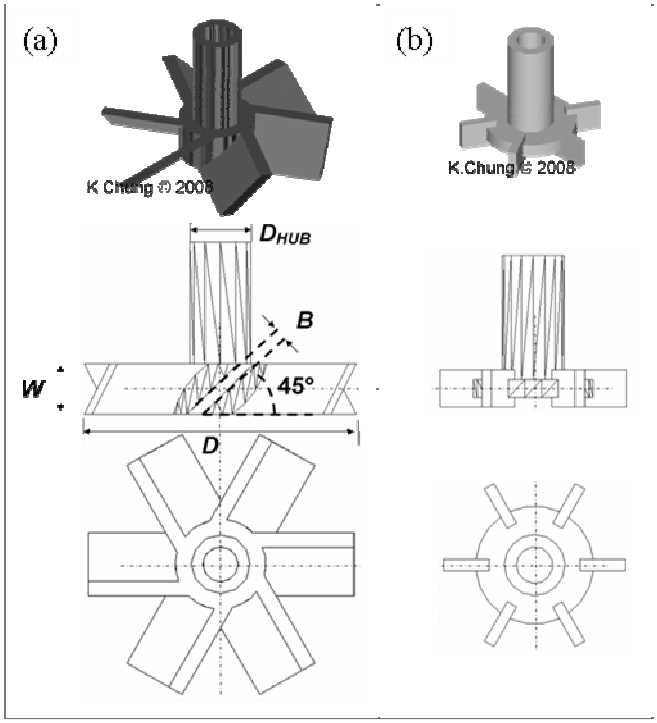

	6-PBTu	6-RDT
D_{HUB} (mm)	5	5
D (mm)	24.5	15
W (mm)	5	3
b (mm)	1.5	1.5

Figure 3.3 Schematic diagrams of (a) 6-PBTu and (b) 6-RDT.

3.1.2 GAS-LIQUID MULTIPHASE EXPERIMENTS

Modifications were made to mixing vessel design adopting single phase mixing to facilitate gas introduction, for the study of two phase gas liquid mixing. As opposed to traditional gas delivery system where a sparger ring is positioned underneath the impeller, a porous glass plate was moulded flush with the vessel bottom, directly underneath the impeller. Not only can the size of bubble sparger be limited, the flow in the vessel is also free from intrusion and the resulting flow field is less disturbed. The porous sintered glass plate is usually used for analytical filtration of very fine precipitates (Scott Duran, UK) and has an average pore size of 10-16 μm (porosity grading as specified in manufacturer's catalogue is 4); the bubbles generated were approximately 100 μm in size. A 20 mm size disc installed at the vessel centre was used to create a uniform bubble distribution across the bottom surface of the impeller (D = 15-24.5 mm). The revised vessel design with gas sparger is shown in Figure 3.4.

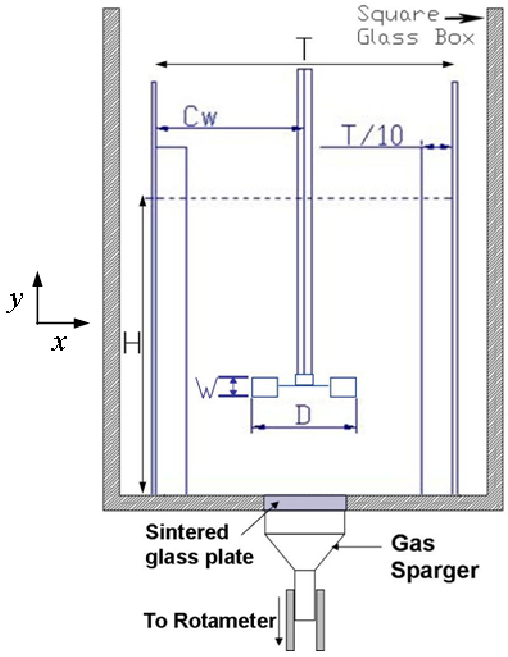

Figure 3.4 Schematic layout of the modified baffled stirred vessels used in gas/liquid multiphase experiments.

Two configurations, (E) and (B) were investigated. The same vessel configuration was employed for the (E) configuration as in the turbulent low viscosity experiments (Figure 3.1(b)). To compare with literature data on large scale vessels, a Rushton Disc Turbine (RDT) with $D = 0.33T$ is used in (B). The impeller was sufficiently small that no commercial unit was available for purchase; hence it was manufactured from polyamide powder by a selective laser sintering (SLS) process at Interdisciplinary Research Centre (IRC), University of Birmingham. The geometry of the 6-RDT impeller is shown in Figure 3.3(b). Various impeller heights (C/H=0.5, 0.33, 0.25) were adopted in this configuration in order to determine the optimal mixing configuration. Two gas flow rates of Q_G = 0.5 and 1.0 vessel volumes per minute (vvm) were used to represent the actual mixing conditions in industrial units.

Compressed air was passed through a rotameter where the gas flow rate can be regulated down to the required level. It is necessary to calibrate the rotameter so the required Q_G can be directly read from the equivalent readings. The calibration, as shown in Figure 3.5, was

carried out using a cylindrical soap film column where the volumetric flow rate was obtained from the rising rate of bubble film.

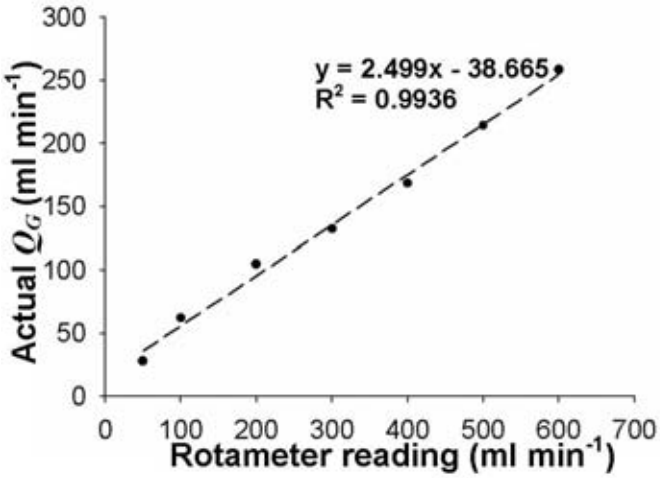

Figure 3.5 Calibration of the rotameter used.

3.2 EXPERIMENTAL TECHNIQUES

3.2.1 POWER DRAW MEASUREMENTS

For the turbulent flow experiments, the tank-averaged specific energy dissipation rate, $\bar{\varepsilon}_T$, was set at 168 Wm^{-3}. An overhead stirrer (IKA Eurostar) was used to provide the drive for agitation. At this power input, the Reynolds numbers (*Re*) obtained were ~ 5520-6000, within the high transitional regime (see Table 3.2). $\bar{\varepsilon}_T$ was determined from the torque exerted on the impeller measured by a Coesfield ViscoMix unit (Coesfeld, Dortmund, Germany). The output of the torque sensor (in mV), was recorded by a chart recorder from Concept Instruments (Stourbridge, UK). A section of a measurement based on two different samples is given in Figure 3.6

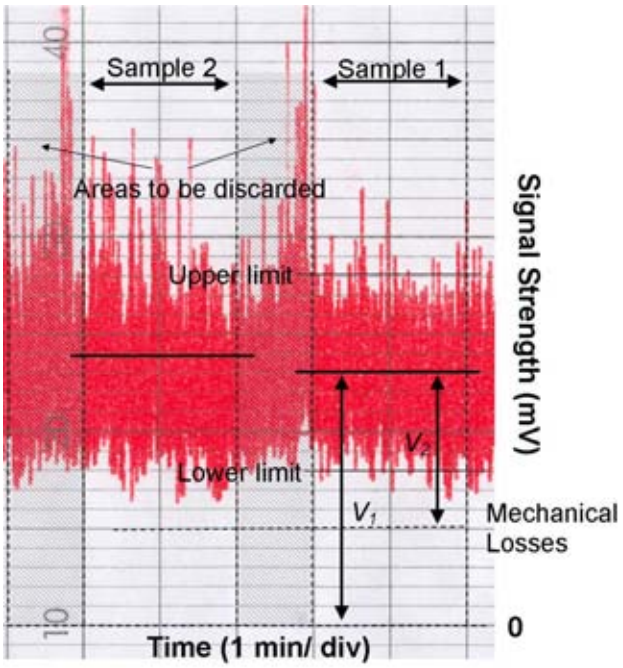

Figure 3.6 Sample from chart recorder

For each measured sample, the motor was allowed to run for two minutes while the time history of the torque reading was recorded. The torque can be approximated by simply averaging the manually determined upper and lower data limit and the actual torque can then be calculated by subtracting this reading from the value recorded for mechanical loss of the motor where no load was applied. Due to the exceptionally low torque measured in this scale, the signal was inevitabily weak with respect to the background noise (i.e. vibration in motor mechanism and impeller shaft), and a high level of fluctuation in the data was observed. Although the inaccuracy may be eliminated by employing a digital data acquisition device, an improved method was developed to analyse data acquired from the existing chart recorder. The scanned chart shown in Figure 3.6 is first split into RGB (red, green and blue) greyscale images as displayed in Figure 3.7. Red marker from chart recorder was blended into the white background (greyscale = 1) in the red element image as shown in Figure 3.7(a), hence only the grid is visible. On the other hand, both the grid and red marker are visible (greyscale = 0) on the green element image as shown in Figure 3.7(b) because green is the complementary colour to red. An image that left only the

marker, as shown in Figure 3.7(c), was obtained when the green element is subtracted from the red element. The relevant *X* & *Y* position of each pixel that has a greyscale reading of 1 was recorded. Finally, coupled with the scaling factor (i.e. mV/pixel), digitisation of data can be completed. This way, the analogue output of chart recorder may be recorded more accurately, where the odd peaks are also taken into account when determining average torque readings.

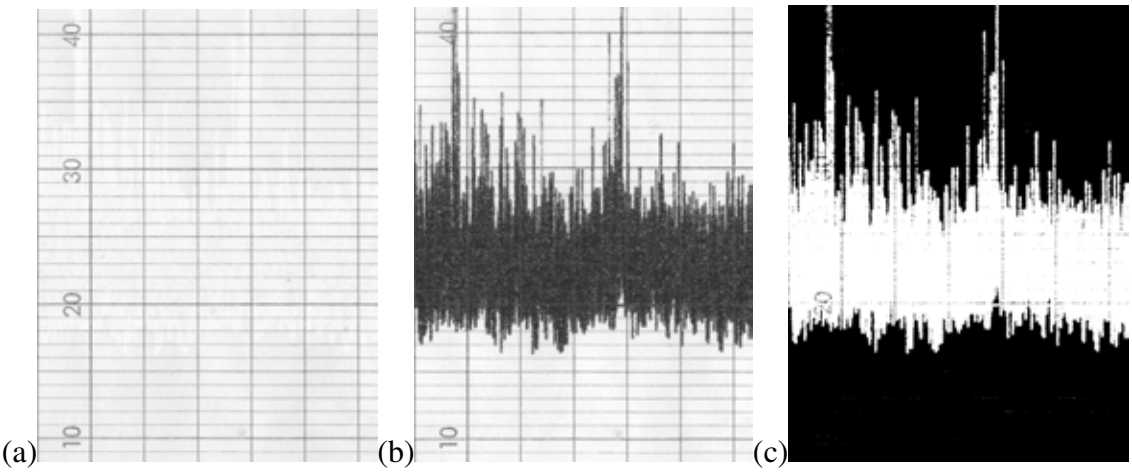

Figure 3.7 (a) Red & (b) Green elements of the scanned chart and (c) Post image subtraction plot.

3.2.2 2-D PARTICLE IMAGE VELOCIMETRY MEASUREMENTS

Flow visualisation was primarily carried out using a TSI Powerview PIV system (TSI, Minnesota, USA). The PIV system consists of four major units; controller (CPU), synchroniser, laser and imaging unit. Proprietary software INSIGHT 6.1 was installed on a Dell Precision 620 workstation (Dell Corp, USA) that controlled the experimental procedures and carried out the post experimental analysis. A dual Nd:YAG (Neodymium-Yttrium-Aluminium-Garnet) laser unit provides laser illumination where energy level used in this work is controlled within 10-200 mJ/pulse (Q-switch delay = 80-130 ms) to ensure a safe operational environment. A series of lens combination mounted on the laser outlet transformed the laser beam (wavelength λ = 532 nm) into a very thin sheet, approximately

1mm thick at the point of measurement. This confines the volume of interest as only those particles at the desired depth were visualised. A synchroniser connected the 1 mega pixel resolution (1000×1016 pixel^2) frame straddling Charged Coupled Device (CCD) camera (PIVCAM 10-30) with the laser emitting unit, to ensure the time difference between image pairs was precisely controlled. The camera was equipped with a Nikkor macro lens having a focal length of 60mm.

Two types of seeding particles were used as the tracer for the liquid phase in this work. In most cases, latex seeding particles doped in Rhodamine 6G with nominal diameter of 3 μm (Duke Scientific Crop, USA) were used. Upon laser illumination, these fluorescent particles emit orange/red light of λ = 602 nm. By installing a 545 nm filter (ALP545, TSI Inc.) on the camera setup, extraneous laser light and excessive noise were effectively filtered out from captured image. As the 3μm particles were supplied in the form of aqueous suspension, it was immiscible with the viscous polymer (PPG) studied. In this case, hollow silver particles were used as a substitute; these particles have a nominal diameter of 10μm (DANTEC Measurement Technology, USA). Incident laser light was reflected from particles in the laser plane onto the CCD camera, hence no filter was required.

Cross-Correlation Analysis

The INSIGHT 6.1 software was used to carry out the first step of post experimental analysis, where localised instantaneous velocity of the liquid phase was extracted from image pairs. Captured images were first divided into interrogation areas (IA) where the size of IA affects the resolution of measurement. The size of IA, L_{IA}, depends on the quality of visualisation which can be affected by various factors (i.e. degree of magnification, size and quantity of seeding particles and clarity of the working fluid). IA in

this work was set to 16×16 pixel^2 where permitted. Instantaneous velocity information (u, v) was given in terms of axial (X) and radial (Y) direction in each of the IA. The predetermined Area of Interest (AOI) within the captured image was broken up into IAs with the use of a Nyquist grid, where 50% overlapping is permitted between adjacent IAs. A combination of Gaussian filter and Fast Fourier Transform algorithm engines were applied on each individual IA for the task of peak searching and cross correlation (Keane & Adrian, 1990; Keane, 1994). The peak search engine picked up identical peak signals from both images and hence any noise, caused for example by light reflection or difference in laser power, in any of the two images would fail the signal-to-noise ratio (SNR) validation. The cross correlation process is illustrated in Figure 3.8 and it highlights the condition for a successful cross correlation.

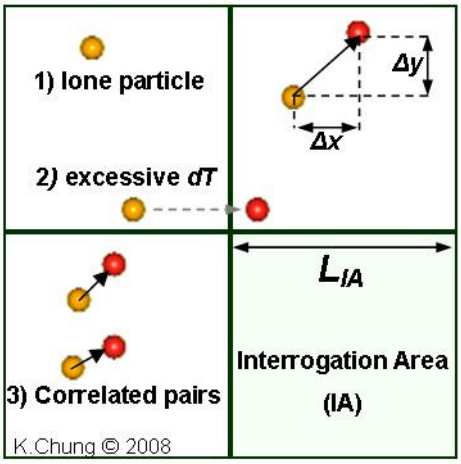

Figure 3.8 Illustration of the cross correlation process and possible scenarios.

The time interval between the two image captures, dT, plays a vital role in the quality of PIV measurements. As a general rule of thumb, the maximum displacement of particle should not exceed a quarter of the length of interrogation area, L_{IA}, to avoid failure in SNR validation, shown as particle 2 in Figure 3.8. Assuming the maximum velocity in stirred vessels equals to the velocity at the vicinity of impeller (U_{TIP}) where energy is at its highest, suitable dT can be determined by

$$dT = \frac{0.25 L_{IA} M}{U_{TIP}} \tag{3.1}$$

where M is the camera magnification.

The instantaneous velocities of particles u, v, in X and Y directions within each interrogation areas, can be determined from particle displacement, Δx and Δy as shown in Figure 3.8, over the controlled time interval, dT,

$$u = \frac{\Delta x}{dT} \tag{3.2}$$

$$v = \frac{\Delta y}{dT} \tag{3.3}$$

It should be noted that any failure during the course of SNR validation will result in a numerical '9.9×10^{9}' velocity entry in the interrogation area instead of an error code. This can lead to under/overestimation of velocity during time-average calculations if such error is not identified. Such erroneous vector entries are removed during data analysis by MATLAB®, more details are given in the next Section.

Due to the turbulent nature in the flow being investigated, 500 image pairs (frames) at 15 fps were required to ensure acquisition of accurate time-averaged data. Details of the accuracy estimation are provided in Chapter 5.

3.2.3 DATA ANALYSIS

Flow information was exported in ASCII data format. The majority of data processing and graphing were carried out using MATLAB® Version 6 and V2006b (Mathworks Inc, USA). The first few entries for a typical vector file are shown in Figure 3.9. The first two

columns give the coordinate of the interrogation area, where the entries, in respect of the whole area of interest, are presented in the order of horizontal (*X*) then vertical (*Y*) direction, as illustrated in Figure 3.10. Column 3 and 4 yield the instantaneous velocities *u*, *v*, in *X* and *Y* direction. It is noted that a vector that failed SNR validation described in previous section was recorded as an abnormal numerical entry, such as those in rows 3-5. Vector of this type can be recognised by a '-1' entry in column 5, and was subsequently replaced by a NaN (not a number) entry in the respective spaces in columns 3 and 4.

X(mm)	Y(mm)	U(m/s)	V(m/s)	CHC
30.333332	55.866665	0.010635	0.051243	1
30.866665	55.866665	0.3156	0.069681	1
31.4	55.866665	9900000256	9900000256	-1
31.933332	55.866665	9900000256	9900000256	-1
32.466663	55.866665	9900000256	9900000256	-1
33	55.866665	0.007225	0.021556	1
33.533333	55.866665	0.002044	-0.152277	1
34.066666	55.866665	0.035108	-0.18658	1

Figure 3.9 Typical vector file.

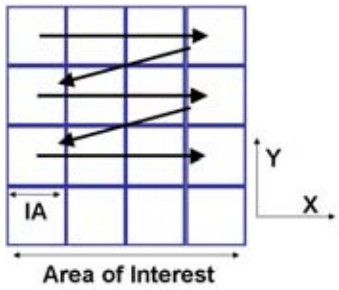

Figure 3.10 Reading order.

Basic vector plots and more advanced vorticity plots can be automatically generated by proprietary software TECPLOT 8.0. However, the MATLAB® software was always used to carry out such task due to its programmability and its ability to carry out more complicated calculations.

3.2.4 RECONSTRUCTION OF 3D FLOW FIELD

In order to visualise the flow in the *z* direction, the lens setup at the laser head is rotated through 90° so that a horizontal laser plane was produced, as shown in Figure 3.11. The movement of the seeding particles within this plane was monitored from underneath the tank by utilising a 45° mirror. Thus, the instantaneous velocities, *u* and *w*, which describe the flow in the *x* and *z* directions, respectively, were measured. Different horizontal planes were investigated so that flow information was obtained at different heights in the vessel.

In order to eliminate the 'tunnel effect' which arises from the cylindrical geometry of the vessel, the camera was also moved horizontally in accordance with the movement of the laser sheet to keep a constant separation with the laser plane; this was achieved by employing manual traverses (SDS Series Linear Translation Stages, Newport Corp, USA). Calibration of the images to relate the number of pixels to an actual length was carried out before each set of experiments. Using the INSIGHT 6 software, the vessel diameter (45 mm) was used as a length-scale. The field of view was kept constant throughout the experiments, to ensure the same resolution in both vertical and horizontal planes. One limitation with this technique is that flow above the impeller is obscured and therefore cannot be visualised, similar to areas which are obscured by baffles in 2-D vertical PIV. Although impellers can be manufactured from acrylic resin or other transparent materials, preliminary tests have shown that the refraction around the edges of these miniature impellers are too great for an undistorted visualisation of the volume above impeller. It should be pointed out that the results can only be used for time-averaged analysis since *u*, *v*, *w* are not measured together simultaneously.

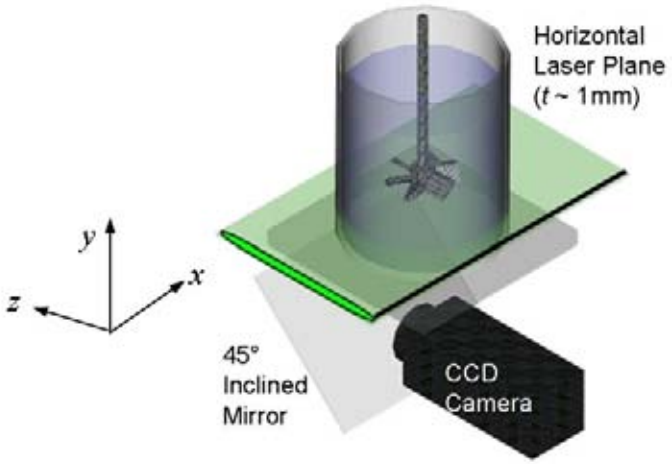

Figure 3.11 Experimental setup for the 3-D reconstruction.

The essence of 3-D reconstruction is to simulate conventional 3-D PIV by obtaining flow information in the *z* direction from the *x*-*z* velocity field, and combining it with the *x*-*y* velocity field. The thickness of the laser sheet was ~1 mm in the area of interest, thus,

horizontal PIV measurements were made at 1 mm intervals along the whole height of the vessel. For the 45 mm tank investigated, a 3-D PIV reconstruction plane required 45 horizontal and 1 vertical planar measurements. The length of the interrogation area, L_{IA}, in the *x-y* direction was set to 1 mm to ensure a consistent presentation of the data.

For any configuration, only *u* and *w* measured along the central row in each horizontal PIV measurement plane represent instantaneous velocities in the *x* and z directions as shown in Figure 3.12. Data from other rows do not correspond to flow along *x* and *z*, and are therefore not used in the reconstruction. By stacking data from the central rows in different horizontal planes, a vertical plane of *u* and *w* data can be constructed in the same format to match the *u, v* vector field obtained from vertical PIV measurements; thus, a vertical plane of *u*, *v*, *w* measurements is constructed. Comparison of the values of the *u* component obtained from the horizontal and vertical planes can be used as an indication of the precision of the measurements. The maximum difference between the *u* components was within ± 3%, which indicates an excellent measurement precision and provides a useful check during the reconstruction process.

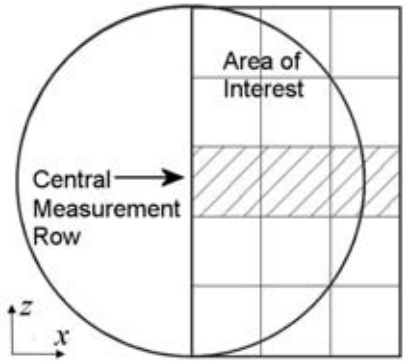

Figure 3.12 Central measurement row where data was used for reconstruction.

3.2.5 ANGLE RESOLVED MEASUREMENTS

Angle resolved measurements were carried out with the addition of an encoder. Off-the-shelf units were unavailable due to the specific needs for these experiments; hence an

encoder was designed and constructed. It consists of three parts: pointer, trigger and base unit. The pointer was fixed on the impeller shaft as shown in Figure 3.13, it cuts an infrared 'beam' at the trigger once every revolution, this in turn giving out a +5V TTI signal. The base unit was designed and built by the author and not only acts as a power supply but also amplifies the signal current to a level that is sufficient to trigger the PIV synchroniser. A full schematic of the encoder design is shown in Appendix A.

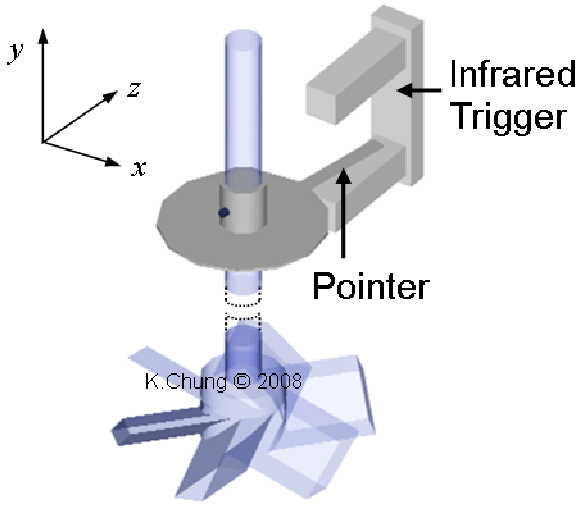

Figure 3.13 Illustration of pointer and infrared trigger mechanism.

The metallic baffle cage employed led to a restricted view of the impeller discharge if the conventional 45º degree imaging plane between two baffles was used; this is not desirable as the main objective of angle resolve measurement is to visualise the trailing vortices in the vicinity of impeller. Therefore a plane 5º in front of a baffle was chosen to obtain an unrestricted view of the area around the impeller. Measurements were taken every degree within a 60° section so that flow information for the whole 360° around impeller can be reconstructed by joining six of these 60° sections end-to-end. With an angular resolution of 1°, it is critical that every measurement captured is at the intended angular position. The conventional method which involved manually repositioning the pointer to match the required angular position was found to be inaccurate. Therefore an alternative method was

applied where the time delay, *dt*, between the signal and actual capture time was controlled as illustrated in Figure 3.14 whilst the angular position of the pointer was permanently fixed. Assuming the fluctuation of impeller speed, *N*, is negligible, *dt* can be calculated by

$$dt = \frac{\theta}{360N} \tag{3.4}$$

where θ is the angular position required.

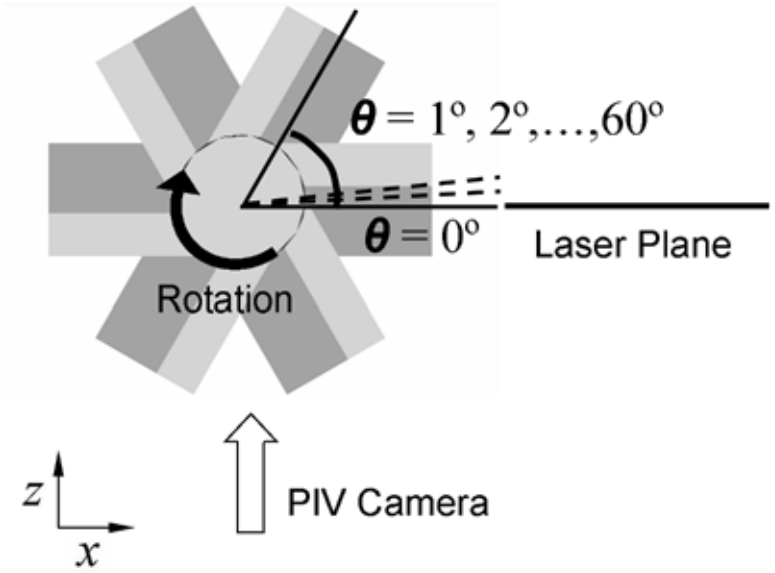

Figure 3.14 Illustration of angular position of measurement plane.

Validation was carried out by replacing the impeller with a protractor, so the angular accuracy can be visually inspected. It was found that time delay always corresponds to the required angle and images were always stably captured at the desired angular position. The validation is shown in Appendix B.

3.2.6 MIXING TIME ANALYSIS

Experimental Setup

PIV provides whole field velocity measurements in the defined area of interest. A more direct quantification of the overall mixing may be obtained from measurement of the mixing time. Utilising the PIV hardware, planar laser induced fluorescence (PLIF) was used to determine the time required for a rapid injection of tracer to be homogeneously mixed within the imaging plane in the stirred vessel. An inherent assumption with this technique is that homogeneity of the tracer within the imaging plane, which covers the entire vertical cross section of the vessel, is representative of the whole. Rhodamine 6G (Sigma Aldrich, UK) was used as the tracer dye since it possesses the high quantum yield and photo-stability required. Once excited by the λ_{ex} = 532 nm laser light, it emits at λ_{em} = 566 nm.

The PLIF experimental technique employed by Hall *et al.* (2004) was improved to minimise the injection volume to reduce the injection time to mixing time ratio; this in turn required a higher injection concentration to achieve a similar final tracer concentration in the tank. 0.4 ml of tracer ($C_i = 8\times10^{-3}$ kg m^{-3}) was delivered to the liquid free surface via a hypodermic syringe connected to a flexible 2.5 mm diameter rubber tube fixed to the wall, so the same injection point was always used near the liquid surface, as illustrated in Figure 3.15 to reduce the influence of the addition of the dye upon the fluid flow as much as possible. The injection point was set at 90° from laser plane as shown in Figure 3.16; this position was chosen because the injected tracer was guaranteed to arrive to the laser plane promptly whilst its momentum did not have a great effect on the flow under investigation. Upon tracer injection, 90 single images were captured at 15 fps; equivalent to 6 s of data which is adequate for the turbulent systems. A higher frame rate of 30 fps could be achieved by coupling frame A and B in frame straddling mode, but this would require an

unacceptably long dT of 3.3×10^4 μs between frames A and B; this particular PIV system is not designed to cope with this lengthy delay (100μs is usually used) hence results in errors. Each individual frame was outputted as a high resolution (1M pixels) image file in Tag Image File Format (tiff). To minimise the degree of random error, each experiment was repeated 10 times.

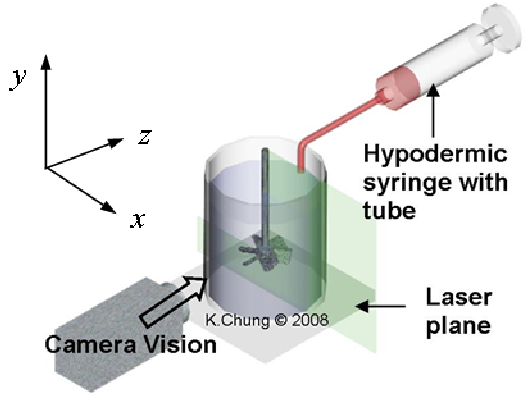

Figure 3.15 Illustration of PLIF setup.

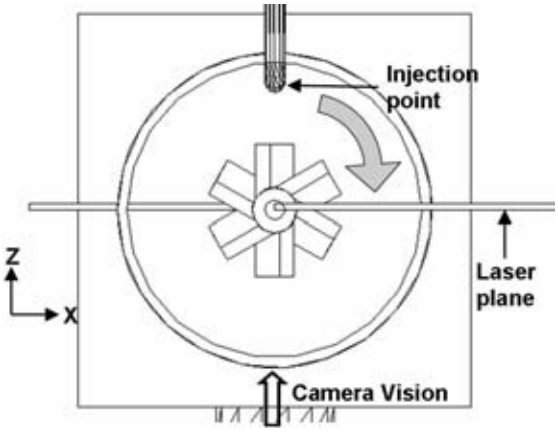

Figure 3.16 Tracer injection point.

Similar to PIV, extraneous λ = 532nm laser light was filtered out by using the λ = 545 nm filter, leaving the captured image relatively clear of noise. The same laser intensity was used in both PLIF and PIV.

Analysis

The temporal concentration history of each individual measuring point was obtained from the greyscale values of the image sequences, and mixing time was determined when greyscale values of all the measuring points reached certain degrees of uniformity. Within the linear range, the tracer concentration at any given point can be obtained from greyscale value by,

$$C_i = C_\infty \frac{G - \langle G_B \rangle}{\langle G_{C_\infty} \rangle - \langle G_B \rangle} \qquad (3.5)$$

Within the linear range, for the Rhodamine 6G dye used, the relationship between the fluorescent intensity, I_F and concentration, C_i can be expressed as (Guibault, 1990),

$$I_F = A \cdot I_0 \cdot \Phi \cdot \varepsilon \cdot b_L \cdot C_i \tag{3.6}$$

Within the linear range, these values remain unchanged. Outside this range at the higher end of concentration scale however, any increase in concentration no longer relates linearly to the greyscale. As a result, a calibration was carried out to determine the upper limit of Rhodamine concentration which can be used. The greyscale was measured over a wide range of final concentrations C_∞. The calibration was compiled into a greyscale versus tracer concentration graph as illustrated in Figure 3.17.

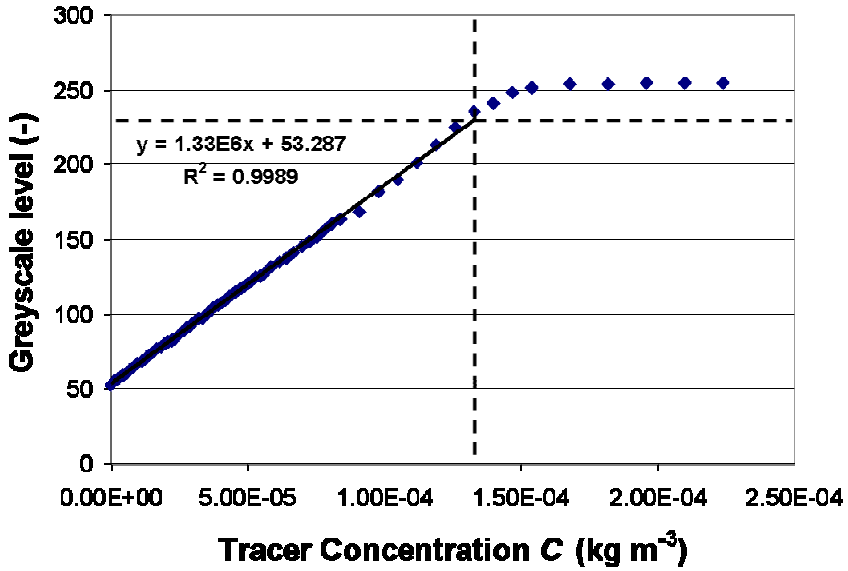

Figure 3.17 Pixel greyscale versus tracer concentration.

It was found that the greyscale value increases linearly with concentration up to 1.33×10^{-4} kg m^{-3}, and the concentration can be calibrated as

$$C_i = \frac{G_i - 53.287}{1.33\times10^6} \tag{3.7}$$

A background greyscale of 53 is present for the camera used and values less than 53 are unusable for the concentration measurements.

Although the dissipation of tracer is ideally analysed on the basis of each individual pixel, the consumption of time and computing power would be uneconomical. Instead, greyscale value was based on a particular region, for example averaging over a line or a block as shown in Figure 3.18.

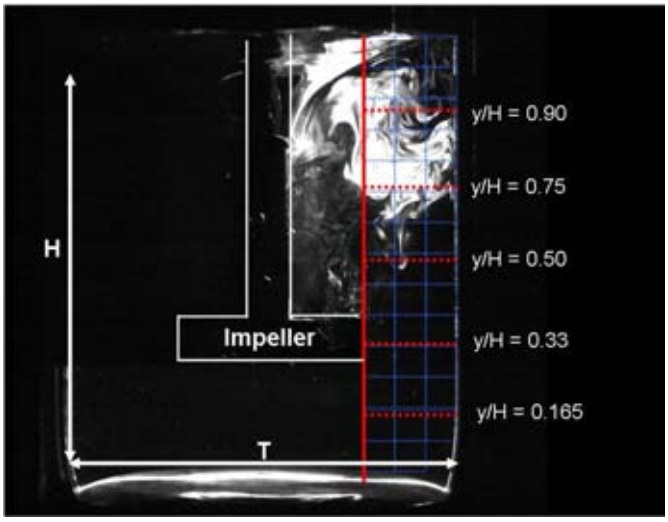

Figure 3.18 Sampling points for different methods. PLIF Image showing a T = 45 mm vessel with U configuration agitated at 625 rpm (t = 0.13 s).

The line-based method (red lines) averages greyscale values from pixels along a line in the radial direction. As a result, temporal concentration at different axial positions can be compared directly. Likewise, the block-based method (blue lines) performed averaging in a specific area for improved accuracy in more complicated system. Each of these averaged readings acts like an individual probe in their respective region; hence the temporal mixedness in various parts of the vessel can be monitored. It is imperative to understand that in both line and block measurement methods, the size of the averaging area in each sample is inversely proportional to spatial accuracy. The time required to achieve a mixedness of 95%, τ_{95}, was found once all averaged readings of C_i at different parts of the vessel settled within ±5% of C_∞.

3.2.7 GAS / LIQUID TWO PHASE MIXING

Experimental

Distilled water was used as the working fluid; therefore the fluorescent seeding particles combined with the optical 545nm camera filter can once again be applied. This aids the filtering of excessive scatter of laser light which occurs at bubble-liquid interfaces during the measurement. Due to the difference in refractive indices, fluorescent light emitted by the seeding particles obstructed by gas bubbles in front of the measurement plane would be distorted and consequently fail the SNR validation, therefore only velocity data for the liquid phase is measured. For the gas phase, the working fluid was dyed with a higher concentration $C_\infty = 1\times10^{-4}$ kg m^{-3} of Rhodamine 6G than that used in PLIF experiments, for a more differentiable appearance between bubbles in front and within the laser plane; this is a critical step for the data analysis. Because of multiple light reflection at the gas-liquid interface, the intensity of the light emitted by Rhodamine is highest at the interface which provides a sharp contrast between liquid and air and, thus, clearly defines the boundary of a gas bubble. In this case, no seeding particles are added. The camera aperture needs to be reduced accordingly due to the higher fluorescence intensity. As with the PLIF experiments, the 545nm optical filter is required for the removal of incident 532nm laser light. As the loss in the vector quantity is minimal in liquid phase measurement, 500 image pairs, as used in the ungassed condition, was sufficient for accurate time-averaged measurements. However, the reduction in imaging quality for the gas phase measurement required the sampling quantity to be increased tenfold to 5000 image pairs.

The total gassed power input, P_G/V = 168 Wm^{-3}, was taken to be the same as for the un-gassed experiments for the ease of comparison. It may be worth to note that P_G is actually a combination of the gassed power input P_g, and hydraulic power term as shown in

$$\frac{P_G}{V} = \frac{P_g}{V} + g\rho_L U_g \tag{3.8}$$

where g is gravity, ρ_L is density of fluid and U_g is gas superficial velocity,

$$U_g = \frac{4Q_G}{\pi T^2} \tag{3.9}$$

The experimental condition for all the gas liquid two phase mixing condition is given in Table 3.3.

3.2.8 MIXING IN VISCOUS NEWTONIAN FLUIDS

Experiments in the low *Re* regime were carried out utilising the same PIV and hardware setup. The working fluid used was polypropylene glycol (PPG) (Sigma Aldrich Ltd., UK), which is a Newtonian fluid. Two different grades of PPG were studied; the molecular masses are 2000 (PPG2000) and 2700 (PPG2700). Whilst possessing the same chemical properties, the only distinction between these two grades of PPG are their viscosities due to the different lengths of polymer chains. The dynamic viscosities, μ, of the two PPGs were tested using a AR1000 advanced rheometer (TA Instrument, USA) with a Carri-Med acrylic cone and plate geometry (60 mm in diameter with 2º angle). A shear stress sweep from τ = 0-200 Pa, (conditions the fluid was likely to experience throughout the experiments) was imposed on the two PPG samples at different temperatures and the steady state shear rate $\dot{\gamma}$, was recorded for each data point. An example of flow curve for the PPG2700 and PPG 2000 sample is shown in Figure 3.19, hence the viscosity,

$$\mu = \frac{\tau}{\dot{\gamma}} \tag{3.10}$$

As with other samples measured, the gradient remained constant throughout the measured range (R^2 = 1) and the fluid was Newtonian.

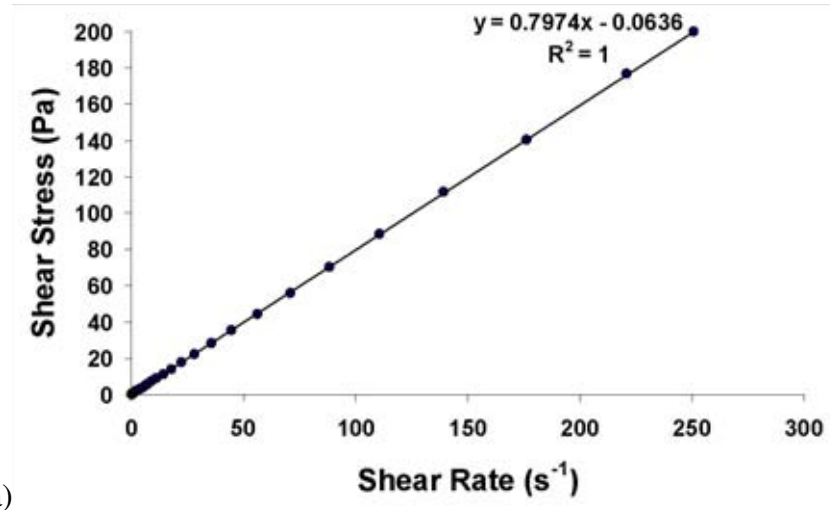

(a)

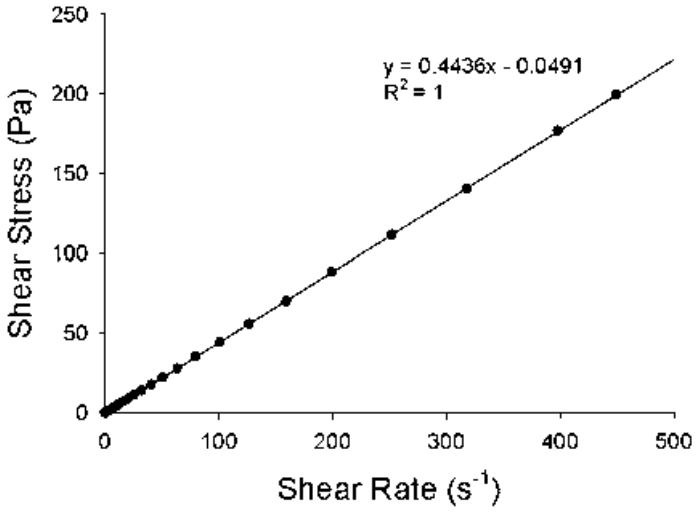

(b)

Figure 3.19 Shear stress versus shear rate plot for (a) PPG2700 and (b) PPG2000 sampled at 20°C.

A summary of the dynamic viscosities of the PPG2700 and PPG2000 fluids is shown in Table 3.1. As the viscosity is highly dependent on the ambient temperature, all experiments were carried out in an air conditioned environment at 20ºC; at this temperature PPG2700 and PPG2000 are approximately 800 and 450 times more viscous than water as used in turbulent low viscosity experiments.

Table 3.1 Viscosities (Pas) of PPG at different temperatures.

Temperature (°C)	PPG2700	PPG2000
20	0.797	0.444
23	0.669	0.367
25	0.605	0.326
26	0.552	(-)
27	0.514	(-)
28	0.502	(-)

The density, ρ, was 1005 kgm^{-3} for both fluids at 20ºC. Various impeller speeds were adopted for (B), (U), (E) and (S) configurations, detailed experimental configurations are shown in Table 3.4 and Table 3.5 for PPG2700 and PPG2000 respectively. Impeller Reynolds number (*Re*) throughout the experiment range was 0.5-16.5 and 1-34 for PPG2700 and PPG2000 respectively; this is within the laminar to low transition flow regime.

As mentioned earlier, hollow silver particles were used in this part of work due to the immiscibility of the aqueous fluorescence particle suspension and the polymer fluid. Silver particles are at least 3 times the size of the fluorescent particles; therefore, the smaller sized grid (16×16 $pixel^2$) is no longer adequate. Instead a 32×32 $pixel^2$ grid was used in the correlation process; the reduced resolution was found not to have a severe effect on experimental accuracy because the requirement of spatial resolution in laminar system is much lower that that in turbulence system, i.e. here the smallest η is 1.9 mm where the η was only 0.0493 mm in the low viscosity system studied elsewhere in this work, although the application of η may not be suitable in laminar system.

PLIF was also applied in a similar manner as in the turbulent low viscosity experiments, however a combination of increased viscosity and insolubility of tracer in polymer prohibited an instantaneous dissolving of Rhodamine 6G powder. This problem was worse in PPG2700 as it possesses a higher viscosity. It was therefore required to carry out the preparations of tracer in a water bath set at 60ºC for 24 hours to lower the viscosities in both samples, allowing the Rhodamine 6G to partially dissolve over the prolonged period. The resulting fluorescent tracer concentration is still much lower than the optimal concentration of 8×10^{-3} kgm^{-3}. No change was observed for the rheological properties of tracer after the extended heat-cool cycle. It is worth to note that the lowered *C* contributed

to a lower fluorescence level I_F in Equation 3.6, which consequently reduced greyscale level G.

3.3 EXPERIMENTAL CONDITIONS

The conditions for experiments in the high transitional regime are given in Table 3.2. Water was used as the working fluid in all experiments.

Table 3.2 Dimensions and experimental conditions of the configurations used in the high transition mixing regime with water as working fluid.

Configuration	*T & H* (mm)	*D* (mm)	*C* (mm)	C_W (mm)	$\bar{\varepsilon}_T$ (Wkg^{-1})	N (rpm)	*Re*
Baffled (B)	45.0	24.5	15.0	22.5	0.168	575	5520
Un-Baffled (U)				22.5		625	6000
Eccentric (E)				15		575	5520
Tilted (T)				N/A		575	5520
Square (S)	41.5		13.5	20.5		595	5712

Whereas the conditions for the gas liquid two phase mixing systems are given in Table 3.3. Water was used as the working fluid in all experiments.

Table 3.3 Dimensions and experimental conditions of the used in the gas liquid two phase mixing system with water as working fluid.

Configuration	*T & H* (mm)	*D* (mm)	*C* (mm)	C_W (mm)	$\bar{\varepsilon}_T$ (Wkg^{-1})	Q_G (vvm)	*N* (rpm)
Baffled (B)	45.0	15.0	15.0	22.5	0.168	0	860
						0.5	950
						1.0	980
			11.25			0.5	1100
			22.5				950
Eccentric (E)		24.5	15.0	15.0		0.5	650
						1.0	700

Finally the conditions of experiments in the laminar regime with PPG2700 and PPG2000 are shown in Table 3.4 and Table 3.5 respectively.

Table 3.4 Dimensions and experimental conditions of the configurations used in the laminar mixing regime with PPG2700 as working fluid.

Configuration	*T & H* (mm)	*D* (mm)	*C* (mm)	$\bar{\varepsilon}_T$ (Wkg^{-1})	*N* (rpm)	*Re*
Baffled (B) / Eccentric (E)	45.0	24.5	15.0	0.611	366	4.8
				1.25	588	7.7
				2.22	811	10.7
				3.6	1026	13.5
				5.5	1233	16.3
Unbaffled (U)				0.611	668	8.8
				1.25	811	10.7
				2.22	954	12.6
				3.6	1098	14.5
				5.5	1257	16.6
Square (S)	41.5		13.5	0.611	420	5.5
				1.25	595	7.8
				2.22	775	10.2
				3.6	1000	13.2
				5.5	1270	16.7

Table 3.5 Dimensions and experimental conditions of the configurations used in the laminar mixing regime with PPG2000 as working fluid.

Configuration	*T & H* (mm)	*D* (mm)	*C* (mm)	$\bar{\varepsilon}_T$ (Wkg^{-1})	*N* (rpm)	*Re*
Baffled (B) / Eccentric (E)	45.0	24.5	15.0	0.611	477	11.3
				1.25	708	16.8
				2.22	907	21.5
				3.6	1114	26.4
				5.5	1313	31.1
Unbaffled (U)				0.611	859	20.3
				1.25	997	23.6
				2.22	1088	25.7
				3.6	1225	29.0
				5.5	1444	34.2
Square (S)	41.5		13.5	0.611	594	14.1
				1.25	886	21.0
				2.22	997	23.6
				3.6	1200	28.4
				5.5	1385	32.8

4. MIXING TIME IN THE TURBULENT REGIME

Substantial information regarding the hydrodynamic behaviour of stirred vessels can be obtained from vector plots and additional analysis with PIV generated data. However, many previous works have taken an integral approach by the measurement or calculation of the time required to mix to homogeneity, i.e. the mixing time (see Section 2.6). Planar Laser Induced Fluorescence (PLIF) was used in this work to quantitatively compare the mixing times of HTE vessels adopting different mixing strategies. PLIF involves the rapid injection of fluorescent tracer dye. The mixing progress is then monitored via the imaging of a plane in the vessel using a laser sheet and CCD camera, similar to PIV (see Section 3.2.2 and 3.2.6). The change in greyscale readings from the pixels on a CCD camera can be used to determine the point of homogeneity. PLIF is a non-intrusive technique and another great advantage holding over other colorimetric methods described in Section 2.6.2 is that it is capable of detecting the tracer concentration only in the specificied plane that is under laser illumination; the tracer dye in the rest of the vessel does not come into contact with laser and therefore causes no obstruction. PLIF tracers (i.e. Rhodamine 6G) offer excellent concentration/greyscale linearity in the usable range under constant laser illumination, which is a highly desirable property (see the calibration graph in Section 3.2.6).

PLIF is a well established technique and there are already numerous reports on the application of PLIF to determine mixing time in stirred vessels (Houcine *et al.* 1996; Fall *et al.* 2001; Hall *et al.* 2005b). Despite of its successful implementation, the technique may be enhanced for HTE application on the ground of practicality and accuracy, as the

mixing time is often very short (τ_{95} < 5s) and the error associated with conventional method described by Hall *et al.* (2005b) may lead to great uncertainties. The improvements made to the original method proposed by Hall *et al.* (2005b) and new data obtained for the different mixing configurations are described and studied in this Chapter.

4.1 DATA ANALYSIS

The 'line' method proposed by Hall *et al.* (2005c) was briefly described in Chapter 3, where the pixel greyscale was measured across *y/H* = 0.165, 0.5 & 0.75 and subsequently averaged as a single reading and plotted as a function of time. A similar example is shown in Figure 4.1, where measurement was taken at *y/H* = 0.165, 0.33, 0.5, 0.75 & 0.9 for a stirred vessel with eccentric (E) configuration.

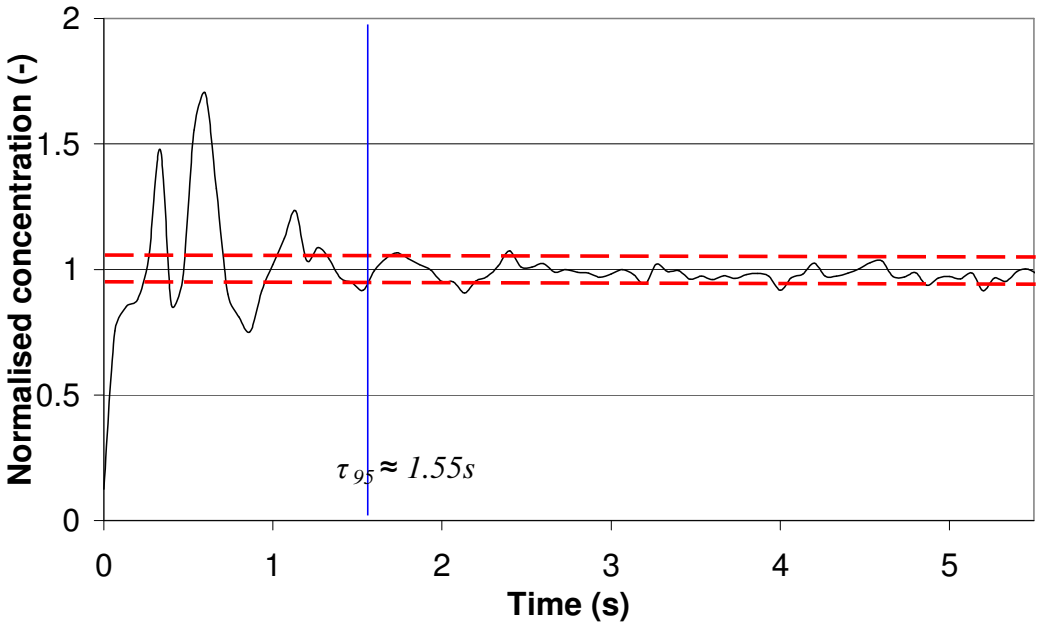

Figure 4.1 Time history of normalised tracer concentration of (E), averaged from measurements across *y/H* = 0.165, 0.33, 0.5, 0.75 & 0.9 from a single experiment.

Following the initial fluctuation, the averaged concentration curve settled within the ±5% line after 1.55s; this agrees with the data reported by Hall *et al.* (2005b) for the mixing time to 95% mixedness, τ_{95}. It should be noted that due to the presence of excessive noise,

the concentration curve occasionally penetrates the ±5% line; improvements on the technique are described later. However, averaging from the five sampling points undoubtedly dampens the fluctuations and hence the mixing time may appear to be shorter. To illustrate this, a breakdown of the average curve, plotting the concentrations from the individual five points, is shown in Figure 4.2.

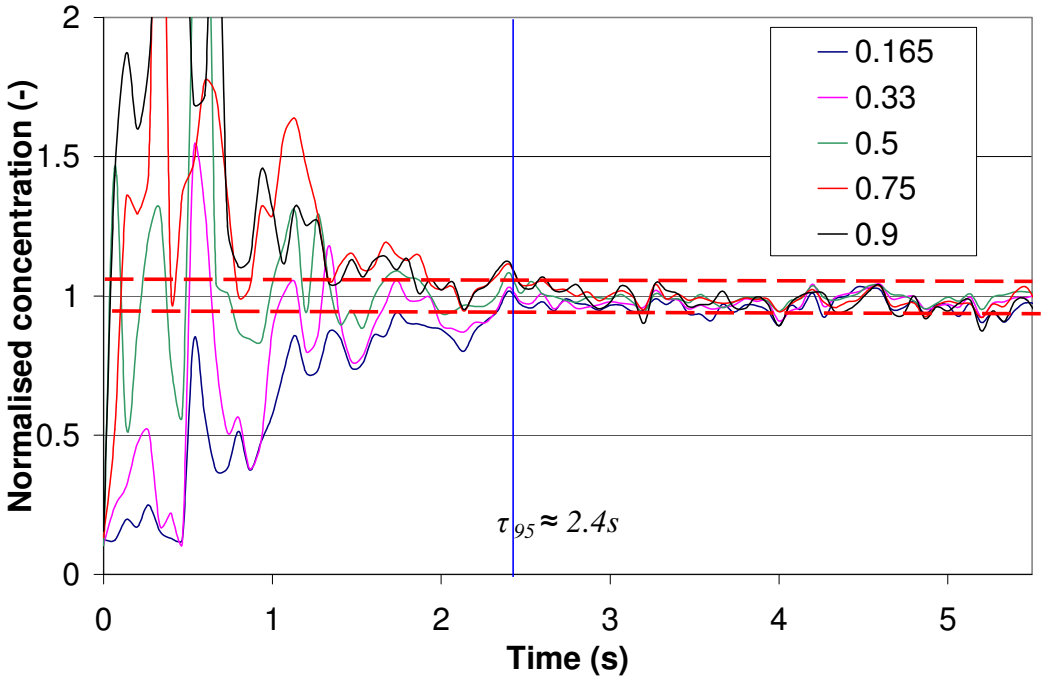

Figure 4.2 Time history of normalised tracer concentration of (E) at *y/H* = 0.165, 0.33, 0.5, 0.75 & 0.9 from a single experiment.

The increased fluctuation in each individual curve immediately becomes obvious. The response of curve with respect to their spatial location corresponded to the path of tracer dye; for example the value of normalised concentration for the curves *y/H* = 0.5, 0.75 & 0.9 changed as soon as the dye was injected at t = 0 s, whilst the tracer required a further 0.4 s to reach level *y/H* = 0.165. The prolonged delay for the tracer to reach the lower half of the vessel is due to the influence of the upper circulation loop. More importantly, it takes a comparatively longer time for tracer concentration at *y/H* = 0.165 to reach homogeneity. Therefore the 95% mixing time should perhaps be taken as the time when concentration curves from *all* sampling points settle within the ±5% line (τ_{95} = 2.4 s in this

case). However, it becomes very difficult to include more than 5 curves on the same graph while keeping each of the curves differentiable; this method is only capable of taking a sample from a limited number of sampling points.

4.1.1 THE LOG VARIANCE APPROACH

It was established that the conventional mixing time analysis may be improved for the HTE application. To address the imprecision and untidiness caused by sampling from a larger number of measuring points, the variance method was applied. The variance, σ^2, from a number of sampling points, n, at a time, t, can be obtained by (Edwards *et al*, 1992),

$$\sigma^2 = \frac{1}{n-1}\sum_{i=0}^{n}(C_i(t) - C_\infty)^2 \qquad (4.1)$$

where C_i (t) and C_∞ are the concentration at sampling point i at time t and the concentration at infinite time (fully mixed) respectively. This method is particularly useful for the block-based analysis, where the measurable region is broken down into much smaller interrogation areas (L_{IA} = 1-10 pixels). Each interrogation area acts as an individual measurement probe. The concentration history from all the samples is combined as one with a reduced damping effect that exists with the previous approach. Each individual interrogation area can be reduced to a suitable size subject to computing power; ideally the size of sampling block is resolved down to a single pixel. For a camera with 1024×1024 pixels there are potentially one million sampling points, but this is rarely achievable with the limited amount of active usable memory in common non-workstation PCs.

The time history of variance from all sampling points in the 45 mm vessel with eccentric configuration is shown in Figure 4.3. Due to the low C_∞ (C_{INJ} = 1.2×10^{-4}kg m^{-3}; C_∞ = 8.38×10^{-6} kg m^{-3}), variance calculated from Eq.4.1 is very small, although it has no effect

on the gradient of the curve. The curve is seemingly much tidier than the concentration profile shown in Figures 4.1 and 4.2. According to Edwards *et al*. (1992), mixing time is determined once the variance falls below a set level or otherwise refered to as the 'cut off point'. This point however, is dependent on the experimental technique employed. Therefore it does not provide a consistent mixing time analysis for a wider range of experiments or if different C_∞ is used. More importantly, as illustrated in Figure 4.3, it becomes very difficult to pinpoint the mixing time as the drop in variance is very minute when the vessel is approaching total mixedness; this is due to the square in Eq.4.1 of the smaller difference between C_i and C_∞. Mixing time in this case can be anywhere between 1.7 and 2 s, or 18% uncertainty.

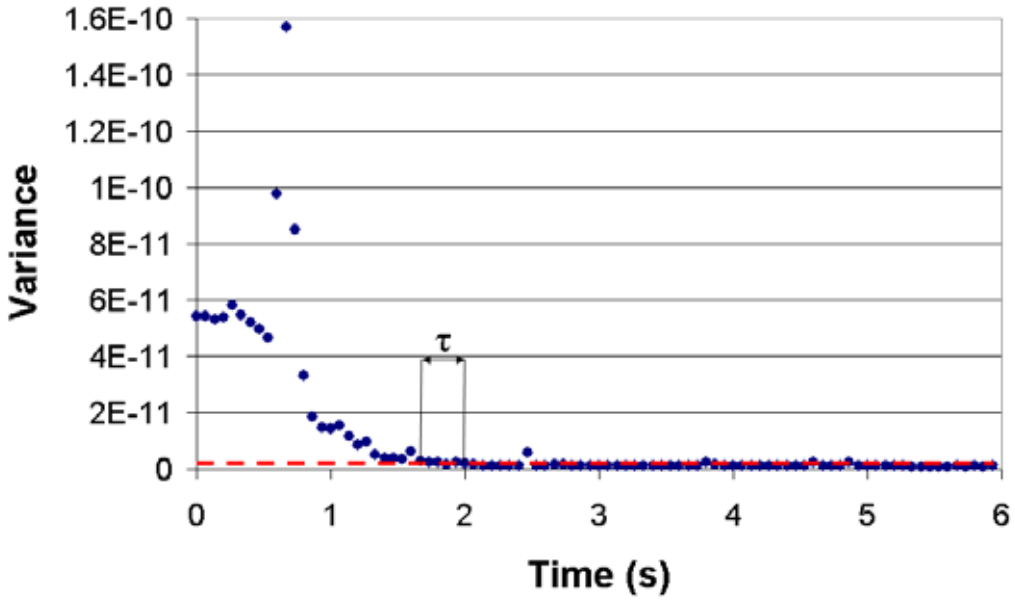

Figure 4.3 Time history of variance of (E) from a single experiment.

In order to discriminate small fluctuations in σ close to the fully mixed condition, Brown *et al.* (2004) described a log variance method. This method introduced a term 'desired mixedness', C_t'. A C_t' of 0 indicates no presence of tracer and C_t' of 1 indicates the system is fully mixed. The logarithm of variance of the desired mixedness is determined by,

$$\log \sigma^2 = \log\left[\frac{1}{n}\sum_{i=1}^{n}(C_{t,i}^{'} - 1)^2\right] \qquad (4.2)$$

Where $C'_{t,i}$ is based upon normalised concentration, therefore when applying Eq. 4.2 to calculate variance, C_∞ is assumed totally mixed ($C_\infty = 1$) and C_i must be normalised. As a result, for the equation governing the conversion from greyscale to concentration,

$$C_{t,i} = C_\infty \frac{G_{t,i} - \overline{G_B}}{\overline{G_{C_\infty}} - \overline{G_B}} \tag{4.3}$$

C_∞ can simply be omitted and concentration is based on the ratio of G and $G_{C\infty}$ following the subtraction of G_B. This simplifies the analytical process and hence helps reducing the demand on computing power.

The time history of log σ^2 using data from the previous example is shown in Figure 4.4. The benefit of this method immediately becomes obvious; the fluctuation at the higher end of C_t' is more observable and more importantly, the degree of uniformity can now be clearly defined at 0.8, 0.85 & 0.9. Upon closer inspection, one may find that the log σ^2 curve does not reach $C_t' = 0.9$. It takes a time, τ, of 1.7 s to reach 85% mixedness. It is apparent that even at equilibrium, there must be still a sizable difference between C_i and C_∞. It was revealed that noise from multiple sources (i.e. reflection of incident laser light on the surface of impeller and liquid free surface, etc) is responsible for the major parts of noise, hence the rest of this Chapter is dedicated to the suppression of such effects.

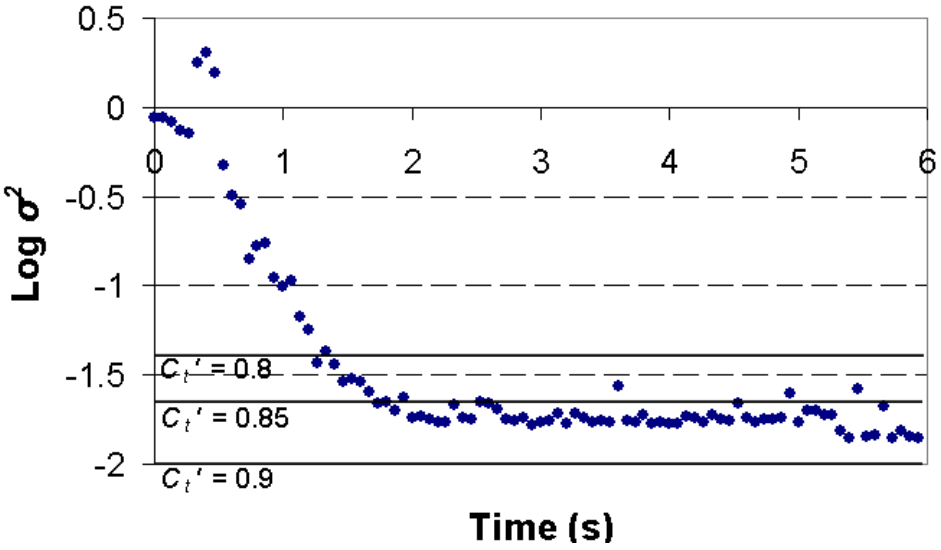

Figure 4.4 Time history of log variance of (E) from a single experiment.

It should be highlighted that despite the log variance method being available in the open literature (Paul *et al.* 2004), it is usually applied to data obtained from a limited number of physical measurement probes (i.e. conductivity or HWA probes). To the author's knowledge, there was no previous attempt to apply the Log Variance method on PLIF data in stirred vessels, which is probably due to the presence of optical noise in the many available sampling points.

4.2 IMPROVEMENTS TO THE LOG VARIANCE METHOD

4.2.1 POINT BASED CALIBRATION AND REFLECTION ELIMINATION

It is a common practice to determine the background greyscale level, $\overline{G_B}$ and greyscale level at equilibrium concentration, $\overline{G_{C_\infty}}$, in Eq. 4.3 from all available pixels in the measurable region prior to and immediately after the experiment, on a universal basis. However a PLIF image of a completely mixed vessel in unbaffled configuration, as shown in Figure 4.5, illustrates that the greyscale level across the measurement area is not uniform. With the contrast and brightness enhanced, horizontal strips and reflections

become clearly visible; if $\overline{G_B}$ and $\overline{G_{C_\infty}}$ were averaged from all pixels as usual in Eq. 4.3, the variance of these averages before injection and at the fully mixed condition will still be vast. Therefore $\overline{G_B}$ and $\overline{G_{C_\infty}}$ should be calibrated for each single measurement point to remove this error.

The free surface of central vortex in unbaffled and eccentric configured vessels reflects laser light, therefore affecting the greyscale levels in the area of measurement. If the side of vessel is taped as shown in Figure 4.5, the reflection can be eliminated altogether, although clearly this area is then no longer available for analysis. As a result, the data in y/H = 0.85 – 1.0 is omitted for greater accuracy in the lower parts of the vessel.

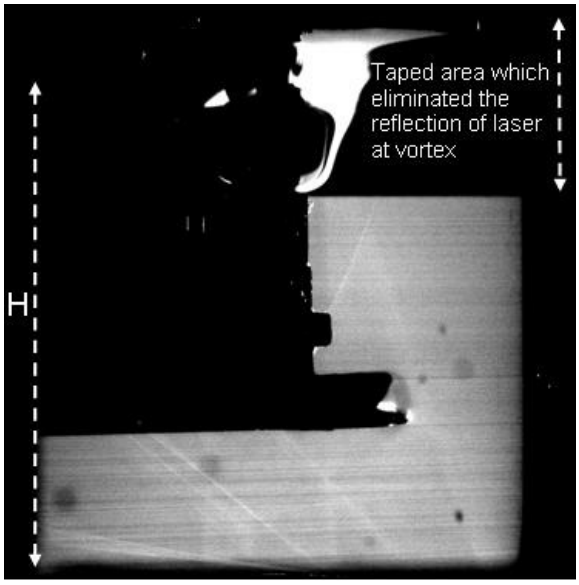

Figure 4.5 A PLIF image showing a completely mixed vessel with (U) configuration. The contrast and brightness of the image was enhanced.

4.2.2 OPTIMISATION OF TRACER CONCENTRATION AND VOLUME

There are two priorities when setting the quantity of tracer to inject: ideally, the concentration of tracer in the injector, C_{INJ} should be kept within the usable range and the resulting $G_{C\infty}$ should be sufficiently higher than G_B so the mixed and partially mixed region is clearly differentiated. In order to satisfy both of these requirements, the injection

volume used, V_{INJ}, is usually large. For example, for a $C_{INJ} = 1.2\times10^{-4}$ kg m^{-3}, V_{INJ} is taken to be 5 ml in order to achieve a very small gain of $\Delta G = G_{C\infty} - G_B \approx 12$; this is simply inadequate as V_{INJ} is then 7% of the total vessel volume. In addition, the duration of injection should be as short as possible in order to minimise its effect on the mixing time. Therefore if V_{INJ} is set to a more appropriate level of 0.4 ml (0.5% of the vessel volume), C_{INJ} will exceed the maximum usable range and *C*/*G* linearity is no longer valid. However, since the log variance method weighs much more on greyscale level towards mixed condition ($C_t' > 0.7$) than the initial stages of mixing ($C_t' < 0.7$), it is reasonable to adopt a much higher C_{INJ}; as long as C_∞ is comfortably within the maximum usable range.

The mixedness at equilibrium condition for the sample shown in Figure 4.5 is 85%. As described previously, the deficit of 15% is due to the noise present. The greyscale levels for any individual pixel can fluctuate at ±2 from $G_{C\infty}$ in some cases; this accounts for 33% of the change in greyscale ($\Delta G \approx 12$). If ΔG is substantially raised with the same level of background noise, this effect can be suppressed. The difference in terms of ΔG for the two examples is clearly visible in Figure 4.6.

(a) 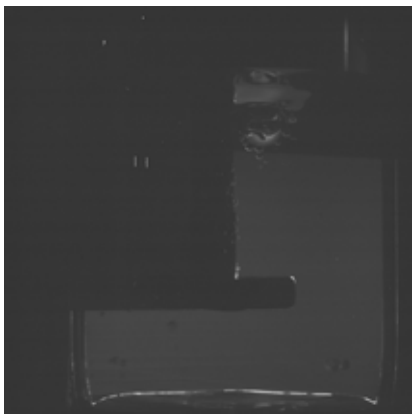 (b) 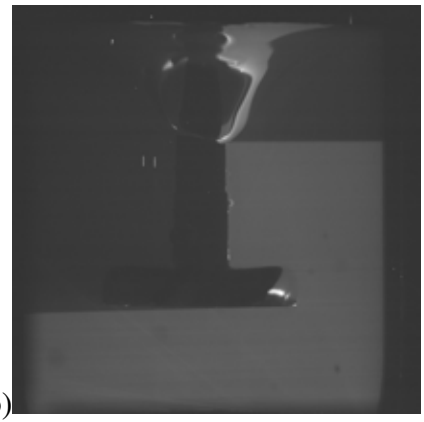

Figure 4.6 Comparison of unmodified PLIF image showing (U) with (a) $C_\infty = 8\times10^{-6}$ kg m^{-3} (V_{INJ} = 5ml, $C_{INJ} = 1.2\times10^{-4}$ kg m^{-3}, $\Delta G \approx 12$) & (b) $C_\infty = 4.5\times10^{-5}$ kg m^{-3} (V_{INJ} = 0.4 ml, $C_{INJ} = 8\times10^{-3}$ kg m^{-3}, $\Delta G \approx 60$).

The effect of C_{INJ} on log σ^2 is shown in Figure 4.7. The same volume of tracer (V_{INJ} = 0.4 ml) was injected in all cases, resulting in a wide range of C_∞ and ΔG ranged from 4-60.

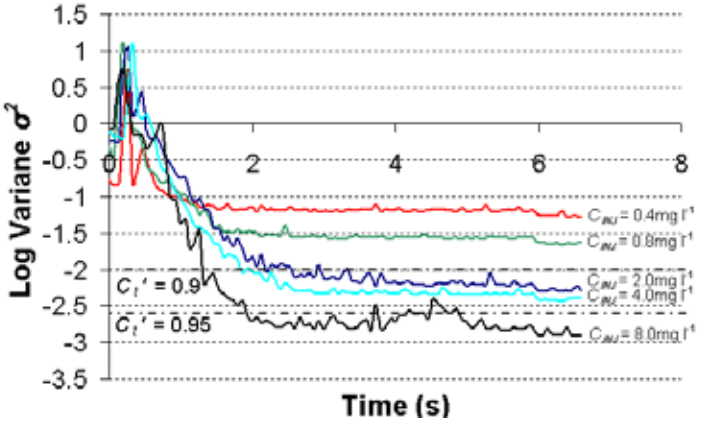

Figure 4.7 Time history of log variance of (E) from experiments with various C_{INJ}.

In the case of C_{INJ} = 4×10^{-4} kg m^{-3}, the average ΔG is 4 and unsurprisingly, log σ^2 only changes marginally before injection and at the equilibrium condition; it only recorded a 70% mixedness when the vessel was fully mixed. Mixedness is gained as the C_∞ increases and background noise lost its dominance. log σ^2 reaches 95% mixedness level when a C_{INJ} = 8×10^{-3} kg m^{-3}, or C_∞ = 4.5×10^{-5} kg m^{-3} is used, here a ΔG of 60 is achieved.

With C_{INJ} = 8×10^{-3} kg m^{-3}, exceeding the maximum allowable concentration for linearity by more than sixty times, it takes 0.8 s for the value of log σ^2 to drop. Although the tracer is being diluted immediately once it is introduced into the vessel, G stays outside the linearity range and does not fall below the upper threshold of 255 until t = 0.8s; the data from this initial stage is not valid and hence log σ^2 at this stage shows no progress of mixing. A C_{INJ} = 8×10^{-3} kg m^{-3} is shown to be sufficient for achieving a mixedness of 95% at equilibrium condition. If the three curves, C_{INJ} = 2, 4 and 8×10^{-3} kg m^{-3} in Figure 4.7 are considered again, one may find that the gradients of the curves all decrease sharply at around t = 2s, which indicates the approach to a completely mixed condition; this somehow gives confidence in the use of C_{INJ} = 8×10^{-3} kg m^{-3}.

Although C_{INJ} may be further increased for an even larger ΔG, in theory achieving an even higher C_t', will inevitably lengthen the un-measurable region (i.e. $Gt,i > 255$). Moreover, a slightly shorter mixing time may be achieved; predictably for a curve in Figure 4.7 with higher C_t', its crossover with $C_t' = 0.95$ should occur sooner. Therefore the impact of using a tracer with C_{INJ} higher than 8×10^{-3} kg m^{-3} on τ_{95} may be carried out as future work. This work however, used $C_{INJ} = 8\times10^{-3}$ kg m^{-3} at $V_{INJ} = 0.4$ ml for PLIF analysis with log σ^2 methods. Again, the τ_{95} obtained may not be an absolute value, but it is absolutely adequate for the purpose of comparing the mixing efficiency across all configurations.

4.3 RESULTS & DISCUSSION

Mixing time analysis with the log variance method was carried out for each configuration. The injection of dye and commanding the start of capturing sequence are carried out manually; this induced a lot of inconsistencies which affect the mixing time, in extreme cases up to 10%. For this reason the experiments were repeated ten times for each configuration; the average of all ten log σ^2 readings at the same temporal position is taken and plotted on Figure 4.8.

The figure shows that although (B) is the most widely adopted configuration in the process industries, it takes ~30% longer to achieve 95% mixedness compared to (E). Visual observation showed that the slower mixing time achieved by (B) is caused by a small portion of tracer being trapped behind the baffles; the delay is considerable in HTE vessels with a shorter mixing time but may not be apparent in larger scales.

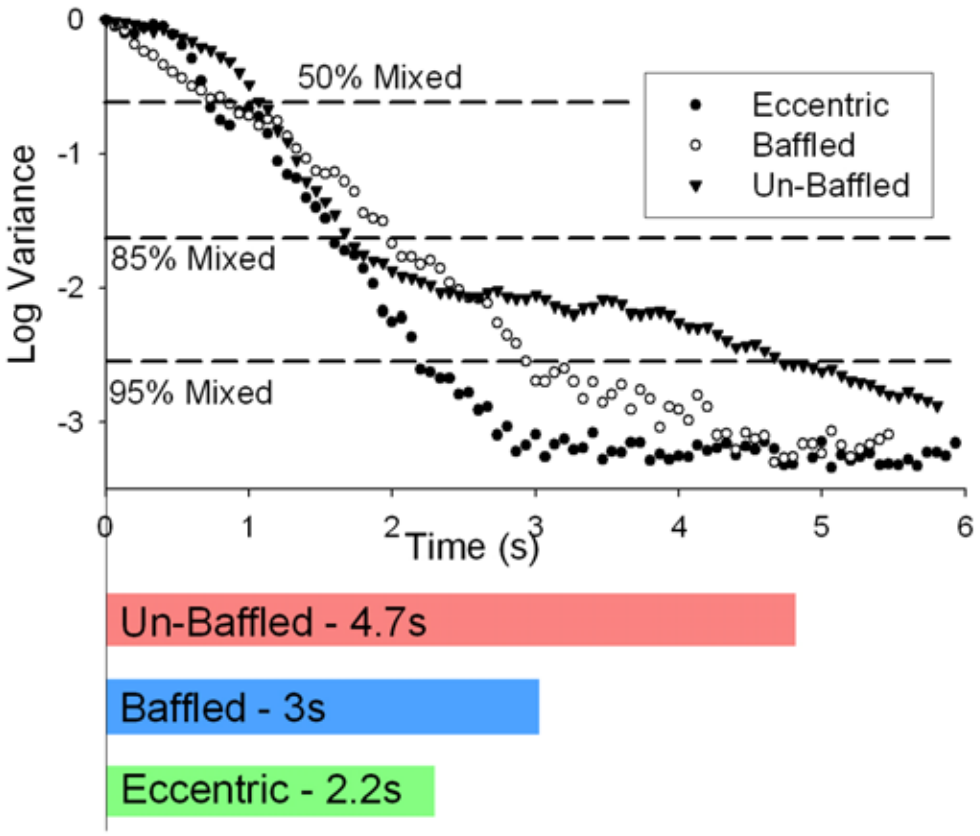

Figure 4.8 Decay in variance of tracer concentration of (U), (B) & (E). Each curve is the average of 10 PLIF experiments.

Vessels in unbaffled configuration achieved the longest mixing time as expected. Surprisingly mixing in the bulk of (U) is similar to (E) up to 1.8 s (i.e. ~ 85% mixedness), but beyond that the rate of mixing is substantially reduced due to inefficient mixing in the regions directly underneath the impeller and in the immediate vicinity of the impeller shaft as shown in Figure 4.9(a). The amount of solid body rotation is at its highest in these regions (r/R = -0.1 – 0.1) and so prevents the interaction between tracer and working fluid. With a reduced solid body rotation in (B) and (E), mixing becomes much more efficient as shown in Figure 4.9(b) & (c).

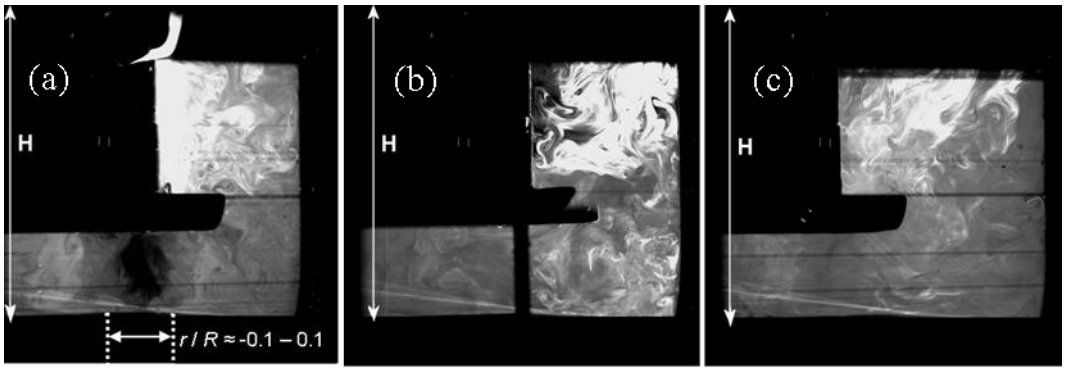

Figure 4.9 Visualisation of tracer dissipation by PLIF 1.3 s after injection in (a) (U), (b) (B) & (c) (E).

Of all the alternative configurations considered, better mixing times were achieved when compared to the conventional baffled configuration, as shown in Figure 4.10. For example, vessels in the shape of cuboid with centreline impeller position (S) (τ_{95} = 2.2s) not only managed the same mixing time to (E), but the curves of decay in variance of both configurations are also identical; the four 90º corners of cuboid vessel actually give better mixing performance than baffles. In terms of mixing time, (S) is an ideal alternative to (E), but with its base shaped as square, more HTE units can be packed into the same space in commercial screening machines.

For the vessel with the PBTu impeller tilted at 15º (T), mixing is more rapid than any other configuration, especially prior to achieving 95% mixedness. The τ_{95} in (T) is slightly shorter than (E) and (S) (τ_{95} = 1.93s). As with (S), alternative configurations such as (T) require a more in-depth research for a solid conclusion.

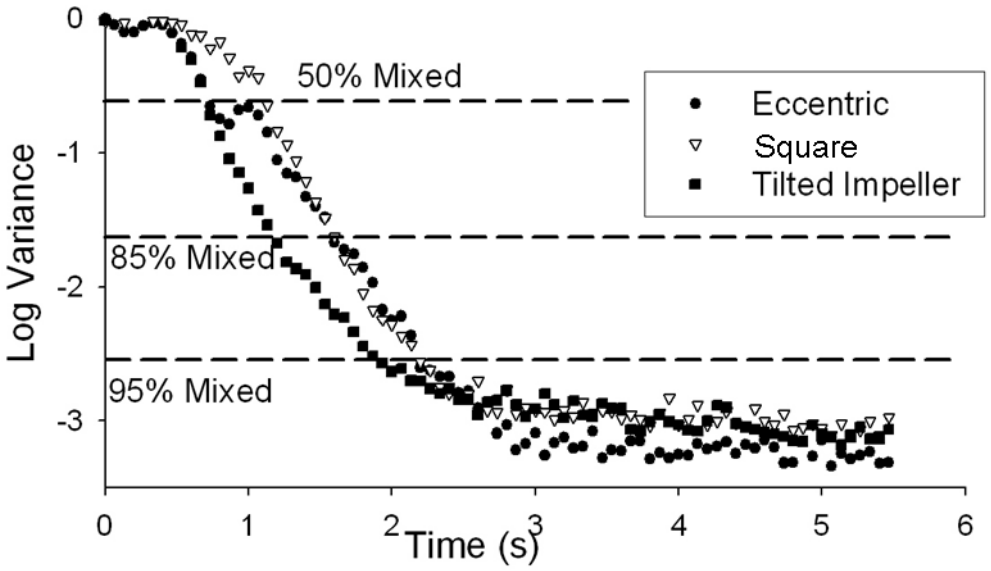

Figure 4.10 Decay in variance of tracer concentration of (E), (C) & (T). Each curve is the average of 10 PLIF experiments.

The τ_{95} of HTE vessels (T = 45mm) adopting various configurations obtained by the log variance method, along with experimental findings from Hall *et al.* (2005b) and estimates using the correlation proposed by Ruszkowski (1994) is shown in Table 4.1,

Table 4.1 Mixing time, τ_{95}, of HTE vessels (T = 45mm) with various configurations.

Configuration adopted	τ_{95} (s)	τ_{95} (Hall *et al.*, 2005b)	τ_{95} (Ruszkowski, 1994)
Unbaffled centreline (U)	4.7	(-)	1.7
Unbaffled eccentric (E)	2.2	1.4	1.7
Baffled (B)	3.0	1.6	1.7
Cuboid (C)	2.2	(-)	1.7
Unbaffled centreline with tilted impeller (T)	1.9	(-)	1.7

Ruszkowski (1994)'s correlation uses only the total power input as follows,

$$\tau_{95} = 5.91 T^{2/3} \left(\frac{\rho V}{P} \right)^{1/3} \left(\frac{T}{D} \right)^{1/3} \qquad (4.4)$$

hence the τ_{95} of 1.7 s is uniform across all configurations. This agrees with the finding of Hall *et al.* (2005b) as the mixing time determined by conventional method is 1.4s and 1.6s for (E) and (B).

Mixing time analysis by log variance method as applied in this work generates results vastly different from that of Hall *et al.* (2005b), for example τ_{95} for (B) nearly doubles if log variance method is applied. This is mainly due to the increased accuracy when more samples are taken in a considerably larger area; homogeneity in this case is much harder to achieve. According to Figure 4.8, (B) & (E) only achieved a mixedness of 80% at τ = 1.5s; vessels with such mixedness may be appreciated as fully mixed in conventional methods as those used by Hall *et al.* (2005b). It should be highlighted that results from Hall *et al.* (2005b) suggested that (E) has a shorter mixing time than (B), in agreement with this work.

4.4 CONCLUSION

Conventional mixing time analysis was reviewed and it was found to be inadequate for the mixing in HTE vessels, which often have a very short mixing time. The key weakness of this method is the inability of handling a large number of sampling points; hence sampling can only be carried out at certain key locations throughout the vessel.

Alternatively, the log variance method may be applied to sample tracer concentration from all pixels across the measurable region. This method is usually applied on mixing systems with a few physical measurement probes. To the author's knowledge the log variance method has never been applied on PLIF analysis or any other optical techniques, probably due to the noise present and the difficulty to achieve homogeneity in data from many sampling points. Analytical and experimental improvements were made and the resulting

mixing time analysis gave satisfactory results. Mixing times of a 45mm HTE vessel in various configurations were determined. (E), (S) & (T) achieved the shortest mixing time, where the conventional (B) takes an extra second to become fully mixed, due to a small amount of tracer being trapped behind baffle. Concentration profile for (U) is similar to (E) up to a mixedness of 80%, beyond such mixedness the mixing progresses at a much slower rate, due to the presence of an insufficiently mixed region.

When studying the same vessel with identical configuration, mixing times obtained through the log variance method are longer than those reported by Hall *et al.* (2005a) estimated via the conventional method. It was suggested that the vessels in 'fully mixed' condition observed in the conventional method were indeed only 80% mixed; it takes much longer for such vessels to reach the 95% mixedness as defined in this work.

5. RECONSTRUCTION OF 3-D FLOW FIELD

The current level of understanding in the characterisation of fluid dynamics and mixing within HTE vessels is limited to the work of Hall *et al.* (2004; 2005a). The authors have used two-dimensional Particle Image Velocimetry (2-D PIV), measuring only the radial and axial fluid velocity components but not the tangential flow that occurs in some of the un-baffled reactors investigated. Such a tangential flow is expected to be substantial and its measurement is essential for a full description of the flow field inside these HTE vessels.

Three-dimensional PIV (3-D PIV) has been used for flow visualisation in laboratory scale stirred vessels (Hinsch, 1995; 2002), where 3-D flow information within a volume of interest can be generated and presented, for example, in terms of velocity vector plots. 3-D flow information can be obtained using stereoscopic PIV (3-D SPIV) imaging techniques which require 2 PIV cameras mounted at an angle to the image plane, as for example in the Scheimpflug configuration (Prasad, 2000; Yoon *et al.*, 2001). However, 3-D SPIV cannot be used to visualise flow inside HTE vessels due to their miniature size which creates physical space limitations. Alternative arrangements include reconstruction of 3-D flow information from multiple 2-D PIV planes. For flows in stirred tanks, these procedures have been applied to obtain detailed information on the flow structure close to the turbine blades using a combination of angle resolved measurements made in different planes (see for example Escudié *et al.,* 2004).

In this Chapter, a technique which uses detailed 2-D PIV measurements obtained both in vertical and horizontal planes to reconstruct the full 3-D flow field inside a miniature HTE vessel is described; the method also allows the error involved in the use of the commonly adopted isotropic assumption to calculate Turbulent Kinetic Energy (TKE) from 2-D data to be assessed as a function of vessel configuration, i.e. unbaffled, baffled and eccentric agitation.

As described in Chapter 2, TKE can be determined from 3-D PIV data, i.e.,

$$k = \frac{1}{2}\left(\tilde{u}^2 + \tilde{v}^2 + \tilde{w}^2\right) \tag{5.1}$$

where $\tilde{u}^2$, $\tilde{v}^2$ and $\tilde{w}^2$ are the root mean square (r.m.s.) of the fluctuating velocity components.

However, 2-D PIV yields only $\tilde{u}^2$ and $\tilde{v}^2$. Assuming isotropy, the missing fluctuating velocity component in the z direction, $\tilde{w}^2$, can be estimated by a 2-D approximation (Sheng *et al*., 2000), thus

$$k = \frac{1}{2}\left(\tilde{u}^2 + \tilde{v}^2 + \frac{1}{2}\left(\tilde{u}^2 + \tilde{v}^2\right)\right) = \frac{3}{4}\left(\tilde{u}^2 + \tilde{v}^2\right) \tag{5.2}$$

The 2-D approximation only gives identical results to the ordinary 3 component TKE calculation under perfect isotropic flow conditions. However, isotropy can rarely be achieved in a stirred tank, especially under turbulent conditions. Inevitably, therefore, the 2-D approximation is subject to an error due to the omission of $\tilde{w}^2$. As 3-D PIV reconstruction gives the missing $\tilde{w}^2$, this inaccuracy can then be quantified by using an Assumption-Factor, *AF*, defined as

$$AF = \frac{k_3^*}{k_2^*} = \frac{2}{3}\frac{\left(\tilde{u}^2 + \tilde{v}^2 + \tilde{w}^2\right)}{\left(\tilde{u}^2 + \tilde{v}^2\right)} \tag{5.3}$$

where k_3^* and k_2^* is the three and two dimensional k normalised by U_{tip}^2.

On a time-averaged basis, the flow is symmetrical around the vertical axis in an un-baffled stirred tank, therefore one reconstruction was sufficient to represent the whole flow field for this configuration. To investigate flow in the un-baffled vessel with an eccentric impeller configuration, 16 reconstruction planes with a 22.5° separation were used, as illustrated in Figure 5.1a. Likewise, 9 reconstruction planes with a 10° separation were used in (B) (Figure 5.1b).

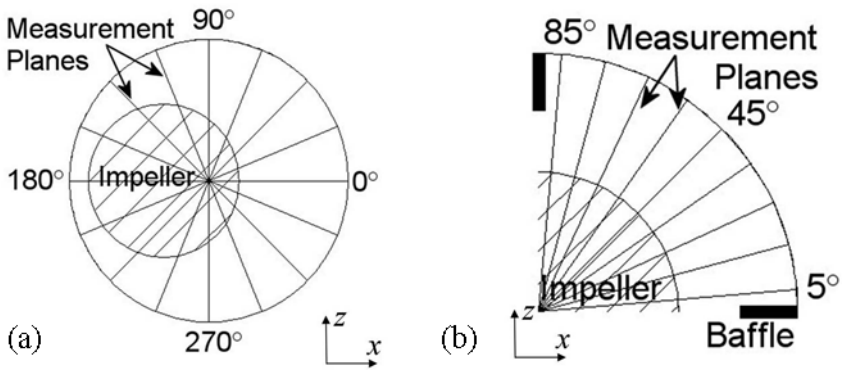

Figure 5.1 Measurement planes for (a) eccentric & (b)baffled configuration.

5.1 TKE CONTOUR PLOTS

For the un-baffled centreline configuration, TKE is not accurately estimated by the 2-D approximation. TKE based on $\tilde{u}^2$ and $\tilde{w}^2$ which represent the tangential flow (Figure 5.2(b)), is substantially higher than the axial-radial flow obtained from the $\tilde{u}^2$ and $\tilde{v}^2$ components (Figure 5.2 (a)) leading to a high level of solid body rotation and inefficient mixing. Thus, the use of 2-D PIV data for TKE calculations in un-baffled vessels is clearly inappropriate, as $\tilde{w}^2$ is significantly higher than both $\tilde{u}^2$ and $\tilde{v}^2$. Large differences in TKE measurements exist throughout the tank (Figure 5.2 (a) and (c)). In

particular, around the impeller, the values obtained through 3-D reconstruction are much higher than the 2-D approximations, suggesting $\tilde{w}^2$ cannot be approximated by $0.5(\tilde{u}^2 + \tilde{v}^2)$.

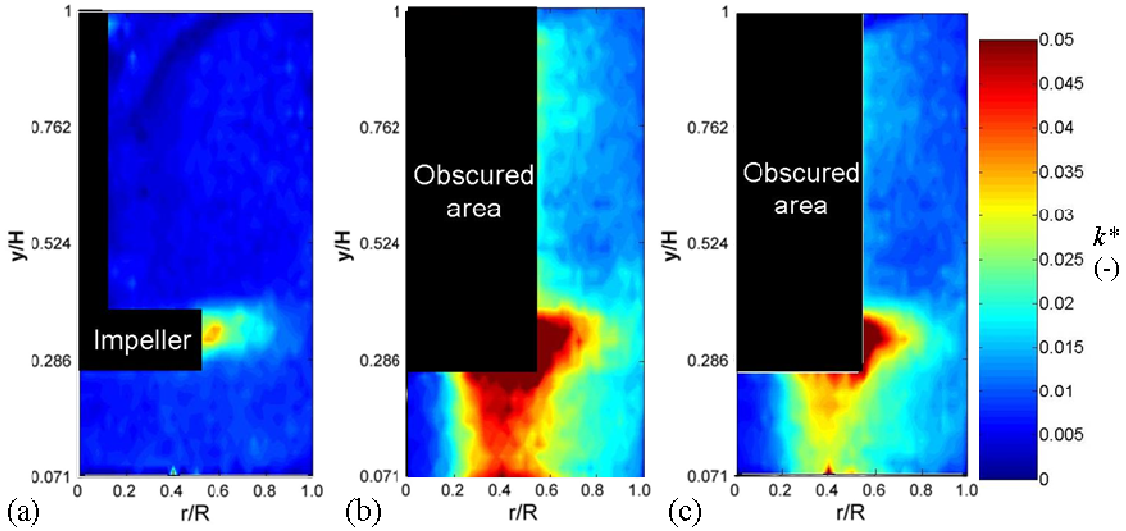

Figure 5.2 TKE distribution in un-baffled stirred vessel based on (a) $\tilde{u}^2$, $\tilde{v}^2$; **(b)** $\tilde{u}^2$, $\tilde{w}^2$; **(c)** $\tilde{u}^2$, $\tilde{v}^2$, $\tilde{w}^2$.

In addition to the improved accuracy of the data, 3-D reconstruction ensures capture of all the flow phenomena. For example, a low TKE zone can be seen in Figure 5.2 (b-c) below the impeller at $0 \leq r/R \leq 0.2$, whereas Figure 5.2 (a) would suggest a low TKE region throughout the lower half of the vessel. Confirmation of this region was obtained through PLIF imaging, Figure 5.3(a), where the tracer is clearly not well mixed with water compared to the rest of the vessel volume. A low energy zone of this kind was not observed in the other (B) and (E) configurations as shown in Figure 5.3 (b)-(c).

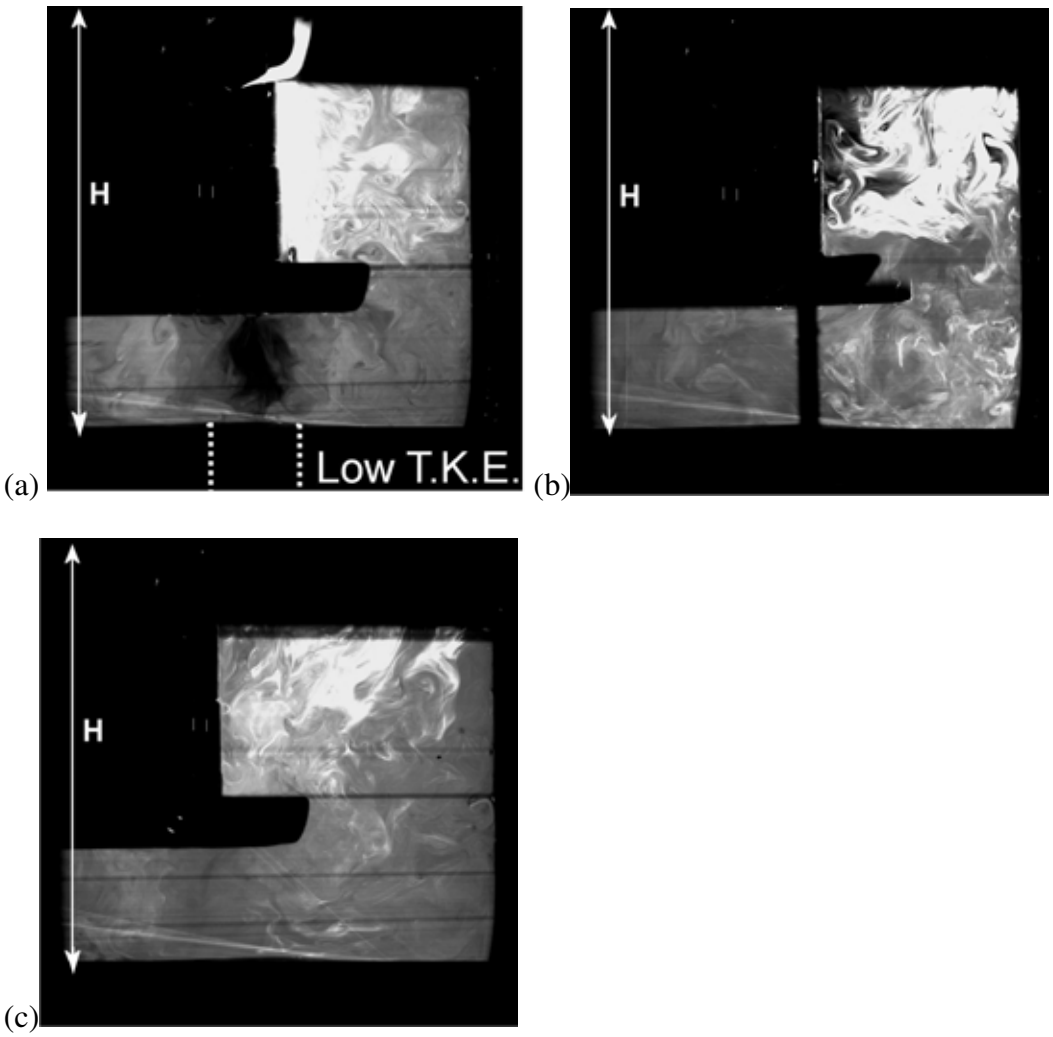

Figure 5.3 Visualisation of tracer dissipation by PLIF after 1.3 s in (a) (U); (b) (B); (c) (E).

In the baffled vessel, 2-D vertical PIV produces a comparable TKE distribution to the 3-D reconstruction method. The TKE maps in the plane (45° in Figure 5.1(b)) halfway between two baffles are very similar, although some small differences are observed very close to the impeller discharge (Figure 5.4). This confirms that the presence of baffles reduces the predominance of $\tilde{w}^2$, and as a result the 2-D approximation is satisfactory. The low energy zone previously observed below the impeller in (U) is no longer present and the kinetic energy is distributed more uniformly across the whole vessel. Unlike (U), the impeller discharge exhibits an axial flow characteristic in all the 9 planes investigated,

which promotes TKE distribution in the *y* direction. This was best visualised in the 5° and 85° planes where the baffle did not obstruct the view of the PIV camera.

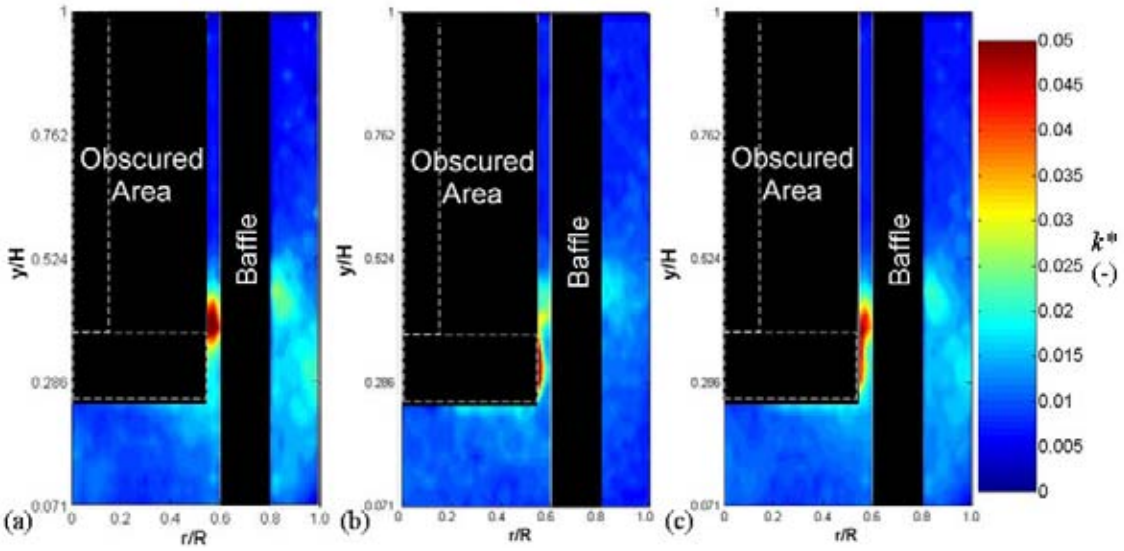

Figure 5.4 TKE distribution in baffled stirred vessel based on (a) $\widetilde{u}^2$, $\widetilde{v}^2$; (b) $\widetilde{u}^2$, $\widetilde{w}^2$; (c) $\widetilde{u}^2$, $\widetilde{v}^2$, $\widetilde{w}^2$.

The 3-D reconstructed TKE maps obtained through the 0° and 180° planes of the un-baffled vessel with an eccentric impeller configuration (C_w = 0.33T) are presented in Figure 5.5(a). Compared with the (U) configuration (Figure 5.2(c)), the kinetic energy is more uniformly distributed throughout the vessel including around the impeller. In the left region close to the wall, -1 ≤ *r/R* ≤ -0.9, there is more energy dissipation in the upward part of the circulation loop than in the downward part, which should promote axial mixing. Throughout the 16 reconstructed planes, the high energy zone surrounding the impeller witnesses its highest TKE levels in the sector between 135° and 180° planes. On the other hand, a near-uniform TKE distribution is observed in the 270° plane but not in the 90° plane, as shown in Figure 5.5(b).

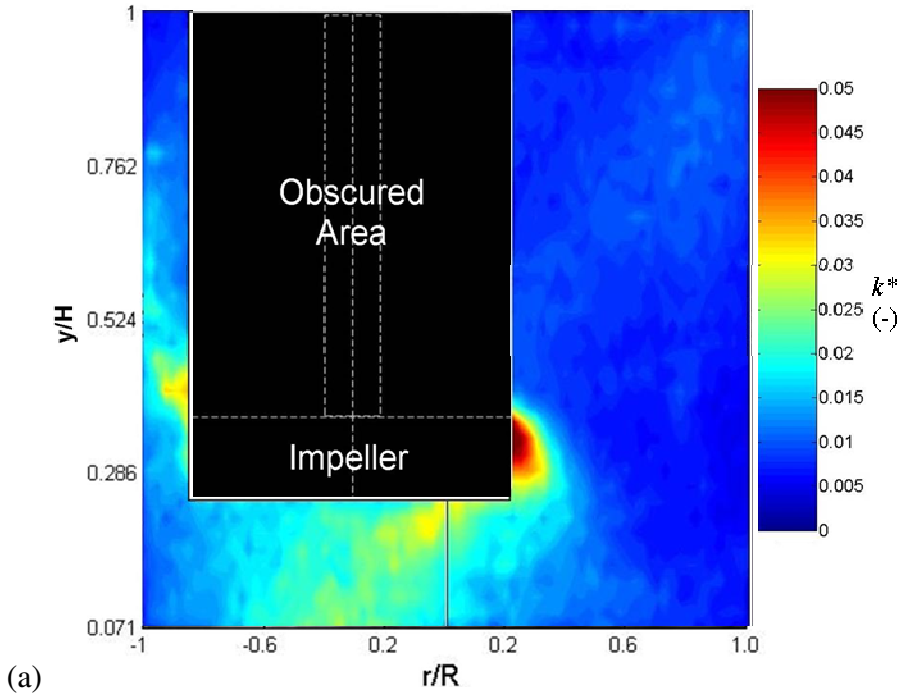

(a)

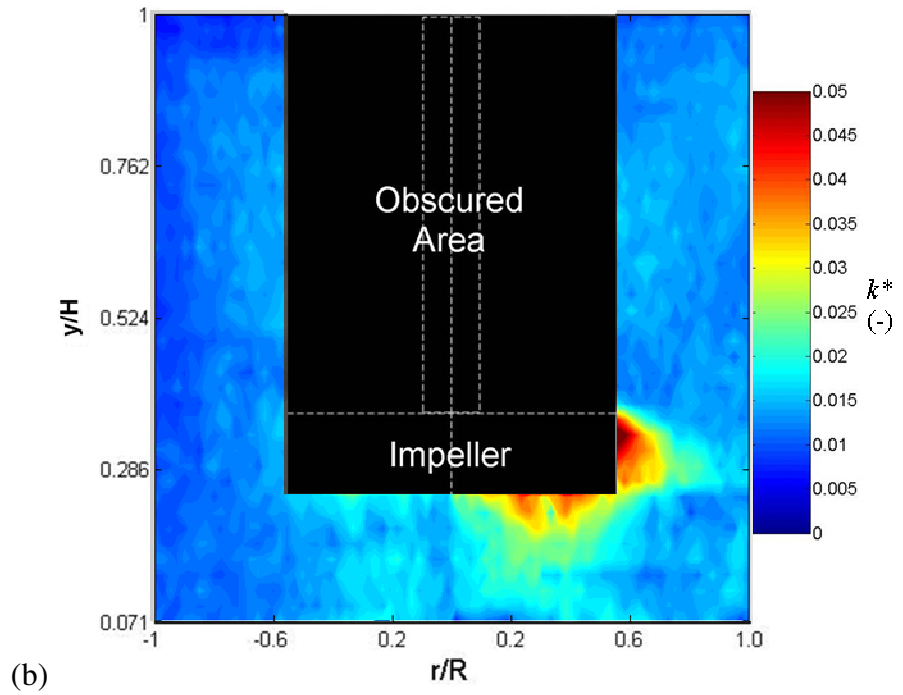

(b)

Figure 5.5 TKE distribution in (E) based on $\tilde{u}^2$, $\tilde{v}^2$, $\tilde{w}^2$ at (a) 0°, 180° planes; (b) 90°, 270° planes.

5.2 ANISOTROPIC TKE DISTRIBUTION IN UNCONVENTIONAL CONFIGURATIONS

Isotropic distribution of TKE in a stirred mixing vessel is desirable but is not generally achieved in trailing vortices or close to the impeller discharge. An isotropic turbulence test can be carried out by comparing $\tilde{u}^2$, $\tilde{v}^2$ and $\tilde{w}^2$ directly; this should also help to assess the appropriateness of the 2-D approximation. Figure 5.6 shows $\tilde{u}^2$, $\tilde{v}^2$ and $\tilde{w}^2$ in two horizontal planes immediately above and below the impeller, for each of the configurations investigated, i.e. (B), (U) and (E). The magnitudes of $\tilde{u}^2$ and $\tilde{v}^2$ are nearly equal for all configurations below and above the agitator. In the baffled tank, the three TKE components are more or less the same underneath the impeller, indicating an isotropic TKE distribution (Figure 5.6 (a)), whilst $\tilde{u}^2$ and $\tilde{v}^2$ are marginally higher than $\tilde{w}^2$ above the impeller (Figure 5.6 (b)). However, in the un-baffled vessel, above the turbine, $\tilde{w}^2$ is notably greater than the other components (Figure 5.6 (d)); such a predominance is even much higher in the plane below the impeller (Figure 5.6 (c)). For the eccentric configuration, in the plane underneath the turbine, $\tilde{w}^2$ is about half its value for (U) configuration, and turbulence isotropy is essentially observed in the right hand half of the vessel radius (Figure 5.6 (e)). Above the agitator, TKE is isotropic along the right hand radius of the plane only (Figure 5.6 (f)). Clearly, therefore, the assumption of isotropy inherent in the 2-D PIV approximation is not valid in the (U) and (E) situations.

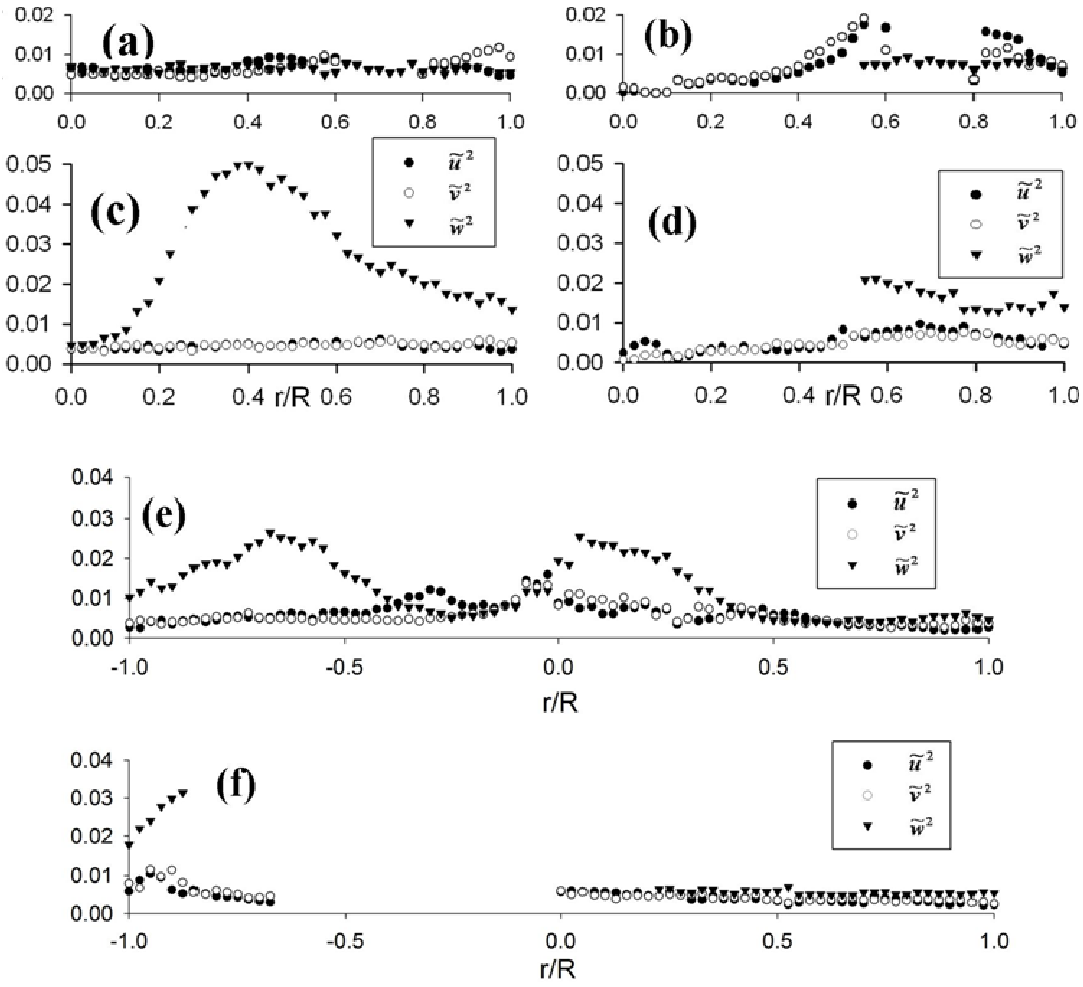

Figure 5.6 Radial profiles of the three fluctuating components measured in (a) (B) at *y/H* = 0.26; (b) (B) at *y/H* = 0.40; (c) (U) at *y/H* = 0.26; (d) (U) at *y/H* = 0.40; (e) (E) at *y/H* = 0.26; (f) (E) at *y/H* = 0.40.

As described above, the accuracy of the 2-D approximation can be quantified through an Assumption-Factor (Eq. 5.3). In (B), the *AF* averaged over the 9 planes is equal to 1.0, as expected, which confirms that the 2-D approximation works very well for this standard case. This also serves to show that the 3-D PIV reconstruction technique yields accurate results. In the un-baffled stirred tank, however, the *AF* averaged across the measurement plane is 2.11, i.e. TKE is underestimated by over a half. Similarly, in the eccentric configuration, *AF* averaged over the 16 planes investigated is 1.33, again showing a considerable underestimation of TKE. Figure 5.7 shows the spatial variation of the plane averaged *AF* values in the vessel for the baffled and eccentric cases. Whilst *AF* is more or

less uniform in the (B) configuration, it fluctuates significantly in the (E) configuration reaching a peak of 1.9.

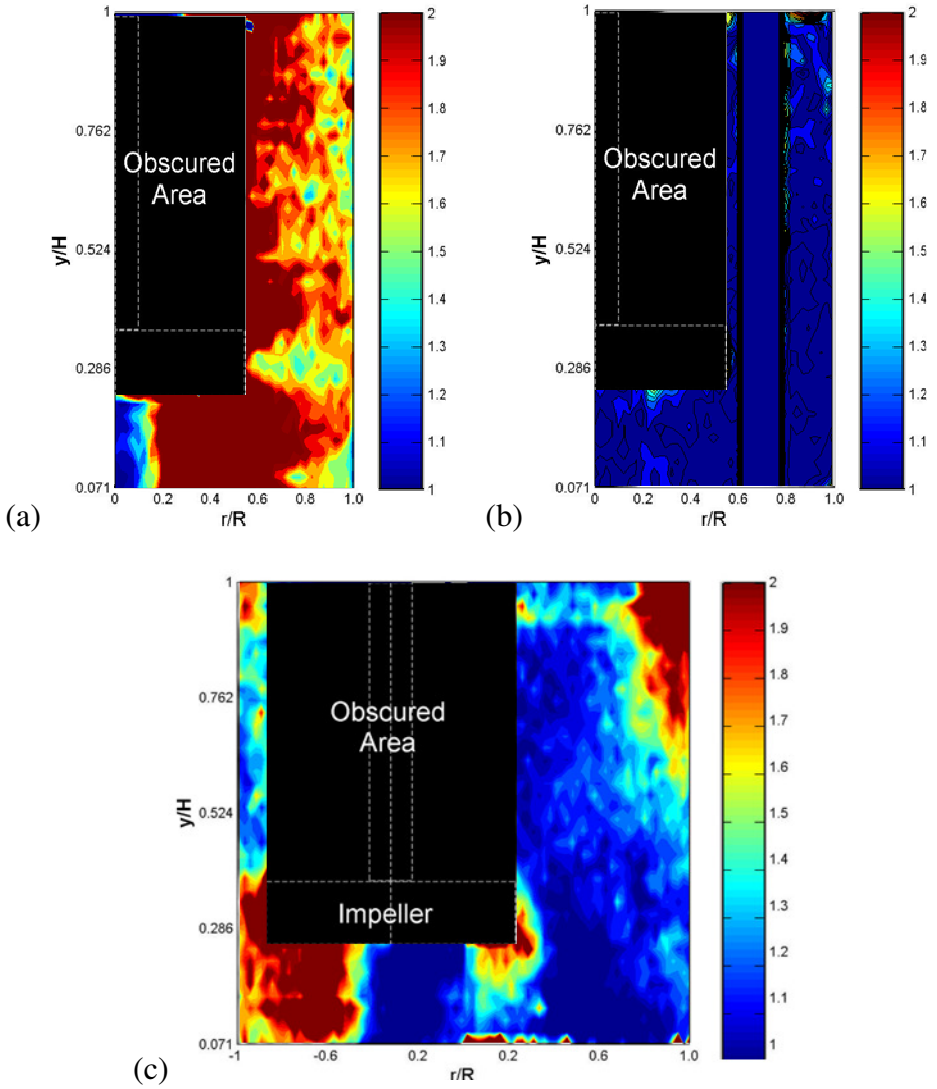

Figure 5.7 Assumption-Factor map in (a) (U); (b) (B) at 45°; (c) (E) at 0°, 180°.

More detailed point-wise distributions of *AF* values are shown in Figure 5.8 for the three different mixer configurations. Whereas the baffled tank has an almost uniform distribution of *AF* values throughout its volume (~ 1.0), in the un-baffled tank, *AF* is lowest in the radial impeller discharge zone (~ 1.5) and increases to reach a maximum below the impeller (~ 5.0). The *AF* map for the eccentric configuration is also non-uniform, however, overall the degree of non-uniformity is less pronounced than for the (U)

case. Areas of high *AF* values exist in the left hand corner below the agitator (~ 2.0), and in the top right hand corner which is the remotest part from the agitator.

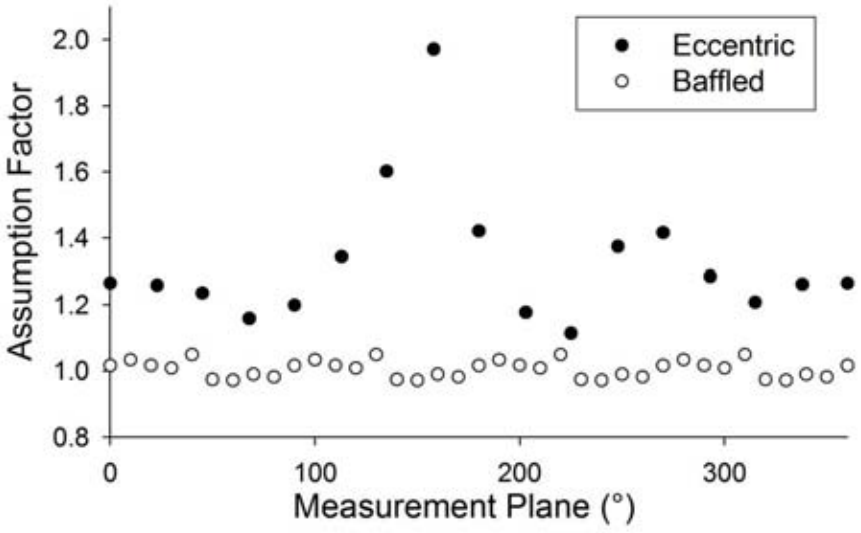

Figure 5.8 Variation of plane averaged AF in stirred vessel.

Due to the large number of horizontal and vertical planes used in the 3D reconstruction of the flow field, only 200 PIV image pairs were used per plane to keep the time-average analysis of the results down to a manageable level. However, this may be considered to be insufficient for an accurate estimation of TKE. Figure 5.9 shows the effect of using smaller and larger sets of images on the accuracy of the TKE estimation. The ratio of the TKE estimated from a given number of image pairs to that estimated from a set of 800 image pairs is plotted as a function of height in the vessel. The results show that little improvement in accuracy is gained by using more than 500 image pairs. The use of 200 image pairs estimates TKE within ±10% of the best estimate obtained from 800 image pairs, and would therefore be considered as the minimum acceptable.

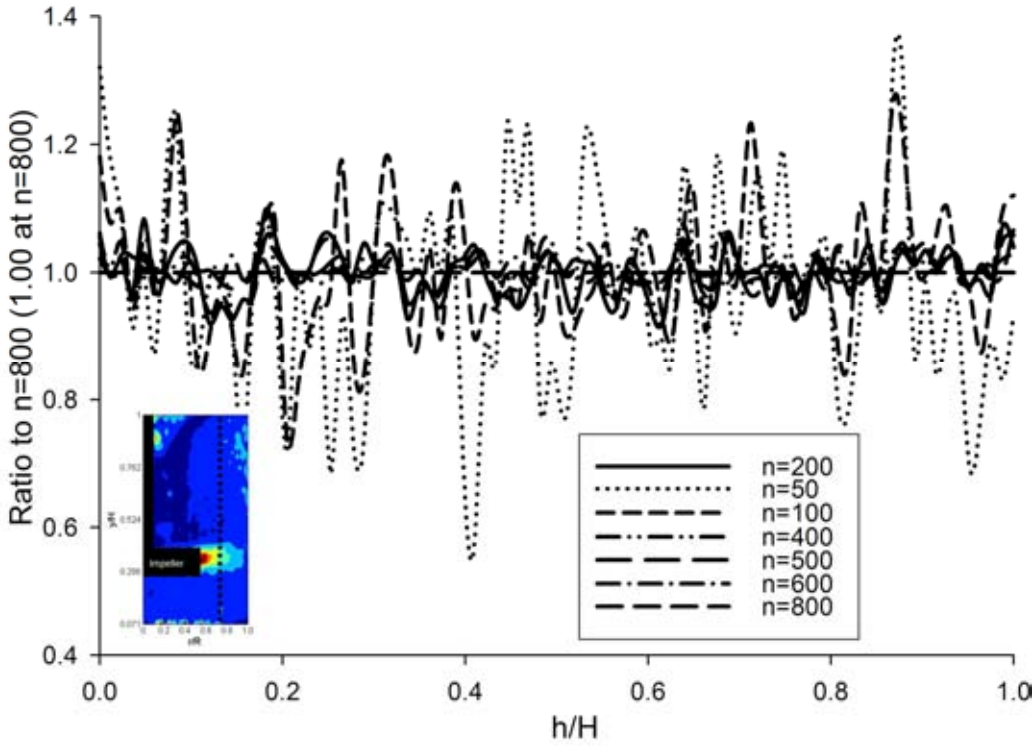

Figure 5.9 Effect of number of image pairs on accuracy of TKE estimation.

A further comparison of (U), (B) and (E) was based on mixing time as measured by PLIF (Figure 5.10); such graph is also displayed in Chapter 4 but shown here again to highlight the effect of TKE on mixing time, τ_{95}. Despite (B) showing a near-isotropic TKE distribution, it takes ~30% longer to achieve 95% mixedness compared to (E). Mixing in the bulk of (U) is similar to (E) up to 1.8 s (i.e. ~ 85% mixedness), but beyond that the rate of mixing is substantially reduced due to inefficient mixing in the 'low' TKE zone below the impeller and around the shaft region (Figure 5.3(a)).

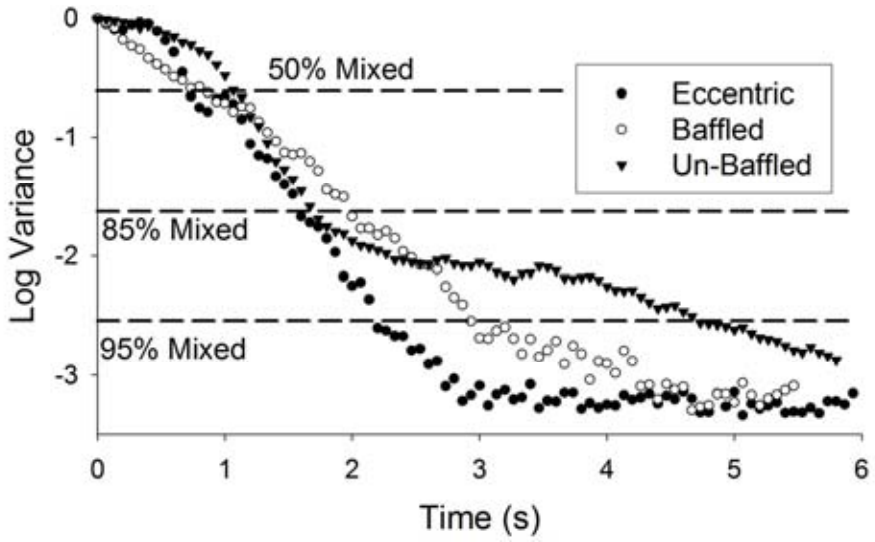

Figure 5.10 Decay in variance of tracer concentration : each curve is the average of 10 PLIF experiments.

5.3 CONCLUSION

A method based on 2-D PIV in vertical and horizontal planes has been successfully employed to reconstruct the 3-D flow field inside a miniature HTE stirred vessel. In a fully baffled vessel, the 3-D results confirmed, as expected, that 2-D PIV measurements may be used for a reasonably accurate estimation of the energy distribution in the 3-D flow field. In an un-baffled vessel, however, 2-D PIV data without 3-D reconstruction give rise to an erroneous estimation of kinetic energy in the vessel, which can be under-predicted on average by a factor of about 2, and by several folds below the impeller. This arises from the omission of the tangential flow component. In an un-baffled vessel equipped with an eccentric impeller, the accuracy of the 2-D PIV assumption varies across the vessel volume with the impeller region being the worst. In this case, the TKE is underestimated by about 1/3 on average, but can be underestimated by a much higher factor in some specific areas of the vessel. Besides miniature HTE reactors, the reconstruction method used here can be applied to any flow field of interest where the isotropic assumption is not valid and the configuration precludes the use of stereoscopic PIV.

6. ANGLE RESOLVED MEASUREMENTS

The work covered in Chapter 5, along with studies from other authors (Hall *et al.* 2004; Hall *et al*, 2005a; Aubin *et al.* 2004), were based on ensemble average PIV measurements which do not account for the periodicities arising from the passage of the impeller blades. However, a number of studies on large scale stirred vessels have been reported in the literature where velocity field and turbulence data have been obtained on the basis of angle resolved PIV or LDA measurements. Yianneskis and Whitelaw (1993) reported that the turbulence quantities in a vessel agitated by RDT could be overestimated by 400% when measurements were made in an ensemble time-average fashion. Similarly Hockey & Nouri (1996) reported an overestimation of 200% in a vessel equipped with a PBTd. Schäfer *et al.* (1998) studied the flow and turbulence structure behind a 45º PBTd with LDA. Not only was a 50% overestimation of TKE with ensemble averaged measurement determined, the vortices structure was also visualised. These studies highlight the importance of angle resolved measurements.

In this Chapter, 2-D angle resolved PIV is used to measure the mean flow and turbulence fields in small stirred HTE vessels of four different configurations, which has not been done before. The work investigates the flow field around a pitched blade turbine and how it evolves with the angle of blade rotation. The hydrodynamics associated with each vessel configuration are studied including visualisation of the trailing vortices and the global flow field, and evaluation of quantities such as the flow number and pseudo-turbulence.

Four equally spaced wall-mounted baffles were used in configuration (B). The presence of the baffles normally restricts the field of view which is accessible to the laser sheet, thus limiting flow visualisation and most importantly so in the impeller discharge region. Hence, the common approach for flow visualisation in the 45º degree plane between two baffles was not followed here, and instead measurements were made in a plane 5º in front of a baffle to obtain an unrestricted view of the area around the impeller.

6.1 FLOW FIELDS

The mean flow field obtained for each of the four vessel configurations by the ensemble average PIV method is depicted in Figure 6.1 in the form of vector velocity plots. Such plots are useful for highlighting the considerably different flow patterns generated by each mixer configuration.

In addition, the global flow field was averaged from 500 measurements made at every degree of impeller rotation throughout the 60º sector between two blades. Animations were constructed by compiling the average vector plots obtained at successive measurement angles into consecutive frames; this way the periodicity present in the flow field could be easily visualised.

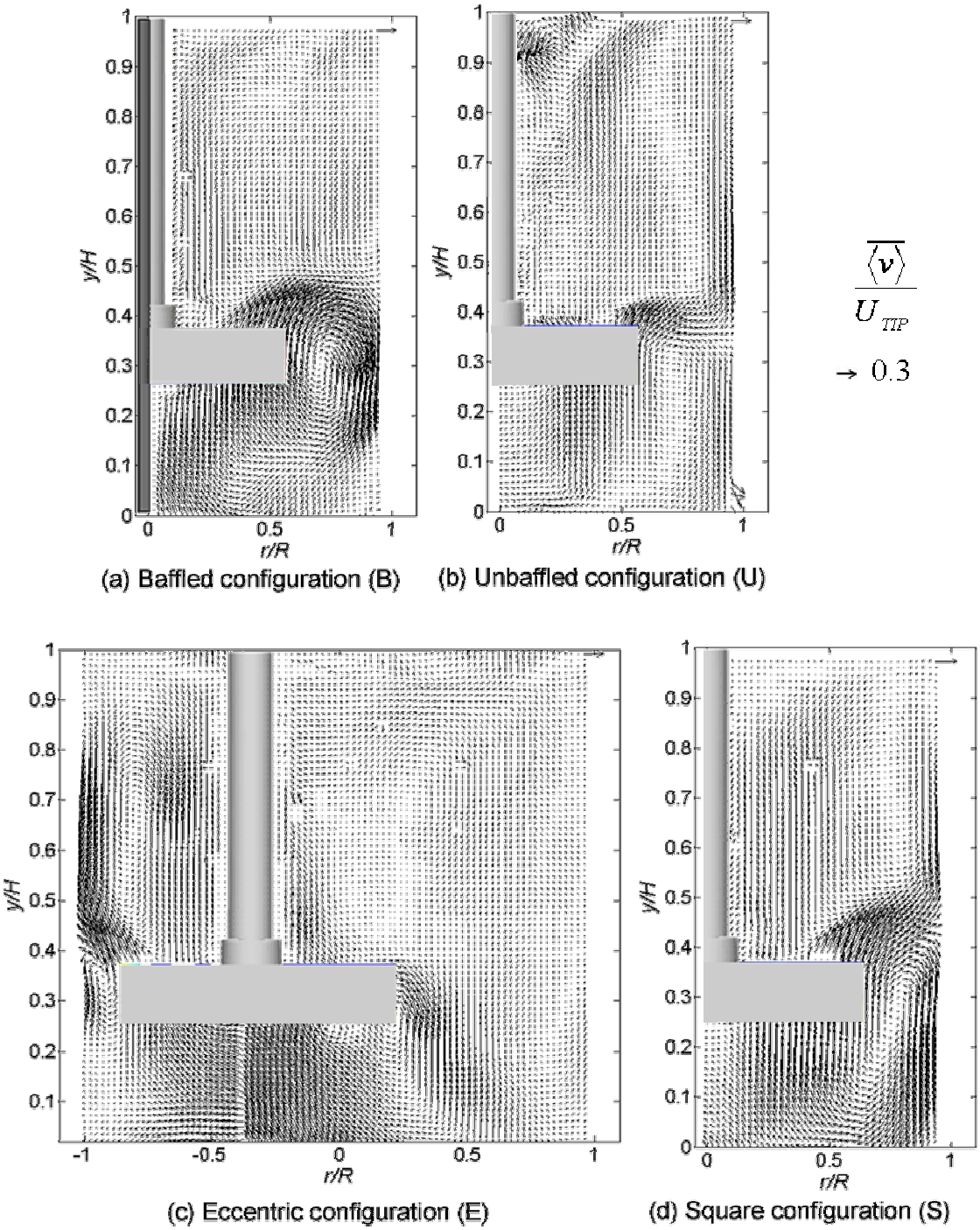

Figure 6.1 Azimuthally-averaged *r-y* velocity vector plots.

The global flow field maintained its characteristics for all angular positions investigated. This is illustrated for the standard (B) configuration in Figure 6.2 where the ensemble time-average flow field is displayed alongside two frames corresponding to θ = 0º and θ = 30º. There is a strong clockwise circulation loop in the region between the impeller and the vessel wall; the second circulation in the upper region of the vessel usually associated

with a PBTu is not clearly visible due to the flow being in the transitional regime. Flow is discharged from the impeller at an angle of approximately 45º and the maximum flow velocity is approximately equal to $0.45U_{TIP}$ in the plane corresponding to θ = 0º. The maximum flow velocity at θ = 30º reduces to approximately $0.35U_{TIP}$ where the flow changes from a predominantly axial-radial direction to include a significant tangential component. The lack of significant differences in the velocity fields beyond a radial position of r/R = 0.8, as shown in Figure 6.2, suggests that periodicity disappears in this region of the flow and picks up again just below the turbine blade where liquid is being drawn into the eye of the impeller. In this particular area there are vast differences in the measured velocity from one angle resolved plane to another, as illustrated in the images presented in Figure 6.2.

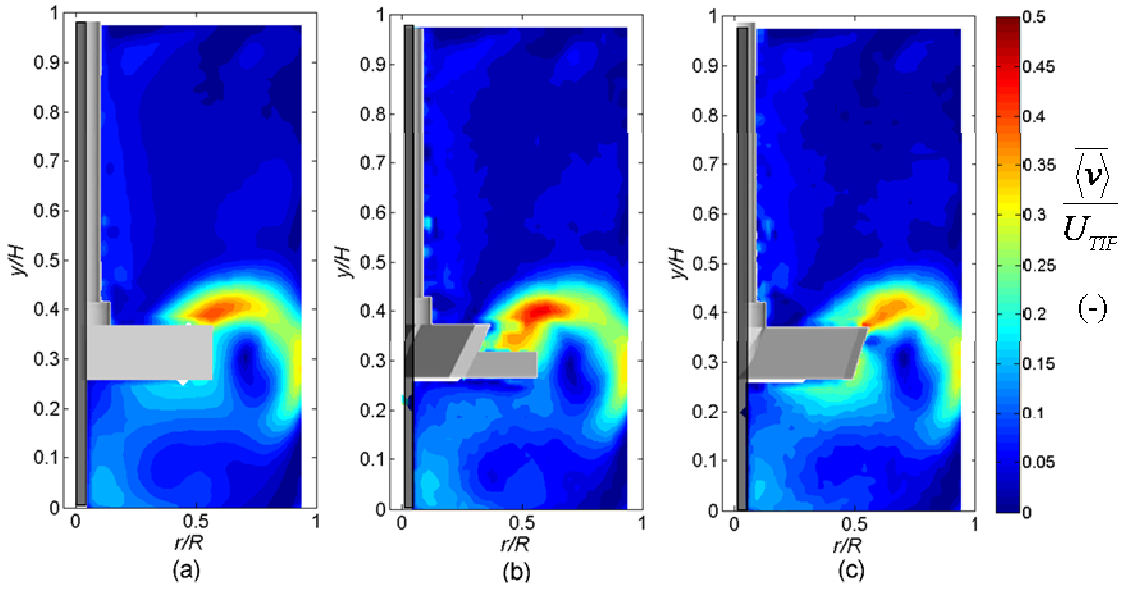

Figure 6.2 Normalised *r-y* velocity plot of (B) configuration by (a) time averaged method, and angle resolved at impeller position (b) θ = 0º and (c) θ = 30º. T = 45 mm, D/T = 0.54, P/V = 168 Wm^{-3}, N = 575 rpm.

In the absence of baffles, the velocity of the combined axial-radial flow in the (U) vessel is generally much lower, as shown in Figure 6.3, the maximum velocity being ~ 0.4 U_{TIP} at θ = 30° in the impeller discharge. A substantial portion of the flow in this case occurs in the

tangential direction, as previously quantified in Chapter 5. Periodicity only exists in the immediate impeller discharge region and directly beneath the impeller. In the 0º plane, as shown in Figure 6.3 (b), flow is discharged in a combined axial-radial fashion at the top corner of the impeller blades; this turns into a predominantly radial discharge in the succeeding planes, as illustrated in Figure 6.3 (c). The predominance of the radial discharge is also captured in the ensemble average measurements, as shown in Figure 6.3 (a). The high velocity region at the top of the vessel close to the impeller shaft is due to the formation of a free-surface vortex.

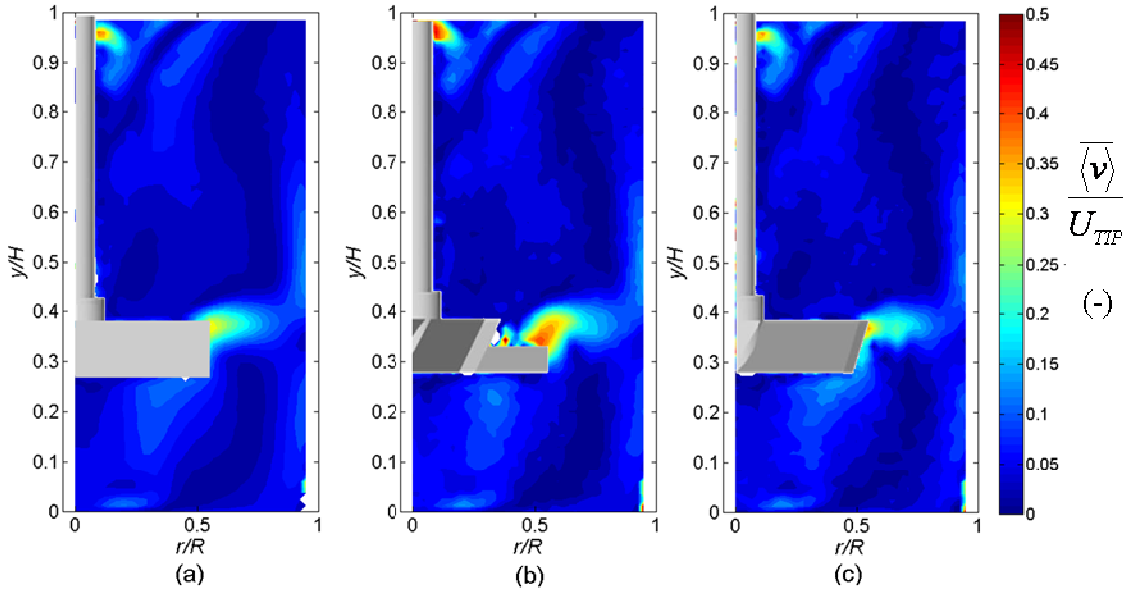

Figure 6.3 Normalised *r-y* velocity plot of (U) configuration by (a) time averaged method, and angle resolved at impeller position (b) θ = 0º and (c) θ = 30º. T = 45 mm, D/T = 0.54, P/V = 168 Wm^{-3}, N = 625 rpm.

The weakness of the axial-radial flow observed in (U) is circumvented by the use of off-centre agitation in the (E) configuration, as shown in Figure 6.4. The velocity field is highly non-uniform with the highest velocities occurring in the narrower region to the left of the shaft. The wider right-hand side region above the impeller plane is the seat of slow flow and looks rather quiescent, with $\overline{\langle v \rangle} < 0.1\ U_{TIP}$. The greatest flow is discharged from the top left hand corner of the impeller blades in the 0º plane; this is about twice the

magnitude of the discharge on the opposite side of the impeller. Furthermore, the lack of baffles seems to cause a radial discharge on the latter side of the impeller (Figure 6.4 (b)), as observed in (U) above, which gets diverted axially downwards in the following angle-resolved planes (Figure 6.4 (c)). The axial inflow immediately underneath the impeller is greatest for (E) compared to the other three configurations. Unlike these configurations, flow in this area shows no suggestion of significant periodicity over the 60º impeller swept sector.

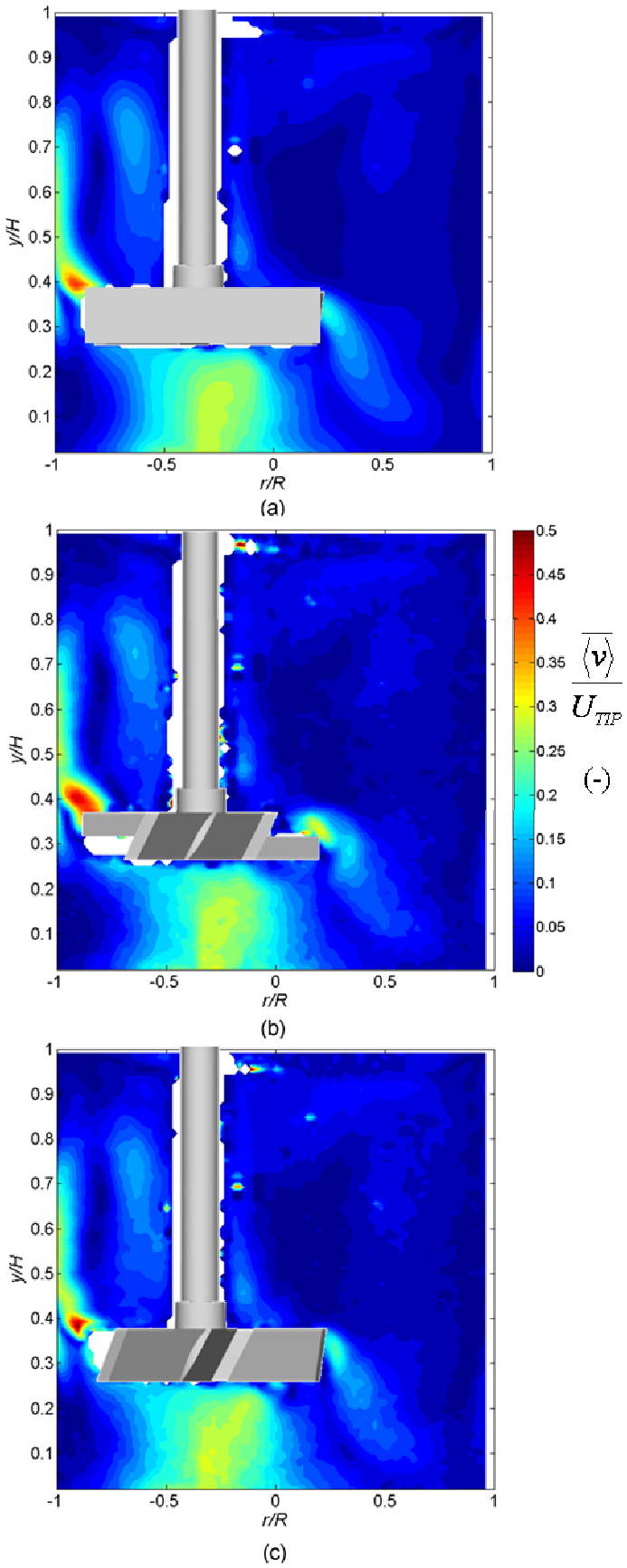

Figure 6.4 Normalised *r-y* velocity plot of (E) configuration by (a) time averaged method, and angle resolved at impeller position (b) $\theta = 0^{o}$ and (c) $\theta = 30^{o}$. T = 45 mm, D/T = 0.54, P/V = 168 Wm^{-3}, N = 575 rpm.

The global combined axial-radial flow field in the square vessel (S) is much stronger than that in either (B) or (U), especially in the lower part of the circulation loop (y/H = 0 to 0.2), as shown in Figure 6.5; the strong combined axial-radial flow is indicative of the weaker tangential flow in this case. A strong axial discharge is observed along the top edge of the impeller blade. Similar to (B) and (U), periodicity is once again observed only close to the impeller, with the strongest combined axial-radial discharge occurring at θ = 0 ° and the greatest axial inflow to the impeller occurring at θ = 30 °. The comparatively superior quality of the flow field in (S) is attributed to the baffling effect of the vessel corners, the flat vessel walls and the slightly larger D/T used.

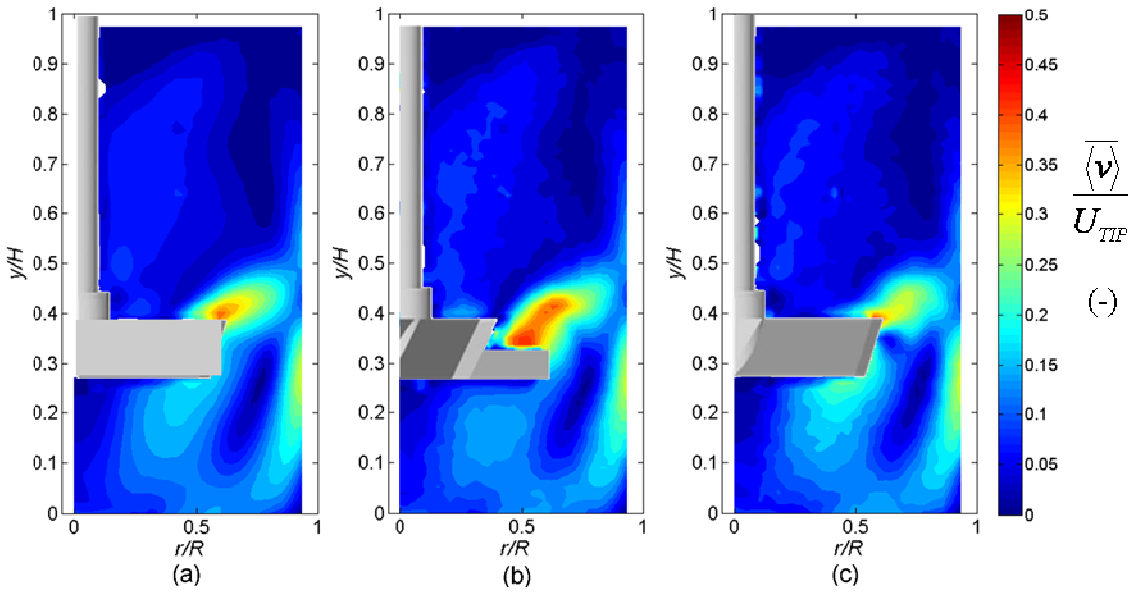

Figure 6.5 Normalised *r-y* velocity plot of (S) configuration by (a) time averaged method, and angle resolved at impeller position (b) θ = 0° and (c) θ = 30°. T = 45 mm, D/T = 0.54, P/V = 168 Wm^{-3}, N = 595 rpm.

6.2 FLOW NUMBER

The flow number, Fl, as covered in Chapter 2, is a parameter used to measure the pumping efficiency of the impeller. This was calculated at every angular position of the impeller for each configuration, thus

$$Fl = \frac{Q}{ND^3} \tag{6.1}$$

For a PBT in a fully baffled configuration, the discharge flow, Q, has been traditionally estimated by analysing velocity data in the axial direction only which represents most of the discharge flow; this, however, is not strictly true for the other impeller configurations investigated here. Given the mixed axial-radial discharge flow emerging from the PBT, Q was in each case obtained by integrating the fluid velocity profile in both axial and radial directions. For this purpose, the velocities were measured at a distance equal to L_{IA}, i.e. 0.5 mm away from the edge of the impeller.

The variation of Fl over the 60º swept sector of the 6-PBTu is shown in Figure 6.6 for the four configurations investigated. Also shown are data obtained in fully-baffled laboratory scale vessels for a 4-PBTd impeller from Khan *et al.* (2004) (T = 0.29 m) and for a 6-PBTu from Gabriele *et al.* (2006) (T = 0.15 m). The trends observed in the HTE vessels are qualitatively similar to the ones reported in the much larger vessels, although Khan *et al*'s data taken at a closer distance to the impeller seem to fluctuate rather differently. The average Fl in the (B) configuration of the HTE vessels is 0.64 which is in agreement with the literature value of 0.62 for a PBT with D/T = 0.5 in high transitional to turbulent flow (Hemrajani & Tatterson, 2004). Khan *et al.*'s value of 0.86 is consistent with the published value of 0.80 for D/T = 1/3, whilst Gabriele *et al.*'s value of 0.86 is significantly higher than the literature value of 0.65 for D/T = 0.45 (Hemrajani and Tatterson, 2004). On the other hand, the value of Fl obtained by Aubin *et al.* (2004) of 0.72 in a vessel agitated by 6-PBTu with D/T = 0.5 (T = 190 mm) was also higher than the literature value of 0.62 for D/T = 0.5 (Hemrajani and Tatterson, 2004). Khan *et al.*'s data seem to suggest that the value of Fl is sensitive to the distance from the impeller at which velocity measurements are made since the liquid surrounding the impeller is quickly entrained in

the discharge stream and can, thus, cause *Fl* to be overestimated. Gabriele *et al.*'s measurements were made at a relatively larger distance of 1.38 mm compared to Khan *et al.*'s value of 0.2-0.36 mm, which could explain the larger *Fl* value he obtained compared to the literature value.

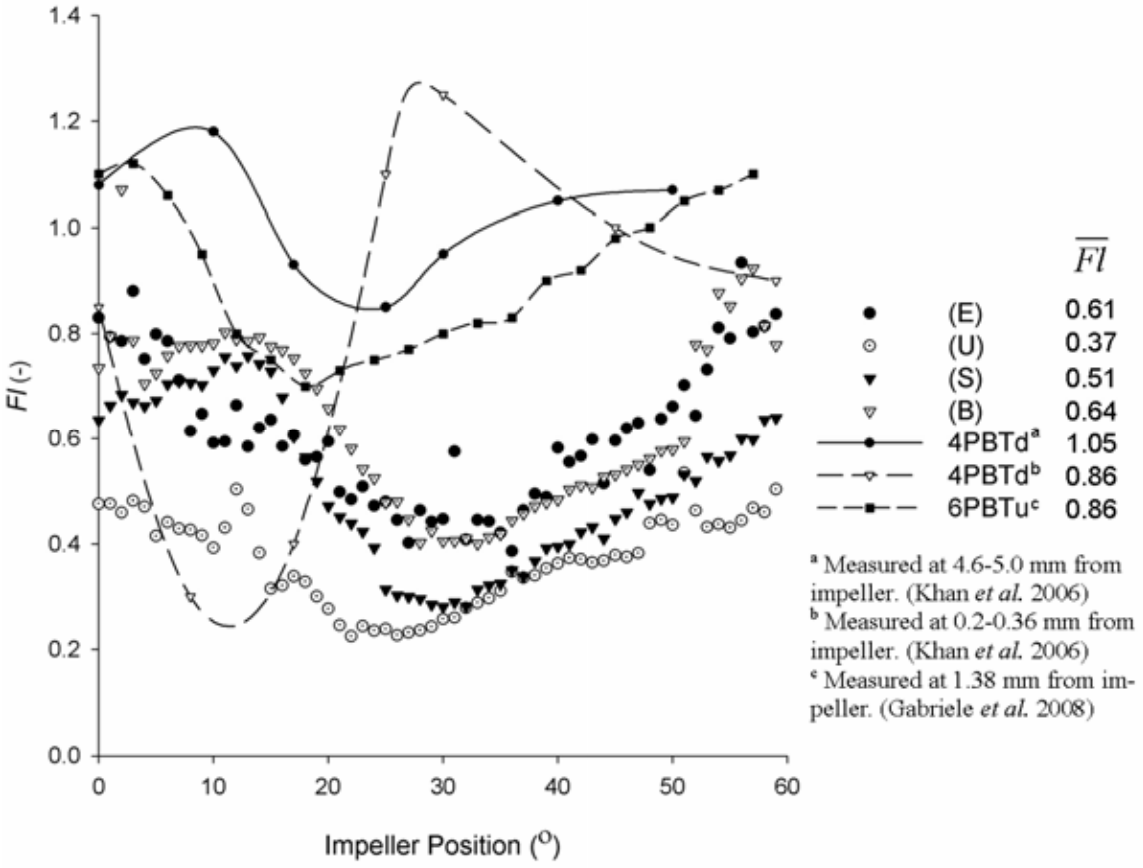

Figure 6.6 Flow number measured at different impeller positions in different HTE vessel configurations. $\overline{Fl}$ shown in legend was averaged over the 60 degree swept angle.

The *Fl* profiles shown in Figure 6.6 are consistent with observations made previously on the flow normalised velocity plots discussed above. For instance, the largest impeller discharge seems to occur in the region $-10° < \theta < +10°$ for all mixer configurations. In the region around $\theta = 25°$, *Fl* drops to a minimum for all configurations, and is as low as 0.25 for configuration (U). Unsurprisingly, the (U) configuration achieved the lowest *Fl* profile with an average value of 0.37, owing to the considerable amount of solid body rotation caused by the absence of baffles and its repercussions on the direction of flow around the

edge of the turbine. A slightly lower *Fl* of 0.64 was measured in the (B) configuration compared to the data of other 6-PBTu studies (Gabriele *et al.* and Aubin *et al.* (2004)), due to the lower *Re* and larger *D/T* ratio adopted in this study. The (E) configuration achieved practically the same pumping efficiency as the (B) configuration with an average *Fl* of 0.61, again confirming the effectiveness of this configuration in HTE vessels where baffles are usually undesirable (Chapter 5 and Hall *et al.*, 2005a). The square vessel (S) had a somewhat lower *Fl* of 0.51 but this can be explained by the slightly higher *D/T* ratio of 0.59 compared to 0.54 for the (B) and (E) systems, as corroborated by the data reported by Hemrajani and Tatterson (2004) for pitched blade turbines which suggest that *Fl* is rather sensitive to *D/T* and reduces with increasing *D/T*.

6.3 VORTICITY

The trailing vortices formed behind each impeller blade can be described by the vorticity, ω, which defines the two-dimensional rotation of a fluid in Cartesian coordinates, thus

$$\omega = \frac{\partial v}{\partial x} - \frac{\partial u}{\partial y} \qquad (6.2)$$

With the angle-resolved velocity data generated by 2-D PIV, vorticity at each impeller angular position can be evaluated with x and y equal to L_{IA}.

By converting the PIV generated data into cylindrical coordinates, iso-surface plots were drawn in 3-D space as shown in Figure 6.7. In this way, trailing vortices generated by the blade passage could be visualised as they extend away from the measurement plane. To aid the visualisation, the relationship between the vortices and the impeller blades from which they were generated are marked on Figure 6.7, where the trailing vortices from the blades preceding and succeeding the blade of interest are also depicted. The vortices were identified by negative vorticity readings for the PBTu used, with the iso-surface plots depicting the outline of volumes with $\omega < -75\ s^{-1}$.

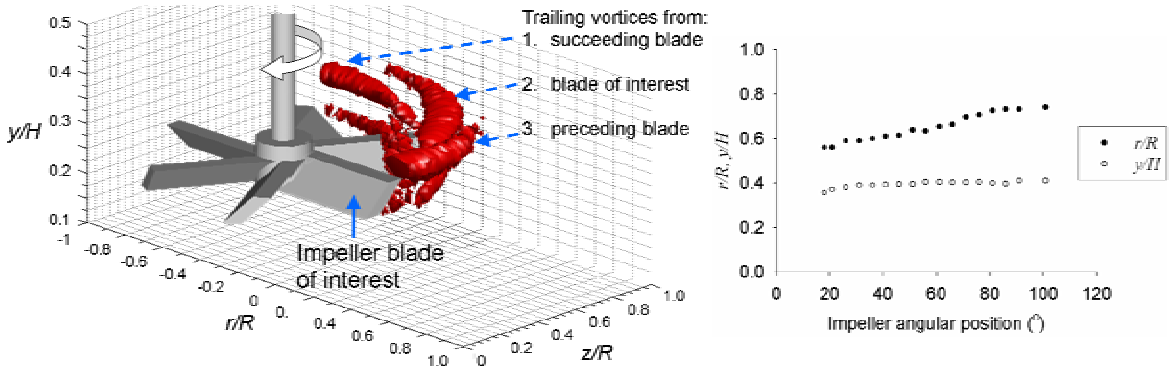

(a) Unbaffled configuration (U)

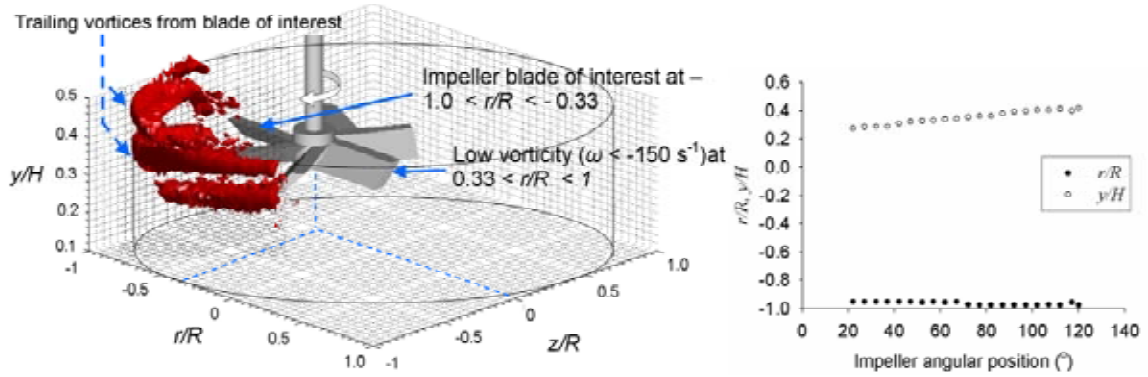

(b) Eccentric configuration (E)

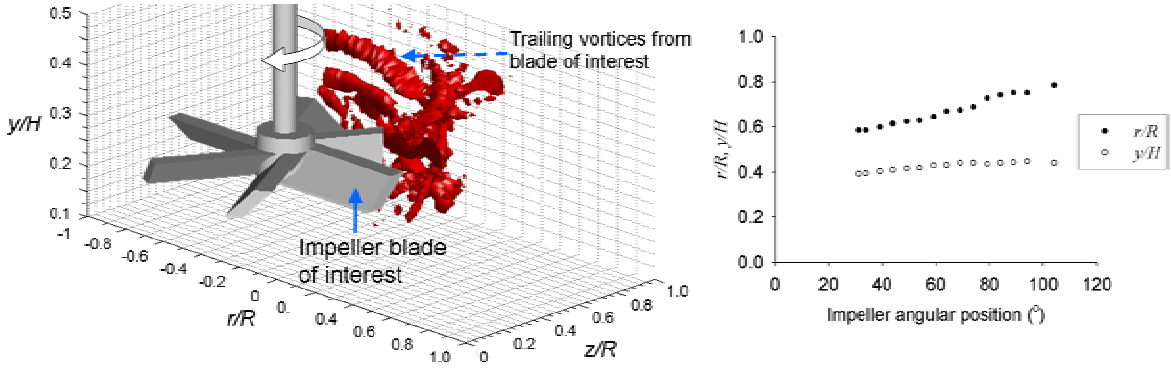

(c) Baffled configuration (B)

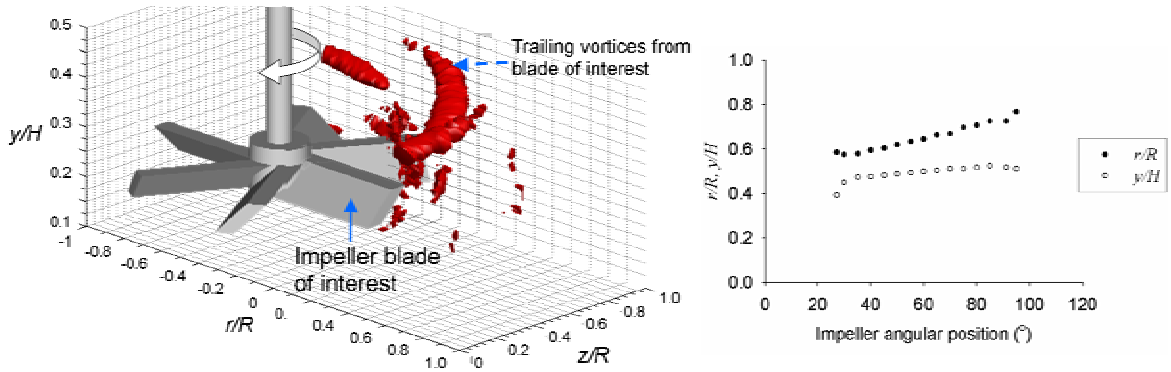

(d) Square configuration (S)

Figure 6.7 Iso-surface plots outlining volume with ω < -75 s^{-1} in different HTE vessel configurations. The location of the vortex axis is also displayed.

The location of the vortex axis was identified by the minimum negative ω in the relative region of interest, and the change in the location of vortex axis with impeller angular position is shown alongside the iso-surface plot in Figure 6.7 for each mixer configuration. As the trailing vortices are generated behind the opaque impeller blades, it may take up to 30º of impeller rotation for them to begin to be seen. In most cases, trailing vortices disappear after 100º of blade rotation, hence the iso-surface plot used vorticity over two consecutive blade passages (i.e. θ = 120º) to construct a complete vortex.

Vorticity was practically zero everywhere in the upper and lower parts of the vessel for the four configurations studied, indicating the absence of vortical structures in these regions of the mixing vessel. Despite the weak flow in the axial and radial directions shown in the velocity plot, the trailing vortices in (U) as shown in Figure 6.7 (a) were clearly visible at 110º after blade passage, which could not otherwise be observed from velocity plots. Each blade had one trailing vortex associated with it. The axis of the vortex rapidly rose to a vertical position of y/H = 0.4 and retained at its axial position while being gradually carried away by the radial flow horizontally to a distance r/R = 0.8, at which point it disappeared. In comparison, however, the vortex in (E) produced on the side of the impeller closer to the centerline at r/R = 0.15 was so weak that the minimum threshold of ω = -75 s^{-1} was not reached, and therefore no iso-surface volume was displayed on this side of the impeller. The vorticity measured in the impeller discharge on the narrower side at r/R < -0.87, however, was much stronger (Figure 6.7 (b)). Exceptionally, in this case, not one but two trailing vortices were generated at the top and bottom of the impeller blade. In a 100º of impeller rotation, the lower trailing vortex rises through the narrow gap between the impeller and vessel wall to join the upper trailing vortex generated by the preceding impeller blade.

In the (B) configuration, the movement of the trailing vortex differs from that reported for a PBTd in larger vessels where the vortex driven by the down-pumping action of the turbine gradually moved downwards whilst holding its radial position (Schäfer *et al.* 1998; Khan *et al.* 2004). For the PBTu considered here, the vortex rose slightly to a higher position of y/H = 0.45 at 130º following the passage of the blade, while translating almost horizontally to a radial position of r/R = 0.85 (Figure 6.7 (c)). The lack of axial vortex movement in the case of the PBTu here compared to the PBTd in the literature is probably due to the difference in the pumping action of the impeller. The highest axial vortex position was achieved in (S) with y/H ~ 0.5 (Figure 6.7 (d)). It follows, therefore, that since the trailing vortices represent the primary source of turbulence generation, the (S) configuration effectively must carry more energy to the upper reaches of the vessel. This may be partly responsible for the improved mixing time achieved in this vessel compared to the (B) configuration as measured by the PLIF method. As shown in Chapter 4, it takes ~30% longer to achieve 95% mixedness in (B) compared to (E) and (S). Mixing quality in the bulk of (U) is, however, substantially reduced.

6.4 PSEUDO-TURBULENCE

Turbulent kinetic energy was determined via both the ensemble time-average method and the angle resolved method. In the ensemble time-average method, the r.m.s. velocity data were extracted from 10 measurements at each degree of impeller angular position; together these represented 600 randomly captured time-averaged measurements. On the other hand, the angle resolved method used 500 velocity measurements at every degree of impeller rotation. Contour maps of ensemble time-averaged TKE and TKE resolved at θ = 0º and θ = 30º in the (S) vessel are displayed in Figure 6.8.

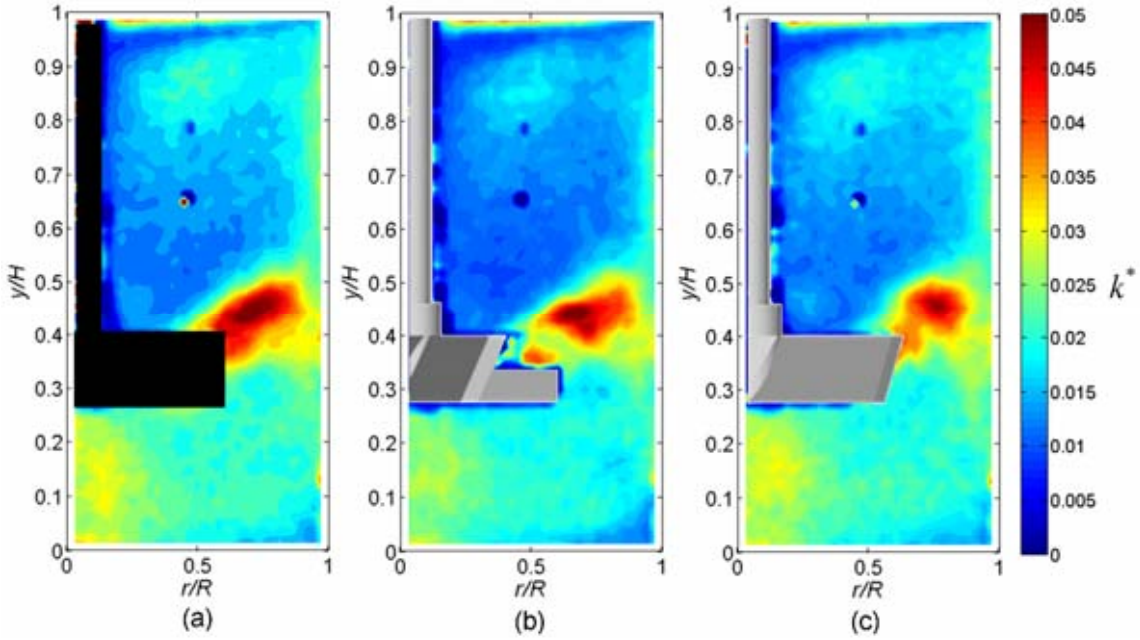

Figure 6.8 TKE plot in (S) configuration determined from (a) ensemble time-averaged method, and from angle resolved measurements at impeller position (b) θ = 0º and (c) θ = 30º. T = 41.5mm, D/T = 0.59, P/V = 168Wm^{-3}, N = 595rpm.

The main difference between the ensemble average turbulence distribution and the angle resolved distributions is observed in the trailing vortex region around the impeller. The region close to the impeller in the ensemble average map exhibits a higher turbulence intensity along the vortex path compared to the angle resolved maps, a sign of pseudo-turbulence being captured by the averaging technique. Everywhere else in the vessel the TKE distributions are essentially the same which confirms the absence of pseudo-turbulence in those regions. Similar observations were made with respect to the other mixer configurations studied, (B), (U) and (E). A comparison between all mixer configurations is shown in Figure 6.9 where the ratio of the maximum time-averaged k^* (approximately equal to $0.05U_{TIP}^2$) to the angle-resolved k^* measured at the same spatial location is plotted as a function of impeller position. Note that the point location of maximum TKE is different for each configuration.

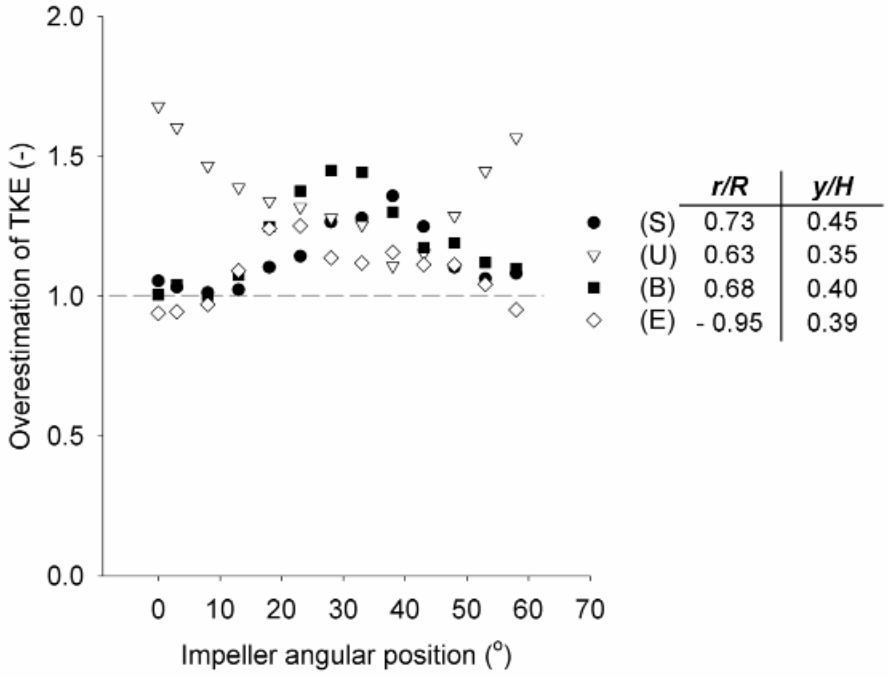

Figure 6.9 Overestimation of TKE in different HTE vessel configurations showing the level of pseudo-turbulence contribution.

The smallest overestimation in TKE by the ensemble average method was achieved in the (E) and (S) configurations, where k^* was overestimated by a maximum of 35% and 44%, respectively. On the other hand, the highest pseudo-turbulence was observed in (U) as the overestimation of k^* was 80%. This is due to a localised region of high vorticity close to the top of the impeller blade, which is smoothed out upon ensemble averaging. Since the flow velocity away from the impeller is much lower than for the other configurations, this effect dominates and leads to the high overestimation obtained in this case. The overestimation in (B) was 60%, which fits between the 50% (Schäfer *et al.*, 1998) and 200% (Hockey & Nouri, 1996) reported in literature for a 4-blade PBT in laboratory scale vessels. These overestimations are still much smaller than the 400% reported by Yianneskis & Whitelaw (1993) for an RDT on the same scale. Such an overestimation of TKE serves to strengthen the argument for angle resolved measurements in turbulent flows.

6.5 CONCLUSIONS

Angle resolved PIV measurements were successfully made in miniature HTE scale vessels of four different configurations. The velocity data were ensemble-averaged at every degree over the 60º sector located between two successive impeller blades. The global flow field revealed that periodicity existed in all configurations, but was limited to the region of impeller discharge and inflow underneath the impeller. The square vessel (S) achieved the strongest axial-radial flow field throughout the vessel amongst all configurations. The average flow number obtained from angle-resolved PIV data agreed with values in the literature for the standard baffled configuration. A lower level of pseudo-turbulence was observed in the HTE scale vessels compared to larger vessels on the laboratory scale, which is partly due to the lower level of TKE achieved in these small vessels. The smallest overestimation in TKE by the ensemble average method was achieved in the (E) and (S) configurations.

The angle-resolved measurements revealed details of the vortical structure behind the impeller blades. The up-pumping PBT employed shed trailing vortices mainly in a radial direction with relatively little axial movement. The highest axial vortex position was achieved in (S), which may have contributed to the improved mixing time achieved compared to the other configurations. The hydrodynamic studies conducted here in the high transitional regime suggest that the (S) configuration performs better than other configurations and is a good replacement for the (B) configuration in commercial HTE units when baffles are undesirable. It is not immediately obvious, however, whether the (S) configuration performs as well in the laminar regime.

7. MIXING IN THE LAMINAR REGIME

The studies made in the HTE vessel have concentrated, so far, on mixing in the high transition to turbulent regime. There are, however, many processes within industry that involve the mixing of highly viscous or rheologically complex fluids. A notable example is polymerisation, where the apparent viscosity of the fluid increases drastically over the course of reaction due to the formation of longer polymer chains. Consequently, at the HTE scale, these processes operate in the laminar regime due to the low values of Reynolds number. Therefore, knowledge of the hydrodynamic behaviour within the HTE vessels in this regime is also critical; such studies were conducted in this Chapter with the use of two different grades of polypropylene glycol (PPG) which exhibit Newtonian behaviour with viscosities of 0.444 and 0.797 Pa s respectively at 20^{o}C.

The mixing behaviour in (B) and (E) configurations was thoroughly examined by Hall *et al.* (2005a). It was concluded that in the laminar regime, the characteristic flow pattern produced by the 6-PBTu resembled that generated by a radial mixing device. Since the mixing mechanism is no longer related to turbulence, rate of strain contours were used to analyse the quality of mixing; this is a very similar method to the TKE analysis in turbulent systems. Pseudo-caverns were also investigated and it was found that the volumes of such features were related to the power input.

7.1 FLUID PROPERTIES

The rheological properties of PPG were examined using an AR1000 Advanced Rheometer (TA Instrument, USA) with cone and plate geometry under steady flow experimental

condition, as described in Section 3.2.8. A linear relationship was obtained between shear stress τ, and the correspondent shear rate, $\dot{\gamma}$, within a range of τ = 0 – 200 Pa, revealing the Newtonian nature of the fluid. As shown in Table 3.1, the dynamic viscosity of the fluid varies greatly with the ambient temperature. The ambient temperature was controlled in the laboratory to 20°C to remove any variation and was closely monitored using an analogue thermometer placed in the vicinity of mixing vessel. The density for both fluids, ρ, was 1005 kgm^{-3} as supplied by the manufacturer.

Table 7.1 Viscosities (Pas) of PPG at different temperatures.

Temperature (°C)	PPG2700	PPG2000
20	0.797	0.444
23	0.669	0.367
25	0.605	0.326
26	0.552	(-)
27	0.514	(-)
28	0.502	(-)

* All experiments were carried out at a temperature of 20ºC.

7.2 CHARACTERISTICS OF THE POWER CURVE

Effective mixing within the HTE system in the laminar regime requires much higher power draw: the maximum power input applied was over thirty times of that used in the turbulent regime. This rise in power draw led to a more accurate torque measurement, due to the proportion of mechanical noise in the total.

The power curve for the four configurations with PPG 2700 as working fluid is shown in Figure 7.1(a) as a log-log plot of the power number, *Po*, for various Reynolds numbers, *Re*. The power curve for (E) and (B) were very similar and the gradient of the slope was -1.1 and -1.2 respectively, this agreed reasonably well with literature on larger scales where the

slope of the power curve in the laminar mixing regime has a gradient of around -1 (Edwards *et al.*, 1992). An interesting trend can be observed in the (U) configuration where the power curve can be broken down to two distinctive slopes, as shown in Figure 7.1(b). Whilst in the lower spectrum of agitation speed investigated ($N < 200$, $Re < 3$), the slope of power curve were measured at about -1.2, it sharply decreases to only -0.75; the appearance of 'double slopes' however, is not obvious in other configurations. Hence it is suggested that there is a change in flow regime and is related to the lack of baffles due to the fact that (U) is the only configuration with a very obvious 'double slopes' in the power curve. Furthermore, the disagreement in power curves across the configurations narrows as flow approaches the transitional regime. In addition, it should be noticed that the power curve observed in (U), (E) and (S) should not be compared directly with the illustrated power curve in Edwards *et al.* (1992), as such curve was based on the standard (B) configuration in larger scales.

The mixing behaviour was analysed in two ways, firstly, by comparison of the hydrodynamic behaviour across all configurations and secondly, by observing the change in flow field for each individual configuration over a range of impeller speeds. The experimental conditions are shown in Tables 3.4 & 3.5.

For the configuration independent experiments on the change in flow pattern studied over a range of very low *Re*, the measurements were based on the change in *N* instead of *P* in the previous cases. This is because of the minute increments in *N*, in some cases as small as 10 rpm; the resulting *P* increments are so tiny that accurate measurements cannot be achieved with the Coesfeld viscomix equipment.

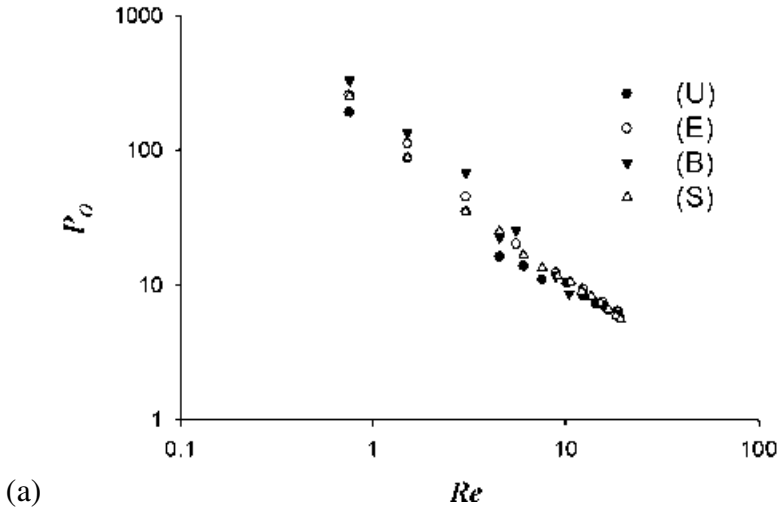

(a)

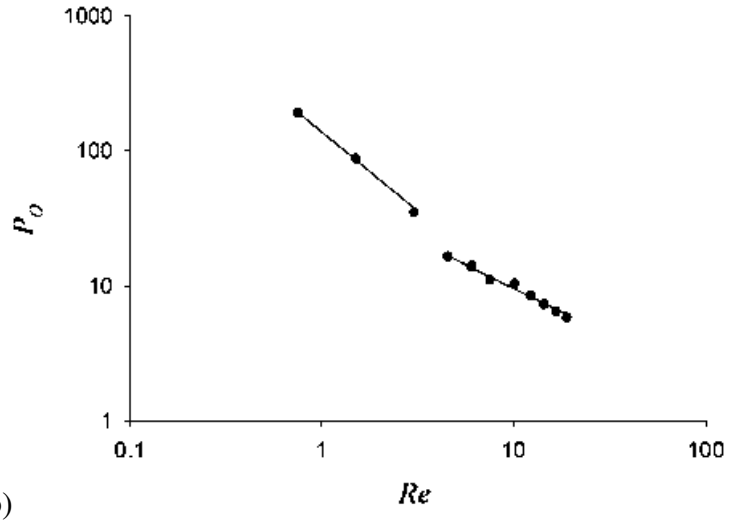

(b)

Figure 7.1 Power curve investigated in PPG2700 for the (a) four configurations investigated and (b) showing only (U) with the two distinctive gradients.

7.3 ENSEMBLE AVERAGED VELOCITY PLOTS

7.3.1. GLOBAL FLOW FIELD IN THE LAMINAR TO TRANSITION REGIME

The global flow maps for the (U) & (S) configurations with both working fluids (PPG2700 and PPG2000) at the highest power input, P = 5.5kWm^{-3}, are shown in Figure 7.2. Despite their differences observed in the transitional regime, i.e. the (U) configuration experiences an exceptionally high level of tangential flow whilst (S) exhibits the highest axial-radial

flow among all configurations; it becomes apparent that there is not much divergence between the two configurations here in the laminar-transition regime.

The impeller generates a radial discharge in both configurations and the flow splits at the vessel wall, subsequently forming two distinctive upper and lower recirculation loops; this is a flow pattern commonly associated with RDT (for example, see Mavros *et al.*, 1996). Since the flow is asymmetric about the central axis in (U), the two loops resembled an upper and lower torus. The four 90º corners in (S) become less effective in laminar flow, but they still affect the global flow field where axial-radial flow is significantly stronger than observed in (U). In both cases, the 50% reduction in viscosity in PPG2000, hence the approximately doubling of *Re* in each case, has little effect on the flow pattern; this is not unexpected as the flow is still within the very low laminar-transition regime.

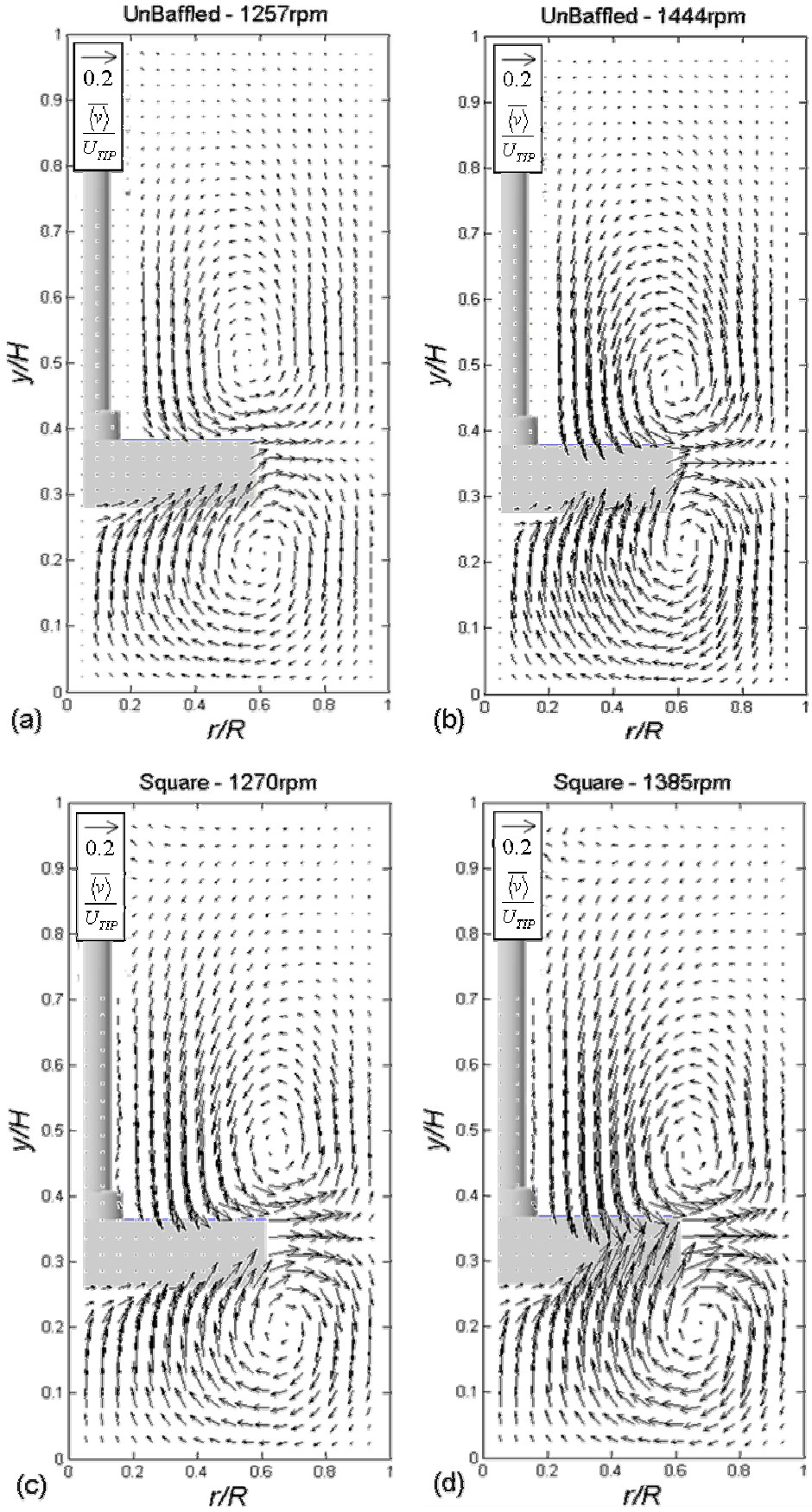

Figure 7.2 Ensemble averaged flow map showing (a) (U) PPG2700 and (b) (U) PPG2000 and (c) (S) PPG2700 and (d) (S) PPG2000, all at P = 5.5 kWm^{-3}.

For the (B) configuration however, the flow fields are far more interesting. As shown in Figure 7.3, Hall *et al.* (2005b) previously obtained flow maps at 45° between two of the baffles using PPG2000. They showed a similar global flow pattern to the (U) and (S) configurations where two explicit upper and lower flow loops are presented.

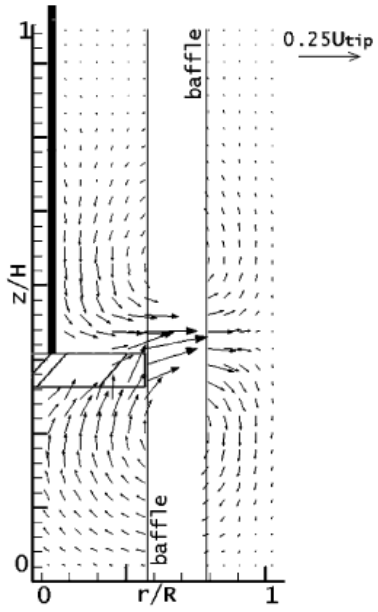

Figure 7.3 Flow map showing (B) in PPG2000 at P = 3.6 kWm^{-3}, measurement was made halfway between two baffles. (Hall *et al.*, 2005).

Alternatively, the measurements in this work were made to examine the flow patterns right behind one of the baffles, i.e. at the 5° plane, as shown in Figure 7.4. If the PPG2000 case (Figure 7.4(a)) is compared with that in Figure 7.3, one can clearly see that the extent of upper and lower recirculation loops is greatly reduced. This is because the torus structure is broken up by the baffles and the majority of flow is squeezed into the region $0.2 < r/R < 0.6$, causing a high level of axial-radial movement in this area. The upper and lower circulation loops were even less observable in the PPG2700 case in Figure 7.4(b).

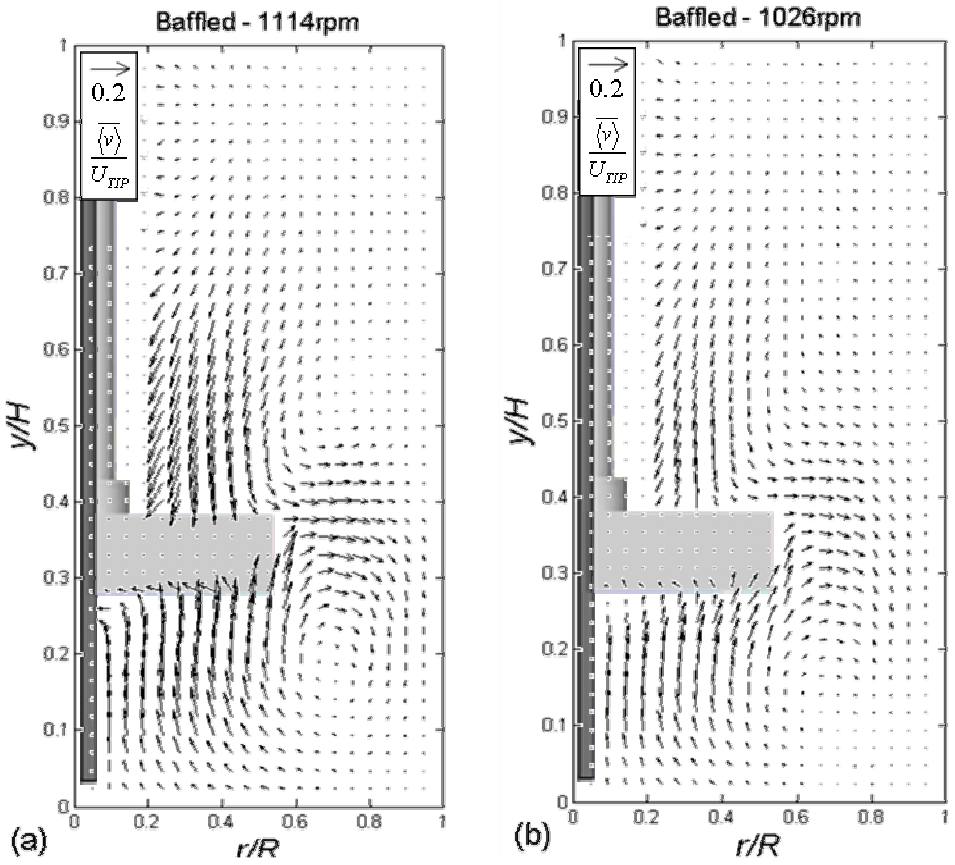

Figure 7.4 Ensemble averaged flow map showing (B) configuration with (a) PPG2000 and (b) PPG2700 as working fluid at P = 3.6 kWm^{-3}. Measurements were made 5^{o} behind one of the baffles.

Likewise, the flow map of (E) is shown in Figure 7.5. The upper and lower circulation loops are highly observable on the right hand side (open side) of the vessel, where impeller is furthest away from vessel wall. On the left (closed) side however, the difference in fluid viscosity or *Re* appears to have an impact on the flow pattern; both the upper and lower recirculation loops in this side of vessel the PPG2700 case are not seen when the fluid is replaced with PPG2000.

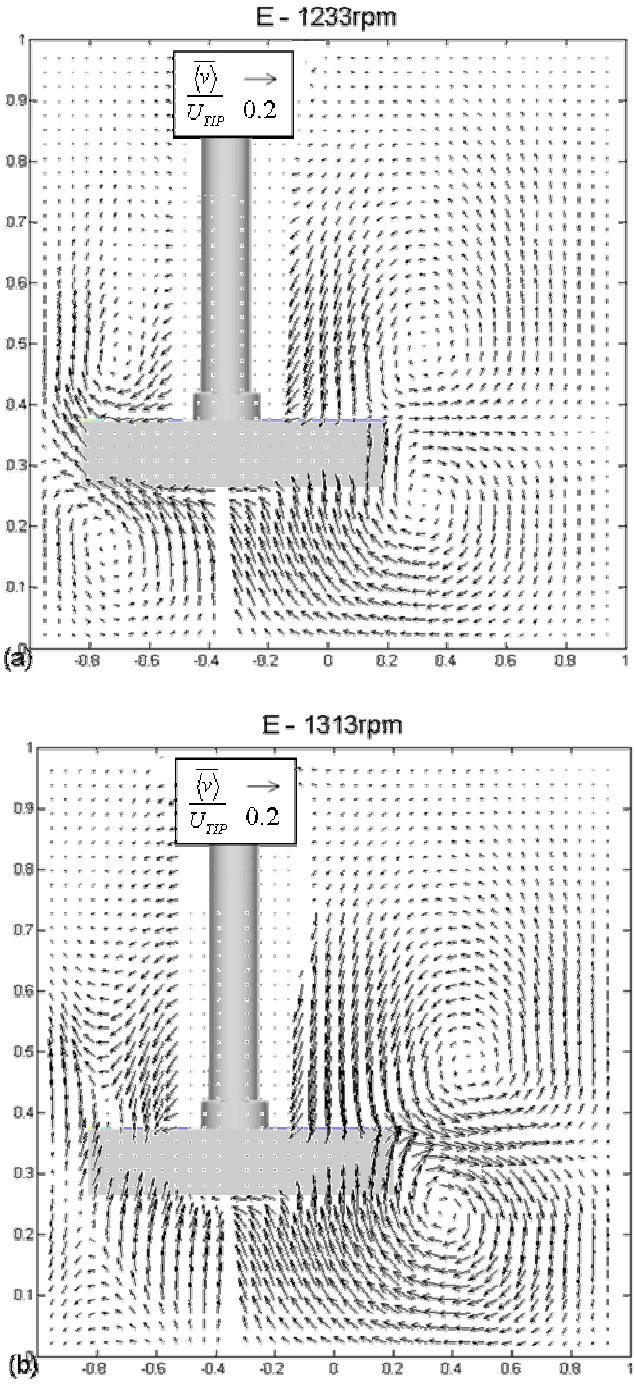

Figure 7.5 Ensemble averaged flow map showing (E) configuration with (a) PPG2700 and (b) PPG2000 as working fluid at P = 5.5 kWm^{-3}.

All configurations on their own, display a common flow pattern within the range of power input, P = 0.6 - 5.5 kWm^{-3}. With the exception of (E), the impact of doubling *Re* by changing the working fluid on the global flow field was also found to be limited to the magnitude of $\overline{\langle v \rangle}/U_{TIP}$ with no visible change in flow field.

7.3.2. GLOBAL FLOW FIELDS AT THE LOWER *Re* RANGE

As shown on Figure 7.1, whilst the log power curve for the (E), (B) and (S) configurations is fairly linear (constant gradient throughout the range of *Re* investigated), the gradient of the curve in (U) changes as a function of *Re*, and had a value of -1.2 at $3 > Re > 0$ ($200 > N > 0$) and -0.75 at $20 > Re > 3$ ($1300 > N > 200$). A possible reason for the change in slope could be a change in the overall flow field.

The ensemble averaged flow maps of (U) in PPG2700 at low *Re* are shown in , where the change in global flow field can be clearly observed. It should be noted that the scale in these vector plots has been greatly magnified for the ease of flow visualisation due to the lowered localised velocity. Flow is initially discharged in a combined axial-radial direction along the top edge of impeller at rotational speed of $150 > N > 50$ as shown in Figure 7.6(a) - (c), a typical behaviour of PBTu. A portion of flow was also discharged radially and formed a lower circulation loop occupying the area in $y/H < 0.33$. No visible difference can be observed in both the flow direction and the magnitude of $\overline{\langle v \rangle}/U_{TIP}$ with increasing U_{TIP} in this range. However, the downward recirculation at $0.2 < r/R < 0.5$ above the impeller begins to form a recirculation loop if *N* is increased further to $N = 200$ rpm in Figure 7.6(d); at this point the impeller still maintains an explicit axial-radial discharge. The discharge along the top edge of impeller turns fully into the radial direction if *N* is allowed to further increase to 300 rpm in Figure 7.6(e). An obvious explanation to this seems to be the closer proximity of the upper recirculation loop to the top edge of impeller; the locus of upper recirculation loop moved from $y/H = 0.65$ and $r/R = 0.35$ in the $N = 200$ rpm case to $y/H = 0.55$ and $r/R = 0.5$ at 300 rpm. The flow at the outer edge of recirculation loop has now moved into a position to interfere with impeller discharge and forced it into a radial direction. Therefore it can be suggested that the switchover from axial-radial to an entire radial discharge between $N = 200 - 300$ is responsible for the

change of gradient in the power curve of (U) configuration. Despite the dramatic change in flow pattern in the upper half of vessel, the lower circulation loop retains its structure throughout the range of *N* studied.

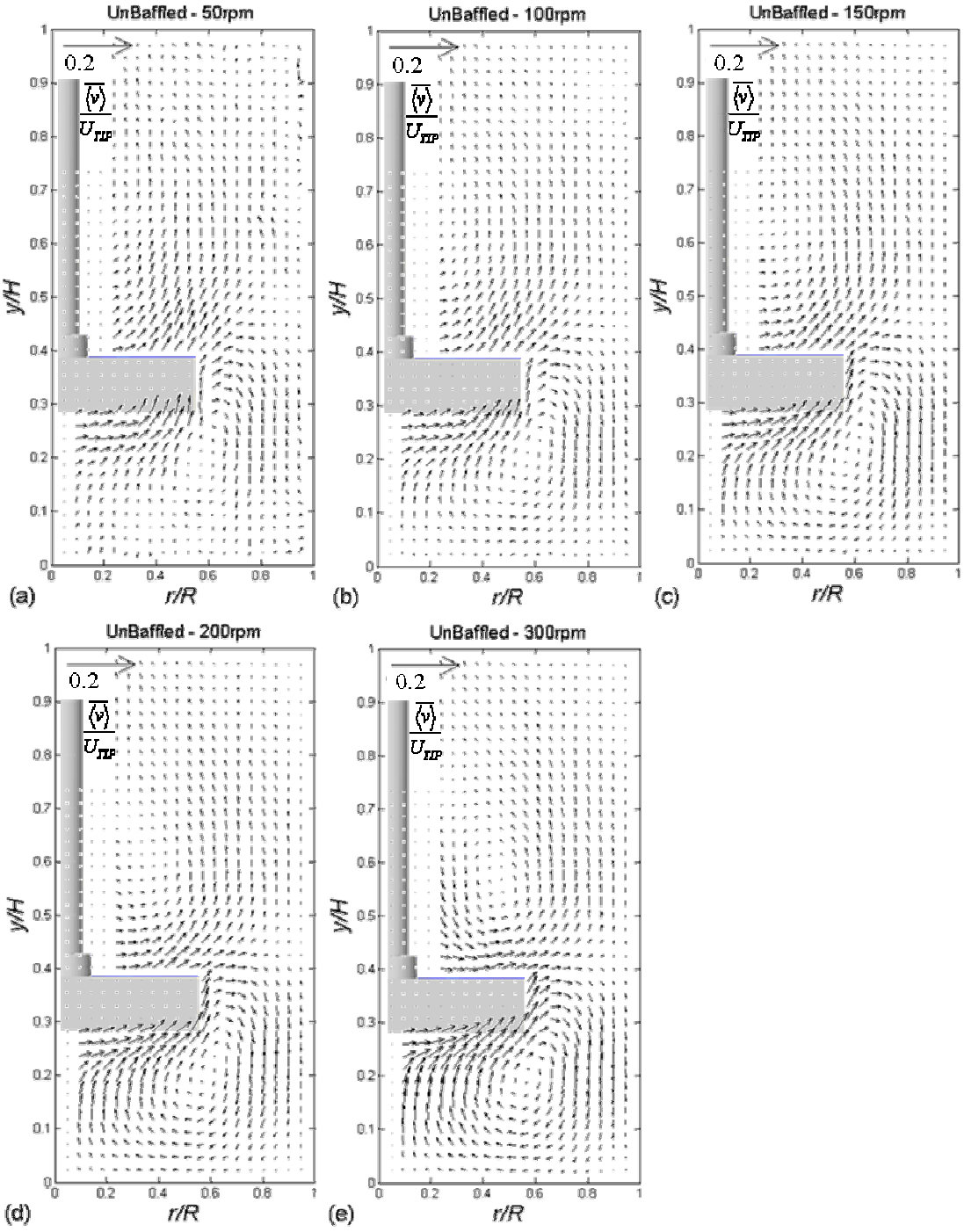

Figure 7.6 Ensemble averaged flow map showing (U) configuration with PPG2700 as working fluid at various agitating speed; (a) *N* = 50 rpm, (b) *N* = 100 rpm, (c) *N* = 150 rpm, (d) *N* = 200 rpm & (e) *N* = 300 rpm.

Meanwhile for the (S) configuration, similar phenomena can also be seen, although the upper circulation loop developed at a lower impeller rotational speed and the switch over from axial-radial to radial discharge is subtler when compared to the (U) configuration. As shown in Figure 7.7, the animation of ensemble averaged flow field of (S) with increasing impeller rotational speed can be directly compared to that in (U) shown previously in Figure 7.7.

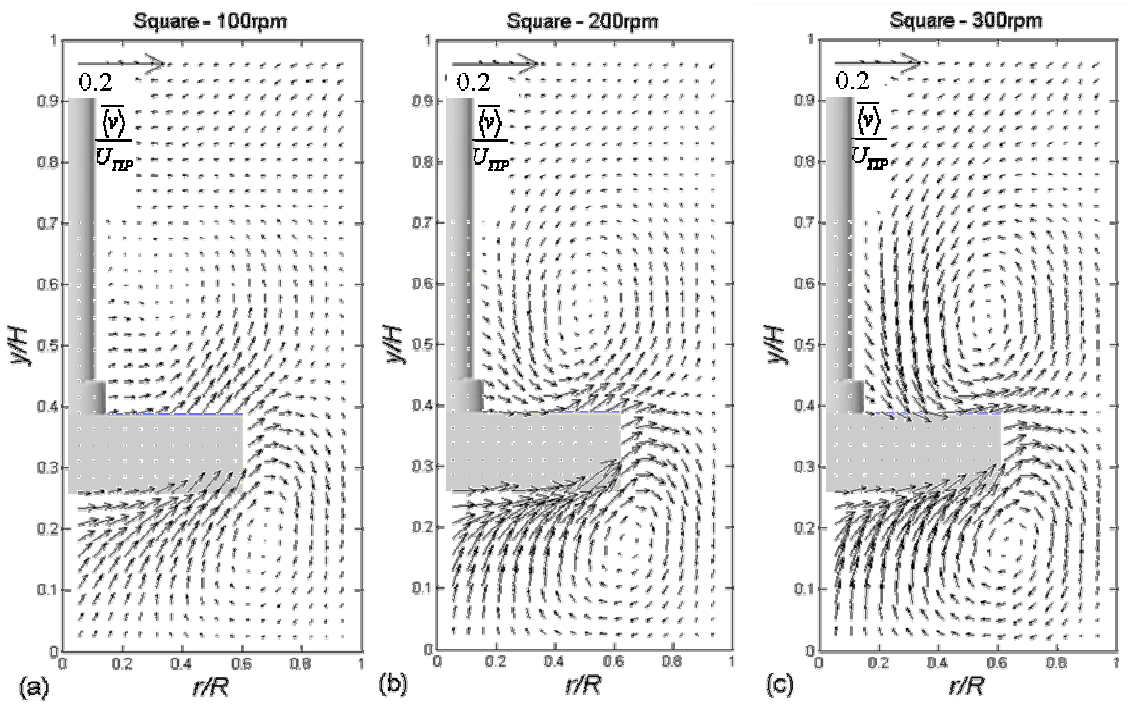

Figure 7.7 Ensemble averaged flow map showing (S) configuration with PPG2700 as working fluid at various agitating speed; (a) *N* = 100 rpm, (b) *N* = 200 rpm & (c) *N* = 300 rpm.

At 100 rpm, the outline of upper circulation loop was already well developed, i.e., the locus of the loop located at *y/H* = 0.6 and *r/R* = 0.35; similar flow pattern can only be observed in (U) at 200 rpm. With (S) at 200 rpm, the upper circulation loop has already travelled to a position (locus of the loop at *y/H* = 0.55 and *r/R* = 0.5) that affects the impeller discharge, where less axial flow can be seen along the top edge of impeller. Further increase in the impeller rotational speed to 300 rpm can no longer affect the location of circulation loop, since the impeller discharge is fully evolved into the radial direction due to the stronger flow.

The similarity between global flow patterns in (S) and (U) suggested that the four 90º corners of (S) have no obvious effect on the flow at the lower *Re* range. The fully development of flow fields in the lower *N* range and a more subtle switchover from axial-radial to radial discharge partially explains the less dramatic change in power curve gradient in (S), which is not observable in Figure 7.1.

The gradient of the power curve in (B) and (E) configurations on the other hand, is found to be constant throughout the low *Re* range studied. Animations of ensemble time-averaged flow field of (B) and (E) with increasing impeller rotational speed is shown in **Error! Reference source not found.** Figure 7.8 and Figure 7.9 respectively.

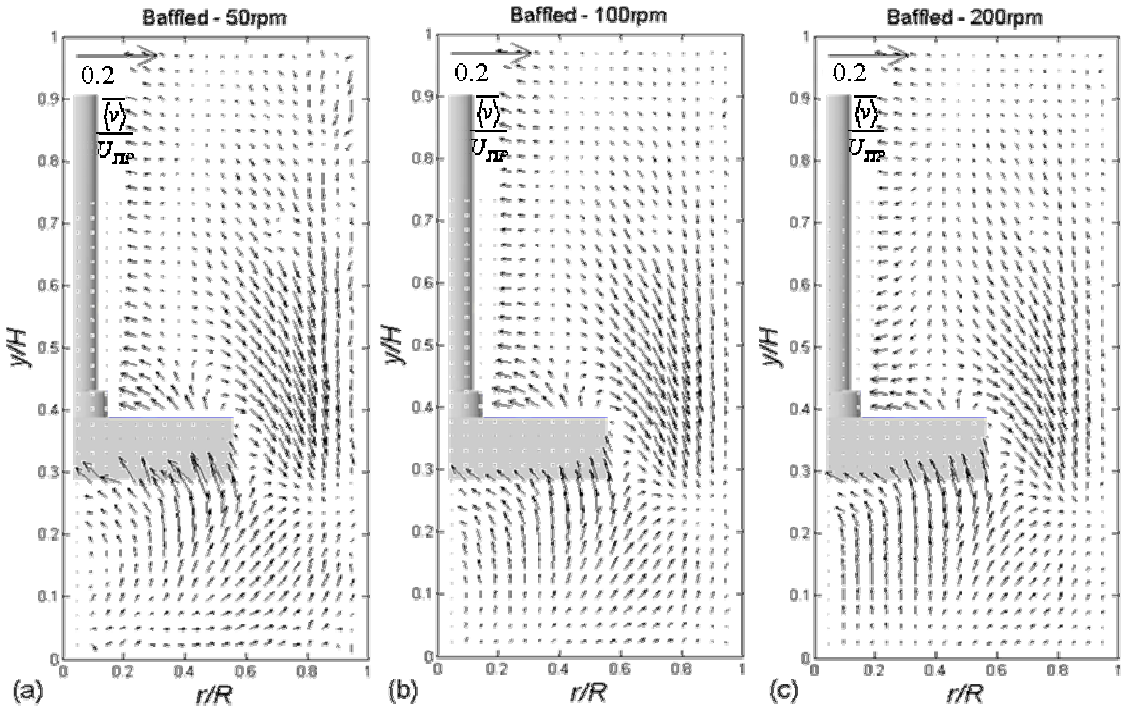

Figure 7.8 Ensemble averaged flow map showing (B) configuration with PPG2700 as working fluid at various agitating speed; (a) *N* = 50 rpm, (b) *N* = 100 rpm & (c) *N* = 200 rpm.

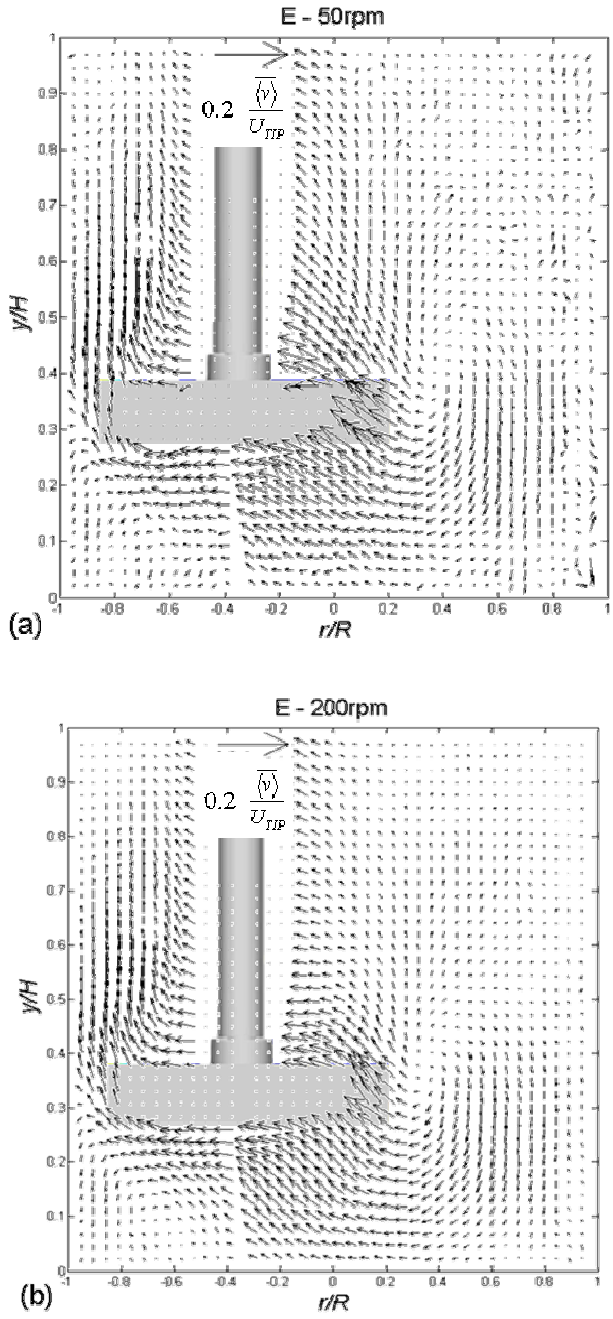

Figure 7.9 Ensemble averaged flow map showing (E) configuration with PPG2700 as working fluid at various agitating speed; (a) *N* = 50rpm, (b) *N* = 200rpm.

No visible change in the global flow field is observed throughout the lower range of *Re* in both configurations; it appears that the flow field is already well developed even at the lowest *Re* case. Furthermore, the rise in *N* does not seems to have a direct impact on the localised $\overline{\langle v \rangle}/U_{TIP}$, although the flow in the upper reaches of the vessel does become less random in both configurations with increasing power input; areas such as these may be

referred to as pseudo-caverns (Hall *et al.*, 2005b) where velocity is so low that no obvious movement can be observed. The increase in $\overline{\langle v \rangle}/U_{TIP}$ with increasing N is much less in (E) when compared to both (U) and (S), and there is almost no change in $\overline{\langle v \rangle}/U_{TIP}$ in (B). The stable growth showed here ensured a constant gradient at the lower end of the power curve, and the power curve illustrated in Edwards *et al.* (1992) is not only suitable for the (B) configuration as intended, but also clearly applicable to (E) configuration.

7.4 PLIF EXPERIMENTS IN THE LAMINAR REGIME

The lack of turbulent eddies in the laminar flow means the rate of mixing may be reduced significantly and the mixing time analysis frequently used in the low viscosity experiments may not be used. For example, performance of mixing in this case should be monitored by the amount of completely un-dyed area which indicates segregation, as shown in Figure 7.10(b), rather than the localised percentage mixedness. The working fluid PPG used in this study exhibits a Newtonian nature, which precluded the formation of caverns, hence the injection point can remain on top of the liquid free surface. In other studies such as Adams *et al.* (2007) for example, where a Herschel-Bulkley fluid was used, the injection point had to be moved to a position within the impeller region or the Rhodamine tracer can never enter the cavern. A video was constructed from sequences of PLIF images for each configuration and can be found in the supplementary CD at the back of this thesis.

7.4.1. IMAGE ANALYSIS

Image analysis that involved a simple thresholding technique was carried out using MATLAB® to analyse the percentage of segregation as a function of time; this technique is similar to the dyed fractional area coverage analysis described by Alvarez - Hernández *et*

al. (2002). As shown in Figure 7.10, the area of impeller was first defined for each image and pixels within such area representing the impeller are substituted with a '0' entry; at this point the total number of pixels with '0' entry, Px_{Imp}, was counted and recorded. It should be noted that the background greyscale level is around 50, therefore the '0' entry will not be confused with any other pixels.

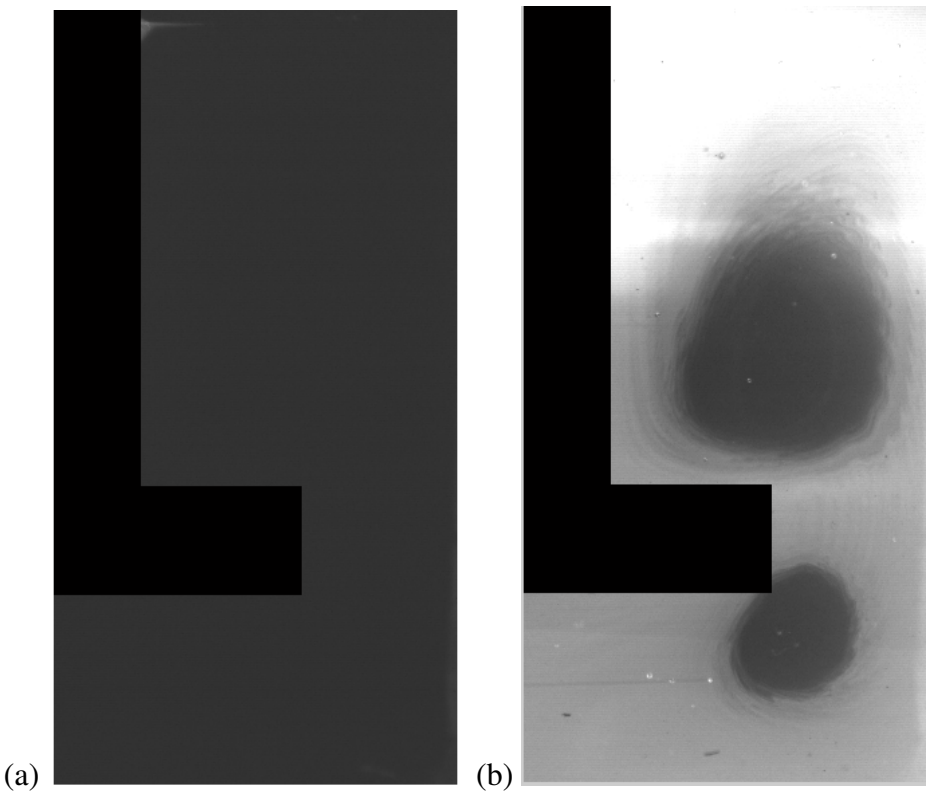

Figure 7.10 Image captured for the (S) configuration with P/V = 0.6kWm^{-3} in PPG2000 at (a) t = 0s and (b) t = 300s after the injection of tracer dye, such images are used for G_i and G_∞ calculation respectively.

For each individual pixel, the greyscale level was determined from the minimum reading of that pixel during the first three frames. The overall background greyscale, G_i, can then be averaged from the many readings obtained, as shown in Figure 7.10(a). Due to the fact that a fully mixed condition cannot be reached even after the full duration of image capture (t = 300s), the greyscale value that reflects the final concentration, G_∞, can only be based on the measurement plane averaged value, with the assumption that the total of 2-D

measurable concentration equals to the concentration of injected tracer. A threshold greyscale, G_T, is set where any pixels with a value below such threshold will be reset to '0', for example,

$$G_T = (G_\infty - G_i)R_T + G_i \tag{7.1}$$

where R_T is a user defined variable to adjust G_T. In this work, R_T used has typical values between 0.45-0.65. Adjustment to R_T is required for each individual experiment due to the different noise level presented; for example in Figure 7.10(b), one may find the greyscale level is much higher in the upper part of stirred vessel due to the reflection from the impeller shaft, where the matt black paint was dissolved and stripped off by the surrounding PPG fluid. Such differences in laser intensity however, only have a minor effect on segregated area measurement because without the presence of tracer dye, PPG in segregated area will not be excited by the elevated laser intensity.

The analysis of a sample image is shown in Figure 7.11 where Figure 7.11(a) is a raw image taken at t = 42 s after tracer injection and Figure 7.11(b) is the threshold processed version. The pixels with a '0' reading at this point, Px_{ZERO}, included the segregated volume, Px_{SEG}, and impeller Px_{Imp}. The percentage of segregation can then be determined by,

$$Segregation = \frac{Px_{ZERO} - Px_{IMP}}{Px_{ALL} - Px_{IMP}} \tag{7.2}$$

where Px_{ALL} is the total number of pixels in the measurable volume; i.e., for a 600×300 pixel^2 region, Px_{ALL} is 18×10^4.

Visual validations were performed manually on various frames of each series of experiments, for example in Figure 7.11, to ensure the R_T applied achieved a satisfactory match of segregation area outline between the raw and processed image.

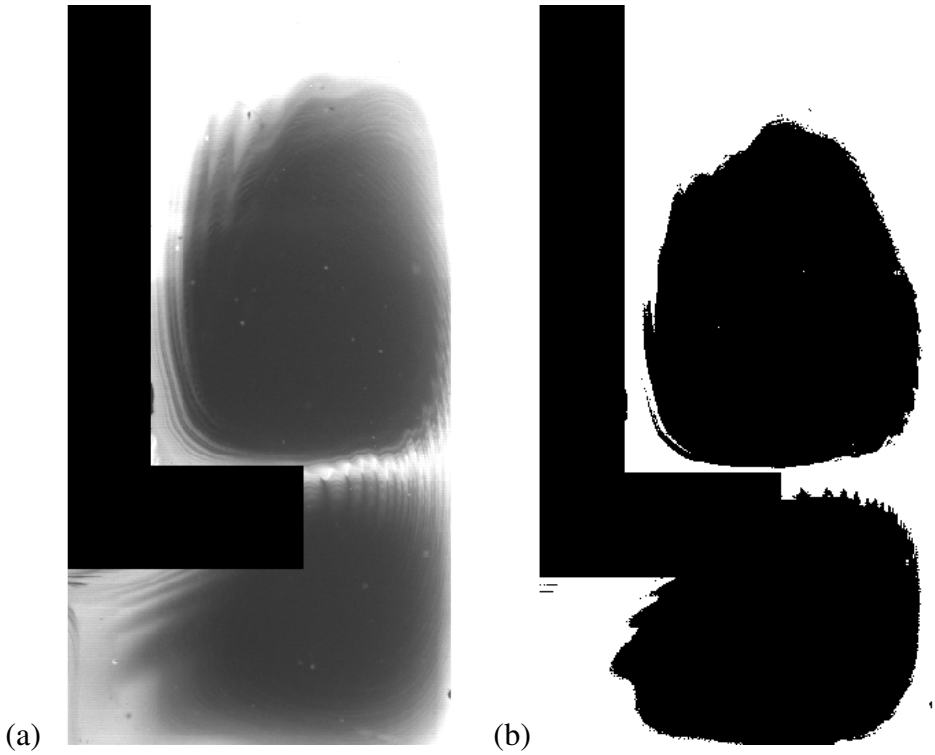

Figure 7.11 (a) Image captured for the (S) configuration with *P/V* = 0.6 kWm^{-3}, *Re* = 14.1, in PPG2000 at *t* = 42s and (b) analysed image after thresolding.

7.4.2. REDUCTION OF SEGREGATED AREA

The decrease of segregated area with time for the (S), (E) & (B) configurations using PPG2000 is plotted in Figure 7.12 for the lowest power input in the range (*P/V* = 0.6 kWm^{-3}, *Re* = 11.3 – 14.1). The relevant percentages of segregation in the images shown in Figure 7.10(a), Figure 7.11(a) & Figure 7.10(b) for the (S) configuration captured at 0 s, 42 s and 300 s respectively can be directly read from this plot as 100%, 50% and 25%.

The mixing performance between the three configurations is comparable in the first 25 seconds (from 100% to 70% segregation) where the dye quickly disperses within the volume of the vessel where velocity is at its highest resulting from the impeller discharge. The segregation in the (B) and (E) configurations continues to drop quickly, although it takes a further 50 s for the segregated area in (B) to shrink from 20% to 10% compared with the (E) configuration. This is due to the very slow movement of the tracer dye in (B) into the circulation loops observed in Figure 7.3. Despite the very significant axial-radial flow component in (S), it is obviously the least efficient configuration in the laminar mixing systems shown here: the rate of decay is much slower then (B) and (E), resulting the existence of more than 20% segregation 300 s after tracer injection.

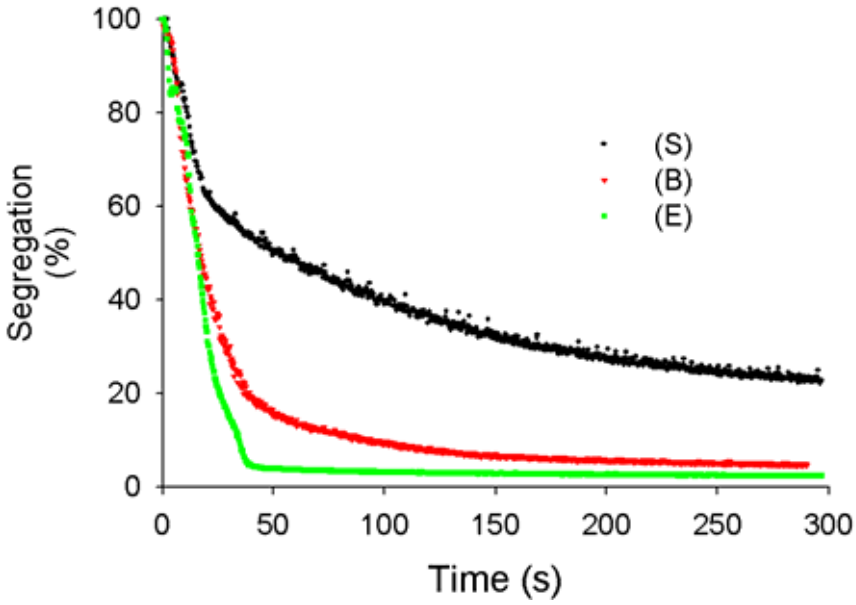

Figure 7.12 Time history of decade in segregated area for (S), (B) & (E) configurations in PPG2000 with P/V = 0.6 kWm^{-3}, Re = 11.3 - 14.1.

In addition, a visual comparison was carried out on the images captured at 10s after tracer injection for (S) and (B) as shown in Figure 7.13, which highlights the strong radial discharge. As described in Chapter 2, Alvarez - Hernández *et al.* (2002) showed that under increased magnification in the PLIF images, tracer dye from the impeller is compressed

radially and elongated vertically outward towards the vessel wall, as shown in Figure 2.22. This results in vertical 'ripples' being captured by the CCD camera and such vertical ripples progressively formed a parabolic profile as they approached the wall. The ripples were also observed in HTE scale for both configurations in this work. The vertical stretch progressively forms a parabolic profile in the (B) configuration, as described by Alvarez - Hernández *et al.* (2002). However in the (S) configuration the ripples stayed vertical without the parabolic stretch throughout their path to vessel wall; such phenomena hinder dye progression to the centre of upper circulation loop. The difference in the profile of ripples between (B) and (S) are most obvious at $0.8 < r/R < 1.0$.

The majority of dye in the laser plane in (B) was observed joining the downward circulation loop whereas the dye in the upper half of vessel joined the circulation loop before it enters the laser plane; such visualisation provided a good understanding on the importance of baffles in breaking the solid body rotation which hinders mixing performance in (S) and (U) configurations.

(a) 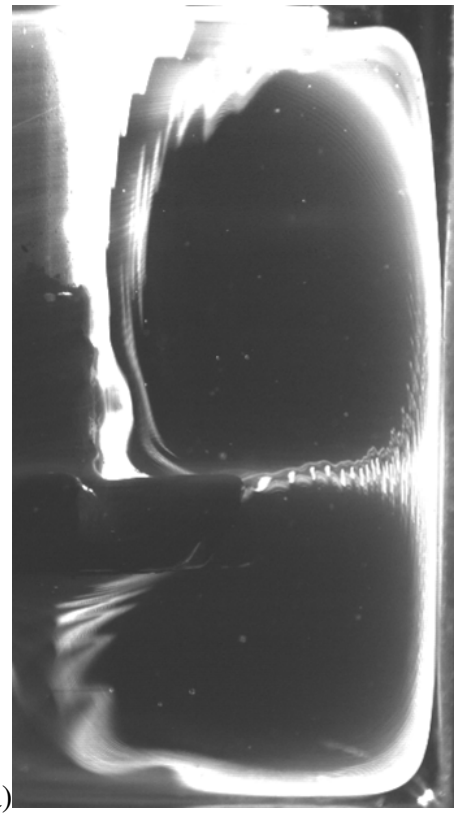 (b) 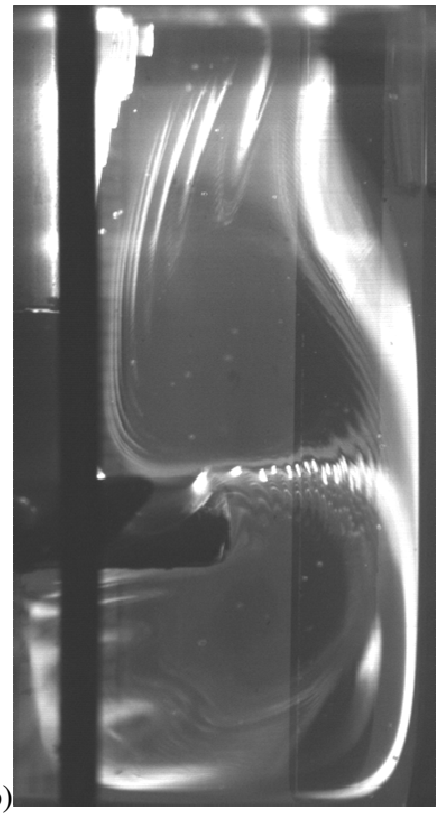

Figure 7.13 PLIF images showing the path of impeller discharge in (a) Square and (b) Baffled configurations in PPG2000 at P/V = 0.6kWm^{-3}. Images were captured at 10s after tracer injection, which is equivalent to 150 impeller revolutions.

Figure 7.14 shows that all configurations displayed similar characteristics before segregation was reduced to 30% at a power input of P/V = 5.5 kWm^{-3} (Re = 35). After 150 s, mixing segregation in (S) and (U) was reduced to a mere 2%. This is primarily due to the increased shear gradient as their flow pattern remained more or less unchanged with increasing power input, as observed earlier. Once again (S) and (U) produced a similar but less efficient mixing performance. Unlike the experiments performed at lower power input, (E) takes a further 20 seconds for the segregation to completely disappear when compared to (B), which is completely mixed in less than 10 s.

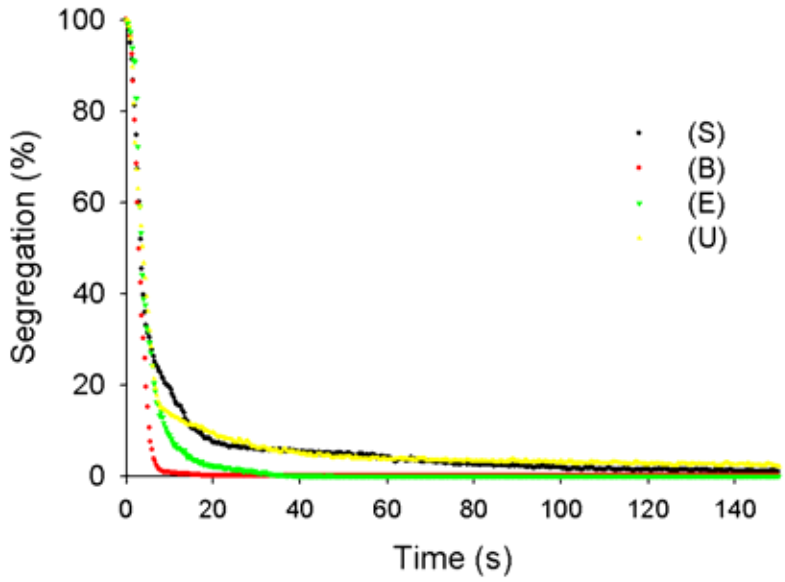

Figure 7.14 Time history of decade in segregated area for (S), (B), (U) & (E) configurations in PPG2000 with *P/V* = 5.5 kWm^{-3}, *Re* = 31.1 – 34.2.

7.5 SHEAR RATES AND RATE OF STRAIN CONTOURS

The nature of laminar flow precludes the generation of turbulent eddies, which is the primary transport mechanism in the low viscosity experiments studied in the previous Chapters. TKE estimation is not therefore applicable to analyse and compare mixing performance across the configurations and power inputs studied here, although turbulence may still be generated when exceptionally high power input is used

It is well established that mixing in laminar regime depends on the relative velocity between fluid packets, otherwise referred to as velocity gradients. Fluid containing large velocity gradients enables a more frequent exchange between different fluid elements than a flow field with uniform velocity and direction; this again highlights that large absolute velocity does not necessarily mean good mixing. Hall *et al.* (2005b) determined the localised rate of strain (ROS), $\langle S_{xy} \rangle$, in the (E) configuration and reported the region with the highest shear is in the impeller plane. $\langle S_{xy} \rangle$ is defined as,

$$\langle S_{xy} \rangle = \frac{1}{2}\left(\frac{\partial \langle U_x \rangle}{\partial y} + \frac{\partial \langle U_y \rangle}{\partial x} \right) \tag{7.3}$$

which is the mean of the shear rate components in the axial and radial directions. The shear rate gradient $\frac{\partial \langle U_x \rangle}{\partial y}$ and $\frac{\partial \langle U_y \rangle}{\partial x}$ may be calculated directly from the localised ensemble averaged velocity field. It is important to understand that any two measurements with equal positive and negative readings are of the same magnitude operating in opposite directions.

The localised ROS of (E) calculated by Equation 7.3 is shown in Figure 7.15(a). It matches the comparable rate of strain contour map by Hall *et al.* (2005b) shown in Figure 7.15(b) very well, especially the horizontal plane of high shear at the impeller level. In this section, the distribution of ROS is analysed for the (U), (B) and (S) configurations which were not reported by Hall *et al.* (2005b), and the relationship between ROS and mixing performance is investigated.

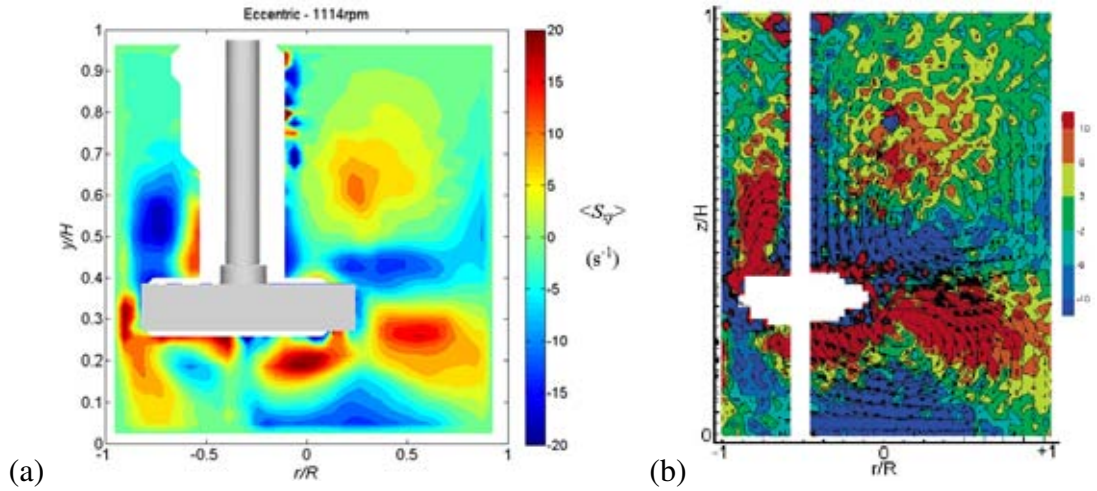

Figure 7.15 Rate of strain contour for (E) configuration in a) PPG2000 with *P/V* = 3.6 kWm^{-3}, calculated by (7.3), which compares well with b) Hall *et al.* (2005b) under the same mixing condition.

For an effective comparison of the ROS distribution across the many configurations investigated, where different impeller speeds were applied to deliver the same power input

per unit volume, it is necessary to normalise $\langle S_{xy} \rangle$ with impeller tip speed U_{TIP}. The normalised ROS distribution in (E) with power input of 0.611 and 5.5 kWm^{-3} are shown in Figure 7.16.

It is obvious that even though $\langle S_{xy} \rangle$ has been normalised with U_{TIP}, the values rise significantly with increasing power input. However, it appeared that the distribution of shear has no relationship with impeller power draw within the range investigated, i.e. the regions with higher shear retain their spatial position. This was also observed in (U), (B) and (S) configuration. High levels of $\langle S_{xy} \rangle$, regardless of polarity, was found to be distributed quite evenly throughout the whole vessel, with only a small area of weak $\langle S_{xy} \rangle$ at above $y/H > 0.8$ y/H and $-0.5 > r/R > -1.0$. This supports the earlier findings that vessels with (E) configuration significantly accelerate the reduction of segregation areas.

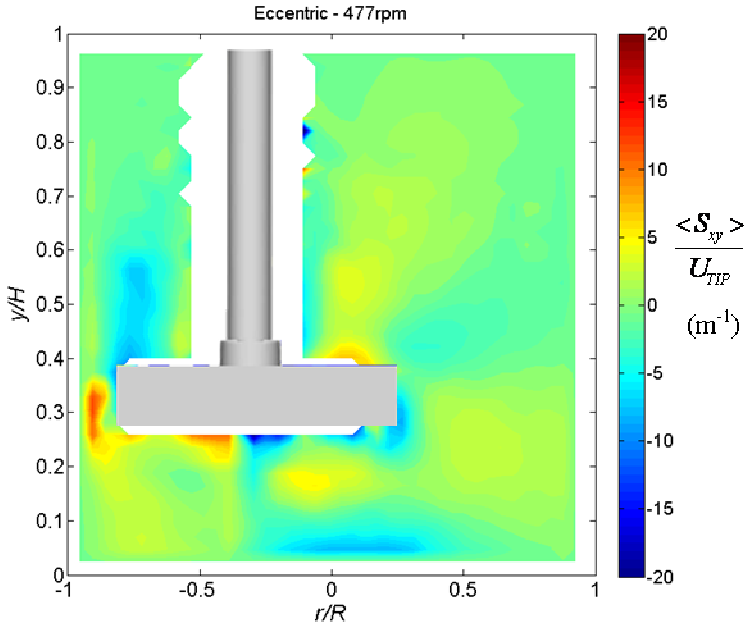

(a)

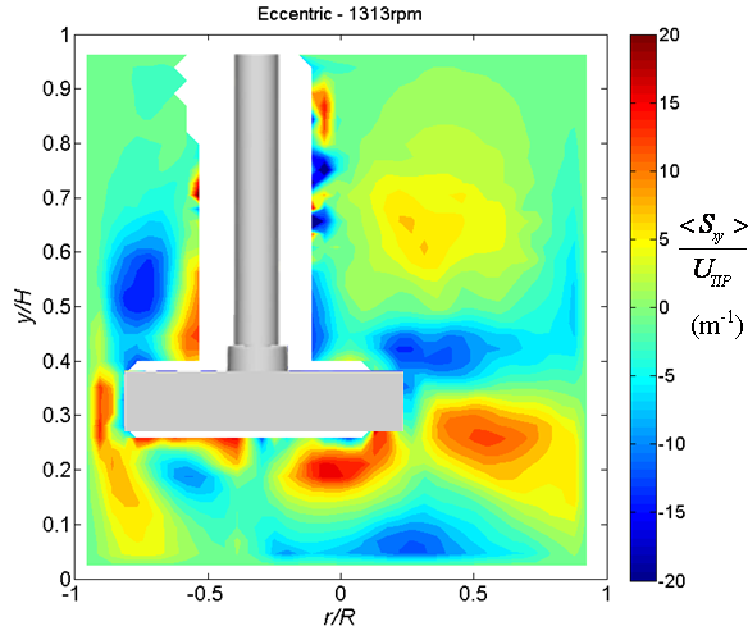

(b)

Figure 7.16 Normalised Rate of strain contour for (E) configuration in PPG2000 with a) *P/V* = 0.611 kWm^{-3} and b) *P/V* = 5.5 kWm^{-3}.

The ROS distribution map in (E) using PPG2700 as working fluid with *P/V* = 5.5 kWm^{-3} is shown in Figure 7.17.

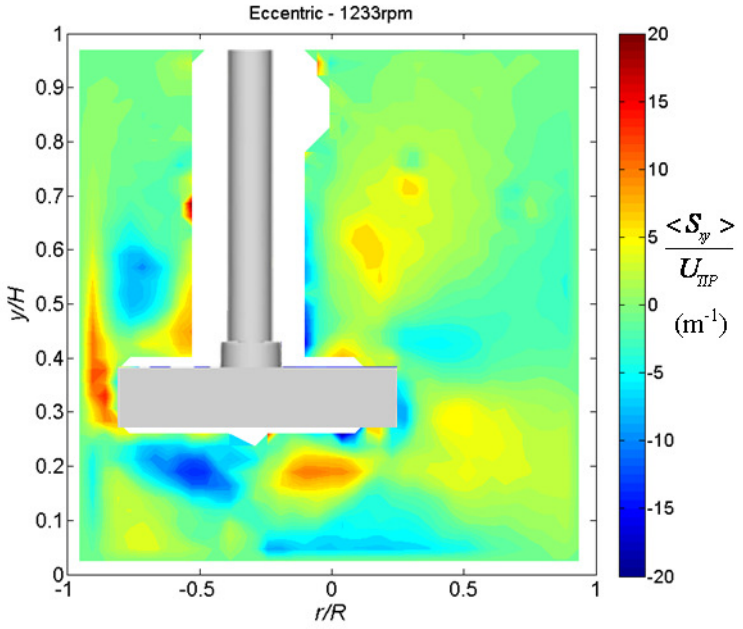

Figure 7.17 Normalised Rate of strain contour for (E) configuration in PPG2700 with *P/V* = 5.5 kWm^{-3}.

With roughly half of the *Re* than the PPG2000 case in Figure 7.16(b), the level of ROS reduced by half in most of the area with high ROS, except the region underneath the left side of impeller. In terms of the spatial location of high ROS regions, again there is no observable change.

For the (B) configuration shown in Figure 7.18**Error! Reference source not found.**, the rate of strain presented is very low compared to the (E) configuration. This is because, as illustrated in Figure 7.4, the particular plane is situated right behind the baffle where the magnitude of axial-radial flow is affected and a conclusion cannot be drawn without the measurement in the tangential direction.

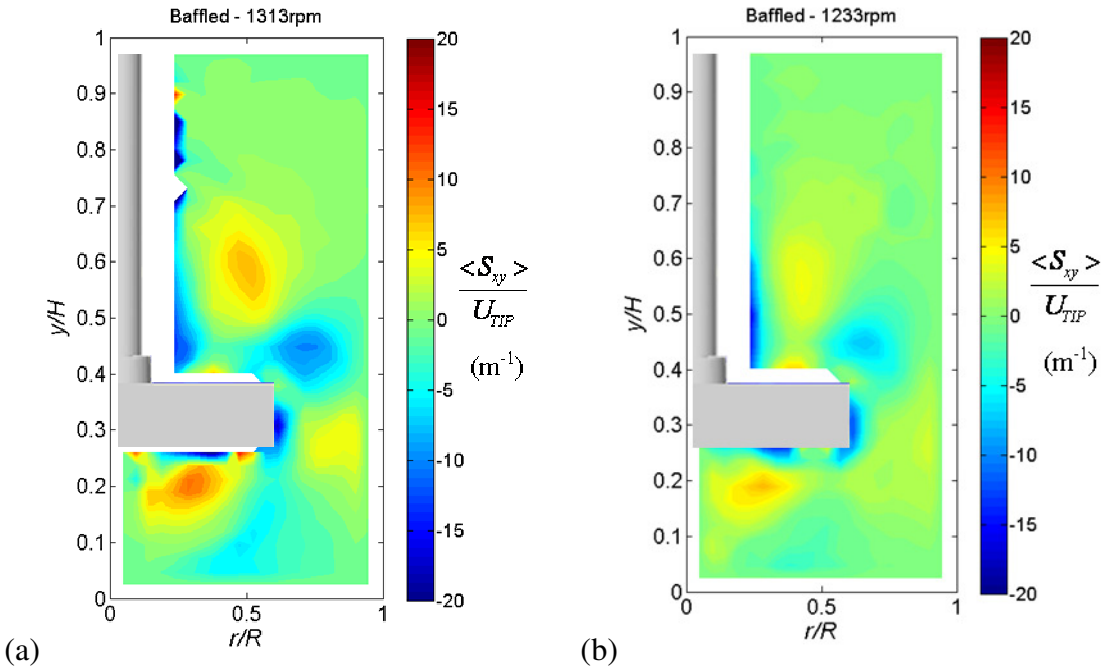

Figure 7.18 Normalised rate of strain contour for (B) configuration with *P/V* = 5.5 kWm^{-3}in (a) PPG2000 and (b) PPG2700.

Almost identical ROS profiles can be observed in (S) and (U) configurations for both PPG2000 and PPG2700 as displayed in Figure 7.19**Error! Reference source not found.**, with a higher magnitude of ROS in (S) because of a larger axial-radial velocity presented

as observed previously in Figure 7.7. The ROS in these two configurations are much higher than that seen in (B) and (E), partly contributed by a slightly higher *Re*.

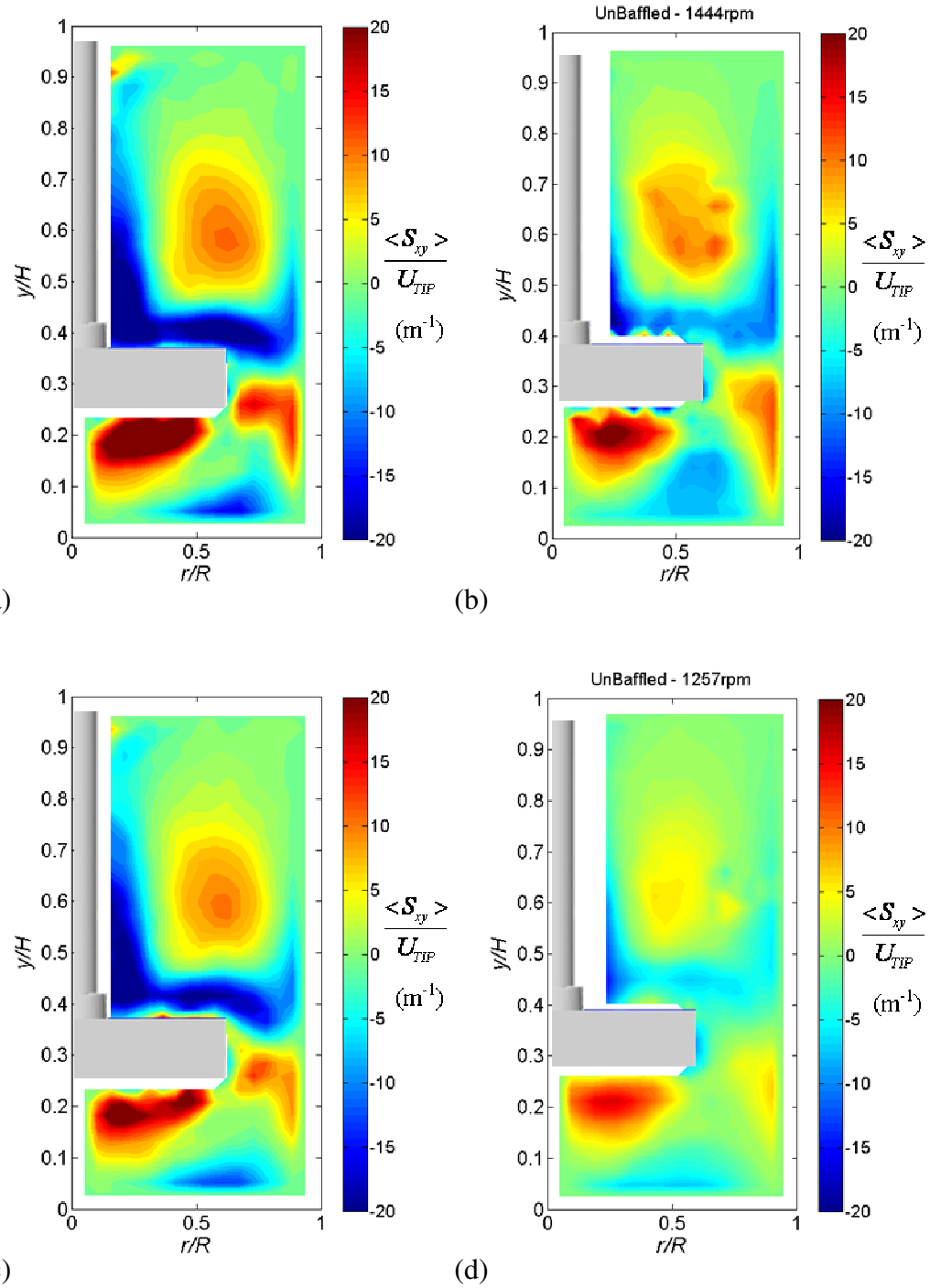

Figure 7.19 Normalised rate of strain contour for (a) (S) & (b) (U) configurations in PPG2000 and (a) (S) & (b) (U) configurations in PPG2700. All with *P/V* = 5.5 kWm^{-3}.

There are three high ROS regions, one with positive $\langle S_{xy} \rangle$ positioned at $0.3 < r/R < 0.9$ above $y/H > 0.5$ within the upper recirculation loop, which is surrounded by another high ROS region with an opposite polarity near the impeller shaft and vessel wall. There is also a region directly underneath the impeller. There is a visible gap between the two high ROS region above the impeller, which is comparatively low in ROS, observed in both configurations. Interestingly, if the PLIF image taken 10s after injection in (S) from Figure 7.13(a) is allowed to be overlapped with the ROS diagram, one will find that the dye injected outside the circulation loop was actually well mixed in the high ROS region outside such area. In order for the dye to extend into the circulation loops it has to cross a gap which is exceptionally low in ROS; this 'segregates' the circulation loops to the rest of vessel. A similar gap may be presented in (B) and (E) but unlike (S) and (U) the position of such gaps is not constant in the azimuthal direction; i.e., the baffles in (B) and the varying distance from impeller to wall changes in (E) with changing angular position of measurement plane are all mechanisms in demoting segregation. As a result, this permanent 'gap' may be responsible for the very low mixing efficiency in (S) and (U), despite the higher apparent axial-radial velocity and ROS.

7.6 CONCLUSIONS

The hydrodynamic and mixing behaviour in the HTE scale vessel were studied in the laminar regime. The use of Newtonian fluid, polypropylene glycol (PPG), eliminates the complication in rheological properties, as well as preventing the formation of caverns at low power inputs due to the absent of yield stress.

In terms of power curve profiles, all configurations except (U) exhibit a fairly constant decade with gradients of about -1; the power curve of (U) can be broken down into two

distinctive gradients of -1.2 and -0.75. It was established that the development of the upper circulation loop which at 200-300 rpm, moved into a position that affects impeller discharge from axial-radial to a completely radial direction which is responsible for the change in power curve gradient. A similar but much more subtle change in flow pattern observed in (S) renders the change in its power curve gradient unnoticeable.

Although (S) in the high power input range displays the highest axial-radial flow velocity among all configurations, its mixing performance studied by a modified PLIF technique was highly inferior compared to the (B) and (E) configurations. This is because as the viscosity of fluid increases, the effects of the four 90º corners are less pronounced, rendering the (S) a hydrodynamic profile only comparable to (U), which is demonstrated by the similarity in their 2-D global flow patterns. Rate of strain contours showed that whilst the shear gradient in the upper and lower circulation loops are high in (U) and (S), there is an obvious gap presented between such area and the rest of vessel; such gap prevents a swift mass transfer between regions in stirred vessel and hence it greatly hinders the mixing performance. Such gap may not be considered as an obstacle in (B) and (E) as the positions of such gaps are not constant in the azimuthal direction.

Therefore, although HTE units with (S) configuration produced a comparable mixing performance to (E) in high transition to turbulent regimes whilst being more compact, they are not recommended to be used in low *Re* or laminar mixing conditions.

8. PHASE VELOCITY MEASUREMENTS IN GAS/LIQUID SYSTEM

Several of the reactions considered at the HTE scale involve multiphase systems, in particular gas-liquid reactions; for example, the hydrogenation of oil and oxidation reactions. However, the understanding of the hydrodynamics of gas-liquid mixing in mechanically agitated vessels has long been hampered by the lack of information on the local properties of the two-phase flow involved. The local phase velocity is one such parameter that is fundamental to a complete description of any two-phase flow, and has been particularly elusive in complex three-dimensional flows such as those encountered in mechanically agitated reactors. There is little work in the open literature, however, that provides a whole-field quantitative analysis of both gas and liquid motion inside a gas-liquid stirred vessel, even though qualitative descriptions of the gas flow patterns have been available for a long time (Nienow *et al.,* 1977).

Recently, Hall *et al.* (2005b) used two-dimensional Particle Image Velocimetry (PIV) to determine the local liquid phase velocities within an eccentrically agitated gas-liquid HTE vessel. The local gas phase velocities, however, were not measured. Montante *et al.,* (2007) and Horn *et al.*, (2007) measured gas and liquid phase velocities simultaneously in a laboratory scale vessel (T = 0.236 m) at a low gassing rate of 0.02 vvm by using two side by side PIV cameras, each imaging one of the two phases. As discussed in Chapter 2, the technique has two main drawbacks:

- Inability to distinguish between gas bubbles inside the laser plane which are the ones that are supposed to be tracked, and bubbles out of the laser plane which should be rejected. This results in over/underestimation of velocity vectors.
- Inability to measure G/L vessels with higher gas flow rates, Q_G, of more than 0.02 vvm (ϕ = 0.0165). The higher bubble density restricts visualisation of the two-phase flow to the region near the wall as it becomes increasingly more difficult to focus on inner planes.

In this Chapter, a novel method is described which enables the in-plane bubbles to be clearly differentiated from out-of-plane bubbles, by addition of Rhodamine 6G dye to the liquid. An image analysis algorithm based on greyscale values has been developed, which enables the differentiation of these bubbles to be made and their velocities to be determined. Thus, time-averaged whole-field 2D velocity plots for the gas phase are obtained. At the same time, the technique allows the local bubble size distribution to be estimated from the processed images. The time-averaged 2D velocity fields for the liquid phase are determined using normal 2D PIV, i.e. by following the movement of neutrally-buoyant fluorescent seeding particles.

8.1 POWER DRAW MEASUREMENTS

Power draw measurements were carried out as per described in previous Section on the standard configuration at $C = 0.33T$, in order to validate the whole field gas velocity map with their corresponding bubble flow region. Measurement for the two gas flow rates, 0.5 & 1.0 vvm are compared against the ungassed condition. Power number, *Po* versus Reynolds number, *Re*, is plotted in the log-log scale and shown in Figure 8.1.

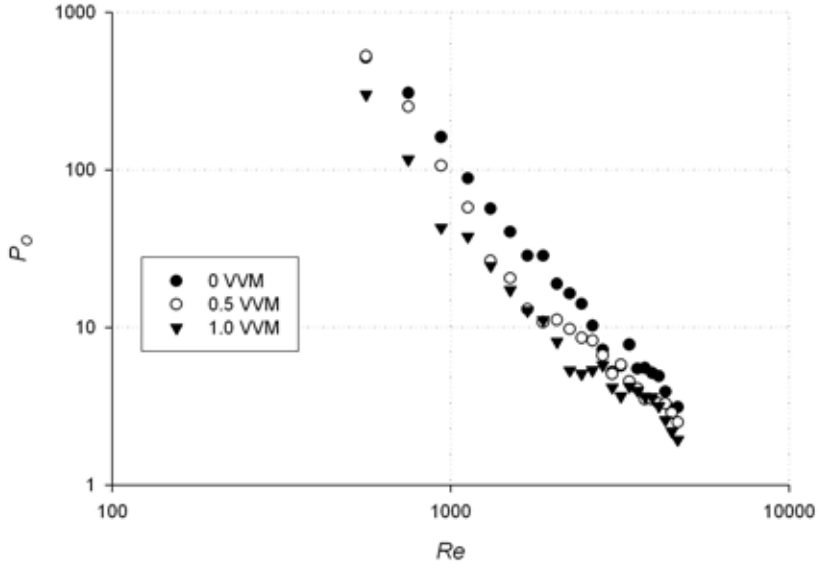

Figure 8.1 *Po* versus *Re* for the standard configuration.

A constant slope is observed for all three gas flow rates, which signifies that the flow is in the laminar/transition flow regime as described by Edwards *et al.* (1992). Whilst the *Po* of the ungassed vessel is the highest throughout the range of *Re* investigated, only a marginal difference is seen between the two Q_G of 0.5 and 1.0 vvm in the majority part of transitional flow regime. There is an obvious drop in *Po* in the Q_G = 1.0 vvm case at *Re* = 3000, indicates the changeover from lower to the higher transitional flow regime. Similar but much milder drop in *Po* is also observed at *Re* = 2000 in the Q_G = 0.5 vvm case but not observed in ungassed vessels. Due to the small sized impeller where *D* = 0.015m (*D* = 0.33 *T*), fully turbulent flow ($Re \geq 10^4$) can only occur when N ≥ 2700 rpm and this is well beyond the capability of the motor used in this work.

According to Nienow *et al* (1977), regime of bubble flow can be foreseen from the power curve which is the ratio of gassed/ungassed power P_G/P against gas flow number, Fl_G. Fl_G is determined from

$$Fl_G = \frac{Q_G}{ND^3} \qquad (8.1)$$

The power curve for Q_G = 0.5 and 1.0 vvm is plotted in log-log scale in Figure 8.2. The data is presented with a high level of fluctuation, especially in the regions with the lower rpm in the 1.0 vvm case. As described in literature where N_{CD} occurs at the lowest P_G/P; this corresponded to N = 450rpm in both gas flow rates (Fl_G = 0.023 & 0.047 for 0.5 and 1.0 vvm cases respectively).

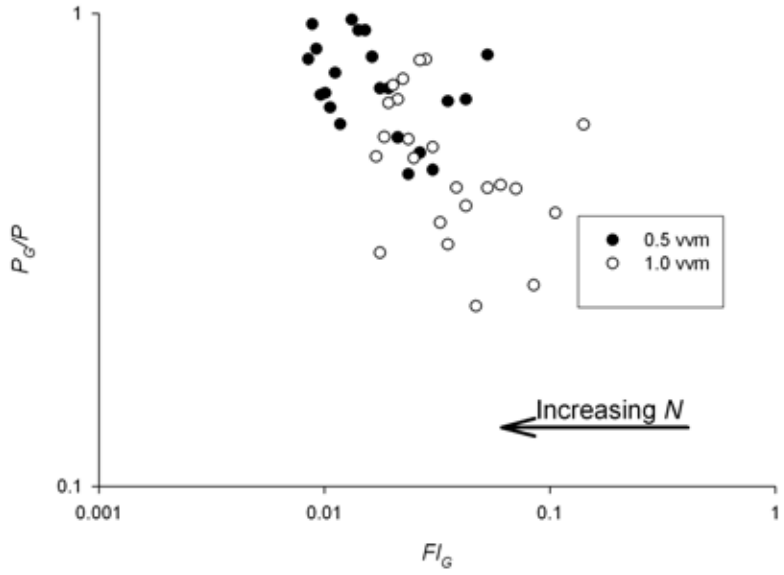

Figure 8.2 Power curve for the standard configuration at Q_G = 0.5 & 1.0 vvm.

However, a clear flooding regime is observed in both cases via the use of high speed camera at N = 450 rpm, which suggested that the lowest P_G/P points from Figure 8.2 does not correspond to N_{CD}; they are merely points along the right hand side of the power curve around N_F. Out of scale in this power curve, N_{CD} is predicted to be at least 1250 and it will be impossible to achieve with the motor used in this work.

8.2 IMAGE ANALYSIS ALGORITHM

The major drawback of the gas phase measurement method proposed by Montante *et al.* (2007) is illustrated in Figure 8.3(a). In the stirred tank (T = 45 mm) used in this study, out-of-plane bubbles exacerbated by reflected light from the in-plane bubbles incident onto

them, making the two groups of bubbles indistinguishable. A more detailed illustration is shown in Figure 8.3(b). Hence measurement included flow information of all the out-of-plane bubbles, which contain a high level of tangential flow, leading to substantial error.

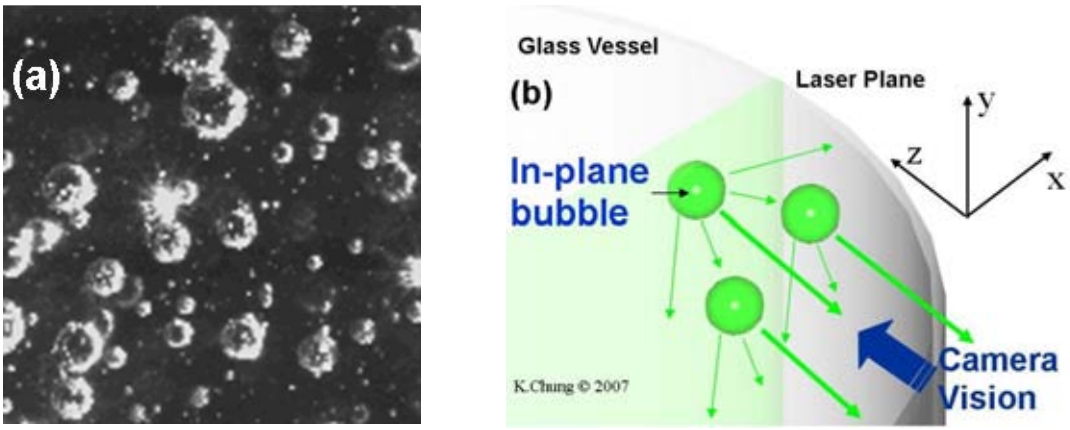

Figure 8.3 (a) Images of bubbles visualised in water without the presence of fluorescent seeding particle nor the use of 545nm optical filter and (b) 3-D graphical illustration.

A method is developed which overcomes this problem and enables the measurement of only in-plane bubbles. Whilst the same PIV setup described above was employed to visualise the size, shape and movement of the in-plane gas bubbles, the usual fluorescent latex tracer particles were not used; instead fluorescent Rhodamine 6G was used to dye the liquid at a concentration of 1×10^{-4} kg m^{-3}. At this concentration the liquid phase in the measurement plane emits fluorescent light and is clearly distinguishable from the gas phase. The intensity of the light is at its highest at a gas-liquid interface, which provides a sharp contrast between liquid and air and, thus, clearly defines the boundary of a gas bubble. Hence the in-plane bubbles can be easily identified as they are surrounded by a 'halo' due to the fluorescence from the liquid phase as shown in Figure 8.4(a). The biggest attribute of this method is that there is a significant difference between the excitation and emitted wavelength of the Rhodamine 6G dye (λ_{ex} = 524 nm and λ_{em} > 555 nm), therefore in theory the light emitted from the in-plane bubbles does not excite the out-of-plane bubbles; the two types of bubbles can now be differentiated as shown in Figure 8.4(b). It may be worth to note that part of the incident laser light can still be reflected from the in-

plane bubbles, causing weakened excitation at the surface of out-of plane bubbles that contribute to noises in the captured image.

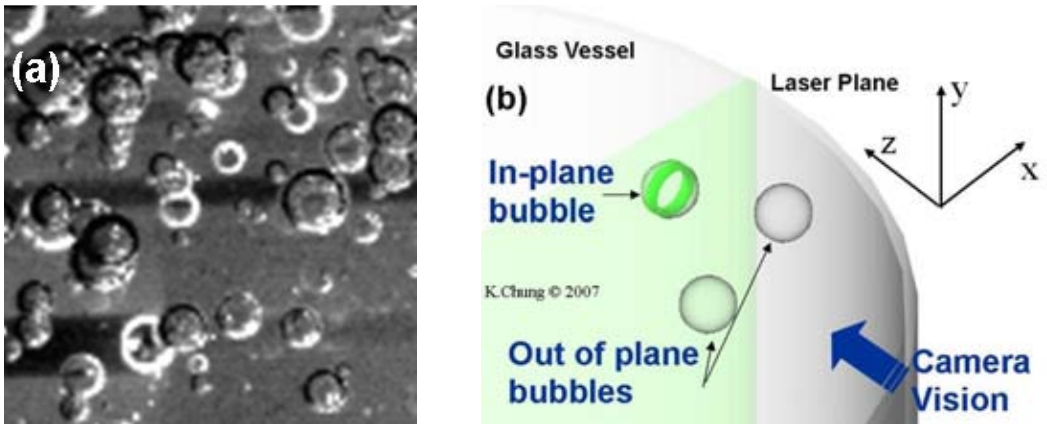

Figure 8.4 (a) Images of bubbles visualised in water dyed with Rhodamine 6G: the use of Rhodamine 6G helps distinguish clearly between the brighter in-plane bubbles surrounded by a halo, and out-of-plane bubbles and (b) 3-D graphical illustration.

Since the Rhodamine dye used to highlight the bubbles and the fluorescent tracers used to track the liquid, both emit light at the same wavelength (λ_{em} = 602 nm), it was not possible to perform both gas and liquid velocity measurements simultaneously, although this is in principle feasible if two cameras are employed and a dye or fluorescent tracers with a different emission wavelength are used. Due to the relatively low number of good quality bubbles detected per image pair, as discussed below, the total number of image pairs acquired per experiment was increased tenfold compared to that used in the liquid measurements, i.e. 5000 frames were used. The size of the IA was also increased by 16 times compared to the liquid measurements, i.e. to 64×64 pixel^2, which was the smallest resolution possible to accommodate bubbles of all observed sizes in the HTE vessel. Obviously, a grid of 64×64 pixel^2 had then to be used to match the local liquid velocity data to that of the gas phase to construct the whole two-phase flow field.

The captured raw images of the gas-phase were processed with a set of image analysis routines developed in house, constituting the new algorithm, prior to use of the standard PIV INSIGHT

6 software to determine the local velocities. A flowchart summarising the major steps followed in the analysis algorithm is shown in Figure 8.5. The algorithm concerned was written using MATLAB® Release 2006b equipped with the image analysis toolbox (Mathworks Inc, USA).

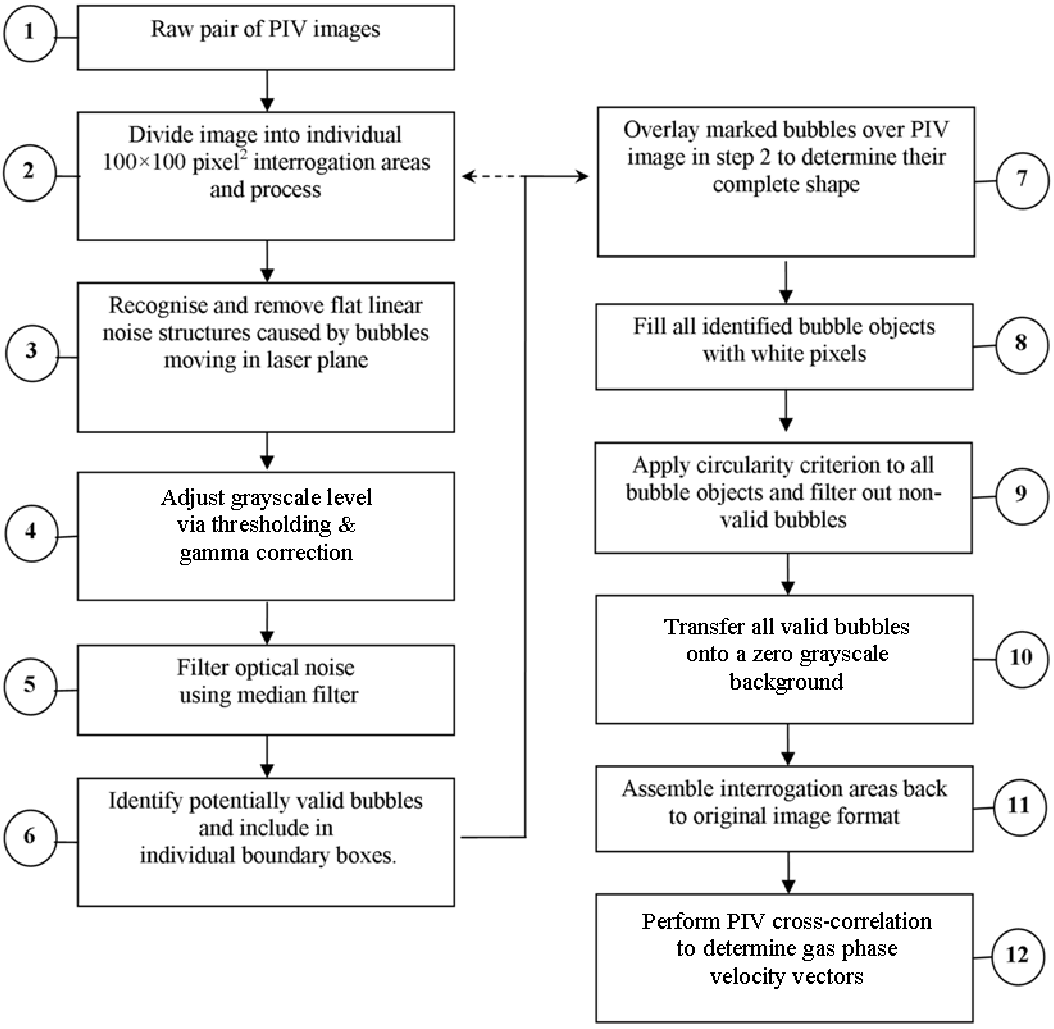

Figure 8.5 Flowchart of gas-phase image analysis algorithm.

8.2.1. IN-PLANE / OUT-OF-PLANE BUBBLE DIFFERENTIATION

Detection of a bubble relies on the contrast in greyscale between the bubble interface and the background liquid. Thus, the analysis process was based on recognising the localised variation in greyscale, but a uniform background is rarely achieved due to noise arising from various

sources. To minimize the effect of noise, bubble detection was performed using local background information by dividing the raw images into small 100×100 pixel^2 interrogation areas with 50% overlap. Figure 8.6 illustrates four overlapping interrogation areas and a single gas bubble which assumed to be less than 50 pixels in diameter (from observation of raw images, the diameter of these bubbles do not exceed 15 pixel). Overlapping ensured that the whole gas bubble will always be contained within at least one interrogation area.

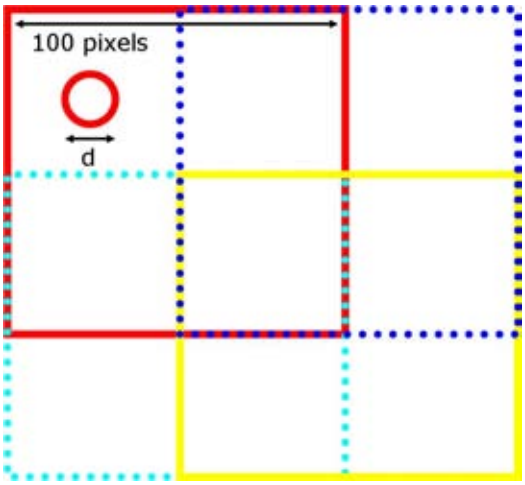

Figure 8.6 Illustration of overlapped interrogation area and a single gas bubble.

A raw image of gas bubbles as obtained from the PIV is shown in Figure 8.7.

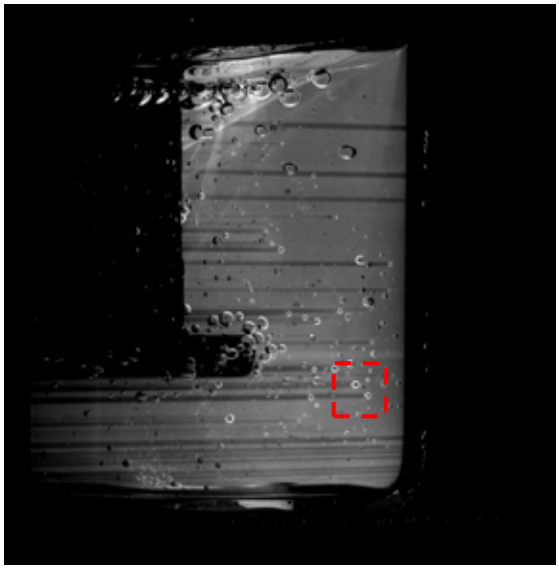

Figure 8.7 Raw image captured, showing an eccentric aerated vessel with 6-PBTu at C/T = 0.33, Q_G = 0.5 vvm & P_G/V = 168 Wm^{-3}. Highlighted square indicates the area chosen for algorithm demonstration.

Gas bubbles moving in the plane of measurement generate another optical problem as they tend to obstruct the incident laser light, thus creating horizontal dark strips, this often presents problems in PIV imaging (Bröder & Sommerfeld, 2002). A typical raw image of gas bubbles obtained from PIV which illustrates this effect is shown in Figure 8.8.

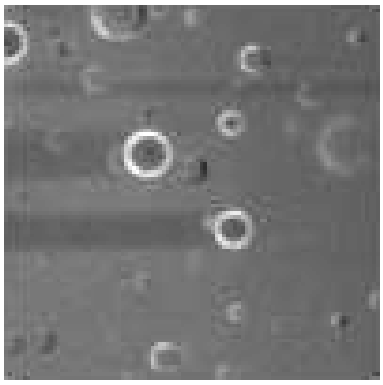

Figure 8.8 Sample interrogation area (100 × 100 pixel^2) extracted from the PIV image.

Although such obstructions do not affect the illumination of subsequent bubbles along the laser path, the dark strips represent an inconsistency in the background greyscale levels which downgrade the quality of bubble recognition. These dark strips were removed by Morphological Structure Reduction. Flat linear structuring elements were recognized as shown in Figure 8.9.

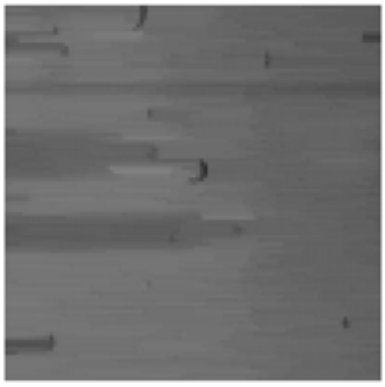

Figure 8.9 Horizontal noise structure recognised.

In this case, the predefined characteristics of these elements included 1 degree of elevation to match the elevation of laser source, and an arbitrary length of no less than 30 pixels which was the assumed maximum bubble diameter, based on preliminary visualisation diagnostics. The background greyscale is thus interpreted by the analysis algorithm as large unbroken horizontal elements which are then eliminated. Therefore, applying image subtraction Figure 8.8 is reduced to Figure 8.10.

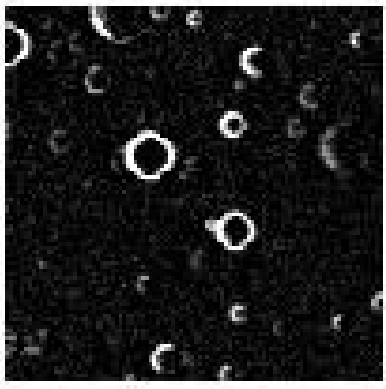

Figure 8.10 Morphological structure reduced image.

The image in Figure 8.10 now shows only the in and out-of-plane bubbles, recognizable by the difference in greyscale level around their edges. This small difference in greyscale may be magnified with a combination of thresholding and gamma correction. To understand the concept of this procedure it is necessary to refer to the image histogram displayed in Figure 8.11, showing the pixel count of each greyscale level from the image in Figure 8.10. Three zones are defined, where zone 1 and 2 represent the darker background and noises with out-of-plane bubbles respectively. Pixels that have a greyscale in the region of 170-255 correspond to signals from in-plane-bubbles, hence they should be preserved. A threshold greyscale, in this case, is set at 170 and any pixel in the interrogation area falls below the threshold is reset to 0, effectively converting the majority

of the out-of-plane bubbles and noise to background and they are eliminated from the image.

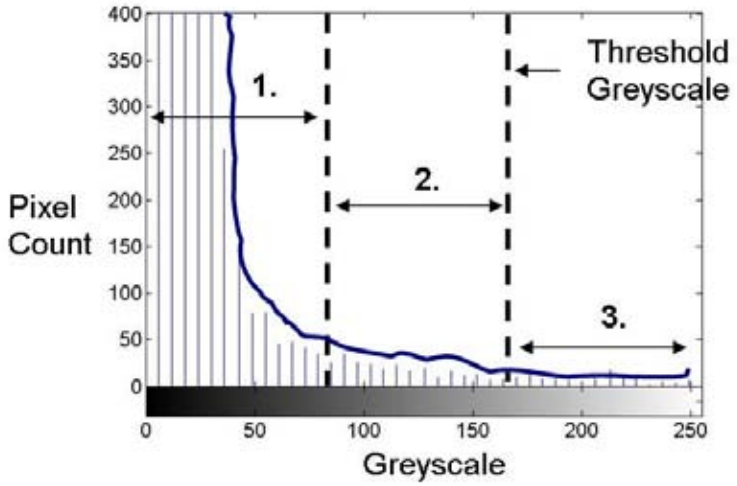

Figure 8.11 Image histogram of Figure 8.10.

However, it is practically impossible to automatically detect the cut off point for threshold greyscale level; there is a chance that signals from some in-plane-bubbles yield a lower than average greyscale of other in-plane-bubbles. Therefore the threshold is deliberately set to a lower level which also means the inclusion of some out-of-plane bubbles; this inevitably leads to inaccuracy. Gamma adjustment can remap the greyscale profile and enhance the greyscale difference between the two types of bubbles, making them more distinguishable. The effect of gamma adjustment on pixels greyscale is illustrated in Figure 8.12. For $\gamma = 1$, a linear profile is produced hence the input/output greyscale is kept at the same ratio. However, if γ is set to more than 1, mapping is weighed towards the lower output values, hence the greyscale level where both types of bubbles exist (i.e. 170-200) is magnified into a much broader region (i.e. 0-150). The resulting greyscale map features a clearer cut off point for further thresholding to be carried out automatically.

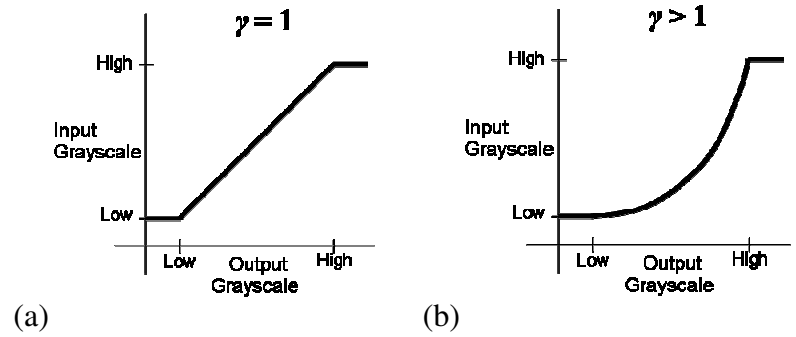

(a) (b)

Figure 8.12 The effect of gamma adjustment on pixel greyscale showing (a) $\gamma = 1$ and (b) $\gamma > 1$

This small difference in greyscale may be magnified with a combination of thresholding and gamma correction, as shown in Figure 8.13. The greyscale level from the majority of the out-of-plane bubbles, along with most of the remaining noise, is only marginally lower than the optimised threshold level and can, thus, be eliminated. Gamma correction is then applied to enhance the contrast between in-plane bubbles and any outstanding noise which results in Figure 8.13.

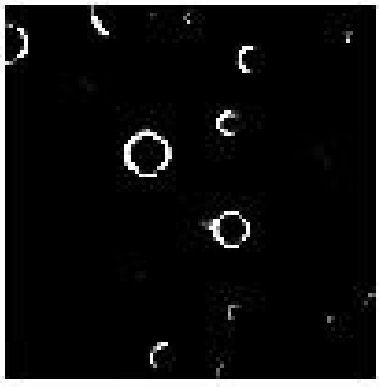

Figure 8.13 Image after thresholding and gamma adjustment.

Noticeably there are some half circles remained that resemble the shape of a crescent. These are from a few possible sources:

1. There are many layers of out-of-plane bubbles between the laser plane and CCD camera, depending on the bubble density in stirred vessel, there is a great chance

that a percentage of in-plane bubbles are partially obstructed by out-of-plane bubbles.

2. Extraneous laser light (λ = 532nm) is reflected from the in-plane bubble surface onto the out-of-plane bubble/liquid interface, exciting the fluorescent tracer in the process, hence fluorescent light is also emitted from the half of out-of-plane bubbles that is being illuminated. In-plane bubbles however, always appear as a full circle because the whole edge of bubble is directly exposed to the incident laser light.

8.2.2. NOISE FILTERING

In some cases, a high level of noise in the form of small grey and black spots referred to as 'salt and pepper' noise may still remain and its removal is essential; this will require an adequate filter. Ordinary smoothing filters which work on the principle of averaging neighboring pixels, will impose a blurring effect on the image, making the in-plane bubbles less distinguishable. The common 'erode & dilate' method which is very effective at filtering a lone peak in an area will, in some cases, cause degradation on the edges of in-plane bubbles, and hence it is also unsuitable (Russ, 2002). Consequently, the median filter was chosen as the most suitable due to its ability to filter out 'salt and pepper' noise whilst preserving the edges, as shown in Figure 8.14.

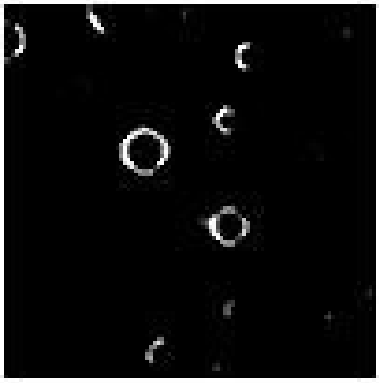

Figure 8.14 Image filtered by median filter.

This filter detects a lone peak value and replaces it with the median value of predefined neighboring pixels, in this case, the 4 nearest-neighbors above and below, and to the left and right of the peak. It is possible to use all of the 8 surrounding pixels in severe noisey cases, but at a significant additional computational cost. It should be noted that the median filter can be repeatedly applied if necessary with only a minor loss in image quality. It is also important to point out that in-plane bubbles below a certain length scale, 5 pixels in diameter in this case, may also be filtered out during the process. This would correspond to small bubbles below approximately 170 μm in diameter, thus introducing a small error in the measured bubble size distribution as well as the mean local gas velocity. With the out-of-plane bubbles and noise filtered out, the pixels remaining in the image represent the edges of in-plane bubbles, as shown in Figure 8.15.

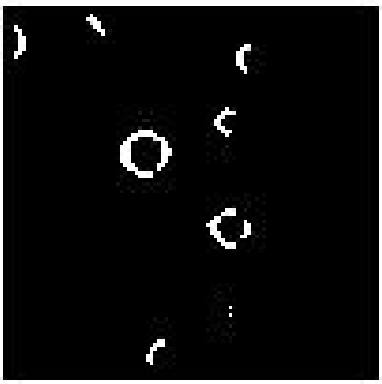

Figure 8.15 Traces of in-plane bubbles after greyscale differentiation.

8.2.3. IN-PLANE BUBBLE EXTRACTION

Having gone through the rigorous greyscale adjustment, described above, a bubble may lose certain parts of its edge and the resulting trace is, consequently, not a full bubble as illustrated in Figure 8.16(a).

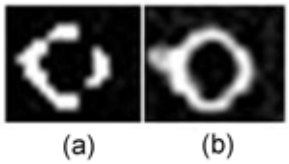

Figure 8.16 (a) Part of bubble that remains after image analysis; (b) the entire bubble perimeter after comparison with Figure 8.10.

However, for accurate edge detection of the in-plane bubbles, the full outer edge of each bubble is required. If the diameter of the bubble can be determined, i.e. if more than 180 degrees of continuous edge is preserved, a coarse estimation of the perimeter of the whole circle can be made using Hough circle analysis (Kimme *et al.,* 1975) as shown in Figure 8.17 (a). Assuming perfect bubble circularity, approximate diameter, d, is determined from the distance between the two furthermost points. A dummy circle is centred with this approximate diameter at every pixel with positive reading '1', which denotes the edge of in-plane bubbles. The centre of the bubble can be located at the pixel with the largest accumulative count of dummy circle occupation, as shown in Figure 8.17 (b). The partial edge of in-plane bubble that was missing previously can be completed with the approximation of bubble centre and estimated diameter.

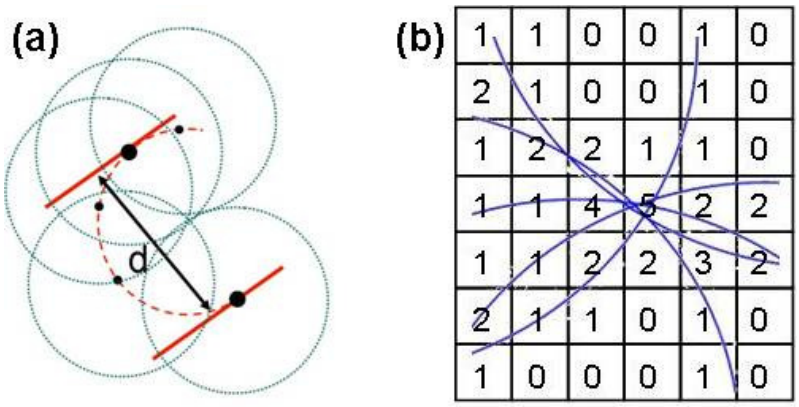

Figure 8.17 (a) Application of Hough circle analysis and (b) bubble centre located at pixel with the most dummy circle occupation (5 in this illustration).

A boundary box is drawn around the edge of this imaginary bubble, which serves as a mini interrogation area containing a signal from a filtered in-plane bubble. The boundary box is then transferred back to its corresponding position on the original image before undergoing greyscale differentiation, i.e. the image in Figure 8.10. Overlaying the two images in this way allows the entire perimeter of the bubble to be determined, as shown in Figure 8.16(b).

Following full determination of all the valid in-plane bubbles, void filling is employed to fill the bubble areas with white pixels. The algorithm will only fill voids with a complete boundary; hence it is necessary to first reconstruct the entire bubble perimeters (Figure 8.18).

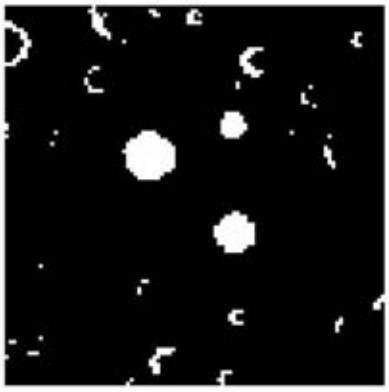

Figure 8.18 Filling the voids within the in-plane bubbles.

The next step is to carry out a circularity test on all the objects identified on the image, where circularity, ϕ, is defined as (Clift *et al.,* 2005)

$$\phi = d_A / d_p \tag{8.2}$$

where d_A and d_p are, respectively, the equivalent diameter of the gas bubble obtained from its area and perimeter, estimated from an image analysis routine imbedded in the algorithm. It should be noted that at this scale (mean bubble size ~ 0.5 mm), gas bubbles in the stirred vessel are almost spherical and their projections, therefore, should be almost circular. Thus, ϕ has to be close to unity for the bubble to be accepted, i.e. $\phi = 1.0 \pm 0.1$ (Figure 8.19).

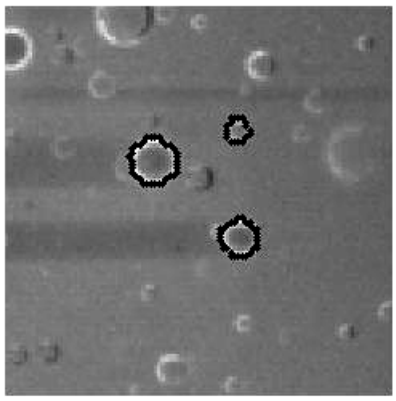

Figure 8.19 Comparing area occupied by in-plane bubbles with original image.

Some in-plane bubbles cannot be reconstructed because they are partially obscured by other out of plane bubbles in the original PIV image (Figure 8.8) and they appear in the form of crescents. Such incomplete bubbles which are also filled with white pixels, are all filtered out by the circularity test. Once all the circular bubbles have been identified, they are transferred onto a zero greyscale (i.e. black) background, as shown in Figure 8.20. Thus, the characteristic greyscale of each individual bubble is retained, and the peaks generated by the Fast Fourier Transforms (FFT) during the cross-correlation of each

individual bubble between the pair of PIV images in the same frame will therefore match each other, thus minimising the likelihood of error.

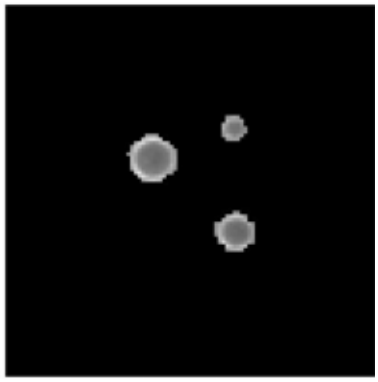

Figure 8.20 original in-plane bubbles pasted into a zero greyscale background for subsequent FFT analysis.

Once all the 100×100 pixel^2 interrogation areas have been analysed, as described above, they are assembled back together in the same original format to reveal the final processed pair of PIV images. Normal PIV cross-correlation is then carried out using the standard INSIGHT software to generate the local gas phase velocity vectors. At significant gas holdups (in this case, $\phi \sim 3\%$) the bubble density is relatively high and the number of successful bubble detections per frame achieved by the above procedure is reduced. This in turn reduces the number of velocity vectors obtained per frame and the quality of cross-correlation in each interrogation area should, therefore, no longer be based upon global statistics. It is, thus, advisable to disable the step in the validation process which is based on vector standard deviation built into the INSIGHT software, in order to minimize the accidental deletion of good vectors.

8.3 VALIDATION

8.3.1. EULERIAN APPROACH

As described earlier, there is a lack of available literature for estimating the behaviour and movement of the gas phase in aerated HTE vessels. Therefore, quantitative validation with existing data is problematic. However, if the agitator is switched off and removed, the bubbles would be expected to rise at their terminal velocity, for which experimental data exists (Clift *et al.,* 2005). The approximate size of individual free rising bubbles in the vessel ranges from 0.3 - 2.6 mm in diameter as measured from the raw images; from Clift *et al.* (2005), U_T will range from 0.03 - 0.33 ms^{-1}.

A typical processed image of bubbles rising in stagnant water is shown in Figure 8.21. Cross correlation of 1000 of these image pairs using the PIV software yields the average vector map for the rising bubbles as shown in Figure 8.22. It is important to note that the use of cross correlation yields the average velocity at given co-ordinates from an ensemble of bubbles (an Eulerian approach); the velocity of individual bubbles is not measured since this would require a different algorithm which includes Lagrangian tracking.

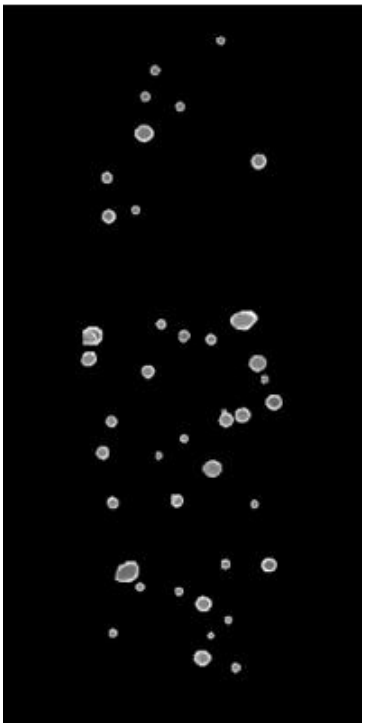

Figure 8.21 Processed image of bubbles rising through stagnant water used in verification experiment.

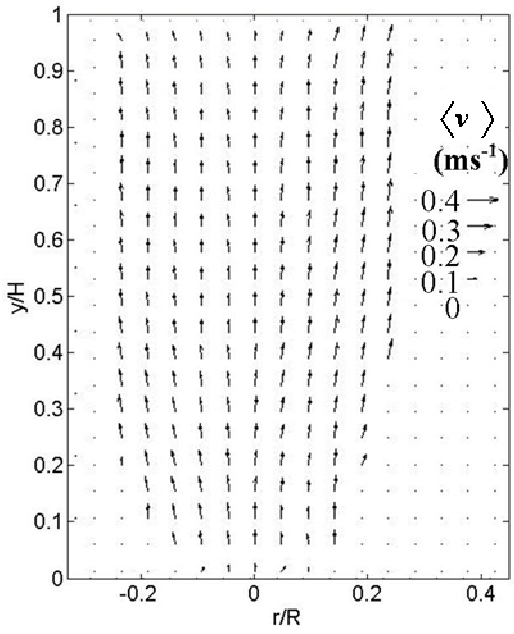

Figure 8.22 Time-averaged gas phase vector map of bubbles rising through stagnant water.

The maximum ensemble averaged velocity $\overline{\langle v \rangle}$ observed in the region *y/H* = 0.9-1.0 shown in Figure 8.22, where U_T is most likely to be achieved, is 0.316 ms^{-1}, whilst the minimum $\overline{\langle v \rangle}$ in the same region is 0.0354 ms^{-1}. This fitted reasonably well into the range described

by the literature. It should also be highlighted that it would be expected from the bubble shape/flow map presented by Clift *et al.* (2005) that free rising bubbles at their terminal velocity in this system will be ellipsoid if their diameter is larger than 1 mm. Visual observations reveal the existence of a few ellipsoidal bubbles, and this suggests that some larger bubbles are travelling close to their terminal velocity.

8.3.2. LAGRANGIAN APPROACH

Verification of the gas phase velocity measurement technique described above was performed by measuring the velocity of a single air bubble rising in water in a vertical glass column with a wide square-section (a Lagrangian approach). The vertical displacement of the bubble was tracked by PIV over three consecutive frames, as shown in Figure 8.23. The velocity results obtained by applying the new image analysis algorithm were then compared to the velocity inferred from manual estimation of the bubble displacement on the PIV images and the bubble travel time inferred from the frame rate. The experiment was repeated 10 times giving an agreement within ±5% between the two methods. Whilst the above test does not constitute a full validation of the new algorithm, it does confirm that large gas bubbles which cannot be clearly identified by normal PIV imaging, can now be traced and their movement can be accurately measured.

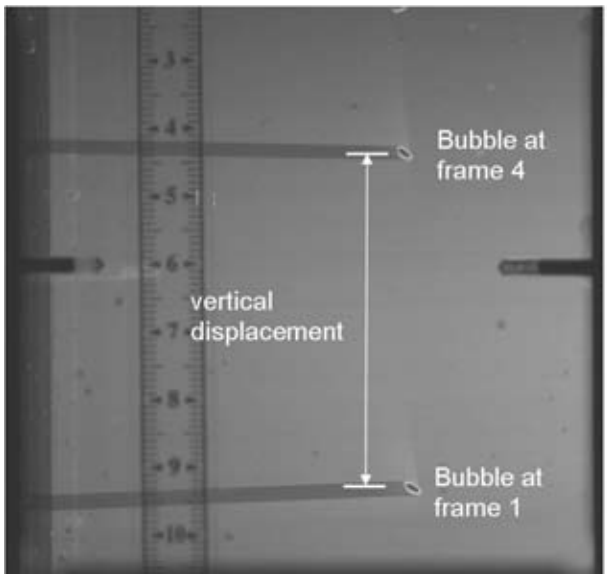

Figure 8.23 Overlapping of two images with three frames apart, showing a single bubble rising though a long glass column.

8.4 G/L PHASE VELOCITY MEASUREMENT ON STANDARD CONFIGURATION

8.4.1. GAS PHASE VELOCITY MEASUREMENTS

The mixing literature does not report actual local values of the dispersed gas phase velocity in a stirred vessel, except for the very limited recent data of Montante *et al*. (2007). The new bubble detection technique introduced here was successfully applied, for the first time, to the measurement of gas phase velocities in a mixing vessel. The gas flow field determined in the mechanically agitated HTE vessel described above is shown in Figure 8.24 for the two gas flowrates used, i.e. 0.5 vvm and 1.0 vvm. It is important to reiterate that this is a time-averaged measurement, obtained from 5000 individual image pairs, and made on gas bubbles of all sizes passing through the measurement grid. As it stands, the algorithm does not differentiate between velocities of different size bubbles at a given point within the flow.

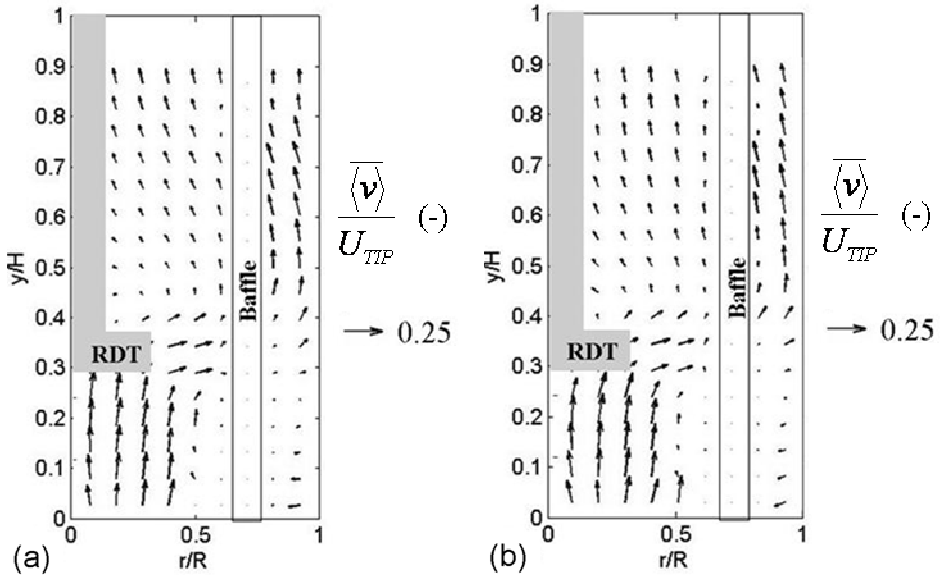

Figure 8.24 Time-averaged gas-phase velocity vector plots for $C = 0.33T$: (a) Q_G = 0.5 vvm, N = 950 rpm, ϕ = 0.032, P_G/V = 168 Wm^{-3}; (b) Q_G = 1.0 vvm, N = 980 rpm, ϕ = 0.054, P_G/V = 168 Wm^{-3}.

At Q_G = 0.5 vvm, gas is dispersed radially from the discharge of the turbine and moves slightly towards the impeller shaft as it rises towards the free surface, with minimal gas recirculation below the impeller. An image taken at 100 frames per second using a high speed camera shows the spatial distribution of the bubbles in Figure 8.25. The shutter speed was such that streaking of bubbles can be noted beneath the impeller and around the shaft region; bubbles have the highest velocities underneath the turbine (~ $0.20U_{TIP}$) and this is confirmed by the velocity vector plot in Figure 8.24 (a).

Figure 8.25 Captured from high speed camera (100fps) footage showing spatial distribution of bubbles at Q_G = 0.5 vvm: bubble streaking can be seen beneath the impeller and around the shaft where gas velocities are highest consistent with PIV measurements determined from new image processing algorithm.

A similar gas phase velocity vector map was obtained at the higher gas flowrate of 1.0 vvm and equal power dissipation per unit volume (Figure 8.24 (b)). Whereas at Q_G = 0.5 vvm there is a hint of a circulation loop beginning to develop above the impeller, at Q_G = 1.0 vvm the bubbles seem to be less affected by the radial flux imparted by the turbine, and rise to the surface with slightly greater velocities and along more or less straight trajectories. These flow conditions are above those of a flooded impeller but below those corresponding to complete gas dispersion where a well-established bubble recirculation loop above the impeller and one below it are expected. In normal circumstances, such a regime is to be avoided as the gas phase is not fully dispersed. In this case, the flow regime was dictated by the limited power capacity of the miniature HTE rig used. An empirical correlation was developed by Nienow *et al.* (1977) for the determination of

bubble flow regime in aerated stirred vessels; the flooding-loading transition speed, N_F, can be calculated from

$$\frac{Q_G}{N_F D^3} = 30\left(\frac{D}{T}\right)^{3.5}\left(\frac{N_F^2 D}{g}\right) \tag{8.3}$$

The speed for complete dispersion condition, N_{CD}, is determined from,

$$\frac{Q_G}{N_{CD} D^3} = 0.2\left(\frac{D}{T}\right)^{0.5}\left(\frac{N_{CD}^2 D}{g}\right)^{0.5} \tag{8.4}$$

The predictions from the correlations of that the flow regime lies between these two extremes with N_F = 350 rpm and N_{CD} = 3000 rpm, although it should be noted that these correlations may not be valid at the HTE scale. In addition, the above correlation was valid for a vessel with impeller clearance $C = 0.25T$ and ring sparger was used as the means of gas introduction. Thus, the much higher power dissipation and rotational speed requirements to work under conditions of full gas dispersion were not available at this scale. The application, however, was used purely to demonstrate the feasibility of the new phase velocity measurement technique.

8.4.2. EFFECT OF GASSING ON THE LIQUID PHASE FLOW FIELD

The velocity field of the liquid phase at Q_G = 0.5 vvm is presented in Figure 8.26 (a). It should be noted that the spatial resolution of liquid phase velocity plots has been greatly reduced to facilitate the comparison with the flow maps of gas phase velocities. This is very different from the gas phase flow field shown in Figure 8.24 (a). The liquid is pumped radially by the turbine with two identifiable circulation loops established below and above the impeller plane. The maximum liquid velocity observed under these conditions is ~ $0.20U_{TIP}$. In the bulk of the vessel above the impeller, the liquid velocities

in the downward part of the circulation loop are rather small; these are dampened by the rising gas. The liquid flow field under ungassed conditions but at the same power input is shown in Figure 8.26 (b) and can be compared with the liquid flow field in the presence of gassing shown in Figure 8.26 (a). The general radial flow pattern is the same under both conditions, the main difference being the considerably higher downward liquid velocities in the upper part of the vessel in the absence of gas.

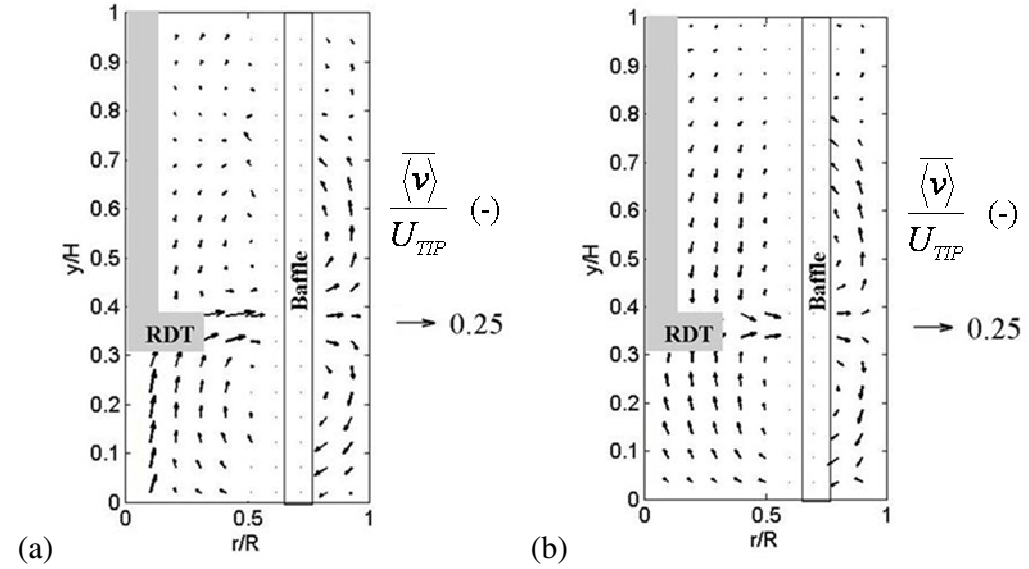

Figure 8.26 Time-averaged liquid-phase velocity vector plot under gassed conditions in (B) for C = 0.33T: (a) Q_G = 0.5 vvm, N = 950 rpm, ϕ = 0.032, P_G/V = 168 Wm^{-3} and (b) ungassed conditions Q_G = 0 vvm, N = 860 rpm, P/V = 168 Wm^{-3}.

8.4.3. THE EFFECT OF IMPELLER OFF-BOTTOM CLEARANCE ON GAS AND LIQUID FLOW

The ability to track the gas phase afforded by the technique developed here, should enable more detailed work to be done on complex gas-liquid flows such as in stirred vessels. As an example, the method was applied to explore the effects of changing impeller off-bottom clearance on the localised two-phase flow, which reveals some interesting effects at the HTE scale used. The results discussed above corresponded to C = 0.33T. The local gas and liquid phase velocity fields were further determined at C = 0.25T and 0.5T, and are

presented in Figure 8.27 and Figure 8.28, respectively. At C = 0.25T, there is a weak radial dispersion of the gas, which improves considerably as the impeller is raised to a height of 0.5T, even though full gas dispersion is not achieved under all three conditions of off-bottom clearance. Similarly, the liquid circulation pattern both above and below the impeller is much more clearly established at the higher impeller clearances.

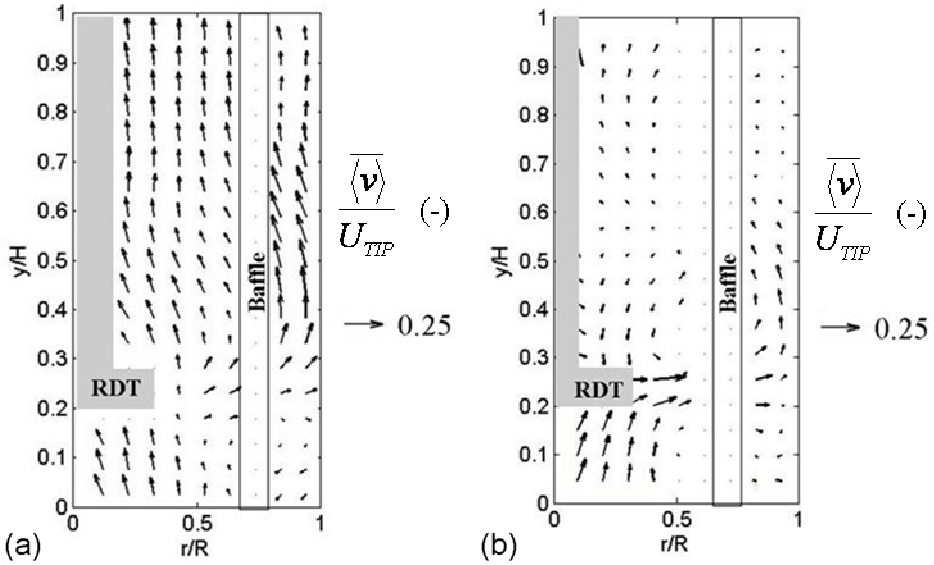

Figure 8.27 Time-averaged phase velocity vector plots in (B) for C =0.25T: Q_G = 0.5 vvm, N = 1100 rpm, ϕ = 0.032, P_G/V = 168 Wm^{-3}; (a) gas phase; (b) liquid phase.

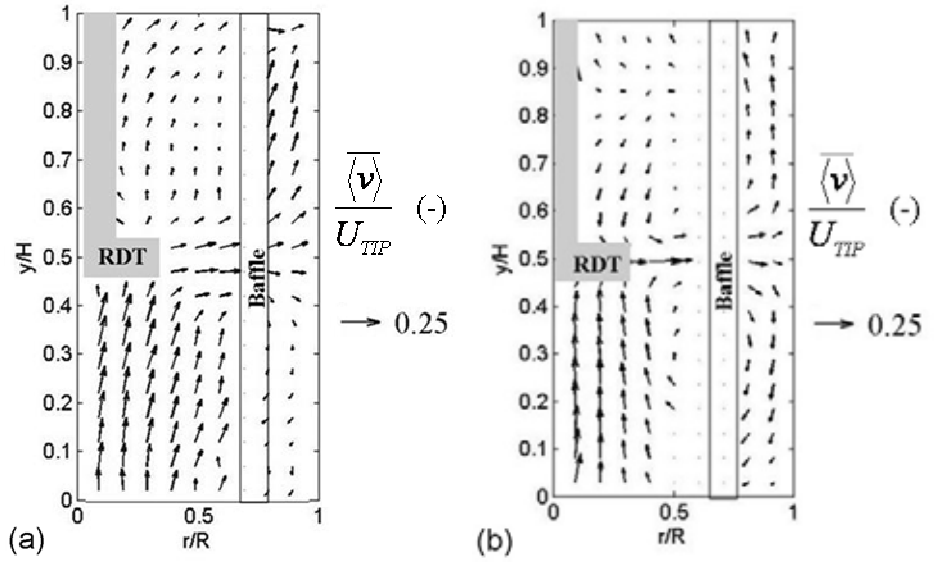

Figure 8.28 Time-averaged phase velocity vector plot in (B) for C = 0.5T: Q_G = 0.5 vvm, N = 950 rpm, ϕ = 0.035, P_G/V = 168 Wm^{-3}; (a) gas phase; (b) liquid phase.

8.4.4. BUBBLE SIZE DISTRIBUTION

The technique enables simultaneous measurement of the bubble size distribution once all the successful bubble detections have been analysed, as described above. The results corresponding to an impeller clearance of 0.33T and Q_G = 0.5 and 1.0 vvm are presented in Figure 8.29. The bubble size distributions shown were based on a large sample of ~ 5×10^4 bubbles successfully measured in the 45 degree plane between two baffles. The measured means were the number mean diameter, d_{10} = 0.5 mm, the Sauter mean diameter, and d_{32} = 0.7 mm for both cases of gas flow. The lack of difference in bubble size is due to the fact that the impeller was not operating under a full dispersion regime. As pointed out above, such a regime was dictated by the limited power capacity of the HTE rig used. It should also be noted, as pointed out above, that due to the tendency of the image analysis algorithm to remove small bubbles (< ~170 μm) as 'noise', there is a cut off point in Figure 8.29, at a diameter of about 200 μm, which introduces and element of bias in the measurements. Furthermore, It should be pointed out that the measurements obtained will probably tend to underestimate the bubble size as the laser plane may not cut bubbles through the central plane. However, given that the estimates in Fig. 17 seem to suggest that most of the bubbles are below 1 mm in diameter (the thickness of the laser sheet), the underestimation error is likely to be fairly small.

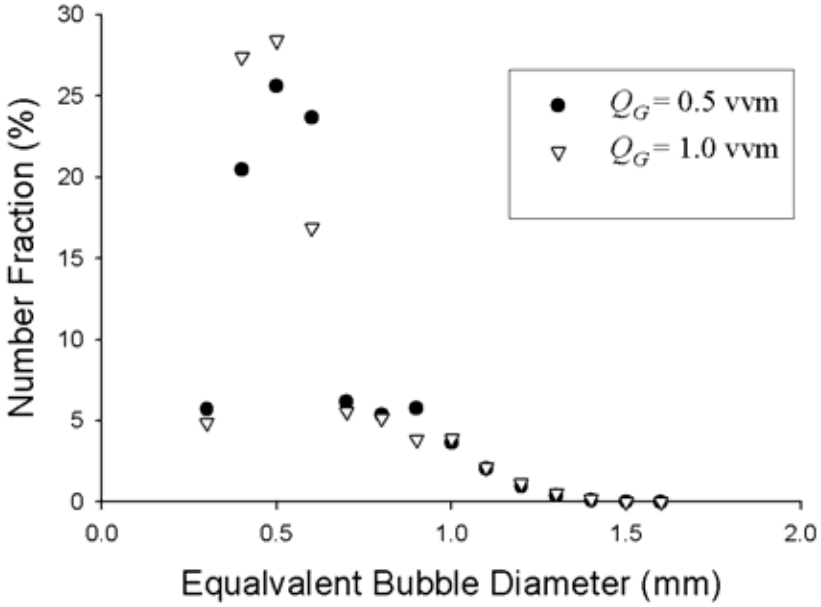

Figure 8.29 Probability Density Function of bubble sizes at *C* = 0.33 *T*.

8.5 G/L PHASE VELOCITY MEASUREMENT ON VESSELS WITH ECCENTRIC CONFIGURATION

8.5.1. G/L PHASE VELOCITY MEASUREMENTS

The gas flow field for the eccentric configuration (E) at gas flow rate of Q_G = 0.5 vvm agitated at the same power input as the standard (B) configurations above (P_G/V_L = 0.168 Wkg^{-3}) is shown in Figure 8.30. The results are dramatically different to the (B) configuration; gas near the bottom of the impeller has a significant radial velocity component. Above the impeller, the gas movement is predominantly upward but there is a greater flow component towards the shaft than for the (B) configuration. The gas flow is at its highest underneath the impeller where a jet of recirculating fluid travelling in the tangential direction is joined by the sparged gas.

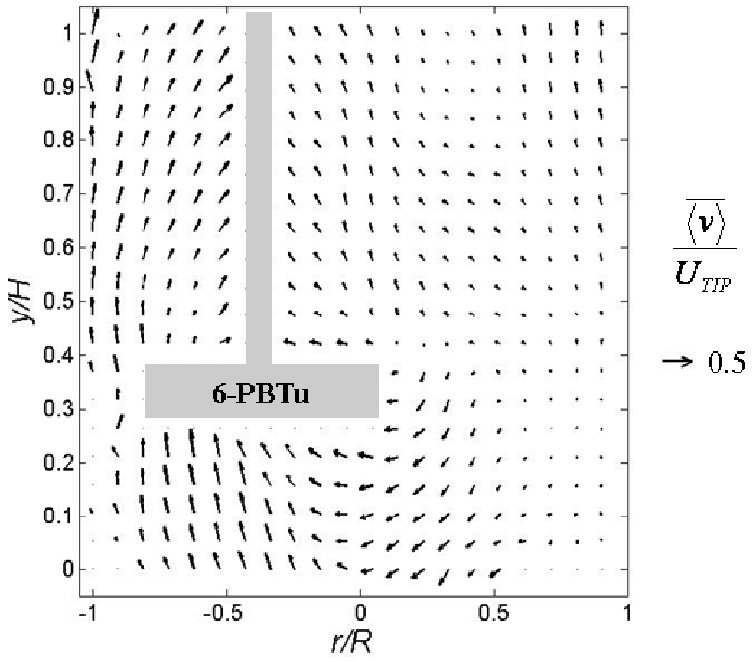

Figure 8.30 Time-averaged gas phase velocity vector plots in (E) for Q_G = 0.5 vvm, N = 650 rpm, ϕ = 0.05, P_G/V = 168 Wm^{-3}.

Unlike in the (B) configuration with the RDT, the majority of gas in the (E) configuration is dispersed in the vertical direction by the 6-PBTu in the region close to the tank wall. Minimal radial discharge can be observed, as would be expected for the liquid phase with this class of impeller.

As for the (B) configuration, when direction of the gas is predominantly upward, the velocity of the gas is augmented by buoyancy and is higher than that of the liquid phase. This becomes apparent in the liquid recirculation zone (r/R = 0-1.0 and y/H = 0.33-1.0). Liquid is drawn into the impeller in the downward direction and a high level of axial liquid flow is exhibited (Figure 8.31). The gas bubbles, however, are seemingly not following the flow, or in places even moving against it. The buoyancy force prevents the gas bubbles from proceeding further down the vessel, hence creating a 'gas free' area at the impeller level. More interestingly, there is no gas discharge in the right hand side of impeller where r/R = 0.2-0.7. In the same area, liquid is discharged in the axial direction.

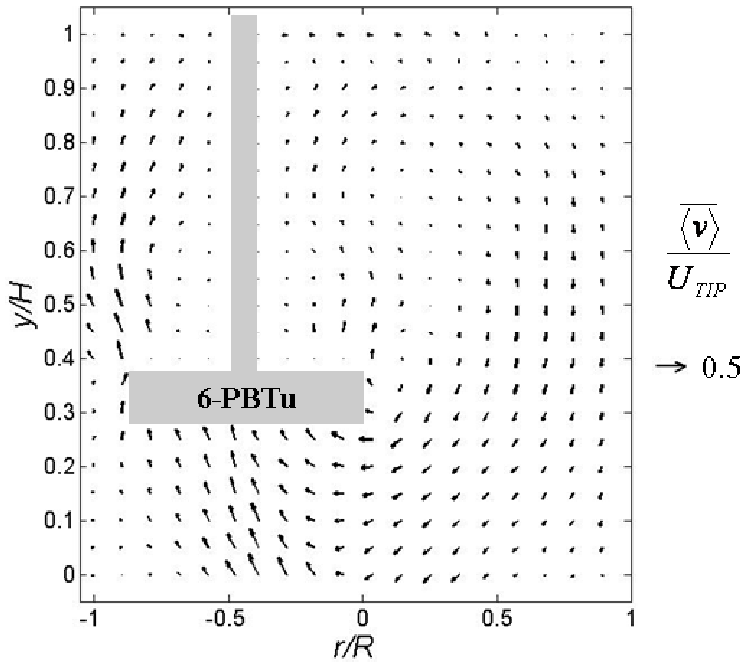

Figure 8.31 Time-averaged liquid phase velocity vector plots in (E) for Q_G = 0.5 vvm, N = 650 rpm, ϕ = 0.05, P_G/V = 168 Wm^{-3}.

The gas holdup is found to be 0.05 and 0.058 for the two gas rate 0.5 and 1.0 vvm, respectively, slightly higher than observed for the (B) configuration.

Figure 8.32 shows the gas phase velocity field at Q_G = 1 vvm. Again as with the (B) configuration, no obvious difference in terms of flow pattern is observed when Q_G is doubled.

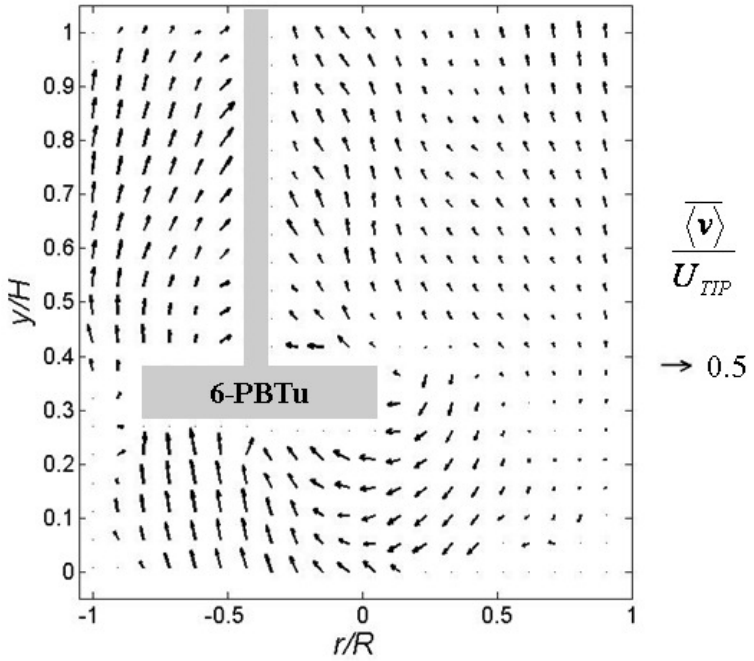

Figure 8.32 Time-averaged gas phase velocity vector plots in (E) for Q_G = 1.0 vvm, N = 700 rpm, ϕ = 0.058, P_G/V = 168 Wm^{-3}.

The liquid phase flow field under ungassed conditions, shown in Figure 8.33, can be compared directly with the liquid flow field under gassing shown in Figure 8.31. The influence of the gas phase is very significant as the maximum liquid velocity in the ungassed case can be twice that observed in the aerated vessel. However, this doubling in velocity only occurs in the impeller discharge at the left side of impeller closest to the vessel wall. The upward flow generated from the circulation loop on the same side of impeller, significantly reduces the flow travelling to the rest of the vessel volume, and hence the large circulation loop seen in Figure 8.31 at *r/R* = 0-1 is missing. The liquid is discharged radially on the right hand side of impeller, with no obvious movement in the axial direction.

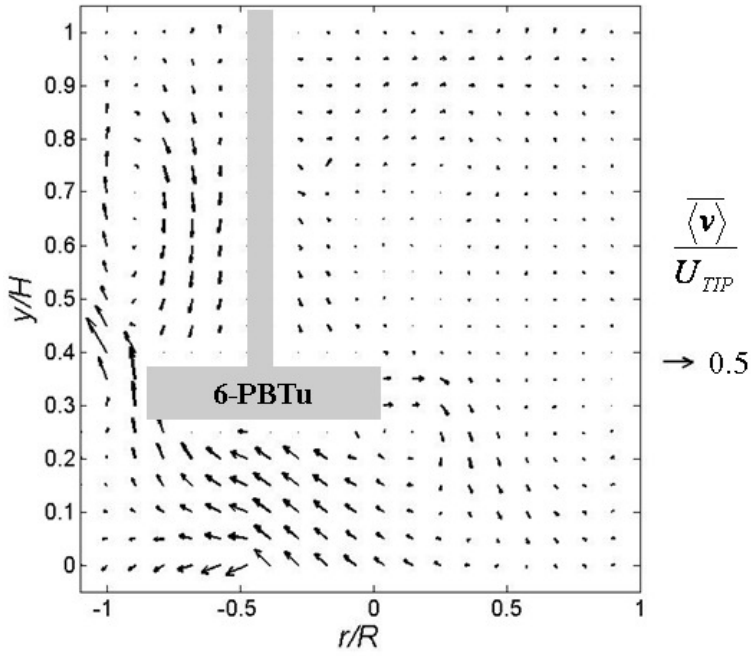

Figure 8.33 Time-averaged liquid phase velocity vector plots in ungassed (E) for Q_G = 0 vvm, N = 575 rpm, P/V = 168 Wm^{-3}.

8.5.2. EFFECT OF GASSING ON TURBULENT KINETIC ENERGY IN THE LIQUID PHASE

Contour maps of turbulent kinetic energy distribution in liquid phase for the (E) configuration, under ungassed and aerated conditions are shown in Figure 8.34 (a) and (b), respectively. Without gassing Figure 8.34 shows that the levels of TKE in the bulk are much higher than the vessel with Q_G at 0.5vvm. In this case, the highest levels of TKE are concentrated in the lower left part of the tank, and TKE gradually decreases with distance until it is at its lowest at the top right corner of the vessel. In sharp contrast, TKE is very low in the lower left corner in the aerated case, and this 'dead zone' can be confirmed by Figure 8.31, where low liquid velocities are observed in the same area.

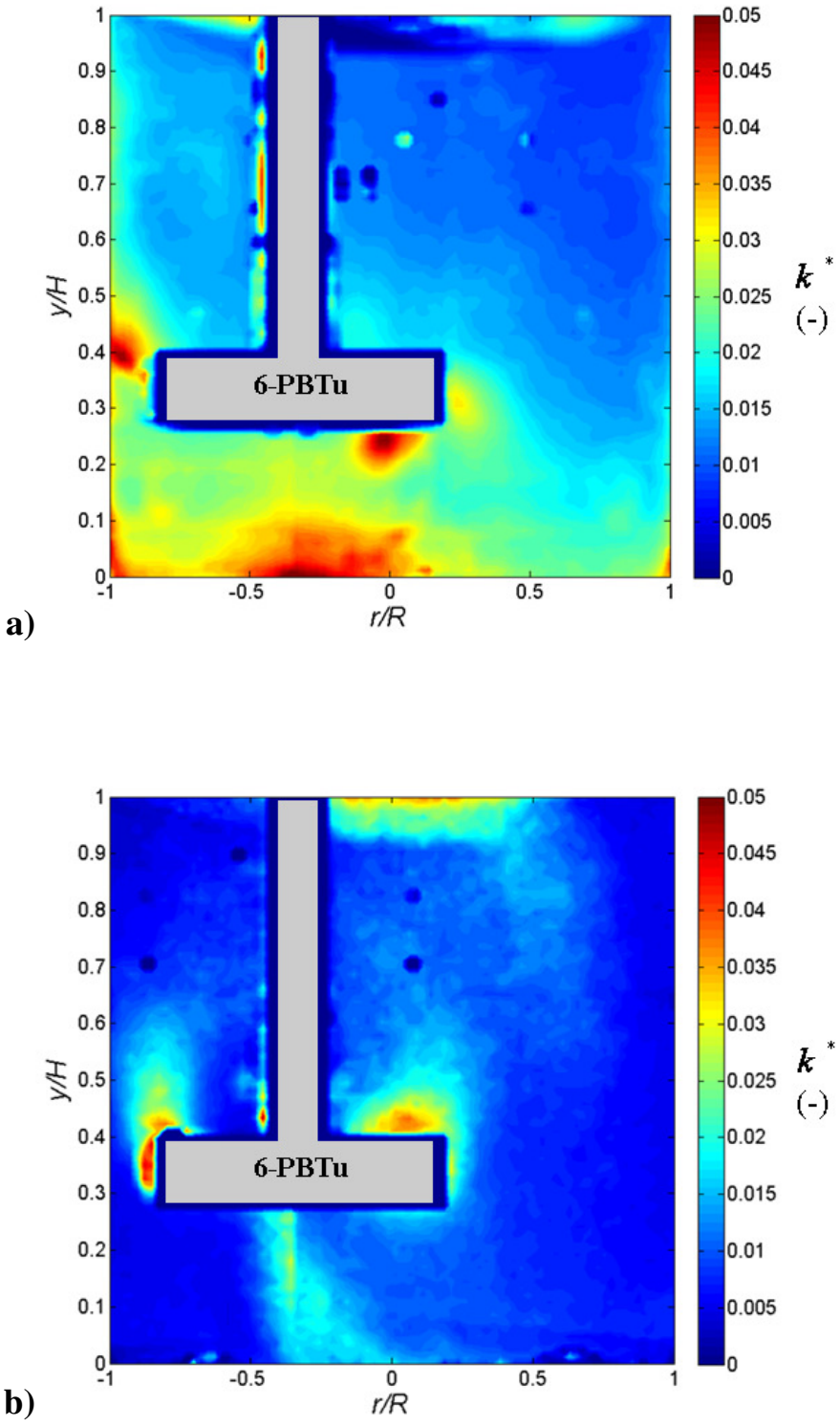

Figure 8.34 Contour plot of TKE distribution for the (E) configuration in (a) the ungassed case; (b) Q_G = 0.5 vvm.

For the gassed case (Figure 8.34b), the values of TKE also reflects the downward liquid recirculation at *r/R* = 0-1.0 above impeller level. As described earlier, this is the region where liquid flow is met with the uprising bubbles, and the levels of TKE are highest at

this point. For this reason the distributions of TKE are very different between the gassed and ungassed cases.

These differences are illustrated more clearly in Figure 8.35 which shows the ratio of localised TKE distribution between aerated and ungassed condition in (E). In the region underneath the impeller, the ratio of TKE in most of this area is no more than a third. This agrees well with the findings of Aubin *et al.* (2004), where the TKE decreased in bulk region when gas was introduced. However, an opposite result can be observed in the liquid recirculation loop above the impeller, and the TKE in this region is up to 1.5 times the values for the ungassed case. An even higher ratio is observed in the TKE discharge zone above impeller.

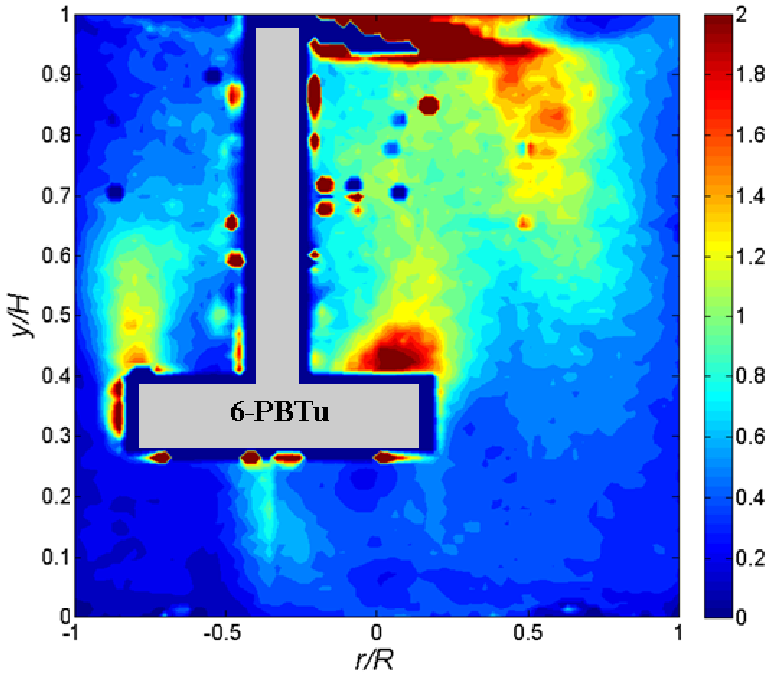

Figure 8.35 Ratio of TKE between the gassed and ungassed conditions shown in Figure 8.34.

8.6 CONCLUSION

A new algorithm based on image analysis techniques and programmed in MATLAB® language has been successfully employed to condition the raw images of a gas liquid flow captured by standard 2D-PIV. The algorithm transforms the in-plane bubbles into tracer particles, which enables the local velocities of the gas phase to be obtained on average using cross correlation techniques. The algorithm also allows simultaneous estimation of the local bubble size distribution, an invaluable parameter in the description of any two-phase flow.

A verification was achieved by comparing the velocities of a single bubble rising through water measured both manually and with the new algorithm. This new algorithm is applicable to measurements in two-phase gas-liquid flows at any macroscopic scale. Thus, it has enabled, for the first time, the successful differentiation of in- and out-of-plane bubbles, and hence the determination of both liquid and gas flow fields inside a miniature HTE stirred vessel. The results obtained showed qualitative agreement with previous experimental observations of global gas phase flow patterns in stirred vessels. They also enabled the effects of the gas phase on the liquid flow field to be determined by comparing with single phase liquid flow measurements in the same vessel. The effect of gassing on TKE distribution in the liquid phase was also studied; the difference in TKE maps between aerated / ungassed conditions agreed well with previous studies that the pitched blade impeller contributes the same energy regardless the rate of gas flow but in the aerated vessel there is a significant reduction in TKE below the impeller plane.

9. CONCLUSIONS AND FUTURE RECOMMENDATIONS

9.1 CONCLUSIONS

The Particle Image Velocimetry (PIV) and Planar Laser Induced Fluoresce (PLIF) techniques have been utilised to analyse the hydrodynamic behaviour and mixing performance of a miniature stirred vessel (T = 45mm), which serves as a prototype of the many small vessels installed in High Throughput Experimentation (HTE). The work carried out in this study can be broadly divided into three categories: single phase transition to turbulent fluid mixing, single phase laminar flow and gas / liquid two phase mixing. As well as the standard fully baffled (B) configuration, four other vessel arrangements were considered. As baffles are usually absent in an industrial HTE unit because of the difficulties involved in the cleaning process, (B) was studied as a benchmark for the other unconventional configurations: unbaffled with centreline agitation (U), unbaffled with eccentric agitation (E), unbaffled with tilting impeller (T) and unbaffled vessel with a square cross section (S).

9.1.1. TURBULENT FLUID MIXING

Commercially available HTE units usually feature simple impeller designs with a large D/T ratio; in this work a pitched blade turbine (PBT) impeller was equipped with D = 0.54T. The small impeller size prohibits the development of a fully turbulent flow (Re > 10^4) unless a substantial power input is applied. At P/V = 168Wm^{-3} with water as working fluid, the flow resides in the high transitional regime ($Re \approx 6000$). However the study carried out by Hall *et al.* (2004; 2005a) on the effect of scale using 2-D PIV stated that the

turbulence quantities in the smaller scale (T = 35–45 mm) with transitional flow is directly comparable to the larger vessels (T = 60–88 mm) in the turbulent regime, hence conventional turbulence analysis such as Turbulent Kinetic Energy (TKE) analysis can be applied.

In this study, a method based on 2-D PIV in vertical and horizontal planes was employed to reconstruct the 3-D flow field inside the small vessel. The results produced by the reconstruction method confirmed that 2-D PIV measurements may be applied on (B) for a reasonably accurate estimation of TKE distribution in the 3-D flow field. However for (U), 2-D PIV measurement gives rise to an erroneous estimation of TKE which can be under-predicted on average by a factor of about 2, and by several folds below the impeller; this arises from the omission of the tangential flow component. Similarly for (E), the TKE is on average underestimated by about 1/3 with the use of 2-D PIV and its accuracy varies across the vessel volume where the impeller region being the worst.

Furthermore, the precision of 3-D reconstruction was immediately realised when the 3-D reconstructed TKE map of (U) was compared to an image from PLIF. The area with low TKE readings underneath impeller matches very well with the region that is last to be mixed; this is not shown in the 2-D TKE map with the isotropic assumption. The successful implementation of 3-D reconstruction in miniature HTE reactors suggests that it can be a viable method for any flow field of interest, if an isotropic assumption is not valid and the configuration precludes the use of stereoscopic PIV.

On the other hand, turbulence quantities measured by ensemble averaged methods may also include pseudo-turbulence caused by periodicity, which is frequently reported in literature (Yianneskis & Whitelaw, 1993; Hockey & Nouri, 1996; Schäfer *et al.*, 1998). As

a result, angle resolved PIV measurements were made in the above configurations as well as (S). The velocity data were ensemble-averaged at every degree over the 60º sector located between two successive impeller blades. Animation of global flow field was studied and periodicity was found in all configurations, but was limited to the region of impeller discharge and inflow underneath the impeller. The square vessel (S) achieved the strongest axial-radial flow field amongst all configurations throughout the vessel. A lower level of pseudo-turbulence was observed in the HTE scale vessels compared to larger vessels on the laboratory scale reported in the above literature, which is partly due to the lower level of TKE achieved in these small vessels. The smallest overestimation in TKE by the ensemble time average was achieved in the (E) and (S) configurations.

The above flow field and TKE studies provided adequate qualitative interpretation of the mixing process; further mixing time analysis provides a more direct comparison on the mixing efficiency across all the configurations studied. Conventional mixing time analysis was reviewed and it was found to be inadequate for the mixing in HTE vessels, which often have a very short mixing time. A log variance method (Edwards *et al.* 2004) was applied to sample tracer concentration from all pixels across the measurable region. This method is usually applied on mixing systems with a few physical measurement probes. Analytical and experimental improvements were made for better consistency and rendered the log variance method usable with many sampling points; for example a much elevated injected tracer concentration in exchange with a reduced tracer volume can effectively increase the contrast between the unmixed regions without lengthening the injection time. The resulting mixing time analysis gave satisfactory results. (E), (S) & (T) achieved the shortest mixing time (τ_{95} = 1.9-2.2s), where the conventional (B) took an extra second to become fully mixed, due to a small amount of tracer being trapped behind baffle. Concentration profile for (U) is similar to (E) up to a mixedness of 80%, beyond such

mixedness the mixing progresses at a much slower rate, due to the presence of the above mentioned insufficient mixing region. On a like-for-like basis, mixing times obtained through the log variance method are longer than those results reported by Hall *et al.* (2005a) via conventional method. It was suggested that the vessels in 'fully mixed' condition observed in conventional method was indeed only 80% mixed; it takes much longer for such vessels to reach the actual 95% mixedness. In addition, the correlation from Ruszkowski (1994) that relates P and vessel geometries to mixing time, was found not only giving an underestimated mixing time, but also unsuitable for unconventional configuration.

The angle-resolved measurements also revealed details of the trailing vortices behind the impeller blades. The up-pumping PBT employed shed trailing vortices mainly in a radial direction with relatively little axial movement. The highest axial vortex position was achieved in (S), which may have contributed to the improved mixing time achieved compared to the other configurations.

The average flow number, Fl, obtained from angle-resolved PIV data agreed with values in the literature for (B). For a PBT impeller with $D = 0.54T$, Fl was found to be 0.64; the small Fl was caused by the large D/T ratio (Hemrajani and Tatterson, 2004). Fl for (S), (E) and (U) was found to be 0.51, 0.61 and 0.37 respectively.

Therefore, in the high transitional to turbulent regime, the hydrodynamic studies conducted suggest that the mixing performance of (S) configuration was not only on par with (E), yet it is possible to pack more units in the confined space of HTE rig, due to the absence of curvature. Nevertheless both (S) and (E) configurations are good replacements for the (B) configuration in commercial HTE units when baffles are undesirable.

9.1.2. MIXING IN THE LAMINAR REGIME

The study of hydrodynamic and mixing behaviour in the HTE scale vessel was extended into the laminar regime; The mixing performance of (S) configuration, which was excellent in the turbulent regime, was again being studied as a probable substitute for (B) and (E). Polypropylene glycol (PPG), a Newtonian fluid, was used to eliminate the complications in rheological properties, as well as preventing the formation of caverns at low power inputs.

In terms of power curve profiles, all configurations except (U) exhibit a fairly constant decade with gradients of about -1; the power curve of (U) can be broken down into two distinctive gradients of -1.2 and -0.75. It was established that the development of the upper circulation loop which at 200-300 rpm, moved into a position that affects impeller discharge from axial-radial to a completely radial direction, may be responsible for the change in power curve gradient. A similar but much more subtle change in flow pattern observed in (S) renders the change in its power curve gradient unnoticeable.

Although (S) in the high power input range displays the highest axial-radial flow velocity among all configurations, its mixing performance (studied by a modified PLIF technique) was highly inferior compared to the (B) and (E) configurations. This is because as the viscosity of fluid increases, the effects of the four 90º corners are less pronounced, rendering the flow only comparable to (U), which is demonstrated by the similarity in their 2-D global flow patterns. Rate of strain contours showed that whilst the shear gradient in the upper and lower circulation loops are high in (U) and (S), there is an obvious gap presented between such area and the rest of vessel; such gap prevents a swift fluid transfer

between regions in stirred vessel and hence it greatly hinders the mixing performance. Such gap may not be considered as an obstacle in (B) and (E) as the positions of such gaps are not constant in the azimuthal direction.

Therefore, although HTE units with (S) configuration produced a comparable mixing performance to (E) in high transition to turbulent regimes whilst being more compact, they are not recommended to be used in low *Re* or laminar mixing conditions.

9.1.3. GAS / LIQUID PHASE VELOCITY MEASURMENTS

Gas and liquid flow fields were measured in the 45mm vessel using image analysis and PIV. As well as the PBT in (E) configuration, a Rushton disk turbine (RDT) was also used in (B). A new algorithm based on image analysis techniques and programmed in MATLAB® language has been successfully employed to condition the raw images of a gas / liquid flow captured by standard 2D-PIV. The algorithm separates bubbles that are the ones supposed to be tracked, and bubbles out of the laser plane which should be rejected. It then transforms the in-plane bubbles into particles, which enables the local velocities of the gas phase to be obtained on average using cross correlation techniques. The algorithm also allows simultaneous estimation of the local bubble size distribution, an invaluable parameter in the description of any two-phase flow. The results have been verified with both quantitative and qualitative means.

This new algorithm is applicable to measurements in two-phase gas-liquid flows at any macroscopic scale. Thus, it has enabled, for the first time, the successful differentiation of in- and out-of-plane bubbles, and hence the determination of both liquid and gas flow fields inside a miniature HTE stirred vessel. The results obtained showed qualitative

agreement with previous experimental observations of global gas phase flow patterns in stirred vessels. They also enabled the effects of the gas phase on the liquid flow field to be determined by comparing with single phase liquid flow measurements in the same vessel. The effect of gassing on TKE distribution in the liquid phase was also studied; the difference in TKE maps between aerated / ungassed conditions agreed well with previous studies that the PBT impeller contributes the same energy regardless the rate of gas flow, but in the aerated vessel there is a significant reduction in TKE below the impeller plane.

9.2 FUTURE RECOMMENDATIONS

This study involved a 6-PBTd ($D = 0.54T$) in the liquid phase experiments and a 6-RDT ($D = 0.33T$) in the gas/liquid multiphase flow. As the impeller provides the primary source of turbulence, research can be carried out to study the many other impeller designs, for example impeller types (from flat paddle to more complicated Lightning A310), as well as fundamental impeller designs (number of blades, blade attack angle, very large *D/T* ratio). Studies on other vessel configurations are also recommended, such as the impeller clearance, *C/H*, and the number of baffles. Moreover, tilting impeller configuration (T) was only briefly reviewed in the mixing time analysis and it produced by far, the shortest mixing time among all configuration studies in the turbulent mixing regime. This showed its potential as a replacement of (E) and further studies should be carried out.

Mixing in the turbulent regime was studied using an angle-resolved 2-D PIV technique, as well as ensemble averaged 3-D reconstruction. Both measurement techniques proved superior to the conventional ensemble averaged 2-D PIV measurements. Due to the limitation of computing power at present, the combination of the two, i.e. 3-D reconstruction from angle resolved 2-D PIV measurement, will simply be uneconomical.

Yet if more powerful workstations are available in the future, coupling with an image capturing mechanism that can robotically carry out tasks such as traversing the laser unit and automatic image capturing, there are no reason why the combination of the two techniques cannot be done. For example the recently developed system V3V by TSI Inc., that produced a 3 Dimensional 3 Component (3D3C) with the use of 2 laser planes, one each in the vertical and horizontal direction offer this possibility.

Moreover, the 3-D reconstruction has not yet been carried out in (S), although it may be simpler to do than any other configurations. Because of the absence of curvature, multiple vertical PIV measurements can be made along the Z axis, which include the *u*-*v* velocity vectors in the X-Y direction as shown in Figure 9.1(a). When the data is allowed to be rotated 90°, the velocity data in the X direction will effectively become vectors in the Z direction in Figure 9.1(b). Hence 3-D reconstruction can be carried out from one set of multiple X-Y plane measurements along the Z axis.

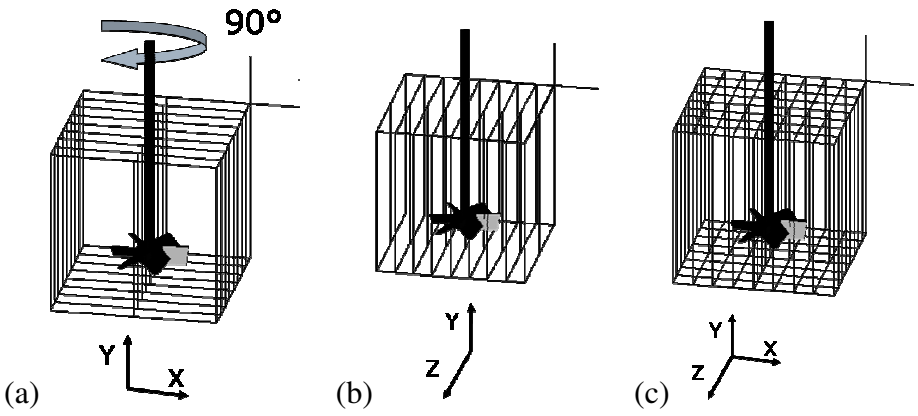

Figure 9.1 Illustrations showing alternative 3-D reconstruction technique, note that the planes included velocity vectors in (a)X-Y direction, (b) Y-Z direction and (c) X-Y-Z direction.

If the spatial resolution of the PIV camera is further increased, i.e. using new cameras with larger CCD arrays combined with alternative lens that has a higher magnification factor,

can ensure a better validity of the Smagorinsky model or any other SGS closure model in terms of local energy dissipation rate estimation. An increased spatial resolution could also give a more accurate PLIF measurement; even micro-mixing performance can be obtained directly from PLIF measurements.

For the study of single phase laminar mixing, non-Newtonian fluids can be used, so the effect of complex fluid rheology (i.e. cavern formation) could be investigated.

As far as multiphase PIV measurements were concerned, further studies can be carried out. For example, Q_G should be reduced to achieve complete gas dispersion, which is more in line with the processes carried out in the industries. The relationship between global gas holdup and the measurement accuracy can also be further studied.

The other important aspect in multiphase mixing is the solid / liquid systems, which had never been studied in HTE scaled vessels. As well as analysing basic parameters such as just complete suspension speed, N_{JS}, phase velocities can also be measured using PIV. This can be achieved if the refractive indices of seeding particles and fluid can be matched so that the solid particles do not cause any interference with liquid phase measurement. In terms of the solid phase velocity measurements, particles can easily be doped with Rhodamine and applied as tracer particles. If necessary, a similar image processing algorithm as used in gas phase velocity measurement can be applied to condition the images prior to PIV processing. Such studies may even be extended to gas/liquid/solid three phase systems.

APPENDIX A. SHAFT ENCODER CIRCUIT DIAGRAM

The shaft encoder employed in Chapter 6 for the Angle Resolved Measurements was independently design and built by the author and since its completion it has been used in numerous projects. The primary object is to generate a 5V output signal every time the infrared (IR) beam between the slots of the slotted optical switch is disturbed (i.e. the 'pointer' passes through the slot once every revolution of impeller), shown as component number 5 in Figure A1. The components were purchased from RS Components (UK) and their RS part numbers, along with their description, are given in Table A1.

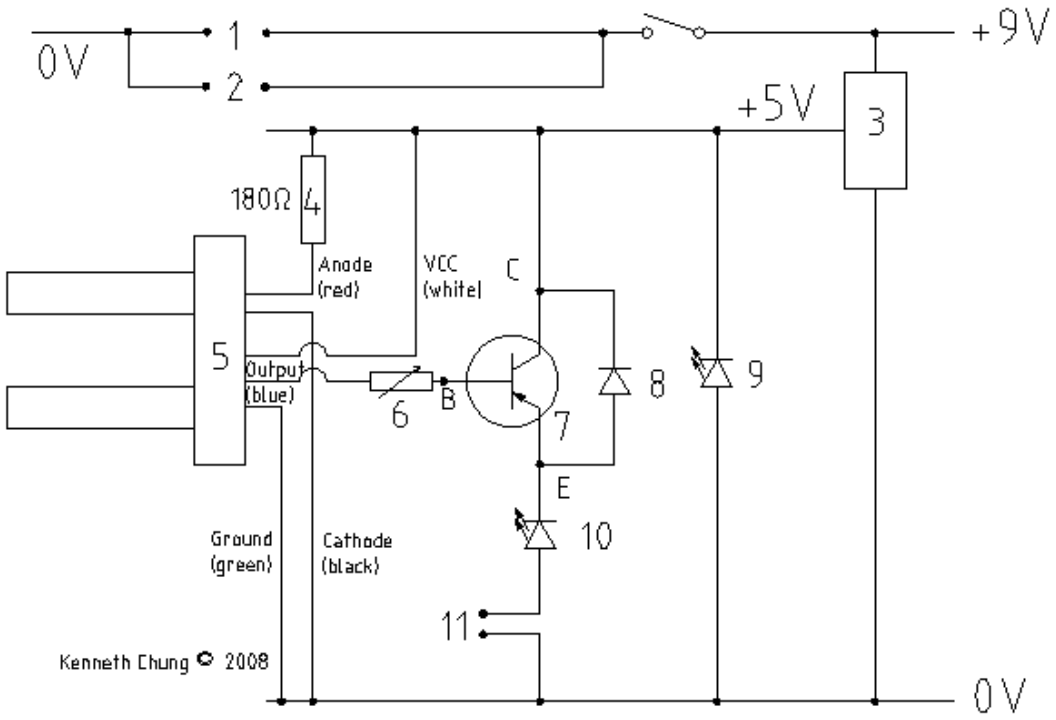

Figure A1 Circuit diagram of the shaft encoder.

Table A 2 Description of the components and their RS part numbers.

Item #	RS # (Manufacturer parts #)	Component detail
1	508-116	9V battery drawer
2	486-678	DC adaptor connection
3	466-7051 (TEL 5-1211)	DC/DC convertor. DC in 9V out 5V 1000mA
4	2508141231	180Ω resistor for 3.5V / 0.02A (± 5%)
5	455-0919 (OPB815)	Slotted optical switch
6		Variable resistor
7	296-116 (BC556)	PNP Amplifier transistor
8	447-2566 (JPAD50)	Diode
9	311-6760	Snap-in Green LED
10	311-6760	Snap-in Red LED
11	546-5143	Connector to Sycroniser

The shaft encoder is powered either by a 9V battery (#1) or DC input (#2). The 9V power input is stepped down to 5V by a DC convertor (#3), to comply with the requirement of the synchroniser.

The current generated by the optical switch is less than 5 mA, which is not sufficient to trigger the image capture mechanism; the synchroniser requires a threshold current of at least 50mA. Therefore, the current is amplified by a PNP transistor (#7). A variable resistor (#6) is used to fine tune the input current to the transistor so the magnified output current can be controlled. The typical current supply by this particular shaft encoder is around 80mA; the signal is clear yet does not present a heavy load on battery. To protect the circuit a diode is used (#8) to prevent the inversion of polarity, which can occur due a number of reasons. A green Light Emitting Diode (LED) (#9) is added to indicate the operational status of encoder and a red LED (#9) is switched on every time the encoder is generating a signal.

It is important to note that the slotted optical switch (#5) must be of the transistor-transistor logic (TTL) type. Without TTL, the signal given out by the optical switch depends solely on the amount of IR captured by the sensor and an analogue signal is then generated; the capturing mechanism may be triggered by the synchroniser many times during a passage of

'pointer'. With the TTL mechanism, the output signal is buffered and digitalised. Only one '1' signal is generated once every revolution, ensuring the quality of angle resolved measurements.

APPENDIX B. SHAFT ENCODER VALIDATION

As described in Section 3.2.5, the time delay between receiving an encoder signal and the actual image capture, *dt*, was used control the angular position, θ, of flow visualisation. The 'pointer' in this case is permanently fixed on impeller shaft; this is different from the method adopted by ordinary PIV users where the 'pointer' is manually shifted in the angular direction to control the capturing angle. Assuming the fluctuation in the impeller rotational speed is minimal, the former should, in theory, much more consistent.

This appendix illustrates the validations made to verify the accuracy of controlling capture angle with the change in *dt*. First the impeller was removed from the impeller shaft and was replaced by a 360 degree protractor. A 45° mirror was used to aid the visualisation from underneath the protractor, similar to the method applied for the horizontals PIV meansurement described in Section 3.2.4. Image sequences were captured at every angle between 0° to 60° and validations were based on the capture stability at a fixed angle, as well as the accuracy of captured angle controlled by *dt*. Animations of the image sequence are included in the supplementary CD-ROM under the folder 'APPENDIX B'.

The capture stability is found to be satisfactory as shown in the animation file '1.avi' where images were captured at a distance so the whole protractor can be visualised and '2.avi' which shows a closeup of the protractor with a fixed artificial reference line. Sample images of the two videos are shown in Figure B1. At a rotational speed of 625rpm, which is the typical *N* used in (U) configuration, it is obvious that the white line

fixed at the same angular position. The laser reflection on the protractor fluctuates because of the oscillation at high rotational speed.

(a)

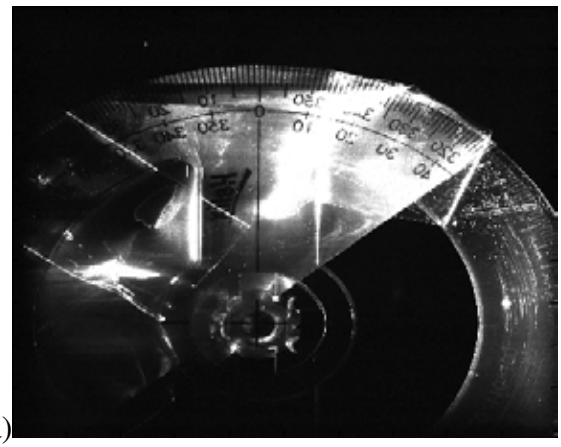

(b)

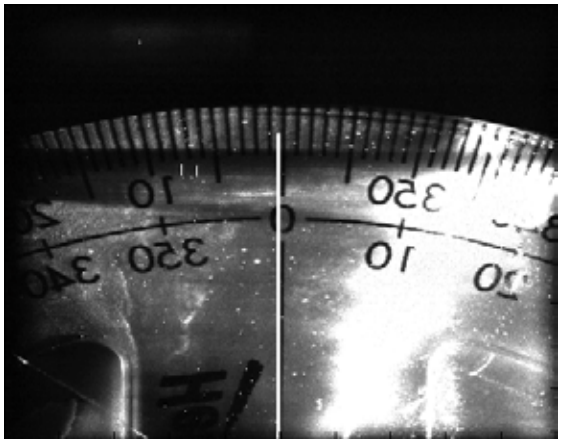

Figure B1 Study of image capture stablility. Images were captured at a fixed angle with protractor rotational speed of 625rpm at (a) a distance that shows the whole protractot and (b) close-up.

In addition to the two videos, an animation is also included in the CD-ROM ('PIV Sample.avi') which is contructed from the actual PIV angle resolved raw image sequences of (E) configuration, and its sample image is shown in Figure B2. Again the stability warrants an accurate PIV measurment. It should also be highlighted that the angular position illustrated in Figure B2 is the $\theta = 0°$ typically used in this work.

Finally the accuracy of angular position controlled by varing *dt* is shown in '3.avi' and its sample image is shown in Figure B3. At a rotational speed of 625rpm, the reference line

stays at every angle specified. The variation in *dt* is now proven to be capable of controlling the angular position of measurement plane accurately.

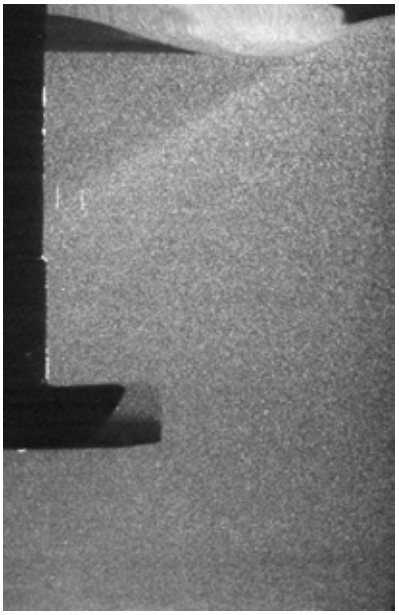

Figure B2 PIV captured image sample form animation 'PIV Sample.avi', angle resolved at θ = 0° in (E) configuration.

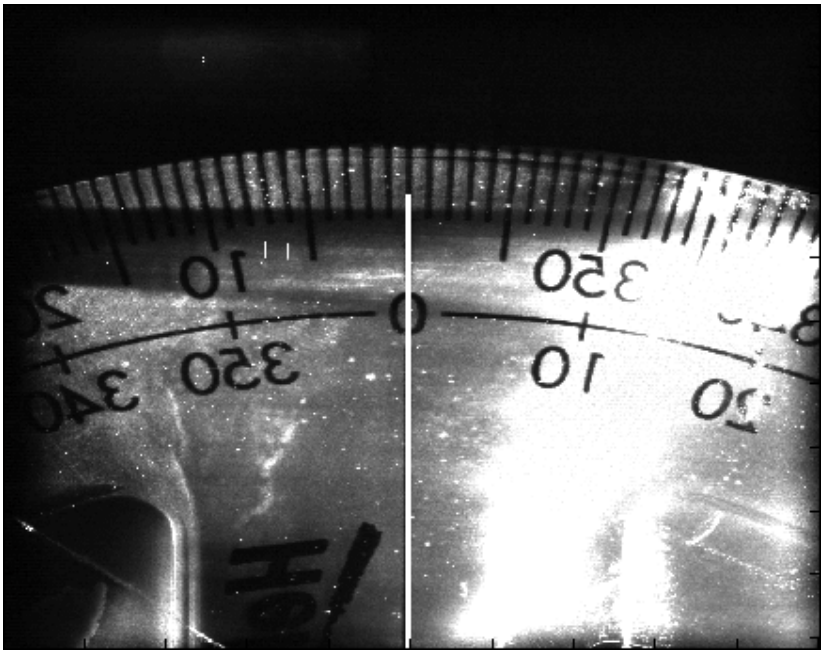

Figure B3 Study of accuracy in *dt* controlled angular measurment position. Images were captured at a every angle in a 0° to 60° section with protractor rotational speed of 625rpm.

APPENDIX C. MATLAB® CODES

All post experimental analysis was carried out with the use of MATLAB® (Version 6 to V2006b) source codes written independently by the author. This appendix publishes a selection of these codes for future references in academic research. Reader should modify the codes accordingly to address their individual needs, as well as making adjustments to the individual parameters for each specific experiements to ensure these codes are used effectively and accurately.

C1. CONTRUCTING A 3-D MATRIX WITH VECTOR FILES

```
clear
clf
display ('-------------------------------------------------')
display ('-----------------3-D Matrix--------------------')
display ('----------------------by-------------------------')
display ('---------------Kenneth Chung-------------------')
display ('--------------------2008-----------------------')
display ('-------------------------------------------------')

d=input ('Impeller diameter (m)? e.g. 0.0245')
T=input ('Vessel diameter (m)? e.g. 0.045')
RPM=input ('RPM?')
n=RPM/60;
Utip = pi*d*n;
%%%Load Vector Files%%%
%%%%%%%%%%%%%%%%%%%%%%%%%%%%%%%%%%%%%%%%%%%%%%%%%%%%%%%%%%%%%%%%%%%%%%%%%%%%%%%
fname1 = input ('Folder directory? e.g. (C:) >> ','s')
fname2 = input ('Folder name? (e.g. TRIAL) >> ','s')
nfiles = input ('Last Frame? (e.g. 499) >> ')
fname3 = [fname1,'\',fname2,'\Vector\',fname2,'00000.vec']
%%One vector file is loaded here, assuming first file ends with
00000.vec%%
s=csvread([fname3],1,0);
%%%Filter out error vectors%%%
xt=find(s(:,5)<1);
s(xt,3:4)=NaN;
s(:,5)=[];
format short e;
%%%Convert from mm to m%%%
s(:,1:2)=s(:,1:2)/1000;
%%%Split raw data into X, Y coordinate and data%%%
x = s(:,1);
y = s(:,2);
z = s(:,3);
%%%Reshape data into matrix%%%
```

```
b = find (y == s (1,2));
b1 = max (size (b));
a = find (x == s (1,1));
a1 = max (size (a));
U =reshape(z,b1,a1);
U = U;
z = s(:,4);
V =reshape(z,b1,a1);
V = V;
X=reshape(x,b1,a1);
Y=reshape(y,b1,a1);

%%%The rest of files are loaded here as a loop%%%
for i = 1 : nfiles;

if i < 10
fname3 = [fname1,'\',fname2,'\Vector\',fname2,'0000',int2str(i),'.vec']
elseif 100 > i & i > 9
fname3 = [fname1,'\',fname2,'\Vector\',fname2,'000',int2str(i),'.vec']
elseif 1000 > i & i > 99
fname3 = [fname1,'\',fname2,'\Vector\',fname2,'00',int2str(i),'.vec']
else
fname3 = [fname1,'\',fname2,'\Vector\',fname2,'0',int2str(i),'.vec']
end

if exist (fname3)>0

s=csvread([fname3],1,0);
xt=find(s(:,5)<1);
s(xt,3:4)=NaN;
s(:,5)=[];
z = s(:,3);
U2 =reshape(z,b1,a1);
z = s(:,4);
V2 =reshape(z,b1,a1);
%%%Stacking data onto the first data file, constructing a 3D matrix%%%
U=cat(3,U,U2);
V=cat(3,V,V2);
end
end
clear U2 V2;
display ('Data Loading Completed')
%%%%%%%%%%%%%%%%%%%%%%%%%%%%%%%%%%%%%%%%%%%%%%%%%%%%%%%%%%%%%%%%%%%%%%%%%%%%
```

C2. VECTOR PLOTTING TOOL

Note: To be run after the completion of code 1.

```
%%%Calculating normalised U,V and velocity magnitude form valid
vectors%%%
%%%%%%%%%%%%%%%%%%%%%%%%%%%%%%%%%%%%%%%%%%%%%%%%%%%%%%%%%%%%%%%%%%%%%%%%%%%%
sz=size(U);
c1=sz(1,3);
for i=1:b1
    for j=1:a1
        clear  ru rv
       ru=find (~isnan(U(i,j,:)));
rv=find (~isnan(V(i,j,:)));
UA(i,j) = mean(U(i,j,ru))/Utip;
VA(i,j) = mean(V(i,j,rv))/Utip;
```

```
Mag(i,j)=(UA(i,j)*UA(i,j)+VA(i,j)*VA(i,j))^0.5
    end
end
%%%%%%%%%%%%%%%%%%%%%%%%%%%%%%%%%%%%%%%%%%%%%%%%%%%%%%%%%%%%%%%%%%%%%%%%%%%%
%%%Contour Plot%%%
contourf(X,Y,Mag,50);
colormap(gray)%%%or (jet) for color%%%
caxis([0 1])%%%minimum to maximum COLOR scale (see help)%%%
set(gca,'DataAspectRatio',[1 1 1])%%%Aspect Ratio in x y z direciton%%%
axis([-0.05 0.9 0 1.0])%%%xmin xman ymin ymax%%%
set(gcf, 'color', 'white');%%%set background color to white%%%
hold on
%%%Vector Plot%%%
quiver (X,Y,UA,VA,2,'-k','LineWidth',1.5);
set(gca,'DataAspectRatio',[1 1 1])
xlabel('x-mm','FontSize',18,'FontAngle','italic')%%%X label%%%
ylabel('y-mm','FontSize',18,'FontAngle','italic')%%%Y label%%%
colorbar('FontSize',14);
```

C3. RATE OF STRAIN (ROS) GRAPHS

Note: To be run after the completion of code 1.

```
%%%Calculating normalised U,V form valid vectors%%%
%%%%%%%%%%%%%%%%%%%%%%%%%%%%%%%%%%%%%%%%%%%%%%%%%%%%%%%%%%%%%%%%%%%%%%%%%%%%
sz=size(U);
c1=sz(1,3);
for i=1:b1
    for j=1:a1
        clear  ru rv
       ru=find (~isnan(U(i,j,:)));
rv=find (~isnan(V(i,j,:)));
UA(i,j) = mean(U(i,j,ru));
VA(i,j) = mean(V(i,j,rv));
    end
end

%%%Rate of strain contours%%%
%%%%%%%%%%%%%%%%%%%%%%%%%%%%%%%%%%%%%%%%%%%%%%%%%%%%%%%%%%%%%%%%%%%%%%%%%%%%
sz=size(X);
a1=sz(1,1);
b1=sz(1,2);

dX=X(2,1)-X(1,1);
dY=Y(1,1)-Y(1,2);

for r=2:1:(a1-1)
    for c=2:1:(b1-1)
z2(r,c)=0.5*(((VA(r+1,c)-VA(r-1,c)))/(2*dX)+(((UA(r,c-1)-
UA(r,c+1)))/(2*dY)));
  end
end

%%%Delete the last row and column%%%
z2(:,b1)=0;
z2(a1,:)=0;

%%%Normalise X Y axis%%%
X=(X-(min(min(X)))+dX)/(T/2);
```

```
Y=((Y-(Y(1,2)-Y(1,1)))-((min(min(Y)))-(Y(1,2)-Y(1,1)))+dY)/0.045;

contourf(X,Y,z2,50,'LineStyle','none');
colormap(jet)
caxis([0 30])
set(gca,'DataAspectRatio',[a1 b1 1],'FontSize',16)
axis([0 1.0 0 1.0])
set(gcf, 'color', 'white');
colorbar('FontSize',14);
xlabel('r/R','FontSize',18,'FontAngle','italic')
ylabel('y/H','FontSize',18,'FontAngle','italic')
```

C4. VORTICITY ISO-SURFACE PLOT

Note: To be run after the completion of code 1. In addition, the 3-D matrix is averaged into a 2-D mean velocity matrix with code 2. Repeat such routine for the 60 degree and a new 3-D matrix is constructed, i.e. X×Y×Degree.

```
sz=size(UA);
a1=sz(1,1);
b1=sz(1,2);
c1=sz(1,3);

dX=X(2,1)-X(1,1);
dY=Y(1,1)-Y(1,2);

%%%Vorticity%%%
%%%%%%%%%%%%%%%%%%%%%%%%%%%%%%%%%%%%%%%%%%%%%%%%%%%%%%%%%%%%%%%%%%%%%%%%%%%%%%%
for degree=1:c1
for r=2:1:(a1-1)
    for c=2:1:(b1-1)

        z2(r,c,degree)=(((VA(r-1,c,degree)-VA(r+1,c,degree))/(2*dX))-
((UA(r,c-1,degree)-UA(r,c+1,degree))/(2*dY)));
  end
end
end
%%%%%%%%%%%%%%%%%%%%%%%%%%%%%%%%%%%%%%%%%%%%%%%%%%%%%%%%%%%%%%%%%%%%%%%%%%%%%%%

z2(:,b1,:)=0;
z2(a1,:,:)=0;
X=(X-(min(min(X))))/(T/2);
Y=((Y-(Y(1,2)-Y(1,1)))-((min(min(Y)))-(Y(1,2)-Y(1,1))))/T;
for degree=1:c1
for i=1:a1
    for j=1:b1
if isnan(z2(i,j,degree))==1
z2(i,j,degree)=0;
end
end
end
T(:,:,degree)=rot90(z2(:,:,degree));
end

clear z2

%%%Converting into polar coodinate%%%
%%%%%%%%%%%%%%%%%%%%%%%%%%%%%%%%%%%%%%%%%%%%%%%%%%%%%%%%%%%%%%%%%%%%%%%%%%%%%%%
```

```
sz = size (T);
x=sz(1,2)
y=sz(1,3)
z=sz(1,1)
%%%Volume in Impeller region is cleard%%%
T(:,1:(x*0.54),:)=0;
%%%Here volume in 61-120 degrees are copied from 1-60 degrees%%%
T3(1:z,1:x,1:60)=T;
T3(1:z,1:x,61:120)=T;
%%%And volume in 121-360 degrees are cleared%%%
T3(1:z,1:x,121:180)=0;
T3(1:z,1:x,181:240)=0;
T3(1:z,1:x,241:300)=0;
T3(1:z,1:x,301:360)=0;
clear T
T=T3;
clear T3
%%%T5 is the counter rotation of trailing vortices%%%
T5=-T;
sz = size (T);
x=sz(1,2)
y=sz(1,3)
z=sz(1,1)

X(1,1)=0;
for i=2:1:x
X(1,i)=i*(1/x);
end

for j=2:1:z
X(j,:)=X(1,:);
end

for k=2:1:y
X(:,:,k)=X(:,:,1);
end

for i=1:1:x
    for j=1:1:z
        for k=1:1:y
            Z(j,i,k)=j/z;
        end
    end
end



for i=1:1:x
    for j=1:1:z
        for k=1:1:y
            Y(j,i,k)=((((k-y)+k)-1)/(y-1))*pi;
        end
    end
end



Rho = X;
Theta = Y;

a2 = size (Rho);
a2 = a2 (1,2);
TZ=Z;
```

```
clear Z X Y
for i=1:1:x
    for j=1:1:z
        for k=1:1:y
TX (j,i,k)= Rho(j,i,k)*(cos(Theta(j,i,k)));
TY (j,i,k)= Rho(j,i,k)*(sin(Theta(j,i,k)));
end
    end
end
%%%%%%%%%%%%%%%%%%%%%%%%%%%%%%%%%%%%%%%%%%%%%%%%%%%%%%%%%%%%%%%%%%%%%%%%%%%%%%%

%%%T4 is trailing vortices and T5 is its reaction%%%
for ag=1
    clf
    nm=y-ag;
    T4(:,:,1:nm)=T(:,:,ag+1:y);
    T4(:,:,nm+1:y)=T(:,:,1:ag);
    T6(:,:,1:nm)=T5(:,:,ag+1:y);
    T6(:,:,nm+1:y)=T5(:,:,1:ag);

p = patch(isosurface(TX,TY,TZ,T4,150))%%%only vorticity of over 150%%%
set(p,'FaceColor','red','EdgeColor','none');
hold on
xlabel('X','FontSize',16)
ylabel('Z','FontSize',16)
zlabel('Y','FontSize',16)
axis equal
set(gca,'DataAspectRatio',[1 1 0.5])
alpha(1.0)
axis([-1 1 -1 0 0.1 0.5])
view([-1 1 0.5])
camlight
lighting gouraud
grid minor
hold off
```

C5. TURBULENT KINETIC ENERGY GRAPHS

```
clear
clf
display ('-----------------------------------------------')
display ('-----Turbulent Kinetic Energy (T.K.E.) Map-----')
display ('----------------------by-----------------------')
display ('---------------Kenneth Chung-------------------')
display ('--------------------2008-----------------------')
display ('-----------------------------------------------')

d=input ('Impeller diameter (m)? e.g. 0.0245')
RPM=input ('RPM?')
N=RPM/60;
UtipSQ = (pi*d*N)^2;



%%%Load Vector Files%%%
%%%%%%%%%%%%%%%%%%%%%%%%%%%%%%%%%%%%%%%%%%%%%%%%%%%%%%%%%%%%%%%%%%%%%%%%%%%%%%%
fname1 = input ('Folder directory? e.g. (C:) >> ','s')
fname2 = input ('Folder name? (e.g. TRIAL) >> ','s')
```

```
nfiles = input ('Last Frame? (e.g. 499) >> ')
fname3 = [fname1,'\',fname2,'\Vector\',fname2,'00000.vec']
%%One vector file is loaded here, assuming first file ends with
00000.vec%%
s=csvread([fname3],1,0);
%%%Filter out error vectors%%%
xt=find(s(:,5)<1);
s(xt,3:4)=NaN;
s(:,5)=[];
format short e;
%%%Convert from mm to m%%%
s(:,1:2)=s(:,1:2)/1000;
%%%Split raw data into X, Y coordinate and data%%%
x = s(:,1);
y = s(:,2);
z = s(:,3);
%%%Reshape data into matrix%%%
b = find (y == s (1,2));
b1 = max (size (b));
a = find (x == s (1,1));
a1 = max (size (a));
U =reshape(z,b1,a1);
U = U;
z = s(:,4);
V =reshape(z,b1,a1);
V = V;
X=reshape(x,b1,a1);
Y=reshape(y,b1,a1);

%%%The rest of files are loaded here as a loop%%%
for i = 1 : nfiles;

if i < 10
fname3 = [fname1,'\',fname2,'\Vector\',fname2,'0000',int2str(i),'.vec']
elseif 100 > i & i > 9
fname3 = [fname1,'\',fname2,'\Vector\',fname2,'000',int2str(i),'.vec']
elseif 1000 > i & i > 99
fname3 = [fname1,'\',fname2,'\Vector\',fname2,'00',int2str(i),'.vec']
else
fname3 = [fname1,'\',fname2,'\Vector\',fname2,'0',int2str(i),'.vec']
end

if exist (fname3)>0

s=csvread([fname3],1,0);
xt=find(s(:,5)<1);
s(xt,3:4)=NaN;
s(:,5)=[];
z = s(:,3);
U2 =reshape(z,b1,a1);
z = s(:,4);
V2 =reshape(z,b1,a1);
%%%Stacking data onto the first data file, constructing a 3D matrix%%%
U=cat(3,U,U2);
V=cat(3,V,V2);
end
end
clear U2 V2;
display ('Data Loading Completed')
%%%%%%%%%%%%%%%%%%%%%%%%%%%%%%%%%%%%%%%%%%%%%%%%%%%%%%%%%%%%%%%%%%%%%%%%%%%%

%%%Calculating mean U,V form valid vectors%%%
```

```
%%%%%%%%%%%%%%%%%%%%%%%%%%%%%%%%%%%%%%%%%%%%%%%%%%%%%%%%%%%%%%%%%%%%%%%%%%%%%%%
sz=size (U)
a1=sz(1,2);
b1=sz(1,1);
c1=sz(1,3);

%%%Mean U%%%
for i=1:1:b1
    for j=1:1:a1
        for k=1:1:c1

                NA(i,j,k)=isnan(U(i,j,k));
        end
    end
end

warning off MATLAB:divideByZero
for i=1:1:b1
    for j=1:1:a1
A=find (NA(i,j,:)<1);
        AU (i,j)= mean(U(i,j,A));
        AV (i,j)= mean(V(i,j,A));
        clear A
    end
end
clear NA
%%%%%%%%%%%%%%%%%%%%%%%%%%%%%%%%%%%%%%%%%%%%%%%%%%%%%%%%%%%%%%%%%%%%%%%%%%%%%%%

%%%RMS Fluctuating Velocity (Sqaured for TKE calculation)%%%
%%%%%%%%%%%%%%%%%%%%%%%%%%%%%%%%%%%%%%%%%%%%%%%%%%%%%%%%%%%%%%%%%%%%%%%%%%%%%%%
for i=1:b1;
    for j=1:a1;
        for k=1:c1;
            UF(i,j,k)=U(i,j,k)-AU(i,j);
            VF(i,j,k)=V(i,j,k)-AV(i,j);
            a=UF(i,j,k);
            UF2(i,j,k)=a^2;
            a=VF(i,j,k);
            VF2(i,j,k)=a^2;
            NA(i,j,k)=isnan(UF2(i,j,k));
        end
    end
end

%%%TKE%%%
%%%%%%%%%%%%%%%%%%%%%%%%%%%%%%%%%%%%%%%%%%%%%%%%%%%%%%%%%%%%%%%%%%%%%%%%%%%%%%%
for i=1:b1;
    for j=1:a1;
        A=find (NA(i,j,:)<1);
            RMSU(i,j)= mean (UF2(i,j,A));
            RMSV(i,j)= mean (VF2(i,j,A));
            TKE(i,j)=(0.75*(RMSU(i,j)+RMSV(i,j)))/UtipSQ;
            clear A
    end
end
%%%%%%%%%%%%%%%%%%%%%%%%%%%%%%%%%%%%%%%%%%%%%%%%%%%%%%%%%%%%%%%%%%%%%%%%%%%%%%%
%%

%%% Rotate data into the right way for plotting%%%
TKE = rot90 (TKE);
```

```
%%%Contourfill graph%%%
%%%%%%%%%%%%%%%%%%%%%%%%%%%%%%%%%%%%%%%%%%%%%%%%%%%%%%%%%%%%%%%%%%%%%%%%%%%%
contourf(X,Y,TKE,50,'LineStyle','none'); %%%Contourfill graph 50
levels%%%
colormap(jet)
caxis([0 0.05])%%%min/max data limit%%%

set(gca,'DataAspectRatio',[a1 b1 1],'FontSize',16)
axis([0 1.0 0 1.0])
set(gcf, 'color', 'white');
xlabel('r/R','FontSize',18,'FontAngle','italic')
ylabel('y/H','FontSize',18,'FontAngle','italic')
colorbar('FontSize',14);
```

C6. LOG VARIANCE MIXING TIME ANALYSIS (PLIF)

```
clear

%%%Define boundaries of ROI%%%
Y1A=100;
Y1B=900;
X1A=100;
X1B=900;

%%%Reduce resolution to reduce processing time%%%
R1=(X1B-X1A)/4;
C1=(Y1B-Y1A)*R1;


C3B=C1+1;

%%%Timing%%%
t = input ('Frame per second?, (fps)?')
t=(1/t);
format short e

%%%File read%%%
fname1 = input ('File directory?','s')
fname2 = input ('File name?','s')

%%%GCB%%%
%%%%%%%%%%%%%%%%%%%%%%%%%%%%%%%%%%%%%%%%%%%%%%%%%%%%%%%%%%%%%%%%%%%%%%%%%%%%
num=0;
if num < 10
fname3 =
[fname1,'\',fname2,'\Image\Single\',fname2,'0000',num2str(num),'.tif']
elseif num<100
fname3 =
[fname1,'\',fname2,'\Image\Single\',fname2,'000',num2str(num),'.tif']
elseif num<1000
fname3 =
[fname1,'\',fname2,'\Image\Single\',fname2,'00',num2str(num),'.tif']
end

A = imread([fname3]);
A2 = reshape(A(X1A:X1B-1,Y1A:Y1B-1),[2 2 C1]);
sz=size(A2);
sza=sz(1,1);
szb=sz(1,2);
```

```
szc=sz(1,3);
for i=1:szc
    GCB(1,i)=min(min((A2(:,:,i))));
    GI(1,i)=mean(mean((A2(:,:,i))));
end
clear A A2
%%%%%%%%%%%%%%%%%%%%%%%%%%%%%%%%%%%%%%%%%%%%%%%%%%%%%%%%%%%%%%%%%%%%%%%%%%%%

%%%GCI%%%
%%%%%%%%%%%%%%%%%%%%%%%%%%%%%%%%%%%%%%%%%%%%%%%%%%%%%%%%%%%%%%%%%%%%%%%%%%%%
nfiles = input ('Number of extra images needed to be solved (AT LEAST
ONE)?')
c = (nfiles-5);
if c < 10
fname3 =
[fname1,'\',fname2,'\Image\Single\',fname2,'0000',num2str(c),'.tif']
elseif 100 > c & c > 9
fname3 =
[fname1,'\',fname2,'\Image\Single\',fname2,'000',num2str(c),'.tif']
elseif 1000 > c & c > 99
fname3 =
[fname1,'\',fname2,'\Image\Single\',fname2,'00',num2str(c),'.tif']
end
A = imread([fname3]);
A2 = reshape(A(X1A:X1B-1,Y1A:Y1B-1),[2 2 C1]);
for i=1:szc
    AB(1,i)=mean(mean((A2(:,:,i))));
end
clear A A2

for c = (nfiles-4) : nfiles
if c < 10
fname3 =
[fname1,'\',fname2,'\Image\Single\',fname2,'0000',num2str(c),'.tif']
elseif 100 > c & c > 9
fname3 =
[fname1,'\',fname2,'\Image\Single\',fname2,'000',num2str(c),'.tif']
elseif 1000 > c & c > 99
fname3 =
[fname1,'\',fname2,'\Image\Single\',fname2,'00',num2str(c),'.tif']
end
A = imread([fname3]);
A2 = reshape(A(X1A:X1B-1,Y1A:Y1B-1),[2 2 C1]);
for i=1:szc
    AB2(1,i)=mean(mean((A2(:,:,i))));
end
clear A A2
AB = cat(3,AB,AB2);
clear AB2
end

sz = size (AB);
R = sz(1,1);
C = sz(1,2);
L = sz(1,3);

for i=1:1:R
    for j=1:1:C
        GCI(i,j)=mean(AB(i,j,:));
    end
end
```

```
clear AB
%%%%%%%%%%%%%%%%%%%%%%%%%%%%%%%%%%%%%%%%%%%%%%%%%%%%%%%%%%%%%%%%%%%%%%%%



%%%Conc%%%
%%%%%%%%%%%%%%%%%%%%%%%%%%%%%%%%%%%%%%%%%%%%%%%%%%%%%%%%%%%%%%%%%%%%%%%%
for c=(num+1):nfiles
if c < 10
fname3 =
[fname1,'\',fname2,'\Image\Single\',fname2,'0000',num2str(c),'.tif']
elseif 100 > c & c > 9
fname3 =
[fname1,'\',fname2,'\Image\Single\',fname2,'000',num2str(c),'.tif']
elseif 1000 > c & c > 99
fname3 =
[fname1,'\',fname2,'\Image\Single\',fname2,'00',num2str(c),'.tif']
end
A = imread([fname3]);
A2 = reshape(A(X1A:X1B-1,Y1A:Y1B-1),[2 2 C1]);
for i=1:szc
    GI2(1,i)=mean(mean((A2(:,:,i))));
end
clear A A2
GI = cat(3,GI,GI2);
clear GI2
end
%%%%%%%%%%%%%%%%%%%%%%%%%%%%%%%%%%%%%%%%%%%%%%%%%%%%%%%%%%%%%%%%%%%%%%%%



GCB=double(GCB);
GCI=double(GCI);
GI=double(GI);

sz=size(GI);
R=sz(1,1);
C=sz(1,2);
L=sz(1,3);

%%%Nominal Grey scale%%%
for i = 1:1:R
for j = 1:1:C
for k = 1:1:L
GI(i,j,k)=(GI(i,j,k)-GCB(i,j));
end
end
end

GCI=GCI-GCB;

%%%Calculate Variance%%%
%%%%%%%%%%%%%%%%%%%%%%%%%%%%%%%%%%%%%%%%%%%%%%%%%%%%%%%%%%%%%%%%%%%%%%%%
for k=1:1:L
   for i=1:1:R
        for j=1:1:C
       Conc(i,j,k)=GI(i,j,k)/GCI(i,j);
        end
   end
end

for k=1:1:L
   for i=1:1:R
```

```
        for j=1:1:C
            T=Conc(i,j,k)-1;
            T2=T^2;
            Conc(i,j,k)=T2;
        end
    end
end

NaaN=isnan(Conc);
Ninf=isinf(Conc);


for i=1:1:R
    for j=1:1:C
        for k=1:1:L
            if NaaN(i,j,k)==1
                Conc(i,j,k)=0;
            elseif Ninf(i,j,k)==1
                Conc(i,j,k)=0;
            else
                Conc(i,j,k)=Conc(i,j,k);
            end
        end
    end
end


for k=1:1:L
    [XA YA]=find(NaaN(:,:,k)==1 | Ninf(:,:,k)==1);
    sz=size (XA);
    saz=sz(1,1);
    VA(1,k)=(sum(sum(Conc(:,:,k))))/(R*C-saz);
    clear sz saz XA YA
end
%%%%%%%%%%%%%%%%%%%%%%%%%%%%%%%%%%%%%%%%%%%%%%%%%%%%%%%%%%%%%%%%%%%%%%%%%%%%%%%

%%%Log Variance%%%
for i=1:1:L;
    LogVA(1,i)=log10 (VA(1,i));
end

clear Conc

%%%Timing%%%
for i=1:1:L;
    TE(1,i)=(i*t);
end
plot (TE, LogVA);
```

C7. IMAGE ANALYSIS ALGORITHM IN PHASE VELOCITY MEASUREMENTS

```
clear
clf

%%%Pre-Defined Variables%%%
MAXLengthPeri=10;
CirIndex=0.90;
```

```
CirIndex2=1.10;
CountBB=0;
Bound=5;
JPSIZEX=1016;
JPSIZEY=1000;

%%%Aera of Interest%%%
ImStart=0;
ImNo=5000;
AOIYmin=400;
AOIYmax=750;
AOIXmin=200;
AOIXmax=800;
Overlap=0.5;
LIA=100;
XLEN=AOIXmax-AOIXmin;
YLEN=AOIYmax-AOIYmin;
TotalAOIX=(XLEN/(LIA*Overlap)-1);
TotalAOIY=(YLEN/(LIA*Overlap)-1);
TotalAOI=TotalAOIX*TotalAOIY;
BRGPLIST(1,1:4)=0;

%%%Data Aqucition%%%
name1=input ('Folder directory? e.g. (C:) >> ','s');
name2=('Folder name? (e.g. TRIAL) >> ','s');

for imageno=ImStart:ImNo
if imageno<10
    I2=['0000',num2str(imageno)];
elseif imageno>=10 & imageno<100
    I2=['000',num2str(imageno)];
    elseif imageno>=100 & imageno<1000
    I2=['00',num2str(imageno)];
    elseif imageno>=1000 & imageno<10000
    I2=['0',num2str(imageno)];
end

%%%Processing of image a or b in an image pair%%%
for imno=1:2
    if imno==1
        imcar='a';
     else
        imcar='b';
    end
name3=[name1,'\',name2,I2,mat2str(imcar),'.tif'];

JPEGDATA=imread([name3]);

%%%Create blank image of similar size to the PIV image%%%
JP2(1:JPSIZEX,1:JPSIZEY)=0;

%%%Threshold for primary filter%%%
maxGS=max(max(JPEGDATA))-100;

GOODGP(1,1:7)=0;

%%%Select and display the AOI under image analysis%%%
for VC=1:TotalAOIY
    for HC=1:TotalAOIX
AOIno=(VC-1)*TotalAOIX+HC;
```

```
disp([num2str(imageno),imcar,' - AOI ',num2str(AOIno),' of
',num2str(TotalAOI)])
Xmin=AOIXmin+(HC-1)*Overlap*LIA;
Xmax=Xmin+LIA-1;
Ymin=AOIYmin+(VC-1)*Overlap*LIA;
Ymax=Ymin+LIA-1;
A=JPEGDATA(Xmin:Xmax,Ymin:Ymax);

%%%Primary filter, if a singal of bubble is not registered, the AOI will
not be analysed to cut processing time%%%
CT = find ( A >= maxGS );
szCT=size(CT);
if szCT(1)>=6
    ISBLANK=0;

%%%Morphological Reduction%%%
background2 = imopen(A,strel('line',10,1));
B2=imsubtract(A,background2);
C2 = imadjust(B2);
clear C B
C=C2;
clear C2
B=B2;

%%%Thresholding%%%
level=graythresh(C)-0.05;
G = im2bw(C,level);
G=imfill(G,'holes');
else
C(1:LIA,1:LIA) = 0;
G(1:LIA,1:LIA) = 0;
ISBLANK=1;
end
clear CT szCT IM

IM=G;

clear G

if ISBLANK==0
sz=size(C);
a1=sz(1,1);
b1=sz(1,2);

%%%Thresholding,Gamma adjustment%%%
level=graythresh(C)+0.05;
E=imadjust(C,[level 1],[0 1],2.0);

%%%Median Filter%%%
D=medfilt2(E,[2 2]);
level=graythresh(D);
G = im2bw(D,level);
BW=G;
s=size(BW);
BRCount = 0;
BRdata (1,1:2)=nan;

%%%Tracing boundaries of all objects remained%%%
for row = 2:1:s(1)
for col=1:s(2)
if BW(row,col),
```

```
BubbleRegion = bwtraceboundary(BW, [row, col], 'N', 8,
100,'counterclockwise');
if(~isempty(BubbleRegion))
    BRCount = BRCount + 1;
s2=size(BRdata);
s3=size(BubbleRegion);
BRdata((s2(1)+1),1:2)=nan;
BRdata((s2(1)+2):(s2(1)+1+s3(1)),1:2)=BubbleRegion;
end
end
end
end

s=size (BRdata);

%%%Combining all overlapping pixels and grouping connecting objects%%%
for i=1:s(1)
    if isnan(BRdata(i,1))==0 & BRdata(i,1)~=0
        tem=find(BRdata(:,1)==BRdata(i,1) & BRdata(:,2)==BRdata(i,2));
        t=size(tem);
        if t(1)>1
        tem(1,1)=tem(2,1);
        end
        BRdata(tem,1:2)=0;
        clear t tem
    end
end
BRd2=BRdata;

s=size (BRd2);
ZeroRows = find (BRd2(:,1) == 0);
s2=size (ZeroRows);
RealRows=s(1)-s2(1);
BRd=removerows(BRd2,ZeroRows);
BRc(1,1:2)=BRd(1,1:2);
for i=2:RealRows
    if isnan(BRd(i-1,1))==1 & isnan(BRd(i,1))==1;
        BRc(i,1:2) = 0;
    else
        BRc(i,1:2)=BRd(i,1:2);
    end
end
clear ZeroRows s s2
ZeroRows = find (BRc(:,1) == 0);
s2=size (ZeroRows);
FinalRows = RealRows-s2(1);
BR=removerows(BRd,ZeroRows);
clear BRd2 BRd BRc RealRows ZeroRows i s2 BRgp
Gp = 0;
BR(1,3)=Gp;
for i= 2:FinalRows
    if isnan(BR(i-1,1))==1;
        Gp=Gp+1;
    end
        BR(i,3)=Gp;
end
FR=find (isnan (BR(:,1)) == 1);
BRGP=removerows(BR,FR);
BRgp=BRGP;
        clear BR FR FinalRows BRGP

%%%Remove small objects%%%
```

```
Gp=max(BRgp(:,3));

for i = 1 : Gp;
    p=find (BRgp(:,3) == i);
    s=size(p);
    t(i,1)=s(1);
    clear p
end
A=[];
t2 = find (t(:,1) <= 5);
st2=size(t2);
st=st2(1);

for i=1:st;
    s=t2(i,1);
t3 = find (BRgp(:,3) == s);
A=cat(1,A,t3);
clear t3
end

BRnwgp = removerows(BRgp,A);

%%%Label individual objects%%%

if isempty(BRnwgp)~=1;
s=size(BRnwgp);
BRnwgp(1,4)=1;
for i=2:s(1)
    if BRnwgp(i,3) == BRnwgp(i-1,3);
BRnwgp(i,4)=BRnwgp(i-1,4);
    else
        BRnwgp(i,4)=BRnwgp(i-1,4)+1;
    end
end
BRnwgp(:,3)=[];
NoGp=max(BRnwgp(:,3));
ResBRnwgp=BRnwgp;

%%%Analyse each individual objects%%%

for m=1:NoGp

clear BRnwgp
BRnwgp=ResBRnwgp;

    Tempdata1=find (BRnwgp(:,3)==m);
    Tdata=BRnwgp(Tempdata1,:);
    Tdata(:,3)=[];
    clear Tempdata1

data=Tdata;

clear A BRnwgp
sz = size (data);

Xdist=max(data(:,1))-min(data(:,1));
Ydist=max(data(:,2))-min(data(:,2));

if Xdist>=Ydist
```

```
    RMEAN=Xdist/2;
else
    RMEAN=Ydist/2;
end

clear C
C(1:2,1)=0;
for t=1:sz(1)
XMEAN2=data(t,1);
Y=data(t,2);
RMEAN2= 6.5;
for i = XMEAN2:1:(XMEAN2+RMEAN2)
    XCIR(:,(i-XMEAN2+1))=(i);
        YCIR(:,(i-XMEAN2+1))=(RMEAN2^2-(i-XMEAN2)^2)^0.5+Y;
end
XCIR2=-XCIR+Bound*XMEAN2;

YCIR2=-YCIR+Bound*Y;
clear C1 C2 C3 C4
 C1(1,:)=XCIR; C1(2,:)=YCIR;
 C2(1,:)=XCIR2; C2(2,:)=YCIR;
 C3(1,:)=XCIR; C3(2,:)=YCIR2;
 C4(1,:)=XCIR2; C4(2,:)=YCIR2;
 C=cat(2,C,C1);
 C=cat(2,C,C2);
 C=cat(2,C,C3);
 C=cat(2,C,C4);

end

C(:,1)=[];

%%%Hough Circle Analysis%%%
Xmax=max(C(1,:));
Ymax=round(max(C(2,:)));
C=round(C);
sz2=size(C);
houghdist(1:Xmax, 1:Ymax)=0;

for p=1:sz2(2)
    x=C(1,p);
    y=C(2,p);
    if x>0 & y>0

    houghdist(x,y)=houghdist(x,y)+1;
    end
end

maxhough=max(max(houghdist));

if isempty(maxhough)~=1;

[r,c]= find (houghdist==maxhough);

%%%Create boundary box for each object%%%
XMEAN2=r(1,1);
Y=c(1,1);
RMEAN2=RMEAN^2;

for i = XMEAN2:1:(XMEAN2+RMEAN)
```

```
    XCIR(:,(i-XMEAN2+1))=(i);
        YCIR(:,(i-XMEAN2+1))=(RMEAN2-(i-XMEAN2)^2)^0.5+Y;
end

XCIR2=-XCIR+2*XMEAN2;
YCIR2=-YCIR+2*Y;

XMIN= floor(min(XCIR2));
YMIN= floor(min(YCIR2));
YMAX= round(max(YCIR));
XMAX= round(max(XCIR));
LB=(LIA-Bound);

%%%Obtain undistorted image saved earlier%%%
G = IM;
sz=size(G);

if XMIN>Bound & YMIN>Bound & XMAX<(LB) & YMAX<(LB)
TIA=G((XMIN-Bound):(XMAX+Bound),(YMIN-Bound):(YMAX+Bound));

TIA=(flipud(rot90(TIA)));

clear BRdata
s=size(TIA);
BRCount = 0;
BRdata (1,1:2)=nan;

%%%Tracing boundaries in the less distorted image and regconising
bubbles%%%
clear r2 c2 s4
[r2 c2]=find (TIA==1);
s4=size (r2);
for i=1:s4(1)
    row=r2(i,1);
    col=c2(i,1);
BubbleRegion = bwtraceboundary(TIA, [row, col], 'N', 8,
100,'counterclockwise');
if(~isempty(BubbleRegion))
s2=size(BRdata);
s3=size(BubbleRegion);
BRdata((s2(1)+1),1:2)=nan;
BRdata((s2(1)+2):(s2(1)+1+s3(1)),1:2)=BubbleRegion;
end
end

s=size (BRdata);
for i=1:s(1)
    if isnan(BRdata(i,1))==0 & BRdata(i,1)~=0
        tem=find(BRdata(:,1)==BRdata(i,1) & BRdata(:,2)==BRdata(i,2));
        t=size(tem);
        if t(1)>1
        tem(1,1)=tem(2,1);
        end
        BRdata(tem,1:2)=0;
        clear t tem
    end
end
BRd2=BRdata;

s=size (BRd2);
ZeroRows = find (BRd2(:,1) == 0);
```

```
BRd=removerows(BRd2,ZeroRows);
clear s4
s4=size(BRd);
BRc(1,1:2)=BRd(1,1:2);
RealRows=s4(1);

BRdnan=find (isnan(BRd(:,1)));
s4=size(BRdnan);
if s4(1)>1
for i=2:s4(1)
    if BRdnan(i-1)==BRdnan(i)-1
        BRdnan2(i,1)=NaN;
    end
end
BRdnan3=find(isnan(BRdnan2));
BRdnan4=removerows(BRdnan,BRdnan3);
else
    BRdnan4=1;
end
BRc=BRd;
BRc(BRdnan,1:2)=0;
BRc(BRdnan4,1:2)=NaN;
clear BRdnan BRdnan2 BRdnan3 BRdnan4 s4 ZeroRows s s2
ZeroRows = find (BRc(:,1) == 0);
BR=removerows(BRd,ZeroRows);
s2=size(BR);
FinalRows=s2(1);
clear BRd2 BRd BRc RealRows ZeroRows i s2 isnotn
isnotn=find(isnan(BR(:,1)));

if isempty(isnotn)==0
s2=size(isnotn);
BR(1,3)=0;
for i=2:s2(1)
    rn=isnotn(i,1);
    rnp=isnotn(i-1,1)+1;
    BR(rnp:rn,3)=i-1;
end
BR(rn+1:FinalRows,3)=i;

FR=find (isnan (BR(:,1)) == 1);
BRgp=removerows(BR,FR);
        clear BR FR FinalRows

        Gp=max(BRgp(:,3));
else
    Gp=1;
    BRgp(1,3)=Gp
end

if isempty(BRgp)==1 | Gp==0
    Gp=1;
    BRgp(1,3:4)=1;
end

for i = 1 : Gp;
    clear p
    p=find (BRgp(:,3) == i);
    s=size(p);
    BRgp(p,4)=s(1);
end
```

```
t2 = find (BRgp(:,4) <= 5);
BRnwgp = removerows(BRgp,t2);
BRnwgp(:,3:4)=[];

if isempty(BRnwgp)~=1
    BRnwgp(:,1) = BRnwgp(:,1)+YMIN-Bound;
        BRnwgp(:,2) = BRnwgp(:,2)+XMIN-Bound;
sz=size(BRnwgp);
BRnwgpgd(1:sz(1),1:sz(2))=0;
BRnwgp=round(BRnwgp);
for i=1:sz(1)
    BRnwgpgd(BRnwgp(i,1),BRnwgp(i,2))=1;
end

%%%Filling hollow objects%%%
BRfilled = imfill (BRnwgpgd,'holes');

if (max(BRnwgp(:,1))-min(BRnwgp(:,1))) >= (max(BRnwgp(:,2))-
min(BRnwgp(:,2)))
d=(max(BRnwgp(:,1))-min(BRnwgp(:,1)));
else
    d=(max(BRnwgp(:,2))-min(BRnwgp(:,2)));
end

L = bwlabel(BRfilled);
RealP  = regionprops(L, 'Perimeter');
RealA = regionprops(L, 'Area');
MajAX = regionprops(L,'MajorAxisLength');
MinAX = regionprops(L,'MinorAxisLength');

sz=size (RealP);

if sz(1)==1
L3=regionprops(L, 'BoundingBox');
L4=L3.BoundingBox;
L1=L4(1,3);
L2=L4(1,4);
ARatio=RealA.Area/(L1*L2);
AR=(RealA.Area/pi)^0.5;
PR=RealP.Perimeter/(2*pi);
Cirity=AR/PR;
AXRat=MajAX.MajorAxisLength/MinAX.MinorAxisLength;
BRnwgp(:,1)=BRnwgp(:,1)+(VC-1)*Overlap*LIA;
BRnwgp(:,2)=BRnwgp(:,2)+(HC-1)*Overlap*LIA;
BRnwgp(:,3)=Cirity;
BRnwgp(:,4)=ARatio;
BRnwgp(:,5)=m;
BRnwgp(:,6)=0;
BRnwgp(:,7)=AXRat;
clear L3
if ARatio>0.9 | AXRat>1.5
BRnwgp=[];
end

else
    SPBRnwgp=BRnwgp;
    L3=regionprops(L, 'BoundingBox');

for i=1:sz(1)
    clear BRnwgp
```

```
P=RealP(i,:);
AA=RealA(i,:);
MaX=MajAX(i,:);
MiX=MinAX(i,:);
L32=L3(i,:);
L4=L32.BoundingBox;
L1=L4(1,3);
L2=L4(1,4);
ARatio=AA.Area/(L1*L2);

AR=(AA.Area/pi)^0.5;
PR=P.Perimeter/(2*pi);
Cirity=AR/PR;
AXRat=(MaX.MajorAxisLength)/(MiX.MinorAxisLength);
[BRnwgp(:,1),BRnwgp(:,2)] = find (L==i);
s=size (BRnwgp);
BRnwgp(:,1)=BRnwgp(:,1)+(VC-1)*Overlap*LIA;
BRnwgp(:,2)=BRnwgp(:,2)+(HC-1)*Overlap*LIA;
BRnwgp(:,3)=Cirity;
BRnwgp(:,4)=ARatio;
BRnwgp(:,5)=m;
BRnwgp(:,6)=i;
BRnwgp(:,7)=AXRat;
if ARatio>0.9 | AXRat>1.5
BRnwgp=[];
end
end
clear L3
end

clear  BRgp A BRCount SPBRnwgp BRnwgpgd BRfilled RealP L RMEAN2 TIA
houghdist BRdata BubbleRegion  C C1 C2 C3 C4 G Gp NoGp RMEAN Tdata XCIR
XCIR2 XMAX XMEAN2 XMIN Xdist Xmax Y YCIR YCIR2 LB YMAX YMIN Ydist Ymax c
col data i maxhough r row s s3 st st2 sz sz2 t t2 v x y

end
end
end

exist BRnwgp;
if ans==1 & isempty(BRnwgp)~=1;
GOODGP=cat(1,GOODGP,BRnwgp);
clear BRnwgp
end

clear B B2 BRdata BRgp BRnwgp BW BubbleRegion C C1 C2 C3 C4 D E G XCIR
XCIR2 XMEAN YCIR YCIR2 a1 b1 background background2 c col data houghdist
i level maxhough p r s s3 st st2 sz sz2 t t2 v x y
end
end
end
    end
end

GOODGP(1,:)=[];
s=size(GOODGP);
GOODGP(1,8)=1;
for  i=2:s(1)
    if GOODGP(i,3:6)==GOODGP(i-1,3:6)
        GOODGP(i,8)=GOODGP(i-1,8);
    else
```

```
        GOODGP(i,8)=GOODGP(i-1,8)+1;
    end
end

GPno=max(GOODGP(:,8));

for i=1:GPno
    tempgp = find (GOODGP(:,8) == i);
    s=size(tempgp);
    GOODGP(tempgp,7)=s(1);
    clear tempgp s
end

%%%Validation by circularity%%%
GOODCIR=find (GOODGP(:,3)>=CirIndex & GOODGP(:,3)<=CirIndex2 &
GOODGP(:,7)>=MAXLengthPeri);
GDGP=GOODGP(GOODCIR,:);
BADCIR=find (GOODGP(:,3)<CirIndex | GOODGP(:,3)>CirIndex |
GOODGP(:,7)<MAXLengthPeri);
BDGP=GOODGP(BADCIR,:);
NewPIC(1:XLEN,1:YLEN)=0;
s=size(GDGP);
for i=1:s(1)
    XX=GDGP(i,2);
    YY=GDGP(i,1);
    NewPIC(XX,YY)=1;
end

%%%Extact bubble from original image%%%
A2=JPEGDATA((AOIXmin-1):AOIXmax, (AOIYmin-1):AOIYmax);
NWPC=imfill(NewPIC,'holes');

for i=1:XLEN
    for j=1:YLEN
        if NWPC(i,j)==1;
            JP2(i+AOIXmin,j+AOIYmin)=A2(i,j);
        end
    end
end

if imno==1
GDGPA=GDGP;
BDGPA=BDGP;
GOODGPA=GOODGP;
NWPICA=JP2;
else
GDGPB=GDGP;
BDGPB=BDGP;
GOODGPB=GOODGP;
NWPICB=JP2;
end
clear A AOIno AR BADCIR BDGP BRGPLIST Cirity GDGP GOODCIR GOODGP HC NWPC
JP2 NewPIC  P  PR  RMEAN  RMEAN2  RealA  ResBRnwgp  Tdata  VC  XMAX
XMEAN2  XMIN  XX  Xdist  Xmax  Xmin  Y  YMAX  YMIN  YY Ydist Ymax Ymin
ans d i imcar isnotn j m s

end

%%%Image Export%%%
name4a=[name1,':\',name2,'Dat\',name2,I2,'a.tif'];
name4b=[name1,':\',name2,'Dat\',name2,I2,'b.tif'];
```

```
NWPICA=uint8(NWPICA);
NWPICB=uint8(NWPICB);
imwrite(NWPICA,[name4a],'tif','compression','none','Resolution',0);
imwrite(NWPICB,[name4b],'tif','compression','none','Resolution',0);
clear name4a name4b
end
```

REFERENCES

Adams, L. W. and Barigou, M. (2007) CFD analysis of caverns and pseudo-caverns developed during mixing of non-newtonian fluids , *Transactions of the Institution of Chemical Engineers Part A*, **85**, 598-604.

Alcamo, R., Micale, G., Grisafi, F., Brucato, A., and Ciofalo, M. (2005) Large-eddy simulation of turbulent flow in an unbaffled stirred tank driven by a Rushton turbine, *Chemical Engineering Science*, **60**, 2303-2316.

Alvarez-Hernández, M. M., Shinbrot, T., Zalc, J. M., and Muzzio, F. J. (2002) Practical chaotic mixing, *Chemical Engineering Science*, **57**, 3749-3753.

Armenante, P. M., Luo, C., Chou, C. C., Fort, I., and Medek, J. (1997) Velocity profiles in a closed, unbaffled vessel: comparison between experimental LDV data and numerical CFD predictions, *Chemical Engineering Science*, **52**, 3483 -3492.

Aubin, J., Le Sauze, N., Bertrand, J., Fletcher, D. F., and Xuereb, C. (2004) PIV measurements of flow in an aerated tank stirred by a down- and an up-pumping axial flow impeller, *Experimental Thermal and Fluid Science*, **28**, 447-456.

Baldi, S. and Yianneskis, M. (2003) On the direct measurement of turbulence energy dissipation in stirred vessels with PIV, *Industrial & Engineering Chemistry Research*, **42**, 7006-7016.

Baldi, S. and Yianneskis, M. (2004) On the quantification of energy dissipation in the impeller stream of a stirred vessel from fluctuating velocity gradient measurements, *Chemical Engineering Science*, **59**, 2659-2671.

Barigou, M. and Greaves, M. (1992) Bubble-size distributions in a mechanically agitated gas--liquid contactor, *Chemical Engineering Science*, **47**, 2009-2025.

Baumann, K-H. and Mühlfriedel, K. (2002) Mass transfer studies with Laser Induced Fluorescence across liquid/liquid interface boundaries, *Chemical Engineering Technology*, **25** , 697-700.

Bröder, D. and Sommerfeld, M. (2002) An advanced LIF-PLV system for analysing the hydrodynamics in a laboratory bubble column at higher void fractions, *Experiments. in Fluids*, **33**, 826-837.

Bröder, D. and Sommerfeld, M. (2007) Planar shadow image velocimetry for the analysis of the hydrodynamics in bubbly flows, *Measurement Science and Technology*, **18**, 2513-2528.

Bouaifi, M, Hebrard, G, Bastoul, D, and Roustan, M. (2001) A comparative study of gas hold-up, bubble size, interfacial area and mass transfer coefficients in stirred gas-liquid reactors and bubble columns, *Chemical Engineering and Processing*, **40**, 97-111.

Brown, D. A. R., Jones, P. N., and Middleton, J. C. (2004) 'Experiment Methods', Chapter 4 in Handbook of Industrial Methods: Science and Practice, John Wiley & Sons, Hoboken, New Jersey, ISBN:0-471-26919-0.

Brucato, A., Ciofalo, M., Grisafi, F., and Micale, G. (1998) Numerical prediction of flow fields in baffled stirred vessels: A comparison of alternative modelling approaches, *Chemical Engineering Science*, **53**, 3653-3684.

Bruijn, W., van't Riet, K. , and Smith, J. M. (1974) Power consumption with aerated Rushton turbines, *Transactions of the Institution of Chemical Engineers Part A*, **52**, 88-104.

Buchhave, P. (1994) 'Particle Image Velocimetry', Optical diagnostics for flow processes, Plenum Press, New York, ISBN:0-306-44817-3.

Bujalski, W., Nienow, A. W., and Huoxing, Liu. **(1990)** The use of upward pumping 45 degree pitched blade turbine impellers in three-phase reactors, *Chemical Engineering Science*, **45**, 415-421.

Calderbank, P. H. (1958) Physical rate processes in industrial fermentation, Part I-: The Interfacial Area in Gas-Liquid Contacting with Mechanical Agitation, *Transactions of the Institution of Chemical Engineers Part A*, **36**, 443-463.

Chang, T. P. K., Watson, A. T., and Tatterson, G. B. (1985a) Image processing of tracer particle motions as applied to mixing and turbulent flow--I. The technique, *Chemical Engineering Science*, **40**, 269-275.

Chang, T. P. K., Watson, A. T., and Tatterson, G. B. (1985b) Image processing of tracer particle motions as applied to mixing and turbulent flow--II. Results and discussion, *Chemical Engineering Science*, **40**, 277-285.

Chapman, C. M., Nienow, A. W., Cooke, M, and Middleton, J. C. (1983) Particle-gas-liquid mixing in stirred vessels. Part II. Gas-liquid mixing., *Transactions of the Institution of Chemical Engineers Part A*, **61**, 82-95.

Cheng, W., Murai, Y., Sasaki, T., and Yamamoto, F. (2005) Bubble velocity measurement with arecursive cross correlation PIV technique, *Flow Measurment & Instrumentation*, 35-46.

Choi, H. M., Kurihara, T., Monji, H., and Matsui, G. (2002) Measurement of particle/bubble motion and turbulence around it by hybrid PIV, *Flow Measurment & Instrumentation*, **12**, 421-428.

Ciofalo, M., Brucato, A., Grisafi, F., and Torraca, N. (1996) Turbulent flow in closed and free-surface unbaffled tanks stirred by radial impellers, *Chemical Engineering Science*, **51**, 3557-3573.

Clift, R., Grace, J. R., and Weber, M. E. (2005) Bubbles, Drops and Particles, Edition Dover, Dover, New York,

Collias, D. J. and Prud'homme, R. K. (1985) The effect of fluid elasticity on power consumption and mixing times in stirred tanks, *Chemical Engineering Science*, **40**, 1495-1505.

Delnoij, E., Westerweel, J., Deen, N. G., Kuipers, J. A. M., and van Swaai, W. P. M. (1999) Ensemble correlation PIV applied to bubble plumes rising in a bubble column, *Chemical Engineering Science*, 5159-5171.

Edwards, M. F., Baker, M. R., and Godfrey, J. C. (1992) 'Mixing of liquids in stirred tanks', Chapter 8 in Mixing in the process industries, Edition 2, Butterworth-Heinemann, Oxford, ISBN:0-750-63760-9.

Elson, T. P., Cheesman, D. J., and Nienow, A. W. (1986) X-ray studies of cavern sizes and mixing performance with fluids possessing a yield stress, *Chemical Engineering Science*, **41**, 2555-2562.

Escudié, R., Bouyer, D. , and Liné, A. (2004) Characterization of trailing vortices generated by a Rushton turbine, *AIChE Journal*, **50**, 75-86.

Fall, A., Lecoq, O., and David, R. (2001) Characterization of Mixing in a Stirred Tank by Planar Laser Induced Fluorescence (P.L.I.F.), *Transactions of the Institution of Chemical Engineers Part A*, **79**, 876-882.

Fomin, N. A. (1998) 'Velocity measurements', Chapter 8 in Speckle photography for fluid mechanics measurements, edited by Adrian, R. J., Gharib, M., Merzkirch, W., Rockwell, D., and Whitelaw, J. H., Springer, Heinelberg, Germany, ISBN:3-540-63767-2.

Fort, I., Drbohlav, J., Kratky, J., Grospicova, M. , and Krouzilova, Z. (1972) *Coll.Czech.Chem.Commun., as cited in Tatterson (1991)*

Fort, I., Placek, J., Kratky, J., Durdil, J., and Drbohlav, J. (2008) *Coll.Czech.Chem.Commun., as cited in Tatterson (1991)*

Frisch, U. (1995) 'The Kolmogorov 1941 theory', Chapter 6 in Turbulence - The lagacy of A. N. Kolmogorov, Edition 1st, Cambridge University Press, Cambridge, UK, ISBN:0 521 45713 0.

Gabriele, A., Nienow, A.W., Simmons, M.J.H. (2008) Use of angle resolved PIV to estimate energy dissipation rates for up- and down-pumping pitched blade agitators in a stirred tank, *Chemical Engineering Science,* in press.

Garcia-Ochoa, F. F and Gomez, E. **(2004)** Theoretical prediction of gas-liquid mass transfer coefficient, specific area and hold-up in sparged stirred tanks, *Chemical Engineering Science*, **59**, 2489-2501.

Gezork, K. M., Bujalski, W., Cooke, M, and Nienow, A. W. (2000) The transition from homogeneous to heterogeneous flow in a gassed, stirred vessel, *Transactions of the Institution of Chemical Engineers Part A*, **78**, 363-370.

Grasso, G., Harji, B., Xue, E., Belochapkine, S., and Ross, J. R. H. (2003) A modified robotic system for catalyst preparation by wet or dry impregnation, *Catalysis Today*, **81**, 369-375.

Greaves, M and Kobbacy, K. A. H. (1984) Measurement of bubble size distribution in turbulent gas liquid dispersion, *Transactions of the Institution of Chemical Engineers Part A*, **62**, 3-12.

Greaves, M and Barigou, M. (1988) The internal structure of gas-liquid dispersions in a stirred reactor, *6th European Conference on Mixing*, Pavia, Italy, 5-24-1988.

Grisafi, F., Brucato, A., and Rizzuti, L. (1994) Solid liquid mass transfer coefficients in mixing tanks: influence of side wall roughness., *Industrial Chemical Engineering Syposium*, **136**, 571-578.

Guibault, G. G. (1990) Practical Fluorescence, Marcel Dekker, New York., as cited in Baumann & Mühlfriedel (2002)

Günkel, A. A. and Weber, M. E. (1975) Flow phenomena in stirred tanks. Part I. The impeller stream, *AIChE Journal*, **21**, 931-939.

Haam, S. J., Brodkey, R. S., Fort, I., Klaboch, L., Placnik, M., and Vanecek, V. (2000) Laser Doppler anemometry measurements in an index of refraction matched column in the presence of dispersed beads: Part I, *International Journal of Multiphase Flow*, **26**, 1401-1418.

Hall, J. F., Barigou, M., Simmons, M. J. H., and Stitt, E. H. (2004) Mixing in Unbaffled High-Throughput Experimentation Reactors, *Industrial & Engineering Chemistry Research*, **43**, 4149-4158.

Hall, J. F., Barigou, M., Simmons, M. J. H., and Stitt, E. H. (2005a) Comparative study of different mixing strategies in small high throughput experimentation reactors, *Chemical Engineering Science*, **60**, 2355-2368.

Hall, J. F., Barigou, M, Simmons, M. J. H., and Stitt, E. H. (2005b) Just because it's small doesn't mean it's well mixed: Ensuring good mixing in mesoscale reactors, *Industrial & Engineering Chemistry Research*, **44**, 9695-9704.

Hall, J. F., Barigou, M., Simmons, M. J. H., and Stitt, E. H. (2005c) A PIV study of hydrodynamics in gas-liquid high throughput experimentation (HTE) reactors with eccentric impeller configurations, *Chemical Engineering Science*, **60**, 6403-6413.

Hall, J.F. (2005d) Fluid mechanics, mixing & mass transfer in high throughput experimentation reactors, *PhD Thesis*, The University of Birmingham.

Hassan, I. T. M. and Robinson, C. W. (1980) Mass-transfer-effective bubble coalescence frequency and specific interfacial area in a mechanically agitated gas-liquid contactor, *Chemical Engineering Science*, **35**, 1277-1289.

Hemrajani, R. R. and Tatterson, G. B. (2004) 'Mechanically Stirred Vessels', Chapter 6 in Handbook of Industrial Methods: Science and Practice, John Wiley & Sons, Hoboken, New Jersey, ISBN:0-471-26919-0.

Hendershot, R. J., Lasko, S. S., Fellmann, M. F., Oskarsdottir, G., Delgass, W. N., Snively, C. M., and Lauterbach, J. (2003) A novel reactor system for high throughput catalyst testing under realistic conditions, *Applied Catalysis A: General*, **254**, 107 -120.

Hill, D. F., Sharp, K. V., and Adrian, R. J. (2000) Stereoscopic particle image velocimetry measurements of the flow around a Rushton turbine, *Experiments in Fluid*, **29**, 478-485.

Hinsch, K. D. (1995) Three-dimensional particle velocimetry, *Measurement Science and Technology*, **6**, 742-753.

Hinsch, K. D. (2002) Holographic particle image velocimetry, *Measurement Science and Technology*, **13**, 61-72.

Hinze, J. O. (1975) Turbulence, McGraw-Hill, New York, ISBN:0-070-29037-7.

Hockey, R. M. and Nouri, J. M. (1996) Turbulent flow in a baffled vessel stirred by a 60° pitched blade impeller, *Chemical Engineering Science*, **51**, 4405-4421.

Honkanen, M., Saarenrinne, P., Stoor, T. and Niinimäki, J. (2005) Recognition of highly overlapping ellipse-like bubble images, *Measurement Science and Technology*, 16, 1760-1770.

Hoogendoorn, C. J. and den Hartog, A. P. (1967) Model studies on mixers in the viscous flow region, *Chemical Engineering Science*, **22**, 1689-1699.

Horn, D., Montante, G., Magelli, F., and Paglianti, A. (2007) Bubble size distribution and turbulent two-phase flow in aerated stirred vessels, *6th International Conference on Multiphase Flow*, Leipzig, Germany, 9-7-2007.

Houcine, I., Vivier, H., Plasari, H., David, R., and Villermaux, J. (1996) Planar laser induced fluorescence technique for measurements of concentration fields in continuous stirred tank reactors, *Experiments in Fluid*, **22**, 95-102.

Jaworski, Z. and Nienow, A. W. (1994) LDA measurement of flow fields with hydrofoil impellers in fluids with different rheological properties, *Eighth European Conference on Mixing*, Rugby, UK, 9-21-1994.

Jähne, B. (2002) Digital image processing, Springer Berlin Heidelberg, Berlin, Germany.

Keane, R. D. and Adrian, R. J. (1990) Optimization of particle image velocimeters. I. Double pulsed systems, *Measurement Science and Technology*, **1**, 1202-1215.

Keane, R. D. (1994) 'Correlation methods of PIV analysis', Optical diagnostics for flow processes, Plenum Press, New York, ISBN:0-306-44817-3.

Khan, F. R, Rielly, C. D., and Hargrave, G. D. (2004) A Multi-Block Approach to Obtain Angle-Resolved PIV Measurements of the Mean Flow and Turbulence Fields in a Stirred Vessel, *Chemical Engineering & Technology*, **27**, 264-269.

Khan, F.R. (2005) Investigation of turbulent flows and instabilities in a stirred vessel using particle image velocimetry, *PhD Thesis*, Loughbourgh University.

Khan, F. R., Rielly, C. D. , and Brown, D. A. R. (2006) Angle-resolved stereo-PIV measurements close to a down-pumping pitched-blade turbine, *Chemical Engineering Science*, **61**, 2799-2806.

Khopkar, A. R., Aubin, J., Xuereb, C., LeSauze, N. , Bertrand, J., and Ranade, V. V. (2003) Gas-Liquid Flow Generated by a Pitched-Blade Turbine: Particle Image Velocimetry Measurements and Computational Fluid Dynamics Simulations, *Industrial & Engineering Chemistry Research*, **42**, 5318-5332.

Kimme, C., Ballard, D. H., and Sklansky, J. (1975) Finding circles by an array of accumulators, *Comm.Associ.Comp.Mach.*, **18**, 120-122.

Kling, K. and Mewes, D. (2003) Quantitative measurements of micro- and macromixing in a stirred vessel using planar laser-induced fluorescence, *Journal of Visualisation*, **6**, 165-173.

Kramers, H., Baars, G. M., and Knoll, W. H. (1953) A comparative study on the rate of mixing in stirred tanks, *Chemical Engineering Science*, **2**, 35-42.

Kresta, S. M. and Wood, P. E. (1993) The flow field produced by a pitched blade turbine: Characterization of the turbulence and estimation of the dissipation rate, *Chemical Engineering Science*, **48**, 1761-1774.

Kudrewizki, F. (1982) Zur Berechnung des Gasgehaltes in begasten, *Riihrkesseln.Chem.Tech.*, **5**, 247-249.

Kudrewizki, F. and Rabe, P. (1986) Model of the dissipation of mechanical energy in gassed stirred tanks, *Chemical Engineering Science*, **41**, 2247-2252.

La Fontaine, R. F. and Shepherd, I. C. (1996) Particle image velocimetry applied to a stirred vessel, *Experimental Thermal and Fluid Science*, **12**, 256-264.

Laakkonen, M., Honkanen, M., Saarenrinne, P., and Aittamaa, J. **(2005)** Local bubble size distributions, gas-liquid interfacial areas and gas holdups in a stirred vessel with particle image velocimetry, *Chemical Engineering Journal*, **109**, 37-47.

Laakkonen, M., Moilanen, P., Alopaeus, V., and Aittamaa, J. **(2007)** Modelling local bubble size distributions in agitated vessels, *Chemical Engineering Science*, **62**, 721-740.

Lamping, S.R., Zhang, H., Allen, B. and Ayazi Shamlou, P. (2003) Design of a prototype miniature bioreactor for high throughput automated bioprocessing, *Chemical Engineering Science*, **58**, 747-758.

Lane, G. L., Schwarz, M. P., and Evans, G. M. (2005) Numerical modelling of gas-liquid flow in stirred tanks, *Chemical Engineering Science*, **60**, 2203-2214.

Law, A. W. K. and Wang, H. (2000) Measurement of mixing processes with combined digital particle image velocimetry and planar laser induced fluorescence, *Experimental Thermal and Fluid Science*, **22**, 213-229.

Marsall, E. M. and Bakker, A. (2004) 'Computation Fluid Mixing', Chapter 5 in Handbook of Industrial Methods: Science and Practice, John Wiley & Sons, Hoboken, New Jersey, ISBN:0-471-26919-0.

Mavros, P., Xuereb, C., and Bertrand, J. (1996) Determination of 3-D flow fields in agitated vessels by Laser-Doppler Velocimetry : Effect of Impeller Type and Liquid Viscosity on Liquid Flow Patterns, *Transactions of the Institution of Chemical Engineers Part A*, **74**, 658-668.

Mavros, P. (2001) Flow Visualization in Stirred Vessels: A Review of Experimental Techniques, *Transactions of the Institution of Chemical Engineers Part A*, **79**, 113-127.

Mazzarotta, B. (1993) Comminution phenomena in stirred sugar suspensions, *AIChE Journal*, **89**, 112.

Meille, V., Pestre, N., Fongarland, P., and Bellefon, C. (2004) Gas/Liquid mass transfer in small laboratory batch reactors: Comparison of methods, *Industrial & Engineering Chemistry Research*, **44**, 924-927.

Melling, A. (1997) Tracer particles and seeding for particle image velocimetry, *Measurement Science and Technology*, **8**, 1406-1416.

Middleton, J. C. (1992) 'Gas-Liquid dispersion and mixing', Chapter 15 in Mixing in the Process Industries, Edition 2, Butterworth-Heinemann, Oxford, ISBN:0-750-63760-9.

Middleton, J. C. and Smith, J. M. (2004) 'Gas-Liquid Mixing in Turbulent Systems', Chapter 11 in Handbook of Industrial Methods: Science and Practice, John Wiley & Sons, Hoboken, New Jersey, ISBN:0-471-26919-0.

Montante, G., Paglianti, A., and Magelli, F. (2007) Experimental analysis and computation modelling of gas-liquid stirred vessels, *Transactions of the Institution of Chemical Engineers Part A*, **85**, 647-653.

Morud, K. E. and Hjertager, B. H. (1996) LDA measurements and CFD modelling of gas-liquid flow in a stirred vessel, *Chemical Engineering Science*, **51**, 233-249.

Moulijn, J. A., Perez-Ramirez, J., Berger, R. J., Hamminga, G., Mul, G., and Kapteijn, F. (2003) High-throughput experimentation in catalyst testing and in kinetic studies for heterogeneous catalysis, *Catalysis Today*, **81**, 457-471.

Nagata, S. (1975) Mixing: Prinicple and applications, Edition 1, Kodansha Scientific Books, Tokyo, Japan, ISBN:0-470-62863-4.

Nienow, A. W., Wisdom, D. J., and Middleton, J. C. (1977) The effect of scale and geometry on flooding, recirculation and power in gassed stirred vessels, *Second European Conference on Mixing*, Cambridge, 3-30-1977.

Nienow, A. W. (1997) On impeller circulation and mixing effectiveness in the turbulent flow regime , *Chemical Engineering Science*, **52**, 2557-2565.

Nouri, J. M. and Whitelaw, J. H. (1990) Effect of Size and Confinement on the Flow Characteristics in Stirred Reactors, *Proc. Int. Symp.on Application of Laser Techniques to Fluid Mechanics*, Lisbon, Portugal.

Prasad, A. K. (2000) Stereoscopic particle image velocimetry, *Experiments in Fluids*, **29**, 103-116.

Raffel, M., Willert, C., and Kompenhans, J. (1998) Particle Image Velocimetry: a practical guide, Edition 1st, Springer, Berlin, Germany, ISBN:3-540-63683-8.

Rennie, J. and Valentin, F. H. H. (1968) Gas dispersion in agitated tanks, *Chemical Engineering Science*, **23**, 663-664.

Rushton, J. H., Costich, E. W., and Everett, H. J. (1950) Power characteristics of mixing impellers, *Chemical Engineering Progess*, **46**, 395.

Russ, J. C. (2002) The image processing handbook, Edition 4th, CRC Press, New York.

Ruszkowski, S. (1994) A rotational method for measuring blending performance, and comparison of different impeller types, *Eighth European Conference on Mixing*, Rugby, UK, 9-21-1994.

Rutherford, K., Mahmoudi, S. M. S., Lee, K. C., and Yianneskis, M. (1996) The influence of Rushton impeller blade and disk thickness on the mixing characteristics of stirred vessels, *Transactions of the Institution of Chemical Engineers Part A*, **74**, 369-378.

Saarenrinne, P., Piirto, M., and Eloranta, H. (2001) Experiences of turbulence measurement with PIV, *Measurement Science and Technology*, **12**, 1904-1910.

Schäfer, M., Yianneskis, M., Wächter, P., and Durst, F. (1998) Trailing vortices around a 45° pitched-blade impeller, *AIChE Journal*, **44**, 1233-1246.

Sharp, K. V. and Adrian, R. J. (2001) PIV Study of small-scale flow structure around a Rushton turbine, *AIChE Journal*, **47**, 766-778.

Sheng, J., Meng, H., and Fox, R. O. (2000) A large eddy PIV method for turbulence dissipation rate estimation, *Chemical Engineering Science*, **55**, 4423-4434.

Smagorinski, J. (1963) General circulation experiments with the primitive equation I the basic experiment., *Monthly Weather Review*, **91**, 99-164.

Spivack, J. L., Cawse, J. N., Whisenhunt, D. W., Johnson, B. F., Shalyaev, K. V., Male, J., Pressman, E. J., Ofori, J. Y., Soloveichik, G. L., Patel, B. P., Chuck, T. L., Smith, D. J., Jordan, T. M. , Brennan, M. R., Kilmer, R. J., and Williams, E. D. (2003) Combinatorial discovery of metal co-catalysts for the carbonylation of phenol, *Applied Catalysis A: General*, **254**, 5-25 .

Tatterson, G. B. (1991) Fluid mixing and gas dispersion in agitated tanks, McGraw-Hill, New York, ISBN:0-07-062933-1.

Tassin, A.L. and Nikitopoulos, D.E. (1995) Non-intrusive measurements of bubble size and velocity, *Experiments in Fluids*, **19**, 121-232.

van't Riet, K. and Smith, John M. (1973) The behaviour of gas-liquid mixtures near Rushton turbine blades, *Chemical Engineering Science*, **28**, 1031-1037.

van de Vusse, J. G. (1955) Mixing by agitation of miscible liquids Part I, *Chemical Engineering Science*, **4**, 178-200.

Warmoeskerken, M. M. C. G and Smith, J. M. (1985) Flooding of disc turbines in gas-liquid dispersions: a new description of the phenomanon, *Chemical Engineering Science*, **40**, 2063-2071.

Yianneskis, M. and Whitelaw, J. H. (1993) On the structure of the trailing vortices around Rushton Turbine blades, *Transactions of the Institution of Chemical Engineers Part A*, **71**, 543-550.

Yoon, H. S., Sharp, K. V., Hill, D. F., Adrian, R. J., Balachandar, S., Ha, M. Y., and Kar, L. (2001) Integrated experimental and computational approach to simulation of flow in a stirred tank, *Chemical Engineering Science*, **56**, 6635-6649.

Zalc, J. M., Alvarez-Hernández, M. M., Muzzio, F. J., and Arik, B. E. (2001) Extensive validation of computed laminar flow in a stirred tank with three Rushton turbines, *AIChE Journal*, **47**, 2144-2154.

Zlokarnik, M. (2001) 'General stirring', Chapter 1 in Stirring : Theory and Practice, Wiley-VCH, Weimheim, Germany, ISBN:3-527-29996-3.